Hydrodynamics of small marine organisms: A mechanistic exploration of traits and trade-offs for flagellates and filter feeders

Dölger, Julia

Publication date:
2018

Document Version
Publisher's PDF, also known as Version of record

DTU Physics
Department of Physics

Centre for Ocean Life
VKR Centre of Excellence

DTU

Ph.D. thesis

Hydrodynamics of small marine organisms

A mechanistic exploration of traits and trade-offs for flagellates and filter feeders

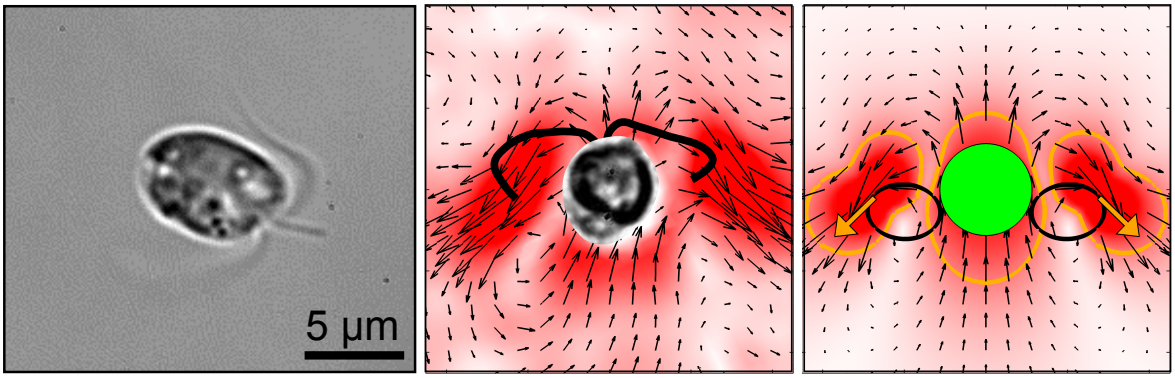

Julia Dölger

2 March 2018

Supervised by Anders Andersen, Thomas Kiørboe and Tomas Bohr

Cover image:
An individual of the flagellate *Prymnesium parvum* (left); measured instantaneous velocity field of *P. parvum* (middle) and modelled velocity field using two left-right symmetric point forces representing the flagella and a no-slip sphere as the cell body (right). Haptophyte image by courtesy of Lasse Tor Nielsen, DTU.

Hydrodynamics of small marine organisms – A mechanistic exploration of traits and trade-offs for flagellates and filter feeders

Typeset using LaTeX

Abstract

Although typically not visible to the naked eye, planktonic organisms play key roles for the functioning of the aquatic ecosystem. They display a huge morphological and functional diversity ranging from microscopic bacteria to meter-sized gelatinous organisms. Due to their intimate interaction with the water as habitat and medium, flows are essential to the survival strategies of plankton. Many, even unicellular, species are motile and create various kinds of flows that accompany swimming and can be used for prey and nutrient collection. On the other hand, the flow disturbances due to prey organisms can also be used by predators for remote detection via flow-sensing. In this study we use mechanistic models to explore and quantify the traits and trade-offs that relate to the swimming, feeding, and predator avoidance in small marine organisms.

Unicellular flagellates create flows with whip-like appendages that in different species can have various numbers, lengths, and beat patterns. We use an analytical hydrodynamics model to distinguish those characteristics. We represent the cell body as a solid sphere and the action of each flagellum by a point force on the water that creates a flow and propels the organism. The different swimming modes are quantified by the number, magnitude, position, and direction of the point forces in the model, which lead to specific flow patterns and kinematics. We use the model to represent two biflagellated haptophyte species that both have a left-right symmetric flagellar arrangement, but different lengths and beat patterns. The time-resolved near-cell flows that are measured with micro particle image velocimetry can be well represented by the analytical model and allow us to assign characteristic average force positions to the two species. By calculating swimming speed, size of the disturbance zone, and advective prey encounter rates for different force positions, we find that equatorial arrangements are favoured for fast and stealthy swimming, while puller swimmers with front arrangements exhibit increased prey encounter rates. We present further possibilities of the model to evaluate the swimming speed due to different forces during a periodic swimming stroke and to calculate characteristics of the helical trajectory for asymmetric swimmers.

A second group of organisms that we investigate are filter feeders that use fibrous filter structures to collect and sieve prey from the dilute suspension that ocean water represents. We study microbial filter feeding on the example of choanoflagellates, which are unicellular organisms that use a single flagellum to drive a feeding flow through a collar filter. The volume flow rates of individuals measured with micro particle tracking velocimetry by far exceeded numerically simulated and analytically estimated maximum flow rates based on the observed flagellum kinematics. This discrepancy and previous findings of so-called flagellar vanes in related species lead us to suggest such a structure in several choanoflagellate species, which can increase the driving force of the flagellar beat and can account for the large measured flow rates as we indicate with computational fluid dynamics and analytical calculations. We further consider a trade-off which leads to optimum filter spacings for maximum prey encounter. The flagellar driving force can create large flow rates through a coarse mesh due to low resistance, while a fine mesh can retain a larger range of prey sizes from the suspension.

Another theme is the emergence of large gelatinous body plans among planktonic filter feeders. Gelatinous organisms are characterised by a much more watery body composition than the typical cell. In order to understand and quantify the general trade-offs for filter feeders with different body plans we developed an energy budget model. The model accounts for energy intake from prey collection and energy expenditure from active flow creation as well as basal respiration. The prey clearance rates of filter feeders are found to be limited by the maximum force that their biological motor can create. The filter area per body biomass needs to be large to prevent starvation. Thus a simple, but wide-ranging result of the model is that larger organisms (with a large biomass) have a stronger need than microbes to increase their area and they do this by becoming gelatinous.

As a last study of this project we explore the effect of prey size on prey capture rates by organisms, which encounter their prey directly on the cell surface. We numerically calculate the advective-diffusive capture of finite-sized prey on a spherical cell in a simple Stokes flow. We find high capture rates both for the smallest and the largest prey, and we identify a minimum of the capture rate for intermediate prey. We rationalise and explain the observed trends in an analytical model for the capture of finite-sized prey. We additionally investigate "sloppy" feeders, which exhibit severe prey losses when the predator-prey contact time is short. Sloppy feeders mainly lose small diffusive particles, such that they predominantly capture the largest prey.

Resumé (Danish)

Planktonorganismer er typisk ikke synlige med det blotte øje, men på trods af dette spiller de en nøglerolle i havets og de ferske vandes økosystemer. De udviser en enorm morfologisk og funktionel diversitet, der strækker sig fra mikroskopiske bakterier til meterstore geléagtige organismer. På grund af vands rolle som levested og medium spiller strømninger en central rolle for overlevelsesstrategier for plankton. Mange arter svømmer og skaber strømninger, der understøtter fødefangst og optag af opløste næringssalte, men samtidigt gør strømningerne organismerne sårbare og synlige for rovdyr, som kan detektere strømningsforstyrrelser. I dette studie bruger vi mekanistiske modeller til at udforske og kvantificere fordele og ulemper ved små marine organismers forskellige strategier for svømning, fødeoptag og beskyttelse mod rovdyr.

Encellede flagellater bruger tynde flageller (svingtråde) til at svømme og skabe fødestrømme, og forskellige arter udviser stor variation i antal, længde og slagmønstre af deres flageller. Vi bruger en hydrodynamisk model til at kvantificere disse karakteristika. I modellen er cellen repræsenteret af en massiv kugle og hver flagel af en punktkraft, der virker på vandet og skaber strømning og fremdrift. Forskellige svømmemåder og strømninger kvantificeres af antal, placering, styrke og retning af punktkræfterne i modellen. Vi bruger modellen til at repræsentere to arter af haptofytter (stilkalger), der begge er udstyrede med to flageller i venstre-højre symmetriske arrangementer, men som har meget forskellige flagellængder og slagmønstre. Modellen beskriver de tidsopløste strømninger nær cellen, som blev målt med mikro-PIV omkring frit svømmende individer, og modellen tillader os at tilordne gennemsnitlige kraftpositioner for hver af de to arter. Ved at beregne svømmehastighed, udstrækning af område med strømningsforstyrrelse og fangstrater for forskellige kraftplaceringer finder vi, at ækvatoriale arrangementer tilgodeser hurtig svømning med lille strømningsforstyrrelse, hvorimod kræfter foran cellen understøtter høj fangstrate. Desuden bruger vi modellen til at beskrive bidrag fra forskellige dele af periodiske svømmetag til svømning, og vi præsenterer en analyse af spiralformede svømmespor for asymmetriske svømmere.

En anden gruppe af organismer, som vi undersøger, er filtratorer, der bruger filtre af tynde fibre til at filtrere det omgivende vand for føde. Som eksempel på mikrometerstore planktonorganismer med denne strategi undersøger vi kraveflagellater, som er encellede organismer, der med en enkelt flagel skaber en fødestrøm gennem et kraveformet filter. Målte strømningsrater for frit svømmende kraveflagellater overstiger med en størrelsesorden analytiske estimater og værdier bestemt med CFD, som baserer sig på den beskrevne morfologi og den observerede bevægelse af flagellen. Denne uoverensstemmelse og tidligere observationer af vingeagtige strukturer på flageller hos beslægtede arter leder os til at foreslå, at sådanne vingeagtige strukturer er mere almindelige blandt kraveflagellater end almindeligt antaget. Med CFD og analytiske estimater viser vi, at de vingeagtige strukturer kan øge strømningsraten og forklare de høje eksperimentelle værdier hos den undersøgte art af kraveflagellater. Vi undersøger videre de afvejninger, der bestemmer den optimale filterafstand med maksimal fangstrate. En given kraft kan skabe en kraftig fødestrøm gennem et groft filter, hvorimod et fint filter kan indfange et bredt størrelsesspektrum af bytte.

Et andet spørgsmål er udviklingen af geléagtige filtratorer blandt plankton. Geléagtige organismer er vandige og har et langt lavere indhold af kulstof end almindelige celler. For at undersøge og kvantificere effekter af kulstofindhold og størrelse af plankton, der lever af filterfangst, har vi opstillet en model for et individs energibudget. Modellen beskriver energioptaget ved filterfangst og energiomkostningerne ved at skabe fødestrøm og opretholde den basale metabolisme. Et simplet, men vidtrækkende, resultat af modellen er, at store filtratorer er tvunget til at være geléagtige for at kunne have tilstrækkeligt stort filterareal til at undgå at sulte. Små encellede organismer er ikke pressede på samme måde, og de kan have almindelig højt kulstofindhold.

I det sidste studie i projektet udforsker vi effekten af byttestørrelse på byttefangst for organismer, der fanger deres bytte direkte på celleoverfladen. Numerisk bestemmer vi fangst af bytte med endelig størrelse på en kugleformet celle i en simpel Stokes strømning med bidrag fra både advektion og diffusion. Vi finder høje fangstrater for både små og store bytteorganismer, og vi identificerer et minimum for fangstraten for mellemstore bytteorganismer. Vi rationaliserer og forklarer de observerede tendenser i en analytisk model med bytte af endelig størrelse. Derudover udforsker vi "sjuskede" organismer, der ikke holder fast i alt bytte, som kommer nær deres celleoverflade, hvis kontakttiden mellem organisme og bytte er kort. Vi finder, at sjuskede organismer primært taber små bytteorganismer, men er bedre til at fastholde de store.

Preface

This thesis is submitted as partial fulfilment of the requirements for obtaining the degree of Doctor of Philosophy (Ph.D.) at the Technical University of Denmark (DTU). The Ph.D. project was carried out at the Department of Physics at DTU, and as a member of the Complex Motion in Fluids Group, during a three-year period from 15 December 2014 to 14 December 2017. I gratefully acknowledge funding support from DTU Physics and from the Villum Kann Rasmussen Foundation, as well as two travel grants from the COST Action MP1305 (Flowing Matter) and three travel grants from the Otto Mønsted Foundation.

Kgs. Lyngby, 2 March 2018

Julia Dölger

Personal acknowledgement

I am thankful that I had the opportunity for this Ph.D. project at DTU Physics and am especially grateful to my main supervisor, Anders Andersen, who I enjoyed working with and who I learned a lot from. He invested a large amount of his time in my supervision and was always extremely friendly, patient, and supportive.

I would also like to thank my co-supervisors Thomas Kiørboe and Tomas Bohr, who I had the privilege to work with. I greatly appreciated that Thomas Kiørboe always had our ultimate goals in mind and made sure that my work progressed in the right direction tackling ecologically important questions. Tomas Bohr is an amazing and fun person to work with and often saw fascinating questions and details, that I had previously missed. I had many valuable and interesting discussions with him and felt very valued by him as a colleague.

In spring 2017 I had the opportunity to spend two months working with Marco Polin at the University of Warwick. I felt very welcomed in his group and enjoyed his supervision and our on-going collaboration. The discussions with Marco and Raphaël Jeanneret, who I also would like to thank, were always inspiring, motivating and packed with valuable wisdom.

I further would like to thank Lasse Tor Nielsen, who I had the pleasure to collaborate with. I very much enjoyed the discussions I had with him and benefited from his knowledge on the fascinating biology of our study species. I would also like to thank him for providing me with images and videos of flagellates for various presentations, papers, and this thesis.

I thank Seyed Saeed Asadzadeh and Jens H. Walther for the collaboration and discussions on the choanoflagellate project.

A further thanks to Kelly R. Sutherland and Keats Conley as well as to Erik Selander for providing me with images of pelagic tunicates and copepods.

I thank Anders Andersen, Hanna Rademaker, Navish Wadhwa, Tomas Bohr, and Bettina Dölger for carefully reading drafts and providing helpful feedback on this thesis.

My main workplace was the FLUIDS Section at DTU Physics, but due to my involvement in the Centre for Ocean Life, I also regularly visited DTU Aqua. Both workplaces provided a stimulating and friendly atmosphere with many nice and open-minded colleagues, which I highly appreciated.

Finally, I am immeasurably grateful for the continuous encouragement and support of my family and friends.

Table of Contents

Version: 2 March 2018

List of symbols

Symbol	Description	Value and units
$()^T$	transposed vector or tensor	
$\partial()/\partial()$	partial derivative	
$\boldsymbol{\nabla}$	gradient	
$\boldsymbol{\nabla}_{\mathbf{x}_\mathrm{p}}$	gradient along the direction $\mathbf{x}_\mathrm{p}$	
$()_\parallel$	vector component parallel to certain reference direction	
$()_\perp$	vector component perpendicular to certain reference direction	
$() \cdot () = ()^T()$	scalar or dot product	
$() \times ()$	vector or cross product	
$() \otimes () = ()()^T$	outer product	
a	radius of sphere or cylinder	m
b	half-length of slender body	m
c	concentration (of prey)	kg m^{-3} or J m^{-3}
d	diameter of tracer particle	m
D	diffusion coefficient	m^2 s-1
$\mathbf{d}$	separation vector	m
$\mathbf{D}$	Stokes drag force on a sphere	N
$\boldsymbol{\mathcal{D}}$	force dipole moment (tensor)	N m
$\mathbf{f}$	force density (per volume or length)	N m^{-3} or N m^{-1}
$\mathbf{F}$	force on water	N
g	gravitational acceleration	9.81 m s^{-2}
G	ingestion rate	
$\boldsymbol{\mathcal{G}} = \boldsymbol{\mathcal{G}}(\mathbf{x})$	Greens function representing the fundamental Stokes flow (tensor)	
H	scope for growth	
$\boldsymbol{\mathcal{I}}$	identity (tensor)	dimensionless
$J(\mathbf{x}_\mathrm{p})$	flux density	m s^{-1}
k	power law exponent	dimensionless
$\mathbf{K}$	force on sphere due to Stokeslet	N
k_B	Boltzmann constant	$1.38 \cdot 10^{-23}$ J K^{-1}
l	filter spacing	m
L	characteristic length	m
$\mathbf{L}$	torque on body	N m
M	characteristic mass	kg

$\mathbf{n}$	outwards normal from surface	
N	integer number	
$p = p(\mathbf{x})$	pressure	Pa
P	power	J s^{-1}
Pe	Péclet number	dimensionless
q	clearance rate per unit length	m^2 s^{-1}
Q	volume flow rate or clearance rate	m^3 s^{-1}
$r = \|\mathbf{x}\|$	distance from origin	m
r_p	spherical radius of prey particle	m
R	general or metabolic cost, often measured as respiration rate	
Re	Reynolds number	dimensionless
S	boundary surface	m^2
Sh	Sherwood number	dimensionless
t	time	s
T	temperature	K
$\mathbf{t}$	force on segment per unit length	N m−1
$\mathbf{T}$	force on body (as opposed to force $\mathbf{F}$ on water)	N
$\mathbf{u}$	velocity of surface element or of prey particle	m s^{-1}
$\mathbf{U}$	characteristic translational velocity	m s^{-1}
V	volume	m^3
$\mathbf{u}_\mathrm{p}$	active prey swimming velocity	m s^{-1}
$\mathbf{v} = \mathbf{v}(\mathbf{x})$	flow velocity	m s^{-1}
$\mathbf{v}^\infty$	external flow	m s^{-1}
$\mathbf{x}$	point in space	m
$\mathbf{X}$	point force position	m
$\mathbf{X}^*$	image point	m
$\mathbf{x}_\mathrm{p}$	point on physical boundary	m
α	volume fraction of filter	dimensionless
γ	Einstein-Smoluchowski friction coefficient	N s m^{-1}
Γ	filter drag parameter	dimensionless
$\delta(\mathbf{x})$	delta distribution	
ϵ	small parameter	< 1
ζ	drag coefficient for slender body	Pa s
Λ	filter drag parameter	dimensionless
μ	dynamic viscosity of water	10^{-3} Pa s
$\xi = \zeta/\mu$	dimensionless drag coefficient	dimensionless
ρ	mass density of water	10^3 kg m^{-3}
ρ_S	mass density of solid body	kg m^{-3}
σ_max	maximum tension	Pa
$\boldsymbol{\sigma} = \boldsymbol{\sigma}(\mathbf{x})$	stress (tensor)	Pa
$\Psi(r, \theta)$	two-dimensional stream function	m^2 s^{-1}
$\boldsymbol{\omega}$	rotational velocity	s^{-1}

$\boldsymbol{\Omega}$	rotational velocity	s^{-1}

List of original papers

Paper I: Julia Dölger, Tomas Bohr, and Anders Andersen. An analytical model of flagellate hydrodynamics. *Physica Scripta*, 92: 044003, 2017.

Paper II: Julia Dölger, Lasse Tor Nielsen, Thomas Kiørboe, and Anders Andersen. Swimming and feeding of mixotrophic biflagellates. *Scientific Reports*, 7: 39892, 2017

Paper III: Lasse Tor Nielsen, Seyed Saeed Asadzadeh, Julia Dölger, Jens H. Walther, Thomas Kiørboe, and Anders Andersen. Hydrodynamics of microbial filter feeding. *Proceedings of the National Academy of Sciences*, 114(35): 9373–9378, 2017

Paper IV: Julia Dölger, Thomas Kiørboe, and Anders Andersen. Dense dwarfs versus gelatinous giants: The trade-offs determining the body composition of planktonic filter feeders. *Manuscript in preparation*

Paper V: Julia Dölger, Raphaël Jeanneret, Anders Andersen, and Marco Polin. Advective-diffusive capture of finite-sized prey by direct interception feeders. *Manuscript in preparation*

1 Introduction

1.1 The trait-based approach to ocean life

Marine ecosystems can be immensely complex with a large number of species, ranging from bacteria and viruses to blue whales, the diverse survival strategies of which are influenced by biotic and abiotic factors of their environment. Basic interactions between organisms are predator-prey interactions, mating, and competition for resources that are often constrained by simple physical laws, for example "large eats small". Unicellular organisms as the base of the food web completely rely on abiotic environmental resources such as light and dissolved nutrients, while larger species are only indirectly affected by those resources through trophic interactions with lower levels. However, there are other external factors such as the physical properties of the water as universal habitat that affect all life forms directly and based on which all physical interactions take place.

What is often lacking in classical ecosystem models is the fundamental understanding of the underlying physical mechanisms that determine how individuals interact with each other and with their changing and fluctuating environment [McGill et al., 2006]. Classical ecosystem models are population dynamics models based on species and can form complex food webs [Murray, 1993]. This approach can be useful for confined ecosystems, where the species interactions, such as "who eats who", are known. However, by exploring the underlying mechanisms that explain individual strategies, we can gain a deeper understanding of the ecosystem and its key players. Through an analysis of individual strategies we can identify the most important characteristics of an organism, so-called functional traits, which determine its functional role and success (fitness) in an ecosystem and which are interrelated through trade-offs [Anderson, 2005; Litchman et al., 2013; Pawar et al., 2015]. The trait-based approach thus aims to describe how structure and function of ecological communities emerge from properties of the individual organism. With this approach ecosystem models can often be greatly simplified and at the same time made more predictive, since species are replaced by individuals with specific trait combinations and functional dependences [McGill et al., 2006; Litchman and Klausmeier, 2008; Follows and Dutkiewicz, 2011; Litchman et al., 2013].

Central to a trait-based description is a quantification of the trade-offs associated with the key traits, i.e., the benefits and costs of a particular trait. The success in executing the three main functions of any organism – to acquire resources, to survive, and to reproduce – is the main determinant of its fitness, but the execution of any one of these functions may conflict with the others. Thus, there are no "super-organisms"

that perform optimally in all respects [Litchman and Klausmeier, 2008; Litchman et al., 2013]. Behaviours, morphologies, and life-histories are shaped by natural selection by balancing these trade-offs, and by environmental conditions that impact the trade-off functions. Trait distributions in nature depend directly on those compromises, and hence, it is a key ingredient in the trait-based approach to quantify trade-offs. Often trade-offs are determined empirically, but preferentially trade-off functions should be based on a mechanistic understanding of the underlying processes to allow deeper insights and better predictive power.

Individual-based and mechanistic approaches have already been used in terrestrial as well as in marine evolutionary ecology [Schoener, 1986; Koehl and Wolcott, 2004]. One example is the derivation of ingestion rate curves as function of prey concentration for organisms with different feeding strategies [Lehman, 1976; Jeschke et al., 2004; Wirtz, 2012]. The mechanistic trait-based approach can be considered as an extension of evolutionary ecology. While evolutionary ecology is also rooted in traits and trade-offs, it mainly uses these for fitness optimization, to explain speciation and to explore adaptive dynamics. The additional step in the trait-based approach is to scale up to species-transcending trait distributions to describe communities and trait biogeographies, and it thus merges evolutionary ecology and classic population and community ecology into its own, new branch of ecology.

One of the most important traits, a master trait relevant to all organisms, is the body size. Based on this continuous physical trait, life in the ocean can be sorted into a hierarchical structure. Many other traits of an organism depend on its size, such as mobility, sensing, and resource acquisition strategies. Also its trophic level, i.e., its height in the food web, and its vital rates change characteristically with size [Fenchel, 1988; Andersen et al., 2016; Martens et al., 2016; Andersen, 2017]. Such dependences on size are often expressed as power laws, which give some of the most important quantitative results of patterns in biology [Schmidt-Nielsen, 1984].

1.2 Hydrodynamics of small organisms

A central aspect that we consider are hydrodynamic mechanisms, since water forms the medium through which all interactions need to be transmitted. Thus we can identify important key traits by the investigation of flows around organisms. On the small length scales that we consider, the fluid provides a substantial barrier to movement and is not easily manipulated to support essential needs such as prey collection. At the same time flow disturbances of moving organisms reach far and attract predators.

The fascinating world of swimming microorganisms has been brought to the attention of physicists by several influential hydrodynamics studies [Taylor, 1951; Lighthill, 1952; Gray and Hancock, 1955; Lighthill, 1976; Purcell, 1977]. Those works introduced the variety of small-scale flows that can be created by aquatic organisms and the physical laws that govern the hydrodynamics and physical interactions of microswimmers. Additionally novel tools for the quantification of swimming patterns and microfluidics became available [Berg, 1971; Raffel et al., 2007]. Many experimental, numerical and

analytical studies followed, which investigated the hydrodynamics of small organisms. The main focus from a physical point of view has been optimal modes of swimming and other physical aspects such as the properties of microswimmer suspensions, where pairwise swimmer interactions as well as macroscopic patterns of such active fluids are studied [Elgeti et al., 2011; Lauga and Powers, 2009].

Multipole expansions of the creeping flow have been an important mathematical tool to study the flows around small organisms. Such mathematical tools allow the approximation of far field flow and characteristic hydrodynamic patterns around swimmers and allow us to estimate forces on slender swimming appendages using fundamental flow singularities [Gray and Hancock, 1955; Brennen and Winet, 1977; Lauga and Powers, 2009]. The solid boundary of swimmer bodies is usually modelled with zero flow velocity at the surface (no-slip), while the squirmer model [Lighthill, 1952; Blake, 1971] as an exception approximates the movement of many short appendages (cilia) as an effective slip velocity on the swimmer surface. The hydrodynamics and prey capture by filter feeders have mainly been studied using the well established tools of hydrosol and aerosol theory [Rubenstein and Koehl, 1977], which mainly focus on efficiency measures relevant to industrial filters [Pich, 1966; Dorman, 1966].

There are only few model organisms such as *Escherichia coli*, *Chlamydomonas sp.* and *Volvox sp.*, the physics of which are being studied extensively [Berg, 2004; Goldstein, 2015], while the morphological and functional variety of ecologically important species is often neglected in hydrodynamics studies [Jones, 1994; Sleigh, 1981]. Further the trade-offs between different functions are usually not explicitly explored, but different mechanisms and their optimisation are rather discussed separately. Many questions regarding emerging patterns in planktonic ecosystems and trade-offs for small marine organisms, which have been addressed mainly by biologists and ecologists, are related to physical mechanisms [Rubenstein and Koehl, 1977; Fenchel, 1986, 1988; Shimeta, 1993; Acuña et al., 2011; Kiørboe, 2011; Kiørboe et al., 2014; Andersen et al., 2016]. The relevant issues lead to many unanswered questions that range from the function and structure of planktonic food webs and the specific trade-offs for swimming and resource acquisition modes to the emergence of gelatinous plankton. Those problems are often more broad and complex than the straight-forward optimisation tasks that might be posed from a narrow physical viewpoint. However, after the essential parameters are disentangled, the mechanisms can often be traced back to simple physical interactions of individuals through and with the ocean water. It is thus an exciting and promising opportunity for a physicist to delve into those unknown realms and to tackle unanswered ecological questions with the tools of physics [Guasto et al., 2012].

Our main goal is thus not necessarily to develop completely new tools, but to use and combine existing methods and results from physics in order to study the survival strategies of individual organisms. The first Ph.D. study at the Centre for Ocean Life using this approach was conducted by Navish Wadhwa [2015], who studied the hydrodynamical traits and trade-offs of zooplankton with a focus on swimming and predator-prey detection.

1.3 Framework and focus of this thesis

The Centre for Ocean Life, which I am part of, is an interdisciplinary collaborative research centre spanning five departments at three different universities. The aim of the centre is to develop and implement the trait-based approach to life in the ocean in order to promote a fundamental understanding and predictive capacity of marine ecosystems. The efforts at the centre are divided in three themes. In the first theme (*Individual*), which my project mainly fits in, we identify the key traits and trade-offs based on a mechanistic understanding of physical interactions [Kiørboe, 2008]. In the second theme (*Models*) the identified traits are used to build trait-based ecosystem models to predict trait distributions and their variations due to temporal changes such as seasonal succession and climate change. The third theme (*Nature*) investigates trait distributions and spatio-temporal patterns in marine environments and tests model predictions. Recently a fourth theme (*Function*) has been added, which explores ecosystem functions such as fishing yield and carbon export with the trait-based approach.

In this Ph.D. project I focus on planktonic flagellates and filter feeders. Our aim is to identify and quantify physical species-overarching traits, which determine the interactions of individuals with their environment and the combination of which leads to individual survival strategies.

Many unicellular marine organisms are mixotrophic and thus not only employ sunlight and dissolved nutrients as resource, but are further able to capture particulate prey. This flexible mixture of strategies, which allows a continuous transition between plants and animals, has recently received increased attention in studies of marine trophic strategies [Flynn et al., 2013; Berge et al., 2016].

In our investigations of flagellates (paper I and paper II) we use an analytical hydrodynamics model and experimental measurements of the kinematics and flow around two mixotrophic haptophyte species to study the effect of flagellar arrangements and beat patterns on vital functions. The essential functions are propulsion to reach favourable locations, the creation of feeding currents to collect prey, and hydrodynamic stealth to avoid the attention of flow-sensing predators. The analytical model includes the cell body as solid no-slip sphere, while the flagellar action is modelled with point forces. The hydrodynamic effect of the flagella as long structures is neglected, so actual force or power investments of the swimmer are hard to determine. However, the model enables us to study near-cell flows essential for prey capture and swimming drag as well as for the size of disturbance zones due to various flagellar swimming modes. In paper II we are thus able to identify trade-offs between swimming speed, advective prey capture, and flow disturbance based on characteristic force arrangements in mixotrophic biflagellates, while paper I presents the general model framework and gives an overview of the potential applications to study further trade-offs related to different motility modes in flagellates.

In paper III and paper IV we study planktonic filter feeders. This feeding strategy involves prey capture on fibrous structures (filters) and is successfully used by microscopic unicellular as well as centimetre-sized zooplankton. One characteristic of such

animals is that the prey size is microscopic and often nearly independent of predator size [Fenchel, 1986; Lombard et al., 2011].

An important group of unicellular filter feeders are choanoflagellates that possess one flagellum which drives a feeding current through a collar filter [Fenchel, 1982; Leadbeater, 2015]. In paper III we use flow measurements on one choanoflagellate species as well as computational and analytical modelling to connect prey encounter rates with morphological characteristics of flagellum, filter, and additional supporting structures in individual organisms.

Beside their different body size and motor design, large planktonic filter feeders are often characterized by more watery, gelatinous bodies than their microscopic opponents. In paper IV we develop a model of the energetics of general planktonic filter feeders with different body compositions that we apply to unicellular choanoflagellates as well as gelatinous tunicates. Using the model we demonstrate that large filter feeders need to become gelatinous in order to support large enough filters, while small organisms have no need to change their body composition.

In paper V we investigate the physical selection of prey sizes by flagellates. The predator-prey size ratio and prey size range can vary significantly in small feeding-current feeders, which encounter everything that arrives in the feeding flow [Gonzalez and Suttle, 1993; Hansen et al., 1997a; Lombard et al., 2011]. We investigate how physical prey encounter and contact are affected by prey size. We numerically and analytically explore the advective-diffusive transport and capture of particulate prey on a towed sphere as a simple model of a direct-interception feeder. For sloppy feeders, which lose a certain fraction of their prey through finite foraging rates, we investigate the influence of contact times by exploring how the prey capture rates for different prey sizes increase towards their asymptotic maximum that represents a perfect absorber.

In this thesis I will first give an introduction to the ecology and biology (chapter 2) and the physics (chapter 3) of the organisms and mechanisms studied. Then in chapter 4 the five studies, each based on one manuscript, are summarised and the manuscripts are included in chapter 5. Finally, in chapter 6, I will conclude on the results and describe further possible developments based on this work.

2 Ecological and biological background

2.1 Fitness and trade-offs

Every life form that wants to guarantee the survival of its species has three main Darwinian missions. It needs to reproduce (first mission) and thus make sure that there will be a next generation, but it can only reproduce if it has enough energy reserves, which it obtains through resource acquisition (second mission). At the same time the organism needs to prevent predation in order to have the opportunity to grow and reproduce (third mission).

To understand marine ecosystems, we need to investigate how different life forms are adapted for these different functions in their specific environment. This is not an optimization task, as from an engineering perspective, with the goal to design the best possible life form. Our aim is to track back evolution to understand how the environment shapes the survival strategy of an individual and how it will react to and influence specific changes and fluctuations. Every environment, with non-living and living factors, offers opportunities and risks that an individual deals with in a unique way, which has led to the survival of its genes (figure 2.1).

In order to define the roles of different organisms in the ecosystem, it is helpful to define a performance, i.e. a fitness measure. Traditionally fitness expresses the growth potential of a species, i.e., the instantaneous or average growth rate of a population. This makes sense intuitively, since a high positive growth rate means that the species thrives and fulfils all its missions. However, in ecosystems with many players this quantity is difficult to directly connect to measurable parameters, e.g., based on morphology. In the trait-based approach we focus on the individual and a few key functional traits, which influence the performance of the organisms, and also relate to the functioning of the whole ecosystem. [McGill et al., 2006; Litchman et al., 2013; Krause et al., 2014].

As an individual performance function we define a scope for growth H [Acuña et al., 2011], which generally has a gain G from resource acquisition, and a loss R due to metabolism and predation mortality, so that we can generally write

$$H = G - R. \tag{2.1}$$

Both terms depend on the functional traits of the organism and the parameters defining the environment (predators, prey, resources, and habitat). In order to analyse

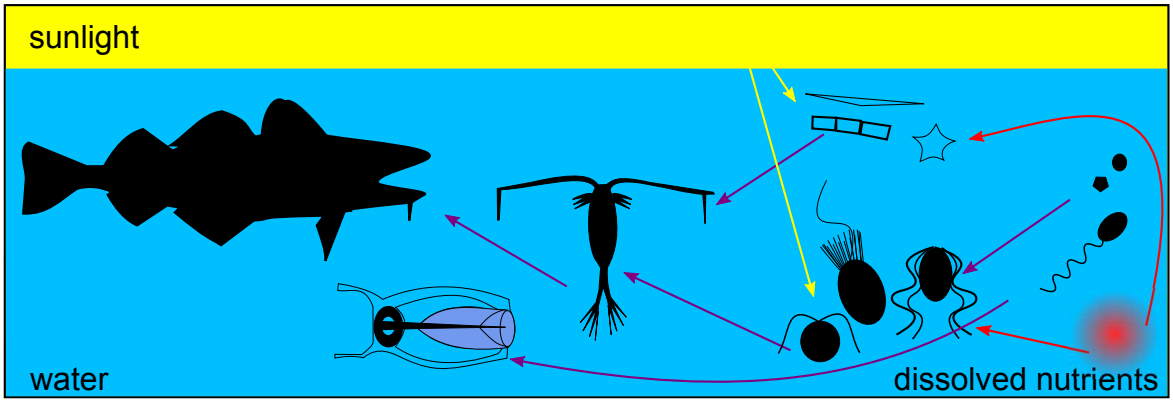

Figure 2.1: Sketch of a simple pelagic ecosystem. Organisms are not to scale. From left to right: fish, gelatinous salp, copepod, (phototrophic) diatoms (top) and flagellates with different trophic strategies (bottom), bacteria and viruses. The arrows indicate resource acquisition: uptake of dissolved nutrients (red), photosynthesis (yellow), prey capture (purple). Resource encounter as well as other interactions with the living (biotic) and with the non-living (abiotic) environment are mediated through the physical properties of the aquatic habitat.

and compare performances, we need to define the relevant external parameters and individual traits, and the functional dependence of G and R on those.

In many cases a performance function such as the scope for growth H cannot be written up at once, since not all dependences are completely clear and quantified. The first step towards a deeper understanding of cost-benefit dependences on functional traits is to investigate the involved trade-offs. There are generally several different trait combinations that lead to similar fitness, since a high benefit often comes with a high cost and vice versa. Thus there is no global optimum strategy and this relates to the diversity of strategies and the ecosystem richness [Weiher et al., 1998]. One important trade-off is the compromise between foraging gain and predation risk [Gilliam and Fraser, 1987; Houston et al., 1993; Kiørboe et al., 2014]. Organisms that collect prey efficiently with high rates invest much energy in the foraging process and experience a high predation risk by being more exposed. There is then the opposite strategy of spending less energy and risking less predation, which in turn leads to lower prey encounter rates. Due to the cost-benefit trade-off the two different strategies could both exist in an environment with intermediate prey availability and predator abundance. However, in food-limited or more risky environments one or the other strategy can out-compete the other. Instead of hiding from or avoiding predators, which is not always easy, some organisms actually invest energy and resources in (active) defence, which again involves a trade-off [Winter et al., 2010].

Trade-offs are often linked to environmental characteristics and physical limitations. In the case of zooplankton with different feeding modes the hydrodynamic properties of the water connect foraging and predation [Kiørboe, 2011, 2016]. In order to capture

prey the organism needs to move water or swim through it in order to feed. The accompanying flows, however, can be detected by predators and thus compromise survival [Kiørboe et al., 2014].

2.2 Scaling

Both in biology and physics, scaling gives important insight into the correlation of different characteristics with the size of a system, which reflect physical optima and limitations [Schmidt-Nielsen, 1984]. The mathematical definition of scaling is the existence of a power law relationship between two variables a and b with an exponent k [Barenblatt, 2003], so that one can write their relation as

$$b = c\, a^k, \tag{2.2}$$

with a coefficient c. In a double-logarithmic plot of $\log b$ versus $\log a$ one can then see a linear relationship

$$\log b = \log c + k\, \log a \tag{2.3}$$

with the slope given by the exponent k. If the relationship is linear with $k = 1$, we have found a constant b/a, which does not depend on a. If the relationship is non-linear with $k \neq 1$, $b/a \sim a^{k-1}$ is not constant, but will either decrease with a, if $k < 1$ or increase if $k > 1$.

We now imagine a to be a measure of size, for example the body mass M. If we intuitively think that by doubling the mass another characteristic will also double its value, we assume that the relationship is linear with $k = 1$. But since this is generally not the case, we cannot simply linearly scale a body and presume its viability, for example by imagining a bacterium that is as big as a blue whale or the other way around, since such an organism would not be able to sustain its function. While the losses and costs $R \sim M^{1-\epsilon}$ often scale linearly with mass ($\epsilon = 0$), or with $\epsilon \approx 1/4$, the physical resource acquisition rate G for a given mechanism often scales with the body length or surface area, due to physical limitations on transport and uptake of food. The ingestion rate $G \sim L \sim M^{1/3}$ scales with the body length for bacteria with diffusive uptake of dissolved nutrients. Thus for increasing mass or volume the relative losses $R/M \sim M^{-\epsilon}$ will outweigh the relative gain $G/M \sim M^{-2/3}$ and thus make this life form infeasible above a certain size [Andersen et al., 2016]. On the other hand, similar problems can occur for the down-scaling of functions. Multicellular organisms with a high cell-differentiation which allows complex mechanisms cannot be down-scaled to the micrometre size range, being limited by size and functions of a single cell.

When we start with empirical (e.g. biological) observations, the observed power laws can hint to the relevant mechanisms that underlie and limit characteristic traits. In the next section I will introduce some empirically found values and scalings of essential performance measures and their implications.

2.3 Essential performance measures and their scaling

Here I will review characteristic rates and their observed scalings with body size measures, and I will explain how they relate to the fitness of individuals and the size spectrum of abundance in the ocean. Finally, I will discuss the observed physical limitations and optima for the dynamic performance of organisms.

The definition of size is somewhat ambiguous [Andersen, 2017], it can for example mean the volume or length of an organism. The mass is typically used as a body size measure, which is usually proportional to the volume, since any organism mainly consists of water and thus has a mass density (mass per volume) which is very close to the density of water. The total mass that corresponds to that of a living organism is often called the wet mass. However, a different measure is the dry mass, which is the mass of the organism after removing all water. The dry mass can be converted to carbon mass, which can be proportionally related to the equivalent amount of energy that can be produced by an organism that ingests this amount of carbon [Schmidt-Nielsen, 1997]. The biomass or energy density (metabolisable energy content per volume) is proportional to the carbon-to-wet mass ratio. It has been found that planktonic organisms with few exceptions are either dense with a characteristic carbon-to-wet mass ratio equivalent to $10^{10}\,\mathrm{J\,m^{-3}}$, or gelatinous with a hundred times lower energy density [Kiørboe, 2013]. Thus one needs to be careful when using carbon mass and volume, since they are not equivalent size measures when considering gelatinous and dense organisms.

2.3.1 Vital rates and size spectrum

As discussed in section 2.1 the performance or fitness of an individual needs to be connected to measurable quantities in order to quantify it in real organisms. There are several characteristic rates that describe the main gains and losses of a living individual. The ingestion rate describes the collected food per time of an individual and is measured as number of prey items or total ingested mass per unit time. It depends on the available amount of prey, i.e., the food concentration c in the water, with a so-called functional response $G(c)$ [Holling, 1959; Hansen et al., 1997b]. At low food availability ingestion increases approximately linear with concentration, while at high concentration it levels off to a maximum ingestion rate (figure 2.2 A). This behaviour is very general, since there are physical limits to the rate at which prey can be handled [Holling, 1959]. The clearance rate $Q = G/c$ describes the amount of water that is cleared of prey per time.

When measuring the ingestion rate at different concentrations, one can fit a functional response with the maximum ingestion rate giving the upper limit. A common functional response form that fits to the feeding behaviour of most zooplankton is the Michalis-Menten or Holling type II response [Holling, 1959; Fenchel, 1988; Hansen et al., 1997b].

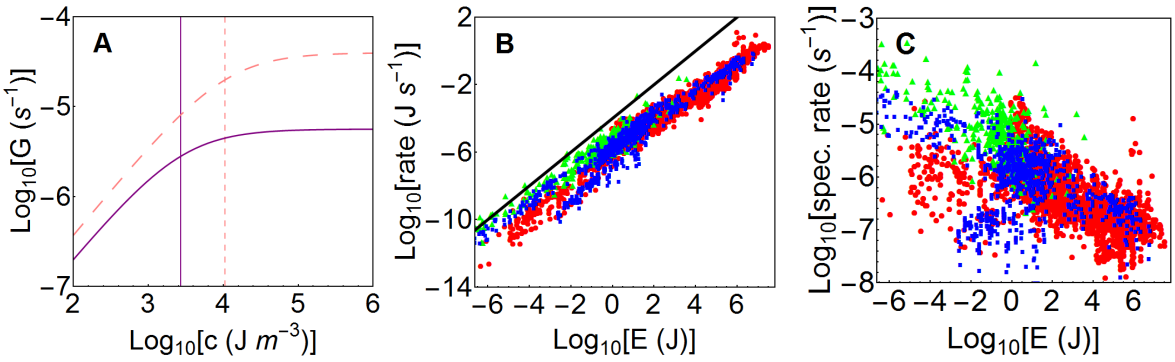

Figure 2.2: Vital rates and functional response. Maximum ingestion rate (green), maximum growth rate (blue) and respiration rate (red) for zooplankton. (A) Functional response (2.4) for a tunicate (purple) and a protozoan (pink, dashed) with the energy-specific maximum ingestion rate as upper limit and the energy-specific maximum clearance rate as maximum slope. The vertical lines mark the characteristic concentrations, where half of the maximum ingestion is reached. Since maximum specific clearance rates are rather constant, while maximum specific ingestion rates decrease with increasing size, larger organisms seem adapted to lower characteristic food concentrations. (B) All rates as functions of the body energy content E compared to a linear scaling with exponent $k = 1$ (black line). (C) Energy-specific rates as functions of the body energy content. Data were taken from Kiørboe and Hirst [2013, 2014]. The respiration rates were converted from oxygen to energy consumption per time with the conversion factor $20\,\mathrm{J\,ml O_2^{-1}}$ [Schmidt-Nielsen, 1997] and carbon mass was converted to metabolised energy with the factor $5.5 \cdot 10^7\,\mathrm{J\,kgC^{-1}}$ [Acuña, 2001; Schmidt-Nielsen, 1997].

In this form the ingestion rate as a function of food concentration can be written as

$$G(c) = \frac{G_{\max}\, c}{G_{\max}/Q_{\max} + c} \tag{2.4}$$

where $G_{\max}$ is the maximum ingestion rate and $Q_{\max}$ the maximum clearance rate that determines the maximum slope of the function (figure 2.2 A). The ratio $G_{\max}/Q_{\max}$ defines a characteristic concentration, to which the organism is adapted and where it reaches half of the maximum ingestion rate. Above that concentration the function levels off and thus there is little additional gain from higher concentrations.

The growth rate of an individual describes the individual rate of mass increase (as opposed to the population growth rate). For comparison of different organisms one can measure a maximum growth rate that is independent of prey concentration such as the maximum ingestion rate [Kiørboe and Hirst, 2013]. Growth of course increases with increasing prey ingestion.

Finally with the respiration rate, i.e., the amount of oxygen respired per time, one can measure the energy expenditure per time (metabolic rate) of animals, which is used for basic maintenance (basal respiration rate) and for foraging (dynamic respiration rate) [Schmidt-Nielsen, 1997]. In many cases the dynamic rate is neglected and the total respiration rate is measured as proxy for the basal rate. Ingestion, growth, and respiration rates can be converted to energy per time and the prey concentration in carbon mass per volume can be converted to an energy density (figure 2.2). The clearance rate generally has the dimensions of a volume flow rate (volume per time).

Intuitively it is clear that, integrated over the average lifetime, the total gained energy by ingestion needs to balance growth, respiration, predation mortality, and reproduction [Litchman et al., 2013]. There are several hypotheses and theories on the scaling of rates with body size, where the metabolic rate is often seen as the most important measurable characteristic of the organism performance that the scalings of other rates depend on [Brown et al., 2004]. Vital rates (in dimensions of gained or lost mass, energy or volume per time) are found to scale linearly or less than linearly with carbon mass and energy content, thus with an exponent $k = 1-\epsilon$. The deviation ϵ from linear scaling can be more easily seen, when considering mass- or energy-specific rates, which have the exponent $k - 1 = -\epsilon$ (figure 2.2 B, C). A common hypothesis assumes so-called allometric scalings of all rates, with quarter powers $\epsilon = 1/4$ (i.e., $k = 3/4$). This was first suggested by Kleiber and the quarter power was reasoned for by theories on optimal branching of transport networks [Kleiber, 1932; West and Brown, 2005]. Since measured scaling exponents ϵ are often closer to 1/4 than 1/3 (an exponent suggested from a surface law) the quarter power scaling is widely accepted. However, the theory behind this exponent and its universal applicability are still subject to debate [Hulbert, 2014].

Mass- or energy-specific metabolic as well as maximum clearance rates across species-overarching size ranges exhibit values ranging between an upper and lower 'universal' constant, while the allometric scaling is only conserved within similar species groups (only the coefficient shifts across groups) [Makarieva et al., 2008]. Maximum ingestion and maximum growth rate, however, apparently do not have such bounds and exhibit a

species-overarching scaling with $\epsilon < 0$ (figure 2.2) [Kiørboe and Hirst, 2014]. Realistic ingestion and growth rates in pelagic ecosystems, on the other hand, will have a natural upper bound due to the limitations of the clearance rate and the maximum available prey concentration.

The vital rates of organisms and their larger predators relate to their relative abundance. It has been found empirically that within logarithmically spaced size classes there is an equal amount of biomass within the ocean ecosystem, with data from organisms as small as bacteria up to large mammals such as whales [Sheldon and Parsons, 1967; Sheldon et al., 1972]. Since the biomass concentration stays roughly constant across size scales, it follows that the number of small organisms (with a small mass per individual) is larger than the number of large organisms. Theoretical arguments for this scaling take into account that the prey ingestion rate (the concentration of the relevant prey times the maximum clearance rate) needs to balance the energetic requirements of the individual, where the preferred prey is assumed to be a certain constant fraction smaller than the predator. The theories predict equal biomass within size classes that relate to trophic levels and thus confirm the empirical Sheldon size spectrum [Kerr, 1974; Andersen and Beyer, 2006; Andersen, 2017].

2.3.2 Force, power, and speed

Now we have introduced the vital rates and related size spectra, but we have not yet talked about physiological limitations that, for example, restrict the maximum clearance rate. The maximum clearance rate relates to a situation where the organism does the best it can in order to collect as much food as possible. Obviously there are limits to how fast food can be transported towards the organism with or without its active help (sections 2.4 and 3.8).

If the organism actively swims or produces flows it needs to invest energy that is transmitted through flagella or muscles, the force and power of which are limited. Marden and Allen [2002] found that for biological as well as man-made motors one can mainly distinguish two scalings of the maximum motor force output, which are tightly linked to the physical performance limits. One scaling regime (group 1) was found with the maximum force as $F \sim M^{0.67}$ with M the motor mass. The exponent is very close to 2/3 and thus points towards a scaling with the cross-sectional area instead of the volume $V \sim M^1$ of the motor. This regime includes types of motors which work with slow translation and which are limited by axial stress, e.g. muscles and linear actuators, but also muscle cells and single molecular motors such as dyneins. The second group of motors were found to produce forces that scale linearly with motor mass as $F \sim M^{1.0}$ (group 2) such that the mass-specific force is constant with an average $57\,\mathrm{N\,kg^{-1}}$. This describes the force limit of complex motors that cycle rapidly and that are limited by fatigue and inertia such as running animals, swimming fish, and piston engines. It was also shown that for piston engines with mass higher than around 10^4 kg the scaling switches from group 1 to group 2.

Another important parameter for motile organisms is the speed of locomotion that has been found to scale linearly with body length for a wide size range from the smallest

to the largest aquatic and terrestrial organisms [Meyer-Vernet and Rospars, 2015, 2016]. In those studies it was additionally argued that universal molecular motor limits together with universal body composition and metabolic rates lead to the observed scaling.

In paper IV we investigate how these physical limits and their scaling can translate into limitations to the clearance rate of actively feeding organisms. For planktonic filter feeders we argue that a constant mass-specific force limit as for group 2 motors leads to constant mass-specific volume flow rates and thus relates the physical limit to the observed upper bound of clearance rates.

2.4 Resource acquisition and sensing modes

Resource acquisition is a central function of all life forms, especially in the open ocean where resources are sparse. Resource types and the way in which they are attained differ for different organisms. The strategies favouring the utilisation of different types (or a mixture) of resources are called trophic strategies. *Osmo-heterotrophs* feed on dissolved organic matter, *phototrophs* (phytoplankton/plants) use light to fixate CO_2 by photosynthesis and additionally collect dissolved inorganic nutrients, *mixotrophs* perform photosynthesis, but can also feed on other organisms, and *heterotrophs* (zooplankton/animals) exclusively feed on prey [Andersen et al., 2016]. In the same order as named these trophic strategies can be structured in size with the smallest (bacteria) as osmo-heterotrophs and large organisms as heterotrophs, since the way in which the different resources are collected make the different strategies only profitable/accessible for certain body size ranges [Andersen et al., 2016]. The diffusive uptake rate of dissolved matter scales with body length L linearly, the uptake rate of photons for photosynthesis roughly scales with the surface area as L^2, while prey uptake has the possibility to scale with the volume as L^3, especially if the predator is able to sweep up prey efficiently at a high Reynolds number and with the aid of remote sensing apparatus. These different scalings are argued to lead to the succession of trophic strategies with increasing size [Andersen et al., 2016]. When taking into account the metabolic cost that scales close to L^3 as shown above, one can see that both osmo- and phototrophy will become completely infeasible above a certain size, where the cost starts to exceed the gain. The heterotrophic mode seems adapted to fit any body size above a lower feasible limit, such that a broad range of organisms are able to use this strategy.

If we look closer at heterotrophic strategies we find different feeding strategies. We can distinguish three feeding modes in the zooplankton that are displayed by characteristically different motile behaviours. The three modes are *cruise feeding* (continuously moving through the water and encountering prey on the way), *feeding-current feeding* or *suspension feeding* (transporting prey towards oneself by creation of a flow), and *ambush feeding* (waiting for prey and individually attacking/capturing it, when it comes close by) (figure 2.3) [Kiørboe, 2011].

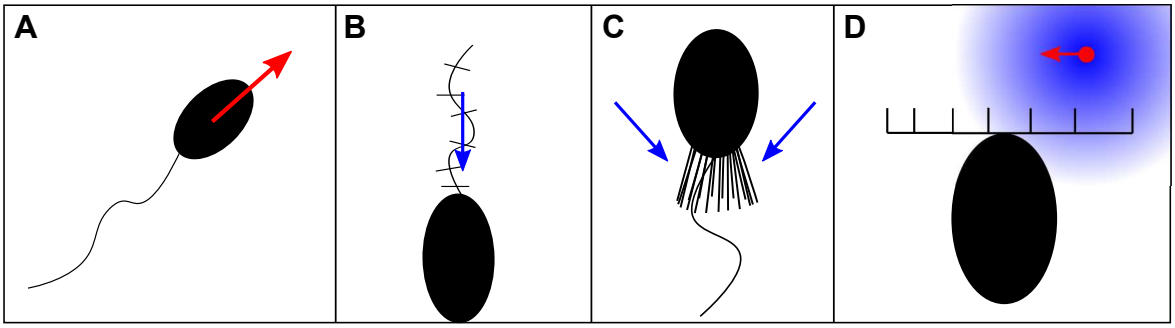

Figure 2.3: Zooplankton feeding modes. (A) Cruising: the predator moves continuously (red arrow) and encounters (passive) prey on its way. (B-C) Feeding-current feeding: the predator (flagellate) creates a flow (blue arrows) toward its body (B) or past a filter structure (C). (D) The predator (copepod) sits still and waits for (active) prey to move past it. In all feeding modes the predator can either rely on direct contact with the prey or additionally use sensing modes such as mechanosensing to remotely detect and attack individual prey and thus increase its effective encounter zone (see the blue flow disturbance zone around a moving prey in (D)).

Characteristic hydrodynamic trade-offs mark the advantages and disadvantages of each mode [Kiørboe et al., 2014; Kiørboe, 2016]. Feeding-current feeding is widely used and includes direct interception feeding on the body itself or on filter structures, but also scanning currents which involve remote detection and individual prey capture [Fenchel, 1986; Riisgård and Larsen, 2001, 2010; Koehl and Strickler, 1981; Kiørboe, 2011]. If prey is captured upon direct contact with the body or an attached structure (direct interception, filter feeding) it is necessary for such a suspension feeder to process a huge amount of water, typically one million times its own body volume, in order to collect enough food in the open ocean [Kiørboe, 2011]. This volume flow rate in suspension feeders is directly related to the maximum clearance rate.

Detection or sensing modes form another general distinction concerning resource acquisition and can be size structured due to their different efficiencies and limitations at different length scales [Martens et al., 2016]. The success and feasibility of sensing modes depend on the relevant and available signals to the organism. These signals can be created by predator, prey or mate directly, but the original source can also be external (e.g. light for vision) or self-created (sound waves for echolocation). Furthermore sensing modes depend on the transmission of the signal through the water as medium, which can be more or less efficient and wide-ranged. And thirdly the organism needs a detector to collect the signal and to transform it into useful information about its environment. All of those features depend on the size of the organism and its prey or predator. Chemosensing is a ubiquitous detection mode that can be used by small as well as large organisms. Bacteria can use it to move towards regions with high nutrient concentrations [Adler, 1966; Berg, 1975]. Other larger organisms can use it similarly or to follow (smell) the trail of a target [Yen et al., 1998].

Since aquatic organisms move a considerable amount of water, when swimming or when creating feeding currents, those flows can be detected using mechanosensors by their predator or prey [Dijkgraaf, 1962; Yen et al., 1992; Kiørboe and Visser, 1999]. An important mechanism of flow sensing relies on the deflection of sensory hairs or similar lever-like structures due to fluid deformation [Martens et al., 2016]. This detection mode can not be used by very small organisms, but e.g. copepods and ciliates that are larger than micrometre size can use it to detect their prey (e.g. flagellates) and their predators (e.g. fish) [Kiørboe and Visser, 1999]. From moving prey absolute flow velocities are detected (figure 2.3 D), since the detecting organism is much larger and does not move due to the flows created by the prey. For the detection of (larger) predators, however, absolute velocities are useless as signal, since the organism itself will move due to the created large-scale current and thus feels no relative velocity, but shear, vorticity and acceleration can still be registered [Kiørboe and Visser, 1999; Visser, 2001]. Vision, hearing and echolocation are only available and used by larger organisms and are not common in the plankton. Martens et al. [2016] give a broad introduction to the different sensing modes of marine organisms throughout size classes and their limitations.

2.5 Motors of eukaryotic organisms

Eukaryotic organisms use either flagella or muscles as main motor systems, which can be used to move the organism body and the fluid around it. There are other mechanisms that can for example provide cell movement along surfaces. Those are, however, not in our focus since we are interested in free swimming and feeding. Flagella are the motors of single cells, while most multicellular organisms use muscles for locomotion. In the following I will introduce both flagella and muscles as motor systems for eukaryotic organisms and discuss their main design and performance characteristics.

2.5.1 Flagella

Eukaryotic unicellular organisms that can propel themselves or create flows by one or several whip-like flagella are called flagellates (figure 2.5). The flagella have a structure and functionality that allows the organism to produce bending waves of various amplitude and frequency along the slender appendages. Although generally the composition of flagella is very complex [Pazour et al., 2005], we can describe a characteristic eukaryotic flagellum with a relatively simple and well conserved structure (figure 2.4) [Gibbons, 1981]. The eukaryotic flagellum has a diameter of 0.2 µm and is entirely covered by the plasma membrane [Hausmann et al., 2003]. The inner motor, the axoneme, consists of a 9x2+2 microtubule structure (figure 2.4). There are 9 doublet-tubules with attached dynein molecules and radial spokes arranged around two central singlet-tubules. The bending waves on the flagellum (without overall stretching) are created by the 'walking' of the dynein arms on neighbouring tubules by subsequently attaching and detaching. By this sliding motion of tubules in different directions at different sides

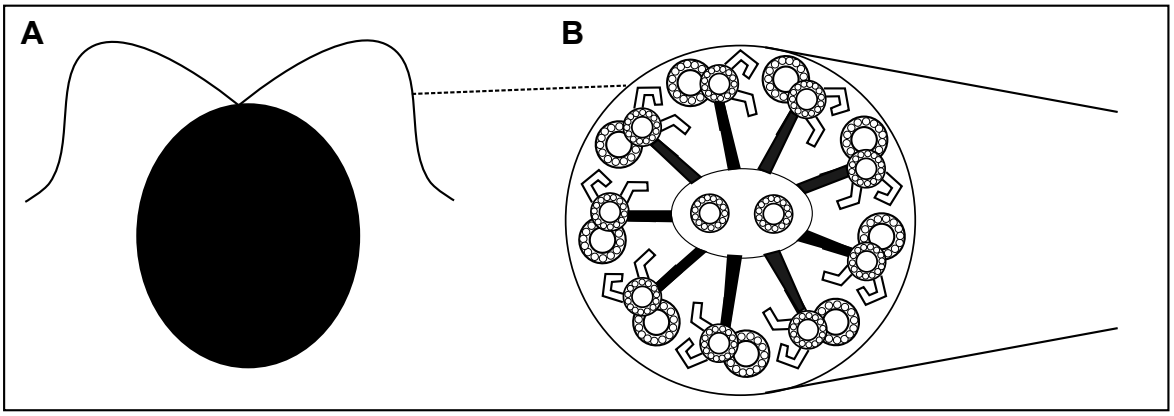

Figure 2.4: Schematic diagram of a eukaryotic flagellum. (A) Flagellate with two flagella. (B) Cross-section of flagellum with a characteristic 9x2+2 microtubule structure. The dynein motors with attached arm-like extensions enable neighbouring doublet structures to slide along each other to create local bending of the flagellum. Sketch adapted from Wan et al. [2014] and Lighthill [1976].

of the flagellum, the flagellum is contracted on one side, while it is extended on the other side, which leads to local bending [Brokaw, 1972; Lighthill, 1976]. The flagellum may additionally be covered by hairs (mastigonemes) or scales which can change its hydrodynamic properties, i.e., the same travelling wave on a flagellum without and with hairs can lead to opposite swimming directions (pushing versus pulling) (figure 2.3 A, B) [Sleigh, 1981; Hausmann et al., 2003].

There is a wide variety of flagellate morphologies and kinematics with varying flagellum lengths, usually some micrometres for freely swimming cells with rare exceptions [Joly et al., 1995]. There can be various numbers of flagella per cell (1, 2, 4, 8,...) and with beat patterns from travelling waves (flagellar beat) to breast-stroke type patterns (ciliary beat) [Sleigh, 1981]. A few examples of planktonic organisms with different flagellar numbers and beat patterns are shown in figure 2.5 A-D. Organisms that are covered by a large number of short flagella, so-called cilia, are often distinguished as ciliates. In this study those multi-flagellated organisms are not in focus. Generally, short flagella that beat in a coordinated breast-stroke type fashion (ciliary beat), are typically called cilia (Latin for eyelashes), since they remind of hairs covering the cell surface.

2.5.2 Muscles

Muscles form the most common biological motor in multicellular animals and have some differences but many functional similarities to the flagellar motor of eukaryotic single cells that was introduced above. There is a certain small number of proteins that build the molecular motor units, which all work with the chemical energy of ATP (adenosine triphosphate). Thus flagella and muscles are based on similar molecular

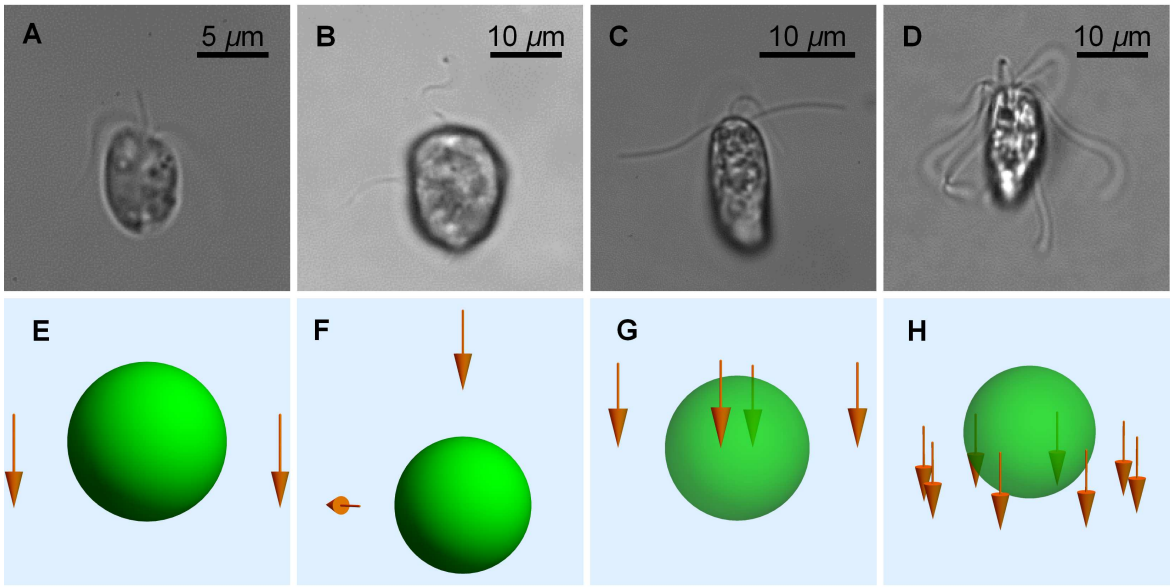

Figure 2.5: Flagellates with different flagellar arrangements and beat patterns. (A)-(D) Microscope images of freely swimming individuals. (E)-(H) Hydrodynamic flagellate models consisting of a no-slip sphere (green) and one point force (orange vectors) for each flagellum. (A) and (E) *Prymnesium parvum*, a left-right symmetric biflagellate (haptophyte) with a haptonema at the front. (B) and (F) *Heterosigma akashiwo* with a longitudinal (puller) flagellum and a transversal flagellum. (C) and (G) *Tetraselmis sp.* with two pairs of flagella that beat in anti-phase. (D) and (H) *Pyramimonas octopus* with eight flagella. Figure adapted from Dölger et al. [2017a]. Microscope images by courtesy of Lasse Tor Nielsen, DTU

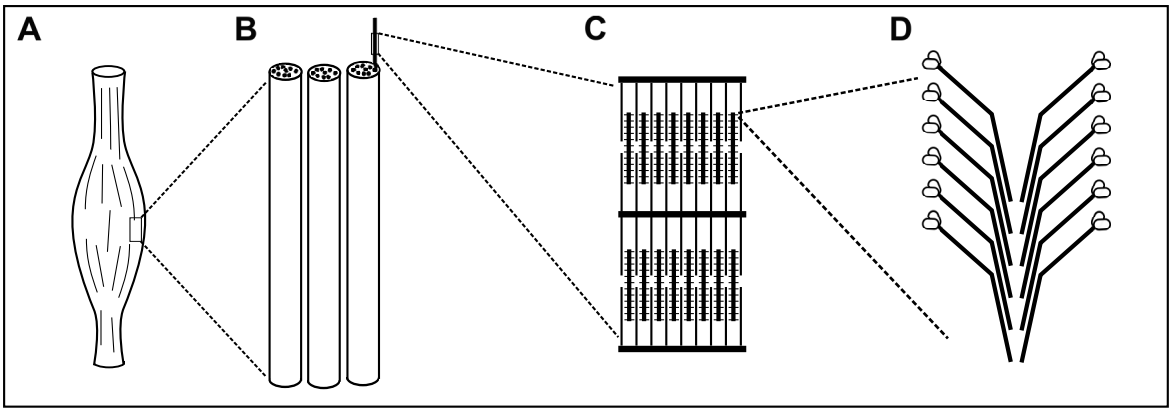

Figure 2.6: Schematic diagram of a vertebrate striated muscle. (A) Whole muscle that consists of muscle fibres (B), which each contain many myofibrils (thin lines). (C) The basic motor unit is the sarcomere, of which two are shown. One sarcomere that is limited by so-called Z-disks (horizontal lines) consists of thick myosin filaments with cross bridges and thin actin filaments that are fixed to the Z-disks. (D) The thick filaments are made of myosin molecules, the structure of which allows them to arrange into filaments and to bind with actin in order to contract the muscle. Sketch adapted from Schmidt-Nielsen [1997, p. 403] and Alexander [2003, p. 17].

principles. In eukaryotic flagella the main proteins are dynein and tubulin, while in muscles, myosin and actin make up the essential force-producing part of the motor [Schmidt-Nielsen, 1997; Vogel, 2013]. A flagellum has the constriction of a set diameter, which limits its use at larger body size to pump fluid efficiently. By combination of flagellar motors one can mainly scale the motor up in two dimensions by arranging flagella next to each other as linings of surfaces. Muscles, however, are more flexible to use as motors across many scales in multicellular organisms from millimetre-sized copepods to metre-sized whales [Schmidt-Nielsen, 1997].

The base unit of a muscle is the sarcomere (figure 2.6 C). By sliding the movable actin filaments across the fixed myosin filaments through actin-myosin cross links the two ends of the sarcomere (Z-disks) are brought closer together, which leads to muscle contraction [Alexander, 2003; Vogel, 2013]. This mechanism is similar to the dynein-tubulin interaction in flagella, which results in only local contraction and extension and thus an overall bending. A typical sarcomere unit is 2.5 µm long in the relaxed state and long chains of sarcomeres (myofibrils) are bundled together into muscle fibres (figure 2.6). A bundle of a certain number of fibres are controlled by a single nerve cell and thus build an effective motor unit. The subunits (sarcomeres, fibrils, fibres) can vary in number and size, depending on the type of muscle [Schmidt-Nielsen, 1997; Alexander, 2003; Vogel, 2013].

In a very simplified dynamical model a thicker muscle with a large cross-section $A \sim L^2$ can produce a high force $F = \sigma_{\max} L^2$ with maximum tension $\sigma_{\max}$ due to many units working in parallel, while a longer muscle can produce higher speeds $v = f_{\max} L$

due to its serial arrangement of units with maximum frequency $f_{\max}$ (or speed per length) [Vogel, 2013]. The output power is thus ultimately limited by the maximum force times maximum speed of the muscle, which then scales with the volume or mass of muscle as $P_{\max} = \sigma_{\max} f_{\max} L^3$, i.e., linear with motor mass.

This maximum power could relate to a constant upper bound in measured mass-specific respiration rates, that has been found for a wide range of size scales and not only for muscle motors [Makarieva et al., 2008; Kiørboe and Hirst, 2014]. The maximum frequency, on the other hand, can be related to maximum speeds in living organisms [Meyer-Vernet and Rospars, 2015]. To obtain the maximum power limit we here assume that maximum frequency and maximum tension can be realised independently. However, this is generally not the case. The force output of muscles is highest at the lowest, even negative speed, while the power output (force times speed) reaches its maximum at intermediate speeds [Wilkie, 1950].

2.6 Study organisms

During this Ph.D. study we investigated the hydrodynamics of different marine plankton. Here I will introduce our main study organisms, haptophytes, choanoflagellates, and pelagic tunicates. Since copepods are one of the most important marine grazers, which feed on flagellates, and since bacteria form a main prey component of all studied organisms, I will further introduce those life forms. I will avoid specialised biological and taxonomical terminology and introduce the relevant organisms in view of their overall trophic role, morphology, and functionality in terms of their physical interaction with their biotic and abiotic environment.

2.6.1 Haptophytes

A classical model organism for many hydrodynamic studies of biflagellates is *Chlamydomonas*, which is a phototrophic algal cell with an almost spherical cell body of a few micrometres in diameter, which swims in a breast-stroke type fashion with two left-symmetrically arranged flagella. This model organism is especially important for the study of the origin of multicellular life [Goldstein, 2015]. However, mixotrophy, i.e., the ability to collect prey in addition to photosynthetic activity, is very common in unicellular marine species, while pure phototrophy as in *Chlamydomonas* or pure heterotrophy as in choanoflagellates (section 2.6.2) is rather rare in flagellates.

Our model organisms in the study on biflagellates are mixotrophic and belong to the group of haptophytes [Nygaard and Tobiesen, 1993; Dölger et al., 2017b]. Haptophytes usually have two, sometimes four flagella, which like the rest of the cell surface may be covered by scales (coccoliths) [Hausmann et al., 2003]. A third slender structure, the haptonema, is typical for haptophytes and extends from the cell similar in structure as the flagellum, but it is not involved in motility. Its length varies between species and individuals and its function can vary, from fixation and gliding on surfaces to food capture [Hausmann et al., 2003; Kawachi et al., 1991; Kawachi and Inouye, 1995].

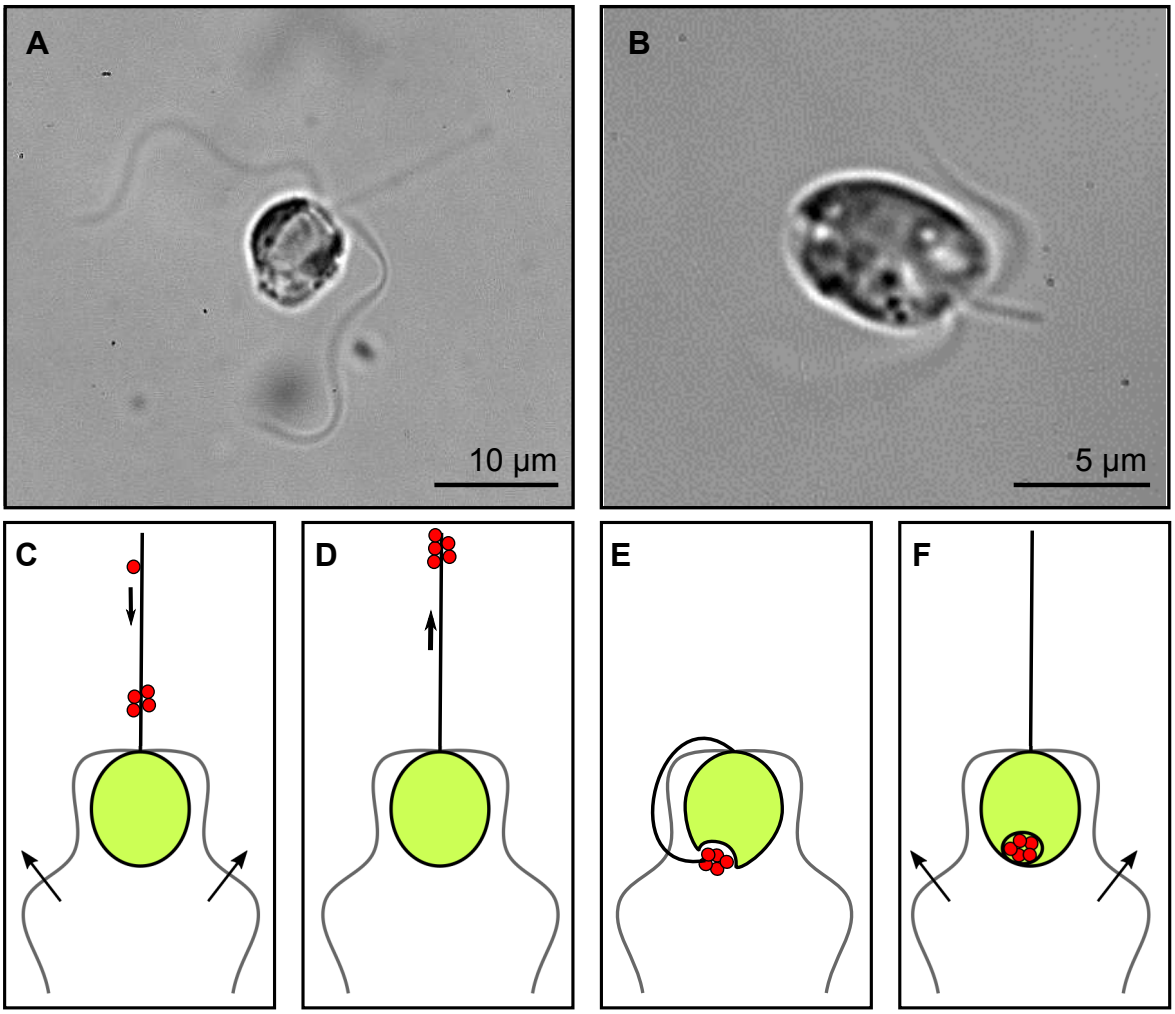

Figure 2.7: Individuals of two biflagellated haptophyte species and function of the haptonema. (A) *Prymnesium polylepis* and (B) *Prymnesium parvum*. (C–F) Sketch of prey capture on the haptonema in *P. polylepis*. The haptophyte captures prey (red) on its haptonema while swimming and collects them at a specific aggregation point (C). While the flagella are paused, the aggregate is actively transported to the tip of the haptonema (D), which is bent towards the back of the cell (E), where the particles are engulfed. The purpose and means of the movement of prey towards the aggregation point are unknown. Figure adapted from Dölger et al. [2017b] and Kawachi et al. [1991].

The two species of haptophytes, *Prymnesium parvum* and *Prymnesium polylepis*, which we investigate each have two flagella that are arranged in a left-right symmetric fashion around an approximately spherical cell (figure 2.7). Both have cells of diameters below 10 µm and are known to ingest prey at the "back" of the cell. Both species are further found to have toxic effects on large and small organisms and they are able to form large blooms [Tillmann, 2003; Fistarol et al., 2003; Schmidt and Hansen, 2001; Majaneva et al., 2012; Holmqvist and Willen, 1993]. *Prymnesium parvum* moves with a ciliary beat, similar to *Chlamydomonas*, and has rather short flagella of around 10 µm length and a short haptonema of a few micrometres length, the purpose of which is unclear. Organisms of this species are able to feed on large prey, which is even bigger than themselves [Tillmann, 1998]. The other contrasted species, *Prymnesium polylepis* has a cell of around 10 µm in diameter with spoke-like extensions. It swims with two long flagella, more than double as long as for *P. parvum*, which are actuated in a planar-wave pattern. The haptonema of this species is between 20 and 55 µm long and has been observed to collect and deliver particulate prey in a complicated fashion (figure 2.7 C-F)[Kawachi et al., 1991].

2.6.2 Choanoflagellates

Choanoflagellates, which we study as microbial filter feeders, form an important group of heterotrophic flagellates [Fenchel, 1982; Leadbeater, 2015] (figure 2.8). Every choanoflagellate has a funnel-shaped collar of 20-50 extending structures, so-called microvilli, with diameters and spacings between them of around 0.1 µm. Prey arriving in the feeding current can be captured on this filter structure. The single flagellum inside the collar moves with a planar wave, which creates the feeding flow through the filter [Leadbeater, 2015; Pettitt et al., 2002; Fenchel, 1986]. Choanoflagellates can form colonies and the related choanocytes form the filtering cells in sponges. Thus next to *Chlamydomonas*, choanoflagellates are an important group of organisms in the study of multicellularity and cell differentiation [Leadbeater, 2015; Roper et al., 2013; Kirkegaard and Goldstein, 2016; Brunet and King, 2017]. Different choanoflagellates have the same basic structure as described, but the cell morphology, collar shape, flagellar length, and beat pattern can differ between species [Leadbeater, 2015; Nielsen et al., 2017]. In some species of choanoflagellates, an additional delicate wing-like structure has been found on the flagellum, the so-called 'flagellar vane' [Leadbeater, 2006; Mah et al., 2014].

The species we studied in most detail is *Diaphanoeca grandis* (figure 2.8) [Andersen, 1988/1989]. Individuals of this species possess a large basket-like structure (lorica), which is only present in some choanoflagellates [Leadbeater and Cheng, 2010]. The lorica of *D. grandis* has a mesh with large openings at the flow inlet that is opposite to the flagellum and it is covered by a fine membranous web with small pore sizes at the other end. The lorica merges into a cylindrical tube, which we call the chimney. The approximately spherical cell measures around 5 µm in diameter with an about 10 µm long flagellum. The collar opens to a maximum width of around 8 µm and the lorica measures around 20-30 µm in diameter [Andersen, 1988/1989; Nielsen et al., 2017].

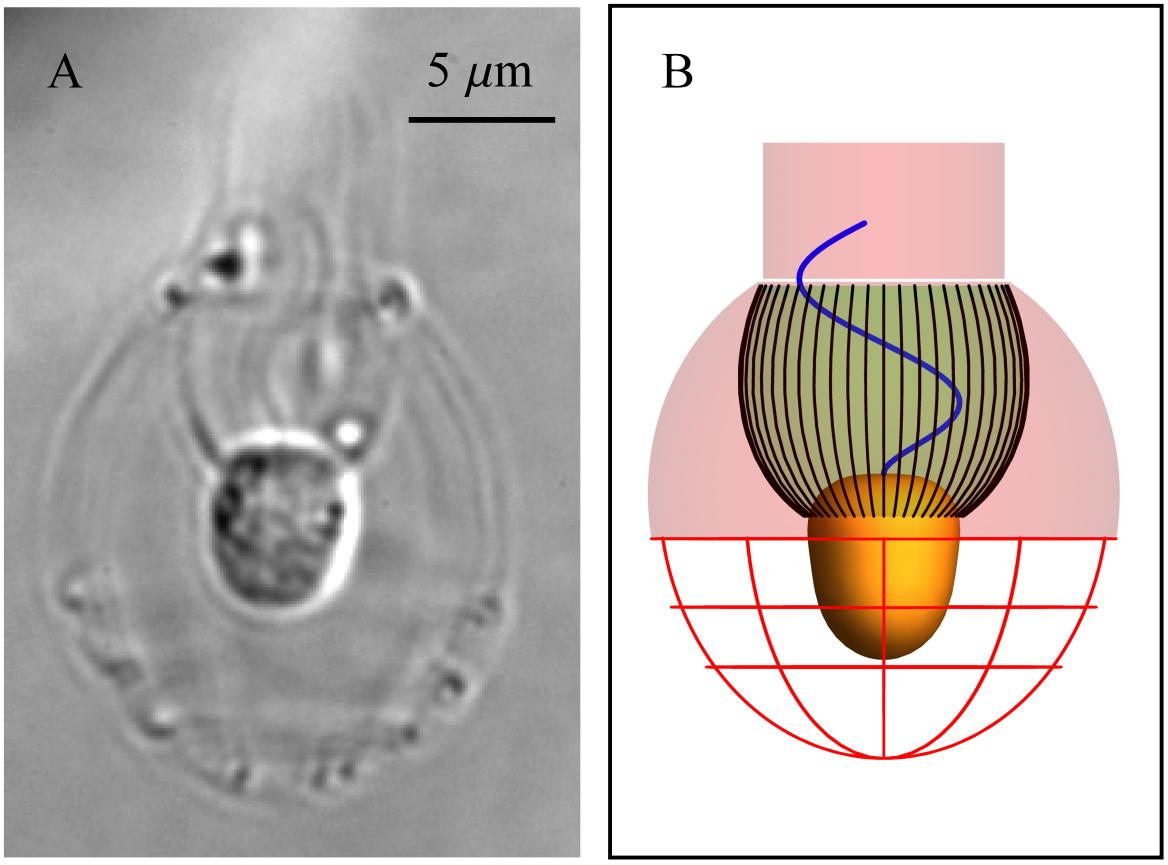

Figure 2.8: Morphology of the choanoflagellate *Diaphanoeca grandis*. (A) Microscopic image of freely swimming individual. (B) Model morphology with cell (orange), collar filter (green surface and black lines), flagellum (blue), and lorica (red). Figure adapted from Nielsen et al. [2017].

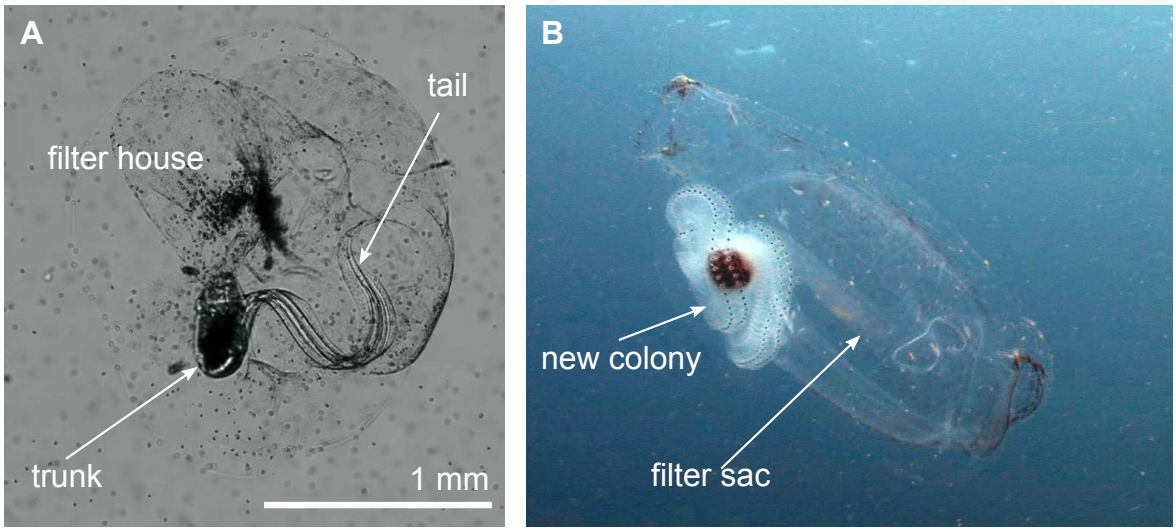

Figure 2.9: Images of two characteristic pelagic tunicates. (A) Appendicularian *Oikopleura dioica*. (B) Salp *Pegea confoederata* (solitary), which just developed a new chain of salps. There is no scale bar available for this image, but typical adult individuals of this species have body lengths of several centimetres. Appendicularian image by courtesy of Keats Conley, University of Oregon and salp image by courtesy of Kelly R. Sutherland, University of Oregon.

In the models of flow through feeding filters, which we apply to choanoflagellates (papers III and IV) we neglect flow circumvention. This assumption is not only valid for species like *D. grandis* with lorica covered by a fine web, but probably also for some aloricate species, which use a flagellar vane to efficiently drive the flow across the filter [Nielsen et al., 2017].

2.6.3 Pelagic tunicates

Pelagic tunicates are freely swimming suspension feeders belonging to the phylum Tunicata that live in the pelagic realm (open ocean) [Bone et al., 1998]. Pelagic tunicates are less well studied than their sessile relatives, the ascidians or sea squirts. One reason for this might be their gelatinous body, which makes them more fragile and less visible. Most pelagic tunicates have an about 100 times lower dry mass or carbon density than non-gelatinous organisms, which categorises them together with more well-known gelatinous organisms such as jellyfish and comb jellies [Madin et al., 1981; Kiørboe, 2013]. Pelagic tunicates capture food on mucous nets and can efficiently collect much smaller organisms than themselves down to bacteria and viruses with a predator-prey body length ratio of up to 10^4 [Lombard et al., 2011; Sutherland et al., 2010].

The different types of pelagic tunicates are appendicularians (larvaceans), salps, doliolids, and pyrosomes, where the last three as so-called thaliaceans have relatively

similar morphologies and life histories. Appendicularians are singular freely swimming millimetre-sized organisms with a direct sexual life history. Their long undulating tail takes up most of their body, thus the alternative name larvaceans due to the morphological similarity to larval stages of many marine organisms (figure 2.9 A). The appendicularian body is surrounded by a mucous filter house that is used for the capture of prey and often has a very complex structure with several chambers and different kinds of filters [Fenaux, 1998]. Thaliaceans are colonial organisms which alternate between sexually reproducing (blastozoid) and asexually reproducing (oozoid) life stages. Morphological characteristics include a transparent body covered by a thin tunic, of size ranging from a few millimetres to several centimetres. Their body is more or less hollow and barrel-shaped with one opening each at the two opposite ends. For prey capture a feeding flow is produced through the cavity by pumping water from the front to the end opening such that it passes a fine-webbed mucous filter. In pyrosomes and doliolids the feeding flow is produced through gill slits that are lined by cilia, while salps use muscle rings to contract and pump water through a large filter sac that stretches across the entire body chamber (figure 2.9 B). The blastozoid form of salps usually arranges into colonies that can be up to several metres long, while the oozoid form is freely swimming [Godeaux et al., 1998]. The flow produced by salps is not only used for feeding with a low filter Reynolds number, but is also effective for jet propulsion at a much higher swimming Reynolds number [Madin, 1990; Sutherland and Madin, 2010a,b].

2.6.4 Copepods

Copepods are one of the most important and abundant grazers (feeding on primary producers) in the ocean. Those small crustaceans are usually a few millimetres in size and are found in all different marine and other aquatic environments [Mauchline, 1998]. Examples of adult copepods are shown in figure 2.10. Morphological characteristics of copepods include the antennules which are covered with setae (hairs) for chemo- or mechanosensing, and several pairs of feeding and swimming appendages. The group of calanoid copepods contains some of the most important freely swimming grazers in the ocean [Mauchline, 1998; Wadhwa, 2015].

All three feeding modes, i.e., cruise, ambush and feeding-current feeding, are found in different species of freely swimming copepods, resulting in different trade-offs concerning the predation risk by larger predators [Kiørboe et al., 2014; Almeda et al., 2017]. Instead of relying on direct interception, copepods with their typical antennules usually have a sensing apparatus which makes them able to detect prey remotely and to increase their effective encounter zone for each feeding mode [Yen et al., 1992]. In addition to mechanosensing via the setae on their antennules (figure 2.10 A), copepods can use their feeding appendages with long, wide-spread “fingers” to efficiently capture and handle prey (figure 2.10 B) [Koehl and Strickler, 1981].

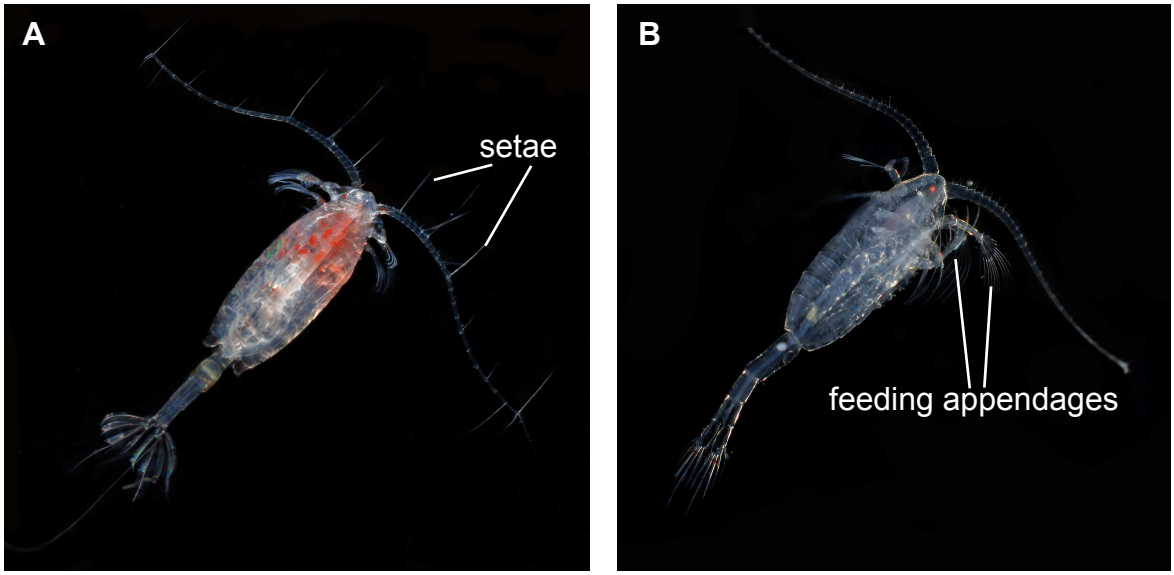

Figure 2.10: Dorsal and lateral view of typical copepods. Both displayed species are rather large with a body length of several millimetres. (A) In this dorsal view of *Paraeuchaeta norvegica* one can see the antennules with flow-sensing setae. (B) Lateral view of *Metridia longa* with feeding appendages. Images by courtesy of Erik Selander, University of Gothenburg.

Ambush feeding copepods such as *Oithona davisae* rely solely on the movement of their prey (by swimming, diffusion, or external flows), both for the transport of prey towards their encounter zone and for the detection through the created flows. When noticing a disturbance in its environment, both due either to predators or to prey, *O. davisae* is able to jump in a very efficient way with high speed towards its prey or away from its predator [Kiørboe et al., 2009, 2010].

2.6.5 Bacteria

While copepods are important grazers of flagellates, bacteria serve as their main prey. Bacteria are prokaryotic organisms, which are abundant everywhere on earth and in all kinds of aquatic environments, but also on surfaces as biofilms, often making them a threat to sterile environments. There are non-motile, but also motile bacteria that can slide along surfaces or freely swim. As prey for pelagic organisms we mainly consider bacteria which are suspended in the water column as plankton. Due to their small size, typically of the order of 2 µm or less, bacteria are never truly still in water, even if they do not swim. Molecular collisions make bacteria wiggle around randomly in water. This random walk of small particles in a fluid is what we call Brownian motion.

However, motile bacteria such as *Escherichia coli* and *Vibrio harveyi* can move much faster and swim freely with the use of bacterial flagella, which are ten times thinner than the eukaryotic flagella and fixed in a rather rigid helical structure [Berg, 2004].

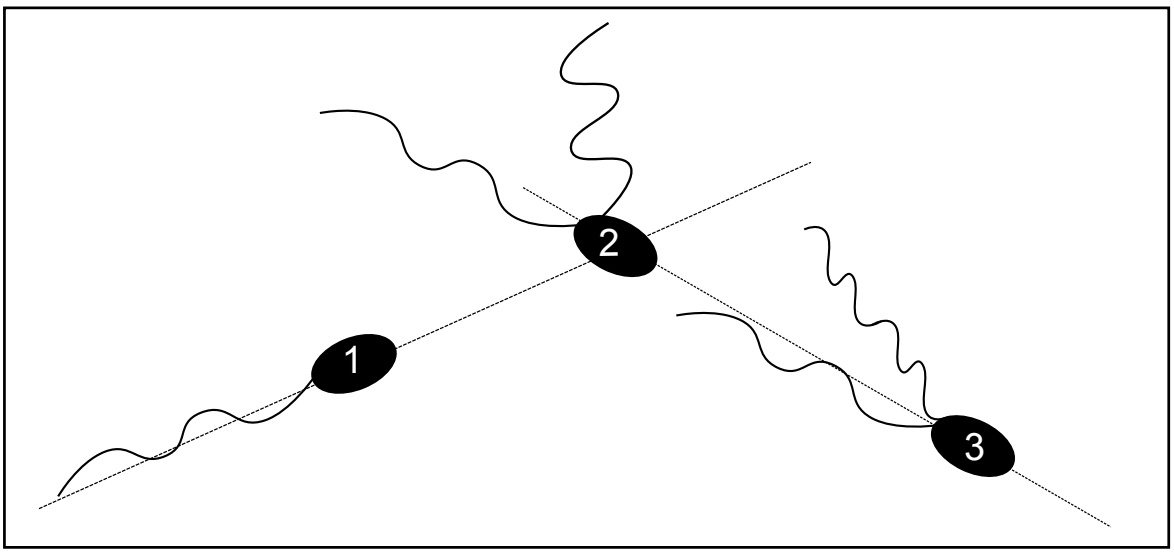

Figure 2.11: Typical tumble event in a peritrichously flagellated bacterium. In a run (1) all flagella are bundled and rotate counter clockwise in a so-called 'normal' mode. One flagellum switches direction to clockwise motion (2) and attains a 'semicoiled' shape. This makes the cell rotate randomly (tumble). Before rebundling in the normal mode in the new run direction, the switched flagellum attains a more tightly wound 'Curly 1' shape (3). Sketch adapted from Berg [2004].

Each flagellum is actuated at its base with a rotary motor. Although seeming relatively simple in their design, bacterial flagella can propel the organism with a speed of up to 50 times their own body length per second. Motile bacteria usually do not move only straight into one direction, but they are also not exactly able to steer into a desired direction. Therefore bacteria have developed a stochastic mechanism, called run and tumble (figure 2.11). In *E. coli*, many flagella that are distributed over the body in a so-called peritrichous arrangement can be bundled together to provide directed motion during swimming. An individual of this species swims on straight paths (run) with neatly bundled counter clockwise rotating flagella and after some time switches one or several flagella to clockwise rotation, by which the flagella unbundle. This process makes the bacterium turn randomly in a movement which is called tumble. After the tumble a new ballistic run can be started by again turning all flagella in the same direction [Berg, 2004].

With simple run-and-tumble mechanisms, such as the one described for *E. coli*, bacteria are able to climb chemical gradients in a process called chemotaxis. Since bacteria are not able to simply steer right towards their target, a directional bias is achieved by varying the frequency of tumbles depending on the gradient of the detected chemical signals, such that the organism finally, in a convoluted but effective way, gets closer to the desired target [Berg and Brown, 1972; Berg and Purcell, 1977].

Due to their run and tumble, bacterial transport through the water, for example towards a predator, can either be seen as a diffusive process with an effective diffusivity or as a ballistic motion with negligible gradient build-up. The transport mechanism will depend on the size of the predator compared to the run length (section 3.8) [Berg and Brown, 1972; Berg, 1972; Visser and Kiørboe, 2006].

3 Physical background

3.1 Basic equations of fluid dynamics

Through (periodic) movement of their body, often with the help of swimming appendages, planktonic organisms interact with the water around them. The Navier-Stokes equations for incompressible flow in a Newtonian fluid describe the velocity $\mathbf{v} = \mathbf{v}(\mathbf{x}, t)$ and pressure $p = p(\mathbf{x}, t)$ of the fluid as a function of time t and position $\mathbf{x}$ [Batchelor, 2000], i.e.,

$$\rho \left(\frac{\partial \mathbf{v}}{\partial t} + (\mathbf{v} \cdot \boldsymbol{\nabla}) \mathbf{v} \right) = \boldsymbol{\nabla} \cdot \boldsymbol{\sigma} + \mathbf{f} = -\boldsymbol{\nabla} p + \mu \nabla^2 \mathbf{v} + \mathbf{f} \tag{3.1}$$

$$\boldsymbol{\nabla} \cdot \mathbf{v} = 0. \tag{3.2}$$

Equation (3.1) expresses momentum conservation (with units of force per volume) and the continuity equation (3.2) expresses the conservation of mass. Parameters characterizing the fluid are the density, $\rho = 10^3\,\mathrm{kg\,m^{-3}}$ for water at 25° Celsius, and the dynamic viscosity, $\mu = 10^{-3}\,\mathrm{Pa\,s}$ for water. The stress tensor for Newtonian incompressible flows is given as

$$\boldsymbol{\sigma} = -p\boldsymbol{\mathcal{I}} + \mu((\boldsymbol{\nabla}\mathbf{v})^T + (\boldsymbol{\nabla}\mathbf{v})), \tag{3.3}$$

with the identity tensor $\boldsymbol{\mathcal{I}}$ and the superscript T denoting a transposed field. In this form the stress tensor is symmetric and it shows the characteristic of Newtonian fluids, where the stress is proportional to the rate of strain $\boldsymbol{\nabla}\mathbf{v}$. The body force density $\mathbf{f}$ is due to external forces such as gravity. Since we consider mainly neutrally buoyant organisms, we will have zero net force for those. We further restrict ourselves to small organisms or structures where we can simplify equation (3.1) drastically. The scaling of the spatial derivatives in equation (3.1) are estimated as $\boldsymbol{\nabla} \sim 1/L$ indicating that flow velocities roughly change by the characteristic speed U and pressures by the characteristic pressure $\mu U/L$ across a distance of the order of L. The Reynolds number of the flow emerges from the non-dimensionalisation of equation (3.1) and is given as the ratio between inertial (acceleration) and viscous (friction) forces, which each scale with size L and speed U, i.e.,

$$Re = \frac{\rho\, U^2/L}{\mu\, U/L^2} = \frac{\rho U L}{\mu}. \tag{3.4}$$

This dimensionless number is very small, i.e., $Re \sim 10^{-3}$, for small-scale biological flows that we investigate where typical scales are, e.g., the body length $L \sim 10^{-5}\,\mathrm{m}$

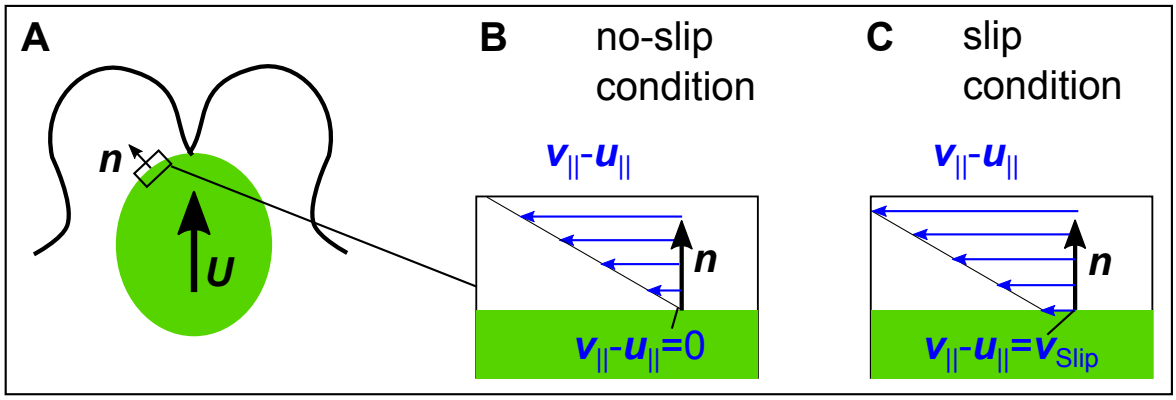

Figure 3.1: Boundary conditions for the flow velocity $\mathbf{v}$ at the surface of a moving body. (A) Flagellate with swimming velocity $\mathbf{U}$ and surface element with outwards normal $\mathbf{n}$. The swimming velocity parallel to the surface element is $\mathbf{u}_{\parallel} = \mathbf{U} - (\mathbf{U} \cdot \mathbf{n})\mathbf{n}$. (B) No-slip boundary condition, where the fluid right at the surface does not move with respect to the body. (C) Slip boundary condition, where the fluid right at the surface has a parallel velocity component $\mathbf{v}_{\text{slip}}$ respective to the boundary velocity.

and the swimming speed $U \sim 10^{-4}\,\mathrm{m\,s^{-1}}$ of a microorganism. In this case of negligible inertial forces, we can approximate $Re \ll 1$, so that equations (3.1) and (3.2) simplify and we obtain the linear time-independent Stokes equations describing the motion of incompressible creeping flows, i.e.,

$$0 = -\boldsymbol{\nabla} p + \mu \nabla^2 \mathbf{v} + \mathbf{f} \tag{3.5}$$

$$\boldsymbol{\nabla} \cdot \mathbf{v} = 0. \tag{3.6}$$

By neglecting the time-dependent term we have additionally assumed that the characteristic time scale T_0, e.g. the period of moving swimming appendages, is smaller or equal to the intrinsic time L/U of the flow [Bruus, 2008]. This defines an additional non-dimensional number $\beta = U/(LT_0)$ that together with the Reynolds number characterises the general flow problem.

To solve the Stokes equations we additionally need boundary conditions which can be given as pressure and velocity at the boundaries of the fluid domain. For swimmers we will consider fixed flow velocities at the swimmer surface, which are equal to the velocities of the surface elements itself, such that the relative velocity between boundary and fluid vanishes at contact (figure 3.1 A, B). This is known as the *no-slip* condition, formally given as

$$\mathbf{v}(\mathbf{x}_\mathrm{p}) = \mathbf{u}(\mathbf{x}_\mathrm{p}) \tag{3.7}$$

with $\mathbf{x}_\mathrm{p}$ a point on the surface of the body and $\mathbf{u}$ the velocity of the surface element. This boundary condition results from the molecular interaction between the fluid and the body and can be used for most continuous flows around solid bodies. However, if

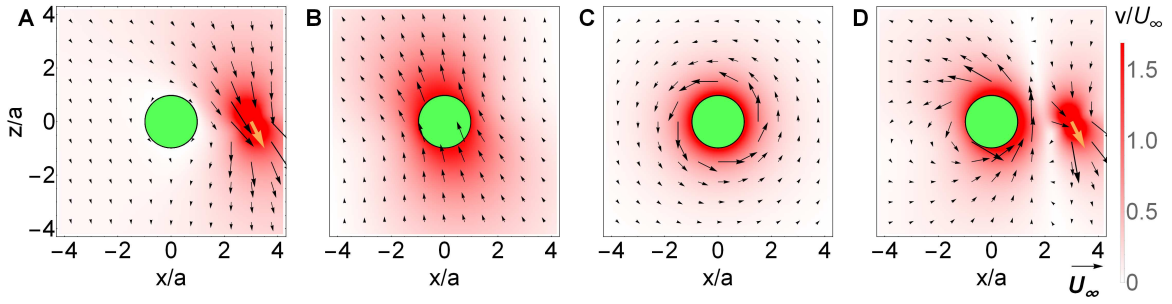

Figure 3.2: Superposition of creeping flows to calculate the flow around a freely swimming model flagellate with cell radius a. (A) Flow due to a point force $\mathbf{F}$ (vector, orange) outside a sphere. (B) Flow due to a translating sphere. (C) Flow due to a rotating sphere. (D) Superposition of the flows shown in (A)-(C) resulting in the flow around the freely swimming model flagellate. The colour maps show the normalized velocity magnitude v/U_∞ with the velocity scale $U_\infty = F/(6\,\pi\,\mu\,a)$. Figure adapted from Dölger et al. [2017a].

the friction between fluid and surface is lowered by, e.g., electrostatic interactions, or if the length scales of the flows become so small that the continuum approximation is partly violated, one can use a boundary condition with *finite slip* (figure 3.1 C), where the tangential flow velocity $\mathbf{v}_\parallel$ relative to the boundary is given as

$$\mathbf{v}_\parallel(\mathbf{x}_\mathrm{p}) = \mathbf{u}_\parallel(\mathbf{x}_\mathrm{p}) + \mathbf{v}_\mathrm{slip} \tag{3.8}$$

with the slip velocity $\mathbf{v}_\mathrm{slip}$. The normal relative velocity will still be zero, since the fluid does not penetrate the body. In addition to the boundary condition on a solid surface we usually have another boundary condition at the boundary of the fluid domain. For freely swimming organisms in an open domain the boundary conditions at infinity are $\mathbf{v}|_{r\to\infty} = 0$ and $p|_{r\to\infty} = 0$.

3.2 Low Reynolds number flows

The Stokes equations (3.5) and (3.6) have characteristic properties, some of which are rather non-intuitive for us who are used to higher Reynolds number flows based on air or water and human size and speed [Stone and Duprat, 2012; Lauga and Powers, 2009]. The Stokes equations are linear and time-independent.

One handy conclusion of the linearity of Stokes flows is that solutions (flows) in the same domain (around the same boundaries) can be linearly superposed (added to each other) to form a new solution. This can, for example, be used to construct microswimmer models for various types of flagellates from known analytical solutions of the Stokes equations (figure 3.2) (see paper I and II).

The time-independence of the Stokes equations gives us the opportunity to calculate flow solutions for every instant separately, just based on the boundary conditions at

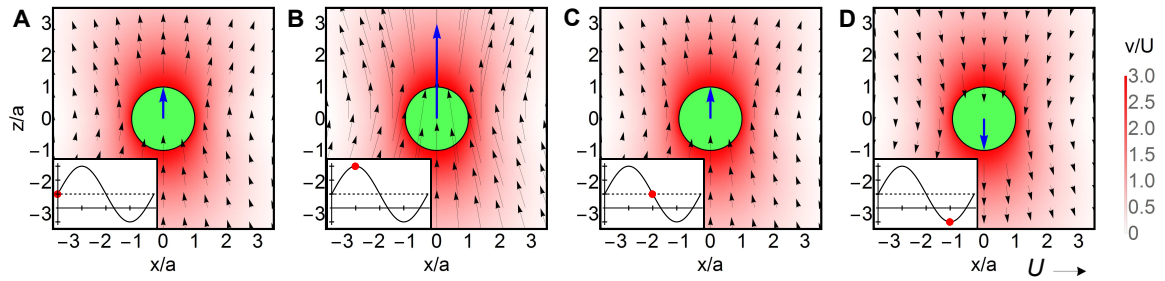

Figure 3.3: Time-sequence of instantaneous velocity fields around a sphere that is moving with periodic velocity variations. Insets show the sphere velocity (solid line, black), which varies with time in a sinusoidal pattern around an average velocity **U** (dashed line, black). The instantaneous velocities are shown as red dots. The colour maps show the normalised velocity magnitude v/U.

this instant. At a very low Reynolds number the flow is instantly dissipated such that there is no trace of the flow pattern from the last instant. History does not matter. This means that we can construct models of flows around moving swimmers, where the time-dependence of the flow pattern lies purely in the kinematics of the swimmer. The kinematics are instant by instant translated into varying boundary conditions that lead to different flow pictures. Figure 3.3 shows an example of a sphere which is moving forward and backward with a sinusoidal pattern. The instantaneous sphere velocities lead to different instantaneous flows.

Another general feature of the Stokes equations is known as *kinematic reversibility*, which also follows from linearity and time-independence. This leads to several surprising conclusions [Stone and Duprat, 2012; Pak and Lauga, 2012]. Assume that we produce a low Reynolds number flow with a certain forcing, e.g. certain boundary velocities on a swimmer surface. Now if the forcing is reversed (or doubled), kinematic reversibility means that we will get exactly reversed (or doubled) flow velocities. In figure 3.3 the forcing is the sphere velocity that changes in a sinusoidal pattern. This simply leads the flow velocities at each point to change in a sinusoidal pattern. Panel (C) and (D) have exactly reversed forcings and thus have exactly reversed flow velocities at every point. Kinematic reversibility led Purcell to formulate the famous scallop theorem, in which he states that a scallop, which swims (usually at $Re > 1$) by opening and closing its rigid shell, would not be able to propel itself at a low Reynolds number [Purcell, 1977]. Such a periodic shape change is classified as *reciprocal motion*. At a higher Reynolds number, where inertia is important, it matters for the translation how fast the shell is closed and opened, i.e., how long the opening and closing time is, while this does not matter in the viscous regime.

We formally define swimming as continuous translation or rotation due to a periodic deformation of the body. Only certain deformations lead to non-reciprocal motion and thus effective swimming. Those deformations are generally different than for higher Reynolds number swimmers. One can not swim in Stokes flow, if in the configuration space a closed cycle does not enclose a finite area [Purcell, 1977; Lauga, 2011].

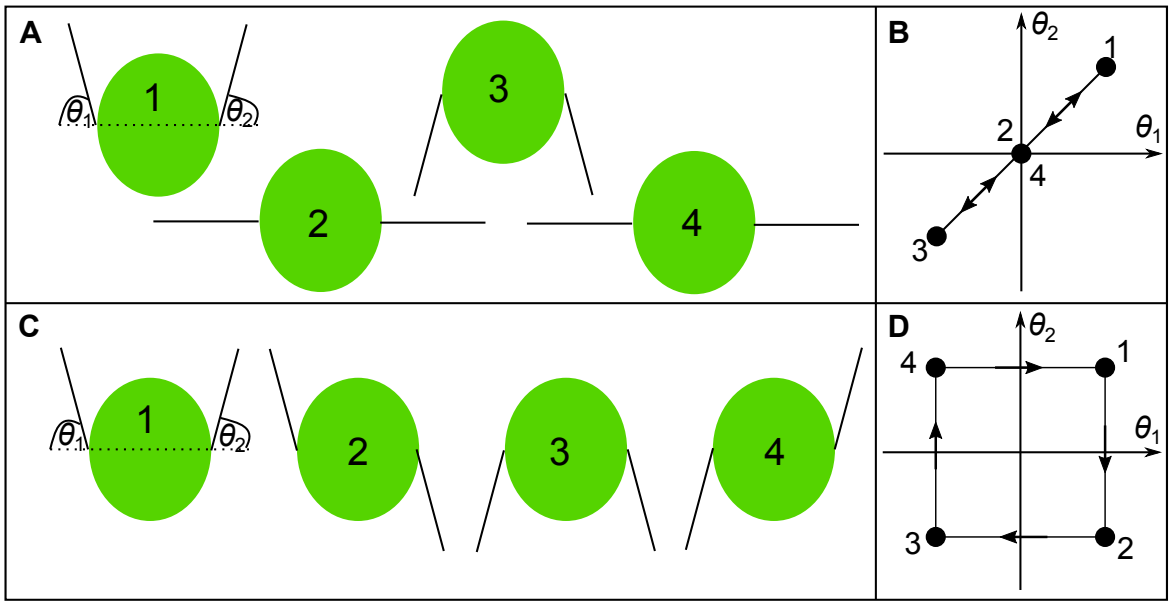

Figure 3.4: Reciprocal (A-B) versus non-reciprocal motion (C-D). (A) Swimming cycle of model organism with two rigid arms that moves periodically by varying the angles θ_1 and θ_2 in a reciprocal way. (C) Swimming cycle of model organism with two rigid arms that moves periodically by varying the two angles in a non-reciprocal way. (B, D) Traced paths in the configuration space. (B) The reciprocal path does not enclose a finite area and cannot lead to a net propulsion. (D) The non-reciprocal path, which does enclose a finite area.

The example of the non-reciprocal swimmer in figure 3.4 is an adapted version of the famous three-link swimmer by Purcell [Purcell, 1977; Becker et al., 2003]. The right arm of this swimmer always does a motion, before the left arm repeats the same with a certain time delay. These are the characteristics of a travelling wave, which is the prime form of non-reciprocal motion that is used by flagellates with propagating bending waves along the flexible flagella [Lighthill, 1976; Lauga and Powers, 2009; Lauga, 2011]. Of course those waves do usually not travel from arm to arm across the body, but separate waves travel along each flagellum.

The *Lorentz' reciprocal theorem* represents a more technical property of Stokes flows. This theorem relates different flows $\mathbf{v}_1$ and $\mathbf{v}_2$ in equal domains, i.e., with the same boundaries, but different boundary conditions. Both flows are solutions of the Stokes equations. The theorem is given as the identity

$$-\int_S (\mathbf{n}\cdot\boldsymbol{\sigma}_1)\cdot\mathbf{v}_2\,\mathrm{d}S + \int_V \mathbf{f}_1\cdot\mathbf{v}_2\,\mathrm{d}V = -\int_S (\mathbf{n}\cdot\boldsymbol{\sigma}_2)\cdot\mathbf{v}_1\,\mathrm{d}S + \int_V \mathbf{f}_2\cdot\mathbf{v}_1\,\mathrm{d}V \tag{3.9}$$

with the volume V of the fluid domain, bounded by the surface S (towards solid bodies and at infinity), the force densities $\mathbf{f}_1$ and $\mathbf{f}_2$ that relate to the respective Stokes solutions, and the surface outwards normal $\mathbf{n}$ [Stone and Duprat, 2012]. This theorem can be used, for example, to calculate the force on a sphere, if it is put into any prescribed creeping flow. I will present this so-called Faxén force in the next section, where I will focus on flows around solid spheres.

3.3 Moving spherical bodies in Stokes flow

Sinking, advected, self-propelled, as well as diffusing small organisms or particles can often be approximated as solid spheres. In the following I will first introduce the classic low Reynolds number flow past a translating sphere and the related drag force, which can be used to estimate sinking speeds and diffusion coefficients of small particles. I will further introduce the fundamental Stokes flow solution as the far-field limit of a towed body. Finally, I will show the Faxén relations, with which we can calculate the force and torque on a spherical particle due to any external Stokes flow.

3.3.1 The flow around a towed sphere

We now consider the Stokes flow past a translating sphere with radius a, which is moving at a constant velocity $\mathbf{U}$. By applying the no-slip boundary condition to the sphere boundary and zero velocity as well as zero pressure at infinity we obtain the velocity and pressure fields from the Stokes equations (3.5) and (3.6), i.e.,

$$\mathbf{v}_\mathrm{T} = U\,\cos\theta\left(\frac{3}{2r/a} - \frac{1}{2(r/a)^3}\right)\mathbf{e}_r - U\,\sin\theta\left(\frac{3}{4r/a} + \frac{1}{4(r/a)^3}\right)\mathbf{e}_\theta \tag{3.10}$$

$$p_\mathrm{T} = \frac{3\mu U a}{2r^2}\cos\theta \tag{3.11}$$

in spherical coordinates, where the z-axis is chosen along the direction of translation $\mathbf{U}$ [Happel and Brenner, 1983]. Such flow fields for different translation velocities can be seen in figure 3.3. The force that the sphere exerts on the water is obtained from the integrated stress on the sphere boundary, from equation (3.3) applied on (3.10) and (3.11), i.e.,

$$\mathbf{F} = -\oint_S \boldsymbol{\sigma}_\mathrm{T} \cdot \mathbf{n}\,\mathrm{d}S = -\oint_S \boldsymbol{\sigma}_\mathrm{T} \cdot \mathbf{e}_r\,\mathrm{d}S = 6\pi\mu a\mathbf{U}. \tag{3.12}$$

Following Newton's third law the water exerts the opposite force $\mathbf{D} = -\mathbf{F}$ back on the sphere. The linear scaling of the viscous force with length, velocity, and viscosity can already be predicted by dimensional analysis of the viscous term in the Stokes equation (3.5) [Happel and Brenner, 1983].

The force balance on the body relates the translational velocity to an external force. If the motion is created by a density difference $(\rho_\mathrm{S} - \rho)$ between the body and the water with a resulting gravity or buoyancy force, the sinking or ascending speed is proportional to the density difference [Happel and Brenner, 1983], i.e.,

$$0 = -\frac{4}{3}\pi a^3(\rho_\mathrm{S} - \rho)g\mathbf{e}_z - 6\pi\mu a\mathbf{U} \tag{3.13}$$

$$\mathbf{U} = -\frac{2a^2(\rho_\mathrm{S} - \rho)g}{9\mu}\mathbf{e}_z. \tag{3.14}$$

with the acceleration $-g\mathbf{e}_z$ due to gravity.

If the random motion of a sphere in water is created by Brownian stochastic forces, the Einstein-Smoluchowski relation relates the diffusion coefficient due to random collisions of fluid molecules with the particle at temperature T to the friction coefficient γ, i.e.,

$$D = \frac{k_\mathrm{B}\,T}{\gamma}. \tag{3.15}$$

The friction coefficient here is given with the Stokes drag (3.12) as $\gamma = 6\pi\mu a$. The Boltzmann constant is $k_\mathrm{B} = 1.38 \cdot 10^{-23}\,\mathrm{J\,K^{-1}}$. At room temperature $T = 300\,K$ (i.e., 26.85° Celsius) the Brownian diffusion coefficient for a particle with radius $a = 1$ µm in water is thus $D = 0.2\,\mu\mathrm{m}^2\,\mathrm{s}^{-1}$ and its mean absolute displacement within $t = 1\,\mathrm{s}$ is $\langle|\mathbf{x}|\rangle = \sqrt{\langle x^2\rangle + \langle y^2\rangle + \langle z^2\rangle} = \sqrt{6\,D\,t} \approx 1.1$ µm, in the order of one particle radius [Stone and Duprat, 2012]. Note that the average absolute displacement in diffusional processes scales with the square root of time as opposed to ballistic motion with velocity $\mathbf{U}$, where the displacement $\langle|\mathbf{x}|\rangle = |\mathbf{U}|\,t$ increases linearly with time.

3.3.2 The fundamental solution

The fundamental solution to the Stokes equations represents the creeping flow due to a point force $\mathbf{f} = \mathbf{F}\delta(\mathbf{x})$ acting on the water and it can be obtained from the flow due to a translating sphere by keeping its force on the fluid constant, but letting the sphere

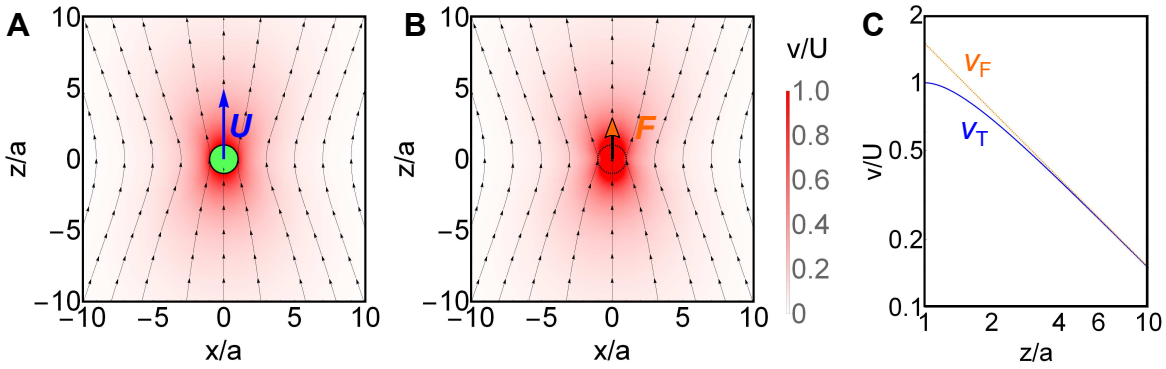

Figure 3.5: Far field flow of a towed sphere. (A) The flow field $\mathbf{v}_\mathrm{T}$ (3.16) due to a towed sphere (green) with radius a and velocity $\mathbf{U}$ (blue). (B) The far field approximation $\mathbf{v}_\mathrm{F}$ (3.17) of a translating sphere, which represents the flow due to a point force $\mathbf{F} = 6\pi\mu a\mathbf{U}$. The spherical boundary is shown here as a black circle. (C) Comparison of the velocity magnitude on the z-axis in front of the sphere. Although the no-slip condition on the sphere surface is not represented by $\mathbf{v}_\mathrm{F}$, the point force flow, which decays as one over distance, approximates the flow $\mathbf{v}_\mathrm{T}$ beyond a distance of a few sphere radii.

radius go to zero. This is equivalent to zooming out to a large distance $r \to \infty$ from a towed particle at the origin, so that we can neglect its finite size (and shape), since $a \ll r$. Conveniently we write the velocity field (3.10) due to the translating sphere as

$$\mathbf{v}_\mathrm{T} = \left(\frac{3}{4r/a} + \frac{1}{4(r/a)^3}\right)\mathbf{U} + \left(\frac{3}{4r/a} - \frac{3}{4(r/a)^3}\right)\frac{(\mathbf{U}\cdot\mathbf{x})\,\mathbf{x}}{r^2}. \tag{3.16}$$

Replacing the velocity with the force expression as $\mathbf{U} = \mathbf{F}/(6\pi\mu a)$ and letting $a \to 0$ results in the fundamental solution

$$\mathbf{v}_\mathrm{F} = \mathbf{F}\cdot\frac{\boldsymbol{\mathcal{G}}}{8\,\pi\,\mu} = \frac{1}{8\pi\mu}\left(\frac{\mathbf{F}}{r} + \frac{(\mathbf{F}\cdot\mathbf{x})\,\mathbf{x}}{r^3}\right) \tag{3.17}$$

$$p_\mathrm{F} = \frac{\mathbf{F}\cdot\mathbf{x}}{4\,\pi\,r^3}, \tag{3.18}$$

that is also known as *Stokeslet* and the flow can be represented by the Greens function

$$\boldsymbol{\mathcal{G}} = \frac{\boldsymbol{\mathcal{I}}}{r} + \frac{(\boldsymbol{\mathcal{I}}\cdot\mathbf{x})\mathbf{x}}{r^3}, \tag{3.19}$$

which is known as the Oseen tensor [Kim and Karilla, 2005]. Since the flow (3.17) represents the far field due to a towed particle, it is important already by itself for the analysis of flows around small sinking particles and organisms (figure 3.5). As seen from equation (3.17) the flow disturbance around a sinking sphere, which is driven by an external force, decays slowly as $v \sim 1/r$. The fundamental solution can also be used as a basis for general Stokes flows and to expand complex flow fields in a multipole expansion in order to analyse their far-field behaviour (see section 3.4).

3.3.3 Faxén relations

We now assume a given Stokes flow $\mathbf{v}^\infty(\mathbf{x})$, which is created by another organism or has another external source, and ask what is the force and torque on a spherical body that is put into this flow environment. The answer is given by the *Faxén laws*. The force and torque due to the external flow $\mathbf{v}^\infty(\mathbf{x})$ on a sphere with centre at $\mathbf{x}_\mathrm{p}$ and with radius a, translation velocity $\mathbf{U}$, and rotational velocity $\boldsymbol{\omega}$ are given as

$$\mathbf{T} = 6\pi\mu a \left[\left(1 + \frac{a^2}{6}\nabla^2\right)\mathbf{v}^\infty(\mathbf{x})\right]_{\mathbf{x}=\mathbf{x}_\mathrm{p}} - 6\pi\mu a\mathbf{U} \tag{3.20}$$

$$\mathbf{L} = 8\pi\mu a^3 \left(\frac{1}{2}\boldsymbol{\nabla}\times\mathbf{v}^\infty(\mathbf{x}) - \boldsymbol{\omega}\right)|_{\mathbf{x}=\mathbf{x}_\mathrm{p}}. \tag{3.21}$$

The original Faxén relations (3.20) and (3.21) are formulated as the force and torque on a sphere, but they can be generalized for bodies with an ellipsoidal shape and also include the stresslet (i.e., the resistance of the body to straining motion) [Faxén, 1922, 1924; Batchelor and Green, 1972; Kim and Karilla, 2005; Stone and Duprat, 2012]. The reciprocal theorem (3.9) can be used to derive this relation from the known solutions on the translating and rotating sphere. We can immediately see that, if the external flow velocity is constant and given as $\mathbf{v}^\infty(\mathbf{x}) = \mathbf{V}$, we obtain zero torque and a force given as $\mathbf{T} = 6\pi\mu a(\mathbf{V} - \mathbf{U})$, which results in the opposite force $\mathbf{F} = -\mathbf{T}$ on the water and with $\mathbf{V} = 0$ we retrieve the force (3.12) for a translating sphere in quiescent fluid.

As one example for the use of the Faxén relations, which is relevant for advective prey capture I will here show the Faxén force and torque on a small spherical particle with radius r_p, which is put into the external flow field produced by a much larger towed sphere that has the radius a and the velocity $\mathbf{U}$. We here assume that the motion of the small particle is influenced by the flow around the bigger sphere, but the bigger sphere remains in its steady motion with constant velocity and is not moved by the presence of the small sphere. If we put the origin in the centre of the larger sphere, the external flow field $\mathbf{v}_\infty = \mathbf{v}_\mathrm{T}$ is given by equation (3.10). The translational velocity $\mathbf{u} = \mathbf{T}/(6\pi\mu r_\mathrm{p})$ and rotational velocity $\boldsymbol{\omega} = \mathbf{L}/(8\pi\mu r_\mathrm{p}^3)$ of the passive small particle, which is located at position $\mathbf{x}$, are calculated with the Faxén relations (3.20) and (3.21) as

$$\begin{aligned}\mathbf{u}(\mathbf{x}) = \quad \mathbf{v}_\mathrm{T} + \frac{r_\mathrm{p}^2}{6}\nabla^2\mathbf{v}_\mathrm{T} = \quad & U\,\cos\theta\left(\frac{3}{2r/a} - \frac{1}{2(r/a)^3} - \frac{(r_\mathrm{p}/a)^2}{2(r/a)^3}\right)\mathbf{e}_r \\ & -U\,\sin\theta\left(\frac{3}{4\,r/a} + \frac{1}{4(r/a)^3} + \frac{(r_\mathrm{p}/a)^2}{4(r/a)^3}\right)\mathbf{e}_\theta \end{aligned} \tag{3.22}$$

$$\boldsymbol{\omega}(\mathbf{x}) = \quad \frac{1}{2}\boldsymbol{\nabla}\times\mathbf{v}_\mathrm{T} = \quad \frac{3}{4(r/a)^2}\,\frac{U}{a}\,\sin\theta\,\mathbf{e}_\phi. \tag{3.23}$$

These two fields now determine the trajectories and rotation of small particles that are influenced by the flow of a large translating sphere. If the particles are passive, i.e., they do not have an active velocity on top of the disturbance field, the rotation (3.23)

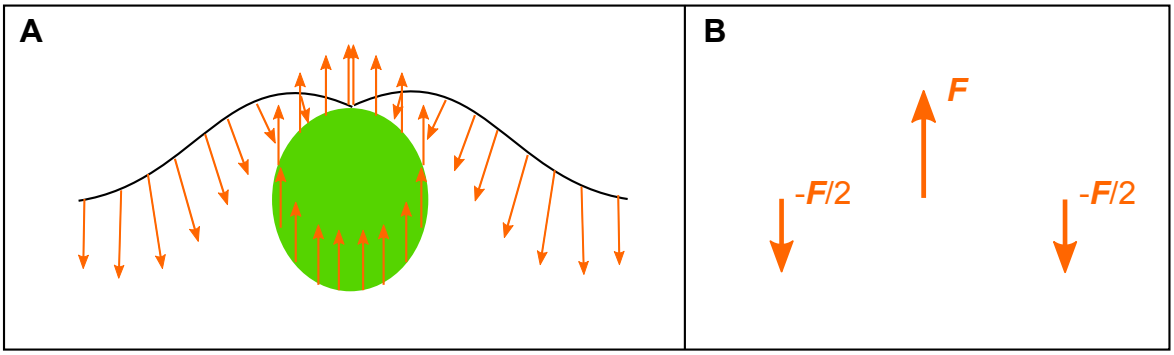

Figure 3.6: The idea behind far field models. (A) An organism swims by a certain motion of each surface element, which leads to a complex arrangement of many forces (in a continuous stress distribution) that act on the fluid. When viewed from the far field the complex force distribution is 'smoothed out' and only those contributions remain that lead to the slowest flow decay. If the contribution with the slowest decay is a force quadrupole, i.e., both the monopole (force) and dipole (strain and torque) vanish, the same far field can be obtained from a characteristic arrangement of just three point forces (B). Less forces are not sufficient to cancel the monopole and dipole, while more forces are not necessary to represent the characteristic far field of such a swimmer.

will not influence their trajectories, since they are spherically symmetric. However, for active particles the local vorticity will rotate their swimming direction and can thus influence their trajectories.

3.4 Integral and far-field representation of Stokes flows

As mentioned before, self-propelled organisms actuate their body in a certain (periodic) way in order to continuously move forward. Close to the organism the flow can be very complex depending on the specific movement, which can vary significantly between different swimmers. However, when zooming out towards the far field, less detailed features can be seen and the flow generally simplifies to characteristic patterns, which are given by the lowest moments of the force distribution on the boundary (figures 3.5 and 3.6). The far field flow does not look the same for all swimmers, but we can distinguish different swimming modes according to the flow field at large distance, with respect to how the forces are distributed. Quantities that can be extracted from far field approximations of flows are the magnitudes and arrangement of the main propulsion forces, the characteristic flow pattern and the decay of the flow speed with increasing distance from the swimmer. Many microorganisms are exposed to flow-sensing predators and they aim to keep their disturbance zones small. For this purpose a fast decay of the created flows with distance is advantageous [Kiørboe et al., 2014; Visser, 2007; Tiselius and Jonsson, 1997].

3.4.1 Integral representation

The flow due to each small moving surface element $\mathrm{d}S(\mathbf{x}_\mathrm{p})$ of the swimmer body can be represented with a point force at $\mathbf{x}_\mathrm{p}$ acting on the fluid. The fundamental Stokes solution (3.17) can be used with the Oseen tensor $\mathcal{G}(\mathbf{x}-\mathbf{x}_\mathrm{p})$ (3.19) to express any creeping flow [Kim and Karilla, 2005]. If the complete stress distribution $\boldsymbol{\sigma}(\mathbf{x}_\mathrm{p})$ is known for a particle or swimmer with total surface S, its complete flow field can be reconstructed with the superposition of all point force flow fields as

$$\mathbf{v} = \frac{1}{8\pi\mu} \oint_S (\boldsymbol{\sigma}(\mathbf{x}_\mathrm{p}) \cdot \mathbf{n}) \cdot \boldsymbol{\mathcal{G}}(\mathbf{x}-\mathbf{x}_\mathrm{p})\, \mathrm{d}S(\mathbf{x}_\mathrm{p}), \tag{3.24}$$

where the force due to each surface element is expressed as $\mathrm{d}\mathbf{F}(\mathbf{x}_\mathrm{p}) = (\boldsymbol{\sigma}(\mathbf{x}_\mathrm{p})\cdot\mathbf{n})\mathrm{d}S(\mathbf{x}_\mathrm{p})$. Equation (3.24) is known as the integral representation of the flow field.

3.4.2 Far-field approximation

Although the integral representation represents the whole flow field, it is often analytically not tractable and not useful to categorise main swimming modes. However, the point force representation can be used to expand the flow in the far field in order to arrive at simple analytical approximations (figure 3.6). With the origin within the swimmer body, the far field is defined by the condition $|\mathbf{x}| \gg |\mathbf{x}_\mathrm{p}|$ for all surface points $\mathbf{x}_\mathrm{p}$. At the lowest order (with the roughest force resolution) we approximate $\boldsymbol{\mathcal{G}}(\mathbf{x}-\mathbf{x}_\mathrm{p}) \approx \boldsymbol{\mathcal{G}}(\mathbf{x})$. With this approximation we do not resolve any detail of the force distribution, but only see the total net force on the fluid, i.e., from (3.24) we obtain

$$\mathbf{v} \approx \mathbf{v}_\mathrm{F} = \frac{1}{8\pi\mu} \oint_S (\boldsymbol{\sigma}(\mathbf{x}_\mathrm{p}) \cdot \mathbf{n})\, \mathrm{d}S(\mathbf{x}_\mathrm{p}) \cdot \boldsymbol{\mathcal{G}}(\mathbf{x}) = \mathbf{F} \cdot \frac{\boldsymbol{\mathcal{G}}(\mathbf{x})}{8\pi\mu}. \tag{3.25}$$

Thus for any body (not only spheres) with a non-zero net force $\mathbf{F}$ on the fluid, the lowest order far field is given by a Stokeslet flow, which decays as the slowest mode with distance as $1/r$.

For a neutrally buoyant organism, however, the net force is zero in the absence of additional external force fields, such that the lowest order of the far-field expansion vanishes. The higher orders, the force multipoles, are calculated from the derivatives of the Stokeslet using an expansion of the Oseen tensor (3.19) in $\mathbf{x}_\mathrm{p}$ about $\mathbf{x}_\mathrm{p} = 0$, i.e., we have

$$\boldsymbol{\mathcal{G}}(\mathbf{x}-\mathbf{x}_\mathrm{p}) = \sum_{n=0}^{\infty} \frac{1}{n!} (\mathbf{x}_\mathrm{p} \cdot \boldsymbol{\nabla}_{\mathbf{x}_\mathrm{p}})^n\, \boldsymbol{\mathcal{G}}(\mathbf{x}-\mathbf{x}_\mathrm{p})|_{\mathbf{x}_\mathrm{p}=0} \tag{3.26}$$

$$= \sum_{n=0}^{\infty} \frac{(-1)^n}{n!} (\mathbf{x}_\mathrm{p} \cdot \boldsymbol{\nabla})^n\, \boldsymbol{\mathcal{G}}(\mathbf{x}), \tag{3.27}$$

where $\boldsymbol{\nabla}_{\mathbf{x}_\mathrm{p}} = (\mathbf{x}_\mathrm{p} \cdot \boldsymbol{\nabla})\mathbf{x}_\mathrm{p}/|\mathbf{x}_\mathrm{p}|^2$ is the gradient along the direction given by $\mathbf{x}_\mathrm{p}$. This multipole expansion (3.27) is analogous to the one in electrodynamics, where point charges instead of forces are used as a basis [Kim and Karilla, 2005].

The force dipole with $n = 1$ in (3.27) represents the lowest order of the far-field expansion for force-free swimmers and thus provides the most simple singularity model, which is used to sort microswimmers into rough categories [Lauga and Powers, 2009]. With the gradient (first spatial derivative) of the Oseen tensor, the flow field due to a force dipole is given as

$$\mathbf{v}_\mathrm{D} = -\frac{1}{8\pi\mu} \cdot \oint_S (\boldsymbol{\sigma}(\mathbf{x}_\mathrm{p}) \cdot \mathbf{n}) \otimes \mathbf{x}_\mathrm{p} \, \mathrm{d}S(\mathbf{x}_\mathrm{p}) \cdot \boldsymbol{\nabla}\boldsymbol{\mathcal{G}} = -\boldsymbol{\mathcal{D}} \cdot \frac{\boldsymbol{\nabla}\boldsymbol{\mathcal{G}}}{8\pi\mu}, \tag{3.28}$$

where the dipole moment $\boldsymbol{\mathcal{D}}$ is defined with the integral above, i.e., as the first moment of the force distribution on the surface.

The dipole flow field can be divided in a symmetric part, the stresslet flow $\mathbf{v}_\mathrm{S}$, and an antisymmetric part, the rotlet flow $\mathbf{v}_\mathrm{RT}$, which represent straining and rotating flows, respectively. For many microswimmers one can distinguish two main forces, one pushing backwards on the fluid (against the swimming direction) due to the action of one or several swimming appendages at some distance in front or behind the body and one which balances the first force and represents the swimmer body moving forward. We now assume two opposite forces, each with a magnitude F, which are separated by a vector $\mathbf{d}$. The flow field in a coordinate system with origin between the forces is given as

$$\mathbf{v} = \frac{\mathbf{F} \cdot \boldsymbol{\mathcal{G}}(\mathbf{x} - \mathbf{d}/2)}{8\pi\mu} - \frac{\mathbf{F} \cdot \boldsymbol{\mathcal{G}}(\mathbf{x} + \mathbf{d}/2)}{8\pi\mu}. \tag{3.29}$$

For the far field we let the separation distance $|\mathbf{d}|$ go to 0, but keep the dipole moment $\boldsymbol{\mathcal{D}} = \mathbf{F} \otimes \mathbf{d}$ constant, i.e., we get

$$\mathbf{v}_\mathrm{D} = -(\mathbf{F} \otimes \mathbf{d}) \cdot \frac{\boldsymbol{\nabla}\boldsymbol{\mathcal{G}}}{8\pi\mu} = \mathbf{v}_\mathrm{S} + \mathbf{v}_\mathrm{RT} \tag{3.30}$$

$$\mathbf{v}_\mathrm{S} = \frac{1}{8\pi\mu}\left[\frac{(\mathbf{F}\cdot\mathbf{d})\mathbf{x}}{r^3} - 3\frac{(\mathbf{F}\cdot\mathbf{x})(\mathbf{d}\cdot\mathbf{x})\mathbf{x}}{r^5}\right] \tag{3.31}$$

$$\mathbf{v}_\mathrm{RT} = \frac{(\mathbf{d}\times\mathbf{F})\times\mathbf{x}}{8\pi\mu\, r^3} \tag{3.32}$$

with the symmetric stresslet flow $\mathbf{v}_\mathrm{S}$ and the antisymmetric rotlet flow $\mathbf{v}_\mathrm{RT}$ [Kim and Karilla, 2005]. Thus we can relate the dipole term, which is given by the gradient of a Stokeslet, to a pair of opposite forces that are brought close together without altering the strain rate and torque that they cause.

The rotlet relates to a point torque $\mathbf{L} = \mathbf{d} \times \mathbf{F}$ and can be derived from the far field of the flow due to a rotating sphere with external torque analogous as the Stokeslet relates to a translating sphere with external force (equations (3.16) and (3.17)). The flow around a rotating sphere with rotational velocity $\boldsymbol{\Omega}$ is given as

$$\mathbf{v}_\mathrm{R} = \frac{\boldsymbol{\Omega} \times \mathbf{x}}{(r/a)^3}. \tag{3.33}$$

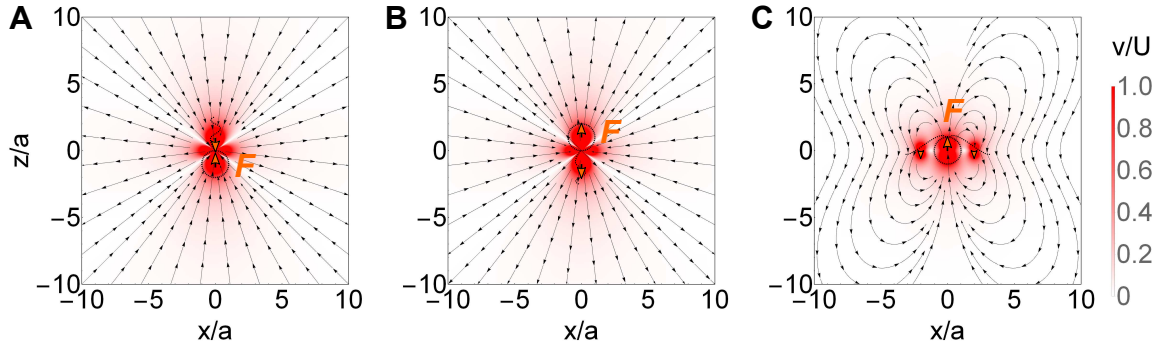

Figure 3.7: Far-field models for self-propelled swimmers. (A) Puller represented by two opposite point forces $\mathbf{F} = F\mathbf{e}_z$ and $-\mathbf{F}$ (stresslet) directed towards each other. (B) Pusher represented by two point forces (stresslet) directed away from each other. (C) Neutral swimmer with force quadrupole as main moment, represented by three point forces $-\mathbf{F}/2$, $\mathbf{F}$ and $-\mathbf{F}/2$ (from left to right) in a left-right symmetric arrangement with separation vectors perpendicular to the force directions. The color map shows the flow velocities scaled with the speed $U = F/(6\pi\mu a)$ of a sphere with radius a, that pushes on the fluid with the force $\mathbf{F}$.

Keeping the torque $\mathbf{L} = 8\pi\mu a^3\mathbf{\Omega}$ constant and letting the radius a go to 0, we arrive at the rotlet flow (3.32).

If the forces are parallel to the separation vector, i.e., if $\mathbf{d} \times \mathbf{F} = 0$, the torque is zero and we remain with a pure straining motion. The total torque on a freely swimming organism must be zero also for antisymmetric stress distributions, since the torque due to the actuation forces is balanced by a rotation of the body analogous to the zero force condition. Thus the rotlet flow component (3.32) will vanish for self-propelled microorganisms [Pak and Lauga, 2012].

3.4.3 Point force models for microswimmers

As mentioned before, neutrally buoyant organisms do not experience a body force and thus have no slowly decaying monopole component (net force) and also no rotlet (net torque) in their flow field. For self-propelled microorganisms one can distinguish between three characteristic stresslet flows (3.31). If the main forces are directed towards each other, i.e., if $\mathbf{F}$ and $\mathbf{d}$ point in opposite directions, the flow is that of a puller (figure 3.7 A). If the forces are directed away from each other the flow is that of a pusher (figure 3.7 B). A third swimmer type is a neutral swimmer with respect to strain, for which the stresslet contribution is zero and only higher order terms come into play (figure 3.7 C) [Andersen et al., 2015a]. The different types relate to swimmers which either create their propulsion forces at the back or front of their body, thus "pushing" or "pulling" themselves through the water, or the neutral ones which do not have any bias towards front or back. The stresslet as far-field

model can describe the (time-averaged) flows of many microswimmers such as bacteria and flagellates. For bacteria with one pushing bundle of flagella aligned with the symmetry axis, the pusher stresslet can even represent the intermediate field relatively close to the organism [Drescher et al., 2011]. For flagellates, such as *Chlamydomonas*, with two or more swimming appendages acting distant from each other, the stresslet flow only matches at large distance or completely vanishes and thus cannot represent the intermediate and near-field patterns due to the too roughly approximated force distribution.

Since many organisms propel themselves with several appendages which are in general not aligned on one axis, one needs to find better suited singularity models for such swimmers. One model for swimmers with two left-right symmetrically arranged propulsion forces is the three point force model, which represents the forces due to each of the two appendages and the moving body each with one point force (figure 3.7 C) [Drescher et al., 2010; Kiørboe et al., 2014; Andersen et al., 2015a].

With the forward pointing force $\mathbf{F}$ acting in the origin, the flows due to the two left-right symmetric backwards acting forces can be expanded using equation (3.27) for the far field, where the distance between the forces becomes small compared to the far viewpoint. Due to zero net force on the swimmer the Stokeslet with its slow decay vanishes and so does any rotational component due to the symmetric force distribution. The stresslet component, which for most swimmers dominates the flow in the far field with the slowest decay, can by a three point force swimmer be suppressed with an arrangement with forces next to each other in a breast-stroke type neutral swimming mode (figure 3.7 C). In this mode the far field flow decays faster with $1/r^3$ as a force quadrupole [Andersen et al., 2015a]. Similarly to the three point force model one can imagine other swimmer types with asymmetric and more than two propulsion forces that lead to neutral swimming modes with fast decays. The forces used in the singularity models can be related to a translational velocity of the swimmer by relating the force $\mathbf{F}$, which has the same magnitude as the sum of the backwards acting propulsion forces, to the drag on the body that is approximated as a sphere with radius a, thus $\mathbf{U} = \mathbf{F}/(6\pi\mu a)$ using the Stokes drag formula (3.12).

3.5 A sphere propelled by a point force

As we have seen, we can represent the far-field flow and the main flow patterns around microswimmers already with few singular point forces acting on the fluid. However, if we want to account for the hydrodynamic forces on the body due to the relative motion of appendages and body and if we want to know the flow close to the body of the organism, e.g. to determine prey encounter rates, we need to represent the boundary conditions instead of just using localised point forces. An analytical model that we use for those purposes represents the cell body as sphere with correct no-slip boundary condition, but the swimming appendages are represented as idealized point forces acting on the water (figure 2.5) [Higdon, 1979a,b; Jiang et al., 2002; Dölger et al., 2017a,b].

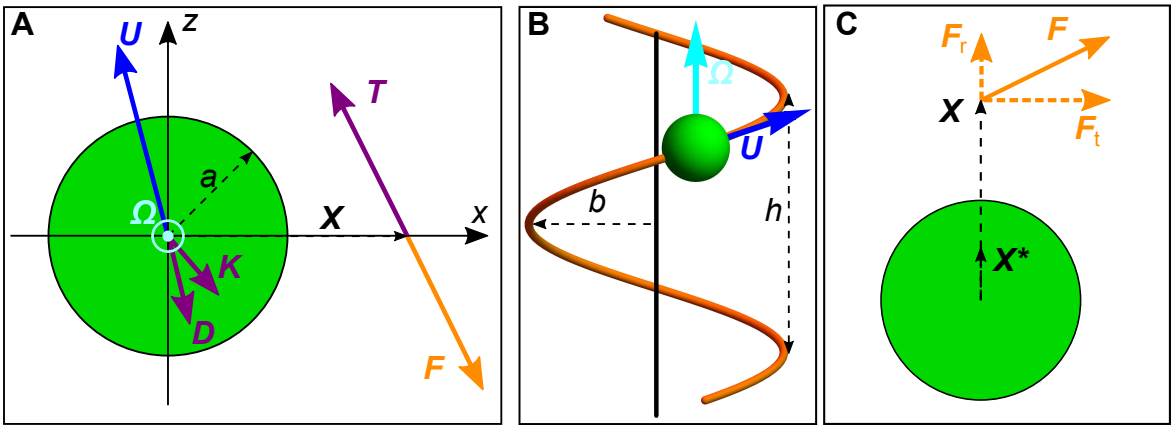

Figure 3.8: Model parameters, swimming kinematics, and image representation for a sphere propelled by a point force. (A) Basic building block with one point force. Sphere (green), point force $\mathbf{F}$ acting on the fluid (orange), forces acting on the organism (purple), i.e., the thrust force $\mathbf{T}$, the Faxén force $\mathbf{K}$ due to the flow produced by the point force, and the Stokes drag $\mathbf{D} = -6\pi\mu a\mathbf{U}$ due to the translational motion with velocity $\mathbf{U}$ (blue). The angular velocity $\boldsymbol{\Omega}$ (light blue) is directed out of the plane in the negative y-direction. (B) Helical trajectory with radius b and pitch h for a sphere translating with velocity $\mathbf{U}$ and rotating with angular velocity $\boldsymbol{\Omega}$ due to several point forces. (C) The flow can be represented as the flow due to a point force $\mathbf{F}$ in a free domain plus image singularities inside the sphere between the sphere centre and the image point $\mathbf{X}^* = (a^2/|\mathbf{X}|^2)\mathbf{X}$. The solution can be divided in the axisymmetric flow due to the radial force component $\mathbf{F}_\mathrm{r}$ and the flow due to the transverse component $\mathbf{F}_\mathrm{t}$. Figure adapted from Dölger et al. [2017a].

For the kinematics of such a swimmer we do not need to know the full flow solution but just the force and torque balance. The point forces are assumed to be connected to the body by a rigid frictionless scaffold, thus transmitting forces directly to the body (figure 3.8 A). In addition to the direct force $\mathbf{T} = \sum_i \mathbf{T}_i$ on the body from the propulsion of the flagella as in the pure point force approximations, we have a Faxén force $\mathbf{K}$ (3.20) acting on the body in the Stokeslet flow [Kim and Karilla, 2005]. This force depends on the propulsion forces $\mathbf{F}_i$ and their positions $\mathbf{X}_i$, which determine the stresses that are created on the spherical body. The swimming velocity is thus, different from the pure point force models, given as $\mathbf{U} = (\sum_i \mathbf{T}_i + \mathbf{K})/(6\pi\mu a)$. Analogous to the translational velocity we can calculate a rotational velocity $\mathbf{\Omega}$ from the torque balance as $\mathbf{\Omega} = (\sum_i \mathbf{X}_i \times \mathbf{T}_i + \mathbf{L})/(8\pi\mu a^3)$, where again the Faxén torque $\mathbf{L}$ depends on the position, direction, and magnitude of the point forces. With a fixed force arrangement of several point forces such a swimmer generally swims in a helix, the shape of which is determined by its translational and rotational velocity (figure 3.8 B) [Dölger et al., 2017a]. For the kinematics of such a model organism, a pure point force model, which has $\mathbf{K} = 0$, is a good approximation, if the forces are placed sufficiently far away from the body, i.e., if $|\mathbf{X}_i| \gg a$.

The flow field due to a point force outside a spherical boundary has first been solved by Oseen [Oseen, 1927], who found the Green's function representation of this solution. For fundamental flows next to solid boundaries, the solution can also be represented with the fundamental solution in a free domain plus so-called image solutions on the other side of the solid surface (i.e., outside the fluid domain) in order to satisfy the no-slip condition. For the flow due to a Stokeslet in proximity of a spherical no-slip boundary the image solutions are, for example, described by Kim and Karilla [2005] (figure 3.8 C). The force component $\mathbf{F}_\mathrm{r}$ normal to the boundary produces an axially symmetric flow which is represented by few low order multipoles at the image point $\mathbf{X}^* = (a^2/|\mathbf{X}|^2)\mathbf{X}$. The force component $\mathbf{F}_\mathrm{t}$ transversal to the spherical boundary needs a more complicated image system with low order multipoles at the image point as well as a line distribution of multipoles between the sphere centre and the image point [Kim and Karilla, 2005].

The flow around a freely swimming model organism can be modelled with the above described flow due to the point force next to a sphere, which is superposed with the flows (3.10) and (3.33) due to the rotational and translational velocities $\mathbf{U}$ and $\mathbf{\Omega}$, which are obtained from the force and torque balance [Higdon, 1979b; Dölger et al., 2017a] (figure 3.2). In the far field at $r \gg a$ the flow field converges to the flow of pure point force models. If the point force distance is much larger than the body radius ($|\mathbf{X}_i| \gg a$), the flow disturbances created by the propulsion forces have no influence on the force on the body. In that case the near flow field is represented by a simple rotating and translating sphere. In the case of near forces the flow field and drag force are influenced due to the non-negligible flow disturbance close to the boundary. For a radial force this means that the drag on the body (opposite to the swimming direction) increases (due to $\mathbf{K}$) compared to a towed sphere, while also the flux towards the body can increase for very close forces, which has implications for the trade-off of swimming and feeding [Langlois et al., 2009].

While we here generally consider spherical bodies, the image solution and Faxén relations can actually be extended to ellipsoidal bodies [Kim and Arunachalam, 1987; Kim and Karilla, 2005], which can provide analytical swimmer models for more general body shapes.

3.6 Forces due to moving swimming appendages

In the above sections I have detailed on Stokes flows and forces on spherical bodies and the arrangement of propulsion forces from swimming appendages. In the following section I will explain, how those propulsion forces are created and can be modelled as a function of the kinematics of a moving swimming appendage.

Swimming appendages of microorganisms are often thin long structures such as the whip-like flagella for unicellular organisms. In order to swim continuously the appendages need to be moved in a periodic pattern. As we have seen, viscous forces scale with the characteristic body length and it is often advantageous to create forces not too close to the no-slip body in order to minimise the Faxén drag on it [Langlois et al., 2009; Dölger et al., 2017a]. Thus long slender appendages are optimised for low Reynolds number swimming.

For slender objects that can be approximated as ellipsoids or cylinders with radius a and length $2b$ with small aspect ratio $\epsilon = a/b \ll 1$ one can use the so-called slender-body theory to calculate the drag forces that lead to propulsion. With this approximation, where one length-dimension is dominant compared to the other two, the flow due to the moving slender body can be represented with a line-distribution of low order multipoles [Gray and Hancock, 1955; Lighthill, 1976; Brennen and Winet, 1977].

Let us first look at the forces on a straight slender body that is moving with velocity $\mathbf{u}$. The drag forces on such a body can be decomposed into a component $\mathbf{T}_\parallel = -\zeta_\parallel \, \mathbf{u}_\parallel \, b$ parallel to the centreline and a perpendicular component $\mathbf{T}_\perp = -\zeta_\perp \, \mathbf{u}_\perp \, b$. The drag coefficients for a slender spheroid can be exactly calculated [Happel and Brenner, 1983; Berg, 1972], i.e.,

$$\zeta_\parallel = \frac{2\pi\mu}{\ln(2/\epsilon) - 0.5} \tag{3.34}$$

$$\zeta_\perp = \frac{4\pi\mu}{\ln(2/\epsilon) + 0.5}. \tag{3.35}$$

The drag coefficients ζ are modified for different cross-sectional shapes, but one important property is relevant for all slender bodies. The force due to motion perpendicular to the centreline is different and approximately twice as large as the force due to motion parallel to the centreline, $\zeta_\perp \approx 2\zeta_\parallel$, which is due to the anisotropy of the fundamental Stokes solution (3.17).

The most simple slender-body theory, the resistive force or local drag theory, relates the force $\mathbf{t}$ per unit length on each segment of a flagellum linearly to its velocity

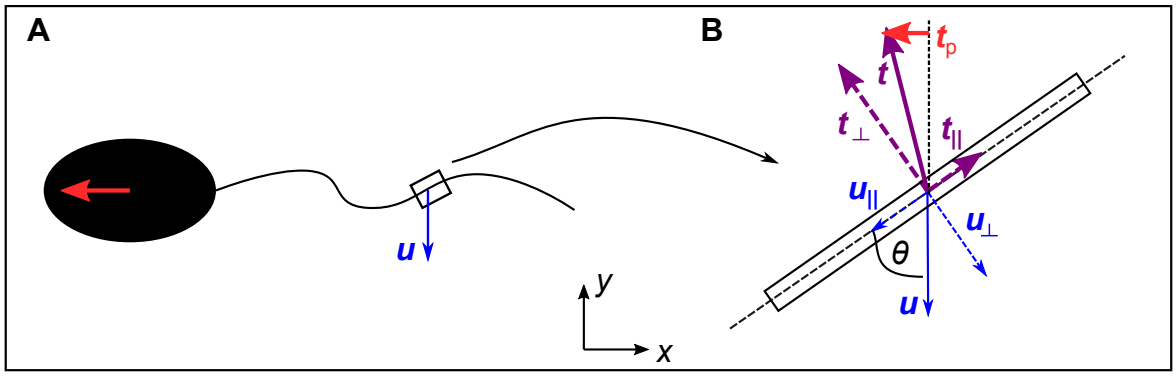

Figure 3.9: Drag anisotropy and drag-based thrust. (A) An organism with a travelling bending wave with local flagellum velocities along the y-direction in the swimmer frame. (B) Each segment of the slender body experiences a drag force $\mathbf{t} = \mathbf{t}_\perp + \mathbf{t}_\parallel$ per unit length that is not aligned with the velocity of the segment (drag anisotropy) and thus leads to a net propulsion force (drag based thrust) $\mathbf{t}_\mathrm{p} = -t_\mathrm{p}\mathbf{e}_x$ perpendicular to the segment velocity according to equation (3.36). Sketch adapted from Lauga and Powers [2009].

components and does not account for interactions between segments due to large-amplitude deformations. The so-called drag-based thrust

$$\mathbf{t}_\mathrm{p} = (\zeta_\parallel - \zeta_\perp)\sin\theta\,\cos\theta\mathbf{e}_x \tag{3.36}$$

is the force, which is produced in the direction perpendicular to the direction of motion of the flagellar segments (figure 3.9) [Lauga and Powers, 2009]. This force, which can be used for flagellar propulsion by travelling waves, only arises due to the drag anisotropy.

A resistive force theory based on sinusoidal shape changes of the slender filament [Gray and Hancock, 1955] leads to the drag coefficients

$$\zeta_\parallel = \frac{2\pi\mu}{\ln(2\,\lambda/a) - 0.5} \tag{3.37}$$

$$\zeta_\perp = \frac{4\pi\mu}{\ln(2\,\lambda/a) - 0.5}, \tag{3.38}$$

which depend on the wavelength λ (i.e., the characteristic length of shape variation).

In resistive force theory, the finite thickness of the slender object is only taken into account as logarithmic correction in leading order, thus the coefficients predicted from classic resistive force theory are often not accurate for realistic flagellar dimensions that are not exponentially thin and for kinematics with large amplitudes that lead to considerable hydrodynamic interaction between segments [Lighthill, 1976; Brennen and Winet, 1977; Lauga and Powers, 2009].

Rodenborn et al. [2013] experimentally observed the thrust, torque, and drag on rotating helices representing bacterial flagella and tested the validity range of different slender-body theories with resistive force theory being the simplest model, which with

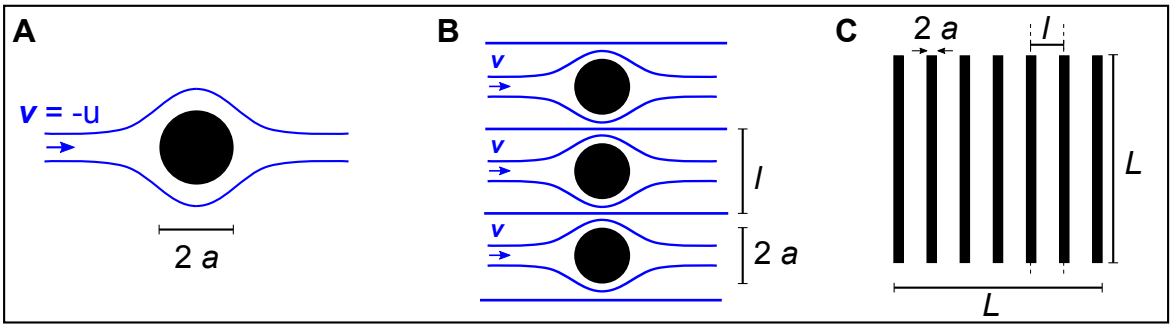

Figure 3.10: Viscous flows around collectors. (A) The viscous flow with velocity $\mathbf{v} = -\mathbf{u}$ at large distance approaches a single collector (sphere or cylinder) with radius a and is diverted around the solid body. (B) In an array of parallel cylinders the flow cannot be freely diverted around each cylinder, but the streamlines are compressed to fit in the respective flow cell of width l. (C) Transversal cross-section of a quadratic parallel-cylinder filter with side length L. In the analysis such a filter is treated as a cut-out of an infinite filter, i.e., no end effects of the periodic array are considered.

the original coefficients (3.37) and (3.38) was found to only be valid for a very small part of the relevant parameter range. A more refined theory with not only Stokeslets but also quadrupole singularities on the centreline [Lighthill, 1976], or the use of regularised Stokeslets [Cortez et al., 2005] on the filament surface were shown to fit the measurements more accurately. The simple resistive force coefficients thus provide a useful analytical tool to make rough estimates of produced forces by slender swimming appendages, but should be used with care.

While slender-body theory focusses on the forces produced by a slender propulsion appendage, the hydrodynamic disturbance around the body, which is propelled by the flagellum, is often neglected. However there are few models that take the body into account [Higdon, 1979b; Wróbel et al., 2016]. Wróbel et al. [2016] derived the analytical flow solution of a regularised Stokeslet outside a sphere, which connects to the above discussed analytical swimmer model using a cut-off function that replaces the diverging force density of the Stokeslet, and the authors also discussed the case of propulsion of a spherical body by a helical flagellum, the action of which is represented by a discretised distribution of regularized Stokeslets.

3.7 The flow past filter structures

Filter structures are commonly used in the plankton for prey capture [Jørgensen, 1955; Fenchel, 1986; Riisgård and Larsen, 2001, 2010]. Here I will introduce the physics of the flow past filter structures that are made of an array of thin filter strands, while in the next section different mechanisms of particle retention are discussed.

The Reynolds number for the filter flow of most suspension feeders is small, since

filter spacings as well as fibre thicknesses are mainly in the micrometre range, even for centimetre-sized organisms [Jørgensen, 1955]. Although higher Reynolds numbers of other flow components in large organisms can affect filtration [Shimeta and Jumars, 1991], we here do not discuss those effects. For the flow past an array of fibres it is natural to first look at the flow past a single fibre. One could use slender-body theory to calculate the force on such an individual fibre, which moves perpendicularly through the fluid. However, for filters it is convenient to look at infinitely long cylinders, which then build an array with a certain periodic flow structure, where end effects are negligible. The cross flow past an infinitely long cylinder can be represented as a two-dimensional flow past a disk. This situation seems similar to the flow past a sphere in 3D that we introduced before. However, there is no solution to the Stokes equations (3.5) and (3.6) for the flow past a single infinitely long cylinder, which is known as Stokes paradox. Only with the addition of some inertial effects, i.e., a finite Reynolds number, the flow can be solved [Lamb, 1932; Spielman, 1977].

Now if we look at the filter as a whole structure, there are several fibres next to each other that hydrodynamically interact. For such porous structures the Darcy relation should hold, which states that the pressure drop, i.e., the force per area, is proportional to the cross-flow speed $\mathbf{v}$ (at large distance) and the viscosity, i.e.,

$$\Delta p = \frac{\xi}{l}\mu v \tag{3.39}$$

with the dimensionless drag coefficient ξ being only dependent on the filter geometry (spacing l and fibre thickness $2a$). This can also be expressed with the drag force $\mathbf{t}$ per unit length of fibre, i.e.,

$$\mathbf{t} = \xi\mu\mathbf{v} = -\xi\mu\mathbf{u}, \tag{3.40}$$

where $\mathbf{u}$ is the velocity of the fibre relative to the fluid and $\xi = \zeta/\mu$ (section 3.6). Since the fluid density and thus inertial effects do not come into play in this relation, it can be concluded that the neighbouring fibres must suppress the inertial effects that are present for the flow past a single fibre. Thus the Stokes paradox is resolved in coherent filter structures and we can still assume creeping flow conditions as long as the Darcy relation holds [Spielman, 1977].

Many biological filters are made of a two-dimensional grid of many individual strands, in which filter spacings and fibre widths are considerably smaller than the dimensions of the whole filter. Thus we here look at the creeping flow past an infinite array of infinitely long parallel cylinders to calculate the average drag or resistance of the filter [Tamada and Fujikawa, 1957; Keller, 1964; Ayaz and Pedley, 1999]. The drag coefficient ξ only depends on the ratio l/a of filter spacing to fibre radius and decreases towards 0 with $l/a \to 2$, i.e., when the filter is completely blocked. For closely spaced cylinders Keller used a lubrication theory to calculate the drag on the filter and with his formula we get [Keller, 1964]

$$\xi = \frac{9\pi}{2^{3/2}}\left(1 - \frac{2}{l/a}\right)^{-5/2}, \tag{3.41}$$

which is quantitatively close to simulated permeabilities up to relative filter spacings of $l/a \approx 4$ [Ayaz and Pedley, 1999; Nielsen et al., 2017]. Tamada and Fujikawa [1957] used the Oseen equations, which linearise the Navier-Stokes equations for small finite Reynolds numbers and calculated the filter permeability with an approximation for widely spaced cylinders, from which we obtain $\xi = 8\pi/\Lambda$ with

$$\begin{aligned}\Lambda =& 1 - 2\ln\tau + \frac{1}{6}\tau^2 - \frac{1}{144}\tau^4 + \frac{1}{1080}\tau^6 \\ & - \frac{53}{345600}\tau^8 + \frac{139}{5443200}\tau^{10} + \mathcal{O}(\tau^{12})\end{aligned} \tag{3.42}$$

and $\tau = 2\pi/(l/a)$, which is valid for $l/a > 4$. Thus one can use equation (3.41) to estimate the drag on narrow filters and equation (3.42) for more widely spaced structures [Ayaz and Pedley, 1999; Nielsen et al., 2017]. Silvester [1983] also proposed a formula as extension of equation (3.42) for widely-spaced rectangular filters, which represents the geometry of some feeding filters more accurately.

Here I only described filtration flows for parallel-cylinder filters that additionally are assumed to be internal, i.e., where filter circumvention is disregarded. Since we consider infinite filter arrays, also the boundary effects of surrounding walls or structures are neglected. Such an assumption is reasonable for fine-meshed filters inside a wide cavity, where the filter resistance due to the mesh dominates the resistance of the channel flow.

Marine organisms use such fibrous filters to collect small prey particles. In the next section the physical mechanisms which underlie the prey encounter rates for suspension feeders are detailed. The focus is on filter feeders and so-called direct interception feeders, which do not have a permeable filter structure but directly collect prey that come in contact with their body [Kiørboe, 2011].

3.8 Physical mechanisms of prey encounter

The prey encounter rate is an important parameter for how capable a marine organism is of surviving in a dilute oceanic environment [Shimeta and Jumars, 1991]. The encounter rate of a predator with its prey is either measured as encountered number or (bio)mass of prey per time. There are different driving forces that lead to encounter between predator and prey. Here I will mainly focus on ballistic, diffusive, and advective transport and I will neglect inertial, gravitational, and electrostatic effects. I will explain how clearance rates for the different encounter mechanisms are calculated on the example of a spherical capture zone and then discuss capture on a fibrous filter.

We consider the prey velocity in the reference frame that is co-moving with the predator in order to calculate the influx into the capture zone. Thus, if the predator moves with velocity $\mathbf{U}$, the prey velocity seen from the co-moving frame is $\mathbf{u} = \mathbf{u}_\mathrm{p} + \mathbf{v} - \mathbf{U}$, where $\mathbf{u}_\mathrm{p}$ is the active prey velocity with uniformly distributed direction and $\mathbf{v}$ is the advective velocity. The advective-ballistic clearance rate is calculated from the inwards flux density $J(\mathbf{x}_\mathrm{p}) = -\mathbf{u}(\mathbf{x}_\mathrm{p}) \cdot \mathbf{n}(\mathbf{x}_\mathrm{p})$ into each surface element with the normal $\mathbf{n}$ directed outwards from the encounter zone. Due to possible random prey motion

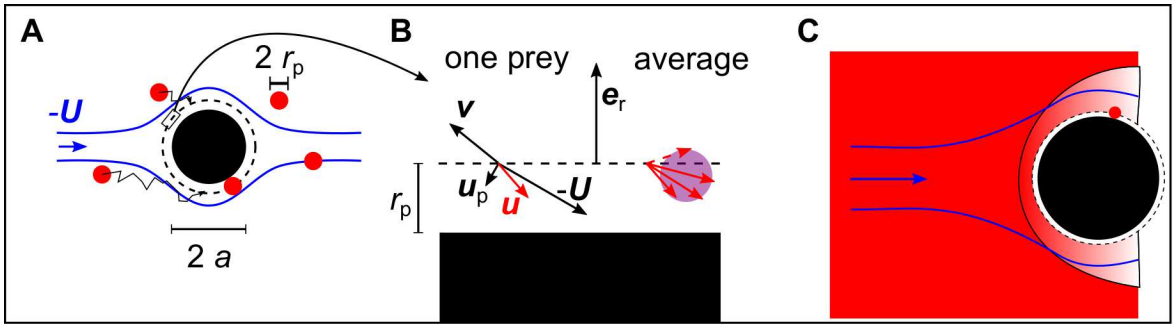

Figure 3.11: Advective, ballistic, and diffusive particle encounter. (A) Particles (red) that initially arrive (in the co-moving frame) with velocity $-\mathbf{U}$, follow the flow (blue) and additionally move randomly. The particles of radius r_p are captured by the predator of radius a (black filled circle). Due to steric interaction, the particles are captured on an encounter surface of radius $a + r_\mathrm{p}$ (dashed circle). (B) Ballistic capture of randomly moving prey. The concentration of prey here is assumed to be equal everywhere. Thus we can look at the prey motion directly at the encounter surface. The prey moves with speed u_p in random directions (purple sphere) and is advected with the flow $\mathbf{v}$, such that the relative velocity is given as $\mathbf{u} = \mathbf{u}_\mathrm{p} + \mathbf{v} - \mathbf{U}$. For the net influx the velocities are averaged over all random prey directions that lead to influx (segment of purple sphere below line). (C) In the advective-diffusive case at a large Péclet number we consider a concentration field (red) that is depleted in a finite boundary layer around the absorber. Sketch (C) from Friedlander [1967].

we need to average the inwards flux density $\langle J(\mathbf{x}_\mathrm{p})\rangle$ with respect to the random angle $\cos\theta$ between prey and predator swimming direction, where we only take into account those prey directions that lead to inwards motion. For the clearance rate we calculate the integral over the surface S and we obtain

$$Q = \int_S \langle J(\mathbf{x}_\mathrm{p})\rangle \mathrm{d}S(\mathbf{x}_\mathrm{p}) \tag{3.43}$$

as a general formula for advective and ballistic motion (figure 3.11 A, B). For diffusion the concentration gradient needs to be taken into account (figure 3.11 C).

To account for the finite size of the prey we extend the encounter surface such that the particle centre position is one prey radius r_p away from the surface when touching the solid collector. For a spherical encounter zone of radius a centred at the origin we thus have an extended radius $|\mathbf{x}_\mathrm{p}| = a + r_\mathrm{p}$ of the encounter zone, where prey is captured upon touch.

3.8.1 Active predator and prey motion

If one disregards the interactions with the fluid medium, prey is encountered purely due to the active motion of prey and predator. We here assume that the predator moves on straight paths considerably longer than its size, while prey moves in random directions, i.e., each prey moves at a given instant in one direction that is randomly assigned. Now the prey usually has on average a certain run time after which it typically changes direction (see section 2.6.4) [Berg and Brown, 1972]. Prey can be considered as always uniformly distributed with constant concentration, if its straight run length is long compared to the predator size [Visser and Kiørboe, 2006]. This is known as the ballistic case. The ballistic clearance rate for prey with swimming speed u_p impacting on a spherical encounter zone with speed U is obtained as

$$Q = \begin{cases} \pi(a+r_\mathrm{p})^2 U \left[1 + \frac{2}{3}\left(\frac{u_\mathrm{p}}{U}\right)^2\right] & \text{if } U \geq u_\mathrm{p} \qquad (3.44) \\ \pi(a+r_\mathrm{p})^2 u_\mathrm{p} \left[1 + \frac{2}{3}\left(\frac{U}{u_\mathrm{p}}\right)^2\right] & \text{if } U < u_\mathrm{p}\ . \qquad (3.45) \end{cases}$$

Note that the expressions for $U \geq u_\mathrm{p}$ and $U < u_\mathrm{p}$ are structurally equal with exchanged predator and prey speed [Gerritsen and Strickler, 1977]. This is the case here due to the spherical symmetry, but not for general shapes of predator encounter zones. If the predator does not move, the ballistic clearance rate (3.45) simplifies to $Q = \pi\,(a + r_\mathrm{p})^2\,u_\mathrm{p}$ for a sphere. For this encounter case we in fact obtain the ballistic clearance rate

$$Q = \frac{1}{4}\,S\,u_\mathrm{p} \tag{3.46}$$

for any arbitrary encounter zone with total surface area S, since with the uniform prey concentration and random prey directions, the average flux density into each surface

element of a still encounter zone is calculated as $\langle J \rangle = (1/4)u_\mathrm{p}$ [Dölger et al., 2017b], [Kauzmann, 1966, p. 79].

On the other hand, if each prey often changes direction and thus performs a random walk with ballistic runs that are short compared to the length of the encounter zone, prey transport and encounter can be viewed as the diffusion of a continuous concentration field. As opposed to purely ballistic encounter, where prey is assumed evenly distributed at all times, diffusion leads to a depletion around the encounter zone. The concentration field is, after establishment of a steady state, determined by the time-independent advection-diffusion equation (for incompressible flow, for which (3.6) is valid):

$$D\nabla^2 c = \mathbf{v} \cdot \boldsymbol{\nabla} c \tag{3.47}$$

with the diffusion coefficient D, which characterizes how fast the prey population spreads, and the drift or advective velocity $\mathbf{v}$. If the underlying small-scale motion of prey is ballistic with run time τ and speed u, the effective diffusion coefficient can be estimated as $D_\mathrm{eff} = u_\mathrm{p}^2\tau/3$ [Lovely and Dahlqvist, 1975]. The ratio of the time scale for diffusive motion versus the time scale for advective motion with characteristic flow speed U is known as the Péclet number which emerges from non-dimensionalisation of (3.47), i.e.,

$$Pe = \frac{UC/L}{DC/L^2} = \frac{L\,U}{D}. \tag{3.48}$$

If $Pe \ll 1$, diffusive transport is dominant and if $Pe \gg 1$, advective transport is dominant.

As boundary condition one often assumes $c = 0$ at the encounter surface assuming a perfect absorber. The diffusive clearance rate (3.43) is calculated from the flux density $J_\mathrm{D}(\mathbf{x}_\mathrm{p}) = -D\boldsymbol{\nabla} c|_{\mathbf{x}=\mathbf{x}_\mathrm{p}} \cdot \mathbf{n}$ into the encounter surface S. For a stationary sphere (i.e., $\mathbf{v} = 0$) the diffusive clearance rate is obtained as

$$Q = 4\pi D(a + r_\mathrm{p}), \tag{3.49}$$

which scales quadratically with prey speed u_p, when diffusion with D_eff is due to active prey motion [Crank, 1975].

3.8.2 Prey encounter in viscous flow

Now, if we include the water as viscous fluid medium, we have not only a random motion for actively swimming prey, but also due to Brownian motion, which is characterised with the diffusion coefficient $D = k_\mathrm{B}\,T/(6\pi\mu r_\mathrm{p})$ (equation (3.15)) with the prey radius r_p and the clearance rate can again be determined from the advection-diffusion equation (3.47).

The prey velocity $\mathbf{u}(\mathbf{x})$ relative to the predator is now not only given by the predator velocity $\mathbf{U}$ and the random prey velocity $\mathbf{u}_\mathrm{p}$, but the prey particle also feels the flow

velocity $\mathbf{v}(\mathbf{x})$, that depends on its location in the flow field. The final prey velocity relative to the predator may also include the Faxén correction to the advection of finite-sized prey (3.22). If random prey motion is negligible, transport is purely due to predator and flow motion and the clearance rate can be solved again with formula (3.43). If the predator is a towed sphere with velocity $\mathbf{U}$ and the flow plus the Faxén correction in the laboratory frame is given as equation (3.22), the advective-ballistic clearance rate can be obtained as

$$Q = \begin{cases} \pi(a+r_\mathrm{p})^2 f\,U \left[1 + \frac{2}{3}\left(\frac{u_\mathrm{p}}{f\,U}\right)^2\right] & \text{if } f\,U \geq u_\mathrm{p} \quad (3.50) \\ \pi(a+r_\mathrm{p})^2 u_\mathrm{p} \left[1 + \frac{2}{3}\left(\frac{f\,U}{u_\mathrm{p}}\right)^2\right] & \text{if } f\,U < u_\mathrm{p}\ . \quad (3.51) \end{cases}$$

with

$$\begin{aligned} f(r_\mathrm{p}/a) &= v_r(|\mathbf{x}| = a + r_\mathrm{p})/(U\,\cos\theta) \\ &= 1 - \frac{1 + (r_\mathrm{p}/a)^2 + 3r_\mathrm{p}/a}{(1 + r_\mathrm{p}/a)^3}. \end{aligned} \quad (3.52)$$

The advective-ballistic clearance rates (3.50) and (3.51) turn out to be of the same structure as the purely ballistic equations (3.44) and (3.45) with the advective speed $f\,U$ at the encounter surface instead of U. Since we here calculate speeds relative to the predator, the advective speed $f\,U$ vanishes at the no-slip boundary. A predator typically moves faster than its smaller prey with $U > u_\mathrm{p}$, such that equation (3.44) should be used, when advection is disregarded. However, when including the flow, the predator-induced advective speed $f\,U < u_\mathrm{p} < U$ becomes smaller than the predator speed and even the active prey speed, since $f \ll 1$. Thus, if we compare the towed sphere to the case of the purely ballistic predator-prey motion, we see the viscous fluid will tend to hinder predator-prey contact compared to ballistic capture (table 3.1). The predator rather pushes its prey away with the fluid instead of creating efficient relative motion. This negative effect can be partially overcome by self-propelled organisms that produce counteracting forces and currents with their swimming appendages [Langlois et al., 2009]. The aim of an effective feeding current is to produce a fast rather than slow decay of the normal flow speed from the no-slip surface such that prey particles from a large region are drawn close to the surface. However, if the local flux into a certain part of the encounter zone is increased, this does not mean that the total clearance rate is higher, since also the size of the inflow surface matters. The viscous effect that prevents prey contact can be further overcome with an increase of the Reynolds number. Some copepods, for example, produce fast jumps in order to shed the fluid layer momentarily and capture prey efficiently [Kiørboe et al., 2009].

If the prey is small ($r_\mathrm{p} \ll a$) and only transported by predator motion, i.e., $u_\mathrm{p} = 0$, the advective clearance rate is calculated as simplification of (3.50) and approximated to

$$Q \approx 2\pi r_\mathrm{p}^2\,U. \quad (3.53)$$

Compared to the purely ballistic expression (3.44) we can here again see that the flow hinders capture (table 3.1). The Faxén correction is often neglected in this estimate for prey capture by a towed sphere, leading to a prefactor of $3/2\pi$ instead of 2π [Spielman, 1977; Kiørboe, 2008].

Now we consider a combination of diffusion and advection, for which we use the equation (3.47) and we use the prey drift velocity $\mathbf{u} = \mathbf{v} - \mathbf{U}$ in the co-moving frame. Since for diffusion we often consider a solute or particles that are much smaller than the absorber, they are generally regarded as point particles. For this limit the advective-diffusive encounter can be seen as enhancement compared to the purely diffusive clearance rate Q_D from expression (3.49), where the Sherwood number

$$Sh = \frac{Q}{Q_\mathrm{D}} \tag{3.54}$$

quantifies this enhancement as the ratio between the actual and the purely diffusive clearance rate. For zero diffusion, the clearance rate for point particles will be zero, since they will never cross the streamlines that are diverted around the absorber. At a low Péclet number $Pe \ll 1$, i.e., where diffusion dominates, the Sherwood number scales as the Peclet number squared, while for large Péclet number $Pe \gtrsim 10$ the enhancement is found to scale as $Pe^{1/3}$ [Berg and Purcell, 1977; Levich, 1962; Pickard, 2006]. In order to consider Brownian diffusion, the finite size of the particles at least needs to be taken into account in the Einstein relation (3.15) for the diffusion coefficient, while the steric interaction (touch at finite distance) is disregarded. For large Péclet numbers one can derive the $Pe^{1/3}$ scaling from thin-boundary layer theory [Langmuir, 1961; Friedlander, 1967]. The basic assumption here is that the solute concentration is depleted only in a layer close to the surface, i.e., the concentration is equal to the bulk concentration outside this layer. By estimating the thickness of the boundary layer one can use the advective clearance rate formula (3.53) with the boundary layer thickness instead of the prey size as an estimate for the extension of the encounter zone. Levich's formula [Levich, 1962; Shimeta, 1993] for the clearance rate on a sphere at large Péclet number is

$$Q = 7.98\, D^{2/3}\, U^{1/3}\, a^{4/3}. \tag{3.55}$$

If we want to include the steric interaction, the encounter zone is given by the prey size r_p, i.e., the thickness of the steric interaction layer, plus the boundary layer thickness. However, here one needs to take into account that the boundary layer does not start at the absorber surface but at distance r_p, since this defines now the surface where the concentration drops to zero (figure 3.11 C) [Langmuir, 1961; Friedlander, 1967]. For a further discussion of advective-diffusive encounter rates of finite-sized prey on a spherical collector, see paper V.

Table 3.1 shows some numerical examples for the analytically calculated clearance rate from the above formulas with ballistic, diffusive, or advective transport (and combinations) of bacterial prey that is captured by a typical flagellate. One can see that the clearance rates that include ballistic prey motion are by far the highest, followed by

Table 3.1: Clearance rates for a spherical predator (flagellate) that encounters typical prey (bacteria).

Case	Equation	Clearance rate ($m^3\ s^{-1}$)
Ballistic (active)	(3.44)	$42 \cdot 10^{-15}$
Diffusive (active)	(3.49)	$3 \cdot 10^{-15}$
Diffusive (Brownian)	(3.49)	$0.03 \cdot 10^{-15}$
Advective	(3.53)	$0.6 \cdot 10^{-15}$
Advective-ballistic (active)	(3.51)	$15 \cdot 10^{-15}$
Advective-diffusive (Brownian)	(3.55)	$5 \cdot 10^{-15}$

The predator is characterised by the radius $a = 10$ µm and the speed $U = 100\,\mu m\,s^{-1}$, the prey has the radius $r_p = 1$ µm and the speed $u_p = 40\,\mu m\,s^{-1}$, if it is active. For ballistic capture the run time is assumed to be long ($\tau > 1\,s$), while in the effective diffusive case the run time is assumed to be $\tau = 0.04\,s$. The values are taken as realistic predator-prey constellations for unicellular marine organisms [Visser and Kiørboe, 2006; Dölger et al., 2017b].

the diffusive capture of active prey on a stationary predator and advectively enhanced Brownian diffusion. The purely ballistic capture with equation (3.44), however, is unrealistic, since it disregards the viscous flow, which needs to be taken into account for a realistic clearance estimate at a low Reynolds number.

3.8.3 Capture on filters

I have now introduced the basic mechanisms of encounter between predator and prey at small scales with the example of capture on a spherical encounter zone. As we have seen, the viscous flows that accompany moving organisms often hinder capture and prey can easily circumvent without contact to the predator. Filter feeders can use the same capture mechanisms as described above, but circumvention is partly prevented by neighbouring fibres in the filter and, most importantly, large prey can be captured by sieving, i.e., prey that is larger than the mesh spacing is captured with 100% efficiency. Thus for sieved prey particles the volume flow rate through the filter is equal to the clearance rate. The importance of the different capture mechanisms for smaller particles that are not sieved is classically determined by filtration efficiencies from aerosol science [Rubenstein and Koehl, 1977; Spielman, 1977; Dorman, 1966; Pich, 1966]. These efficiencies are defined as the actual clearance rate q (per unit fibre length) divided by the ballistic clearance rate $q_0 = 2\,a\,v$ with the projected fibre area $2a$ (per unit length). Sieving is not included in this measure, since only small particles are considered with $r_\mathrm{p} \ll a$. As Shimeta and Jumars [1991] have pointed out, this definition of efficiency might be mathematically convenient, but can be impractical when considering the prey encounter efficiency of suspension feeders, especially when comparing sieved and directly intercepted particles.

The flow close to one cylinder in the filter can be expressed at leading order (close to the no-slip surface) with the two-dimensional stream function as

$$\Psi(r,\theta) = \frac{2v}{\Gamma a}(r-a)^2 \sin\theta. \tag{3.56}$$

The dimensionless coefficient Γ is a function of the volume fraction $\alpha = 2\,a/l$ of the filter [Spielman, 1977]. Formulas for this coefficient in parallel cylinder filters have been given with different estimates [Spielman, 1977]. Instead of integrating the flow velocities

$$v_\mathrm{r} = \frac{1}{r}\frac{\partial \Psi}{\partial \theta} \tag{3.57}$$

$$v_\theta = -\frac{\partial \Psi}{\partial r}, \tag{3.58}$$

one can use the stream function directly to calculate the clearance rate as the flow through a streamtube, the limits of which are given by the contourlines of the stream function (streamlines) that lead to predator-prey contact.

The clearance rate per unit length for direct interception (advective prey capture) on one fibre is thus calculated as

$$q = 2\Psi(r = a + r_\mathrm{p}, \theta = \pi/2) = \frac{4\,v}{\Gamma}\frac{r_\mathrm{p}^2}{a}. \tag{3.59}$$

The total advective clearance rate with the number of fibres N and total width and length L of a quadratical filter is then obtained as

$$Q = N\,L\,q = \frac{L^2}{2\,a}\,\alpha\,q = L^2\,v\frac{2\,\alpha}{\Gamma}\,\left(\frac{r_\mathrm{p}}{a}\right)^2 \tag{3.60}$$

for the capture of small particles (figure 3.10). In comparison, the clearance rate for sieved particles is the total cross flow $Q_\mathrm{Sieve} = L^2\,v$. Since the above estimate is only valid for prey much smaller than the fibre radius, intermediate particle sizes cannot be treated by this framework. However, there have been numerical calculations, for example by Ayaz and Pedley [1999], on the clearance rate of differently sized prey, which interpolate between large sieved and small, directly intercepted particles.

With additional random prey motion one can find analogous formulas as for the spherical collector with the same characteristic scalings for the small and large Péclet number limits [Langmuir, 1961; Friedlander, 1967; Spielman, 1977].

If a suspension feeding predator has to move or to create currents in order to encounter prey, this does not happen without an energy cost. Thus one should consider also the energy that the organism needs to invest (section 3.7). Of course larger flow rates past the filter or collecting body lead to higher encounter rates, but this also requires a larger force. In paper IV we discuss this trade-off for planktonic filter feeders. Another trade-off exists between prey size range and filter flow rate for a given driving force, based on which the filter spacing can be optimised to maximise encounter rates. We discuss this for choanoflagellate filters in paper III.

It should be noted that the here estimated filter flows (section 3.7) and clearance rates calculated for infinite arrays only apply to filter feeders, which create the flow at a distance from an internal filter, and not with ciliary linings directly on the filter elements.

3.9 Experimental methods

In the previous section we have detailed the theoretical background for the physics of swimming and predator-prey interaction in the plankton. However, since we aim to model real organisms, we rely on experiments with living individuals. In this section I will discuss different methods with which the morphology, swimming kinematics, particle motion, and flows can be measured.

3.9.1 Morphology and kinematics

The kinematics of small swimmers can be explored with camera and microscope. Unicellular organisms are observed in small chambers under a microscope, which gives

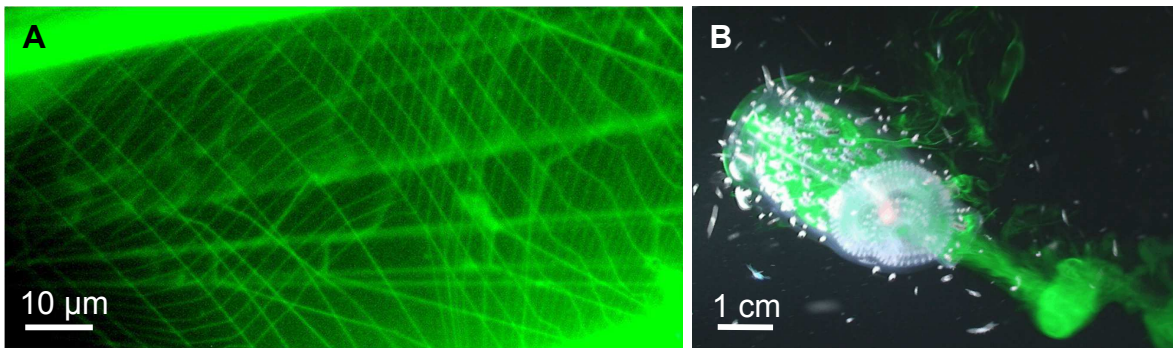

Figure 3.12: Fluorescence imaging methods used for morphological and flow structures of the salp *Pegea confoederata*. (A) Fluorescently stained filter mesh. (B) Swimming individual with fluorescent wake. Images by courtesy of Kelly R. Sutherland, University of Oregon.

them a sufficiently large fluid volume to neglect the boundary effects, while large organisms need large vessels and can be viewed with the low magnification of the camera lens. In order to temporally resolve the swimming kinematics of small organisms, frame rates of typically 1000 frames per second are needed, since a typical swimming cycle of a flagellate takes around $T \sim 10\,\mathrm{ms}$. For the post-processing of the image series, tools such as ImageJ or Matlab can be used to track the motion of the organisms by, for example, tracking specific points (joints) on the swimming appendages and the centre of the body. For a wave-like motion of flexible appendages such as flagella, more tracking points are needed than for swimmers with few joints connecting rigid elements. New methods are available to hold small organisms and measure flagellar forces in optical traps or to make flagella easily trackable with fluorescent labelling [Tadir et al., 1989; Turner et al., 2000].

With one camera only a two-dimensional cross-section of the swimming motion can be viewed. However, swimming kinematics and trajectories can be reconstructed from different view angles or known symmetries of morphology and kinematics. With several cameras or other methods such as holography, it is possible to completely reconstruct 3D motion [Sheng et al., 2006, 2007]. However, those methods usually require expensive equipment, specified set-ups and extensive post-processing [Hobson and Watson, 2002].

The morphology (shape, size) of organisms can be explored with the same methods as for the kinematics on living individuals or with light and electron microscopy and spectroscopy methods on dead organisms, where gold covers, slicing, and various dye can be used to resolve detailed structures. Examples of structural measurements are wet fluorescence microscopy on the mesh of tunicate filters (figure 3.12 A) [Sutherland et al., 2010] and transmission and surface electron microscopy resolving the lorica structure of choanoflagellates [Leadbeater and Cheng, 2010].

In order to obtain the swimming velocity and trajectories of organisms it is not needed to zoom in closely, but the swimmer only needs to be recognized as one point that can be tracked along its path. Besides manual tracking tools such as ImageJ,

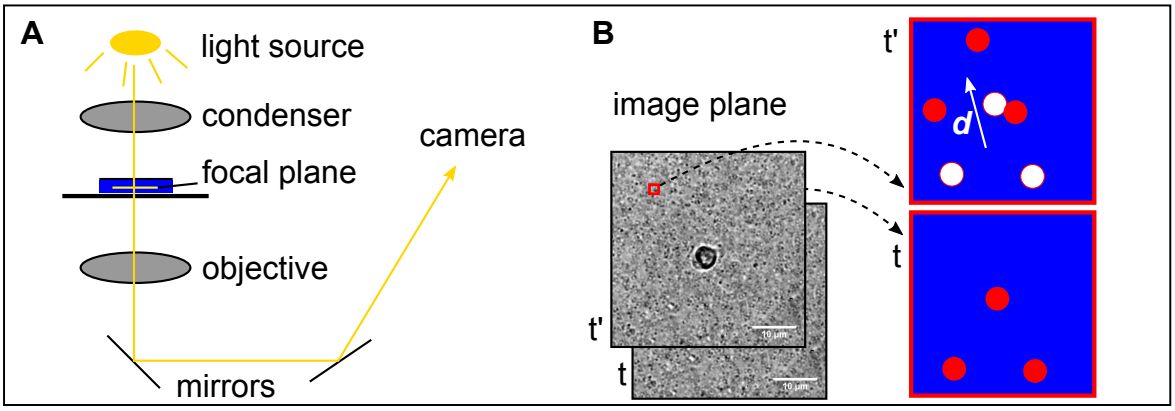

Figure 3.13: Set-up for micro particle image velocimetry (µPIV) as it is used at DTU Aqua. (A) A small volume of water (blue) is imaged in an inverted microscope, where the focal plane defines the slice in which the flow is observed. (B) Two images are taken shortly after each other at time t and t'. The image plane that here shows a haptophyte surrounded by tracer particles is divided into small interrogation windows. In each interrogation window the average particle displacement $\mathbf{d}$ is calculated by image cross-correlation and the velocity in this window is obtained as $\mathbf{v} = \mathbf{d}/(t' - t)$. Sketch (B) adapted from Raffel et al. [2007]. Haptophyte images by courtesy of Lasse Tor Nielsen, DTU.

automatised particle tracking software has been developed for the post-processing of video sequences [Crocker and Weeks; Crocker and Grier, 1996; Drescher et al., 2009]. Interesting alternatives are 3D life-tracking tools, which were mainly developed by Berg [1971] for the tracking of bacteria [Berg and Brown, 1972; Stephens et al., 2008]. In these methods the position of the freely swimming organism is determined, while or shortly after it is recorded such that it can be kept in the frame of view for a long time by moving either the microscope stage or the camera accordingly to mirror its motion.

3.9.2 Flow measurements

The observation of flows around organisms relies on tracers that are assumed to follow the flow faithfully and which can be visualised and tracked to reconstruct the flow velocity field.

As a qualitative method to visualise flow patterns, one can use coloured or fluorescent dye which, for example, has been used to make the vortices visible that are created by jet propulsion in swimming salps (figure 3.12 B) [Sutherland and Madin, 2010b].

The quantitative flow measurements around small organisms are usually based on particle imaging. The flow is related to the motion of particulate tracers that are distributed in the flow. Depending on the situation it can be advantageous to follow individual particles with a method called particle tracking velocimetry (PTV), for

which rather low particle concentrations are needed. The other method is to calculate average particle velocities in small windows that include several particles by image cross correlation in a method known as particle image velocimetry (PIV), for which generally a higher particle concentration is needed than for PTV [Raffel et al., 2007] (figure 3.13 B). The set-ups for both methods are very similar and the standard set-up requires a two-dimensional illuminated thin plane, in which the fluid motion is measured, and a camera that perpendicularly views the plane. For standard velocimetry methods a laser sheet is created to illuminate a two-dimensional fluid layer, but for unicellular organisms, the set-up needs to fit under a microscope and therefore in the µPIV or -PTV method the focal plane of the microscope objective is used to create the "sheet" (figure 3.13 A). The tracers need to be homogeneously distributed and chosen such that they are neutrally buoyant and much smaller than the dimensions of the flow patterns that have to be resolved. Thus for flagellates our collaborators at DTU Aqua use particles of 300 nanometres in diameter to resolve the flows around organisms of a few micrometres in body length (figure 3.13 B). However, since the tracers have to be resolved by the camera they can not be too small and need to provide sufficient contrast to the fluid. A low tracer density can be advantageous when considering the interaction of the particles with the organism. For the flow measurements in choanoflagellates, where the tracer particles are quickly captured by the organism and clog the feeding filter, it was, for example, necessary to keep the tracer density low and thus use a PTV instead of a PIV method [Nielsen et al., 2017].

The temporal and velocity resolution of flows at the micro scale also depend on the Brownian motion of the tracer particles. For characteristic flow speeds U and with the Brownian diffusion coefficient (3.15) for tracers of diameter d the maximum time resolution for µPIV is estimated as

$$\Delta t_0 \sim \frac{4}{U^2} \frac{k_\mathrm{B}\, T}{3\pi\mu d\, N}, \tag{3.61}$$

where N is the number of particles in one window, i.e., the velocities are averaged over this number of particles [Raffel et al., 2007]. The time resolution can be improved, i.e., Δt_0 can be made smaller, by averaging over several frames which are supposed to display the same velocity field. This can be used for repeated flow patterns as for the periodic movements of microswimmers [Dölger et al., 2017b]. By this method the denominator in (3.61) is increased with the factor N_f.

3.9.3 Encounter rates

Predator-prey encounter rates or clearance rates are generally difficult to directly assess, since for the direct measurement, each particle impacting the encounter zone needs to be counted, i.e., the predator needs to be held or tracked at the same time as its prey encounters are monitored.

For filter or other suspension feeders the (advective) volume flow rate through the encounter surface can be related to the clearance. However, for this purpose the

flow needs to be resolved close to the organism, which represents a challenge due to interactions of particles with the organism body.

Tracked prey particles, e.g., bacteria, or Brownian particles in a free domain can be used to calculate an effective diffusion coefficient or parameters of ballistic motion that then can be used in clearance rate formulas. Finally biological experiments on grazing such as incubation experiments and gut content analysis can be used to estimate ingestion rates and to infer encounter rates from that, if the retention and assimilation efficiencies are known.

4 Summary of the results

In the following I summarise the main results of the original research conducted within my Ph.D. project. In total five manuscripts emerged from the Ph.D. study, the papers I, II, and III have been published, and the papers IV and V are in preparation for submission to peer-reviewed journals.

4.1 Paper I: An analytical model of flagellate hydrodynamics

In this paper, which was published in a special focus issue in the honour of Hans Pécseli we present a model of flagellate hydrodynamics, which is based on the superposition of analytical solutions to the Stokes equations. The cell body is represented by a no-slip sphere and the action of each flagellum on the water is modelled by one localised point force, which is imagined to be connected to the body by a rigid and frictionless scaffold (figure 3.8 and section 3.5) [Oseen, 1927; Higdon, 1979b,a; Jiang et al., 2002; Langlois et al., 2009].

The model is useful to investigate the near-cell flows of flagellated organisms and to quantify the trade-offs connected to different swimming styles. For freely swimming, neutrally buoyant organisms the total force and torque on the fluid is zero. With these additional conditions we can construct not only the near-cell flows around freely swimming model flagellates with any time-averaged or periodically varying force arrangement, but also their trajectories and rotational as well as translational swimming velocities (figures 3.8 and 3.2). As examples, we here consider two model flagellates inspired by real species.

The first model swimmer has two flagella moving in a left-right symmetrical ciliary beat, which is modelled by two point forces moving in a periodic manner. This is a common characteristic in self-propelled organisms: appendages need to be moved in a smart periodic manner in order to obtain continuous propulsion. For this analysis we use the fact that at low Reynolds numbers the flow field is time-independent and thus every instantaneous flow field can be modelled by a certain set of instantaneous forces on the water. We divide the periodic beat into four partial strokes, one backwards oriented power stroke furthest away from the cell, one forward oriented return stroke closest to the cell and two transversal strokes between power and return stroke. When analysing the kinematics of the model swimmer we find that the transversal strokes, which are usually neglected, can play an important role for forward propulsion (figure 4.1).

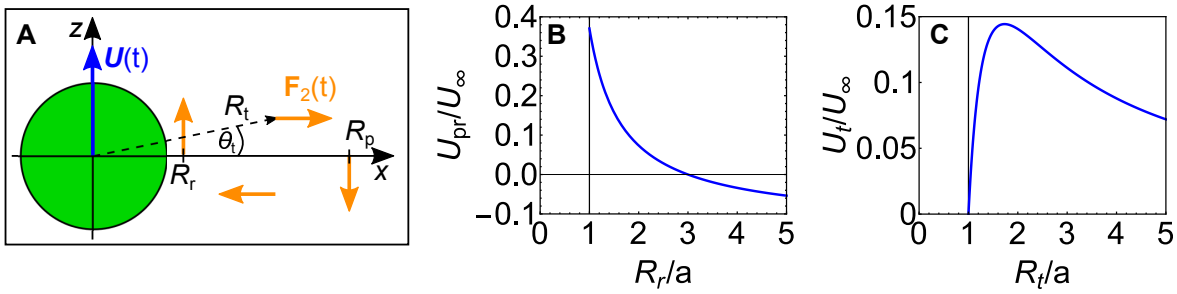

Figure 4.1: Time-dependent model and normalised swimming velocity for a left–right symmetric biflagellate. (A) Right half of model microswimmer with point force $\mathbf{F}_2(t)$ varying during the beat cycle. Forces for power and return strokes are placed equatorially, i.e., $\theta_\mathrm{p} = \theta_\mathrm{r} = 0$ with radial positions R_p and R_r. The transversal forces are placed symmetrically at $\pm\theta_t$ with radial position R_t. (B) Average swimming velocity in the z-direction due to power and return stroke as a function of return stroke distance R_r/a for $R_\mathrm{p} = 3a$. (C) Average swimming velocity in the z-direction due to transversal strokes as a function of transversal force distance R_t/a for $\theta_\mathrm{t} = \theta_\mathrm{opt} = 45\,\mathrm{deg}$. The swimming velocity is highest for return strokes close to the cell and transversal strokes with radial position $R_\mathrm{t} = R_\mathrm{opt} = \sqrt{3}\,a$. Scale velocity $U_\infty = F/(3\pi\mu a)$. Figure adapted from Dölger et al. [2017a].

As a second generic model swimmer we further consider a flagellate such as *Heterosigma akashiwo* with one longitudinal puller flagellum and one tangential flagellum leading to rotation. The produced flows indicate high rotational flows (figure 4.2), especially close to the tangential point force, which might be of importance for feeding currents and optimal prey capture sites. We analyse the trajectory analytically, i.e., the helix pitch and radius, considering point forces of varying magnitude and distance. By comparison to measured trajectories for *H. akashiwo* we hypothesise that its transversal flagellum does not only provide rotation, but also contributes to propulsion and related to that allows large helix radii.

4.2 Paper II: Swimming and feeding of mixotrophic biflagellates

Here we use the flagellate model from paper I to investigate the trade-offs connected to different flagellar arrangements in biflagellated haptophytes.

Haptophytes like many other unicellular organisms are mixotrophic and do thus not only perform photosynthesis and take up dissolved nutrients, but also capture larger particulate prey. For this study we focus on two biflagellated haptophyte species, *Prymnesium parvum* and *Prymnesium polylepis* (figure 2.7). Both swim with left-right symmetrically arranged flagella and both have a slender structure, the haptonema, which extends from the cell front and is sometimes used for prey capture.

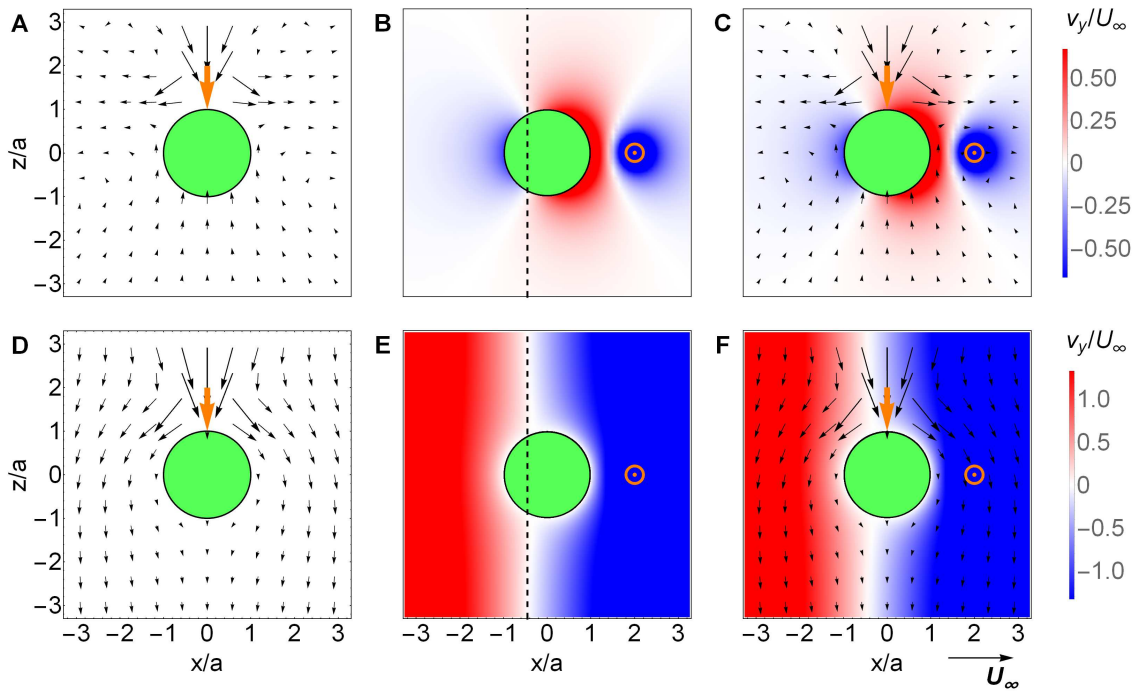

Figure 4.2: Flow fields for model microswimmers with straight, circular, and helical trajectories, respectively. (A)–(C) Laboratory frame of reference and (D)–(F) co-moving frame of reference. (A) and (D) Purely longitudinal flagellum, (B) and (E) purely transversal flagellum with the axis of rotation (dashed lines) indicated, and (C) and (F) both a longitudinal and a transversal flagellum of equal force magnitude $F_1 = F_2 = F$. Point forces (orange). The colour maps show the normalised out-of-plane component v_y/U_∞ with velocity scale $U_\infty = \sqrt{2}F/(6\pi\mu a)$. Figure adapted from Dölger et al. [2017a].

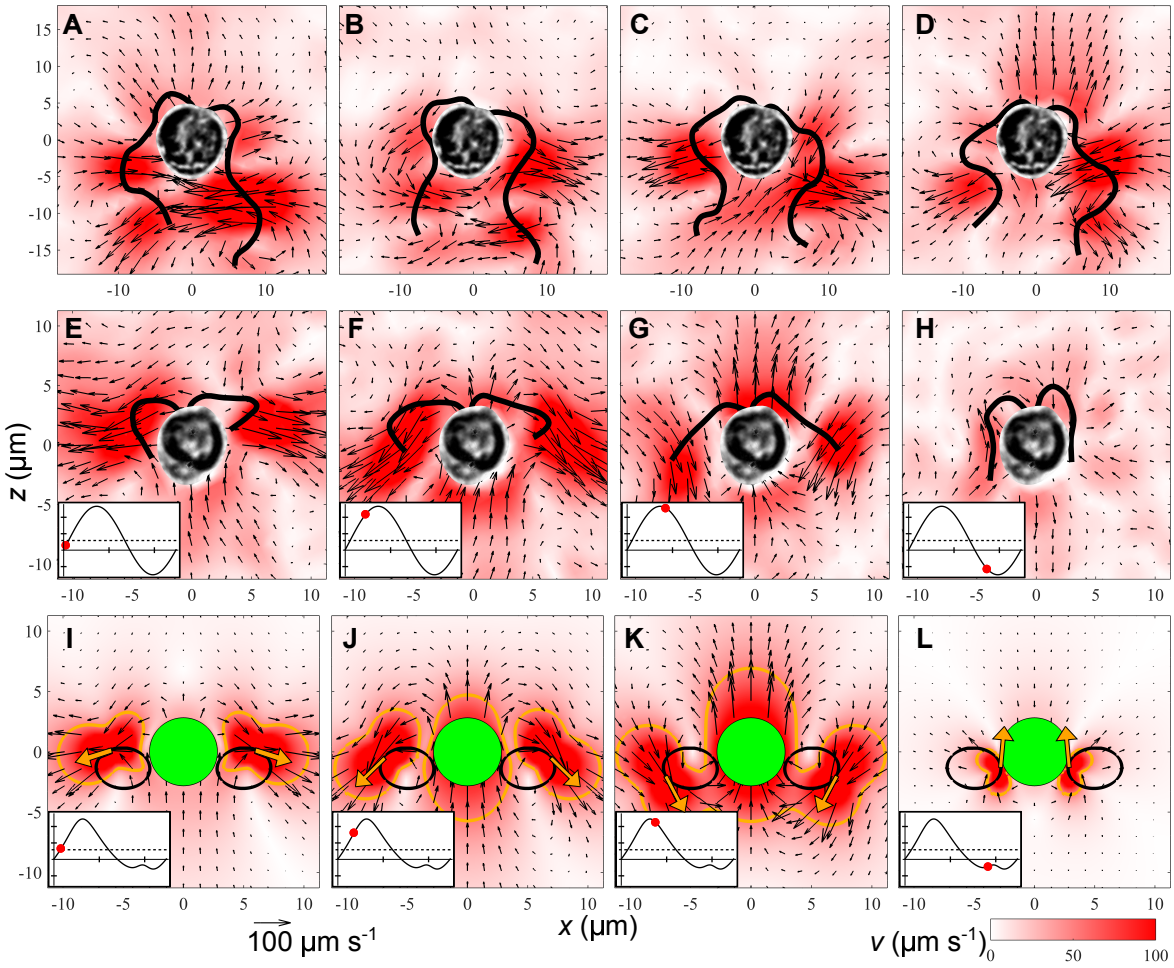

Figure 4.3: Time sequence of measured and modelled instantaneous velocity fields for two haptophytes. (A)-(D) *Prymnesium polylepis*, (E)-(H) *Prymnesium parvum*, and (I)-(L) model for *P. parvum*. Insets in (E)-(L) show the cell velocity (ticks: 50 µm s^{-1}) as a function of time (ticks: 10 ms): Instantaneous cell velocity (solid line, black) with beat cycle phase (filled circles, red) and average cell velocity (dashed line, black). Figure adapted from Dölger et al. [2017b].

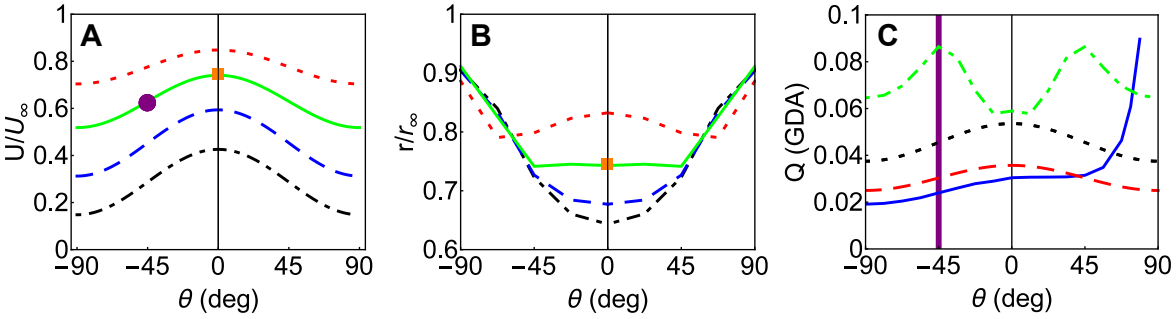

Figure 4.4: Trade-offs between swimming, predator avoidance and feeding for mixotrophic biflagellates. Angular force position θ and radial force position: $R = 1.5\,a$ (dotted-dashed lines, black), $R = 2\,a$ (dashed lines, blue), $R = 3\,a$ (solid lines, green), and $R = 5\,a$ (dotted lines, red). (A) Swimming speed. (B) Size of the disturbance zone for the power stroke of *Prymnesium parvum*. (C) Clearance rate on the haptonema (solid line, blue) and cell (dotted-dashed line, green) with approximations from ballistic predator motion (dashed line, red) and from capture on towed sphere (dotted line, black). Purple (*P. polylepis*) and orange (*P. parvum*) represent the values for the two organisms extracted from the measured kinematics and flow fields. Figure adapted from Dölger et al. [2017b].

For both organisms we used µPIV to measure the flows around the freely swimming flagellates. We visualised the characteristic time-averaged flow fields and we were further able to resolve the instantaneous flow patterns during the beat cycle (figure 4.3 A-H).

Using the average flow fields we were able to determine characteristic average force positions for the two species. The modelled flow fields with accordingly placed left-right symmetric, backwards pointing forces compared well to the measured near-cell flows. We further modelled the time-resolved flow fields of the breast-stroke type swimmer (figure 4.3 E-H) with periodically moving point forces along with the flagella end segments that seem to produce most thrust (figure 4.3 I-L).

To characterise the trade-offs connected to different force arrangements, we calculated the swimming velocity, the size of the flow disturbance zone and the clearance rate for advective capture on the haptonema and cell, each as a function of force positions (figure 4.4). The dependences on angular force position show that equatorial force arrangements as found for *P. parvum* seem optimal for fast as well as stealthy swimming. Force arrangements with 45° to the equator, as in *P. polylepis*, are found to maximise clearance rates on the cell, while puller arrangements with forces in front would optimise prey capture on the haptonema.

We compared the clearance rate estimates for advective, diffusive and ballistic prey capture to the necessary clearance rates at characteristic concentrations of particulate matter in the ocean (guideline daily amount GDA) and we found that the studied species *P. polylepis* generally does not seem to capture enough prey in dilute oceanic

environments to survive without additional photosynthesis. The mixotrophic strategy is thus found to be essential for the observed flagellates in a typical marine environment.

4.3 Paper III: Hydrodynamics of microbial filter feeding

Filter feeding, i.e., the capture of small particles with a feeding current through a mesh structure, seems to be a very successful strategy for heterotrophic microbes that, as opposed to most other unicellular species, can survive purely on prey capture.

In this paper we investigate the filter-feeding strategy of microbes with a focus on choanoflagellates that use one undulating flagellum to drive flow through a collar filter. We estimate the volume flow rate through the filter of the species *Diaphanoeca grandis* with the use of µPTV in several individuals. The estimate based on the flow measurement matches previous incubation experiments and also confirms the approximately needed clearance rate of one million cell volumes per day for the survival in characteristic oceanic environments.

The organism morphology and the flagellar kinematics are measured from image sequences. These characteristics are used to calculate the emerging flow field around *D. grandis* in a computational fluid dynamics (CFD) simulation, where the flagellum is modelled as an undulating slender structure. Both the CFD simulation and analytical estimates of produced forces based on slender-body theory underestimate the clearance rate by about one order of magnitude.

In a few choanoflagellate species traces of a flagellar vane have been observed, which is a thin sheet extending from the flagellum and which in the related sponge cells has been shown to span the whole collar width. When including a 5-µm-wide vane in the simulations we obtain flow fields that fit much better to the observed ones (figure 4.5). With this additional structure the filtering mechanism resembles more that of a peristaltic pump, for which we can make a matching theoretical estimate. From these findings we speculate that the flagellar vane exists in more species than previously assumed.

Another important aspect of filter feeding, which is my main contribution to this study, is the choice of filter spacings which should be small enough in order to not let important prey slip away, but it also should not be too small, since the needed force to create a given flow rate increases dramatically for more narrow filters. This essential trade-off leads to an optimum spacing (figure 4.6 A). In order to calculate the optimum mesh spacing we model the filter as an array of parallel cylinders and assume the Sheldon size spectrum for the prey, i.e., equal amounts of biomass in logarithmic bins of particle size. The encounter rate from sieving is then calculated with the driving force F, the integrated prey concentration for prey diameters from filter spacing l to maximum prey diameter d, and the average filter permeability $\langle\kappa\rangle = l/(a\langle\xi\rangle)$ (section 3.7). We obtain

$$E = F\, C_0\, \frac{a}{\mu} \langle\kappa\rangle \log\left(\frac{d/a}{l/a - 1}\right). \tag{4.1}$$

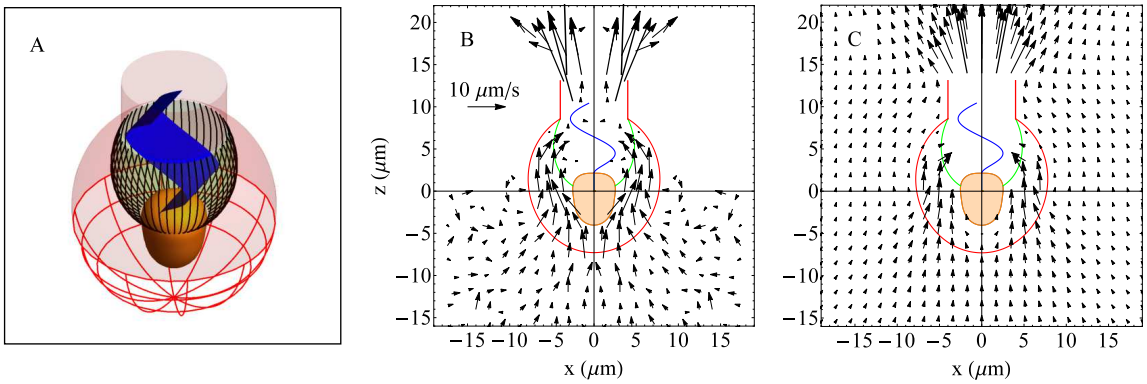

Figure 4.5: Model morphology with a flagellar vane, observed average velocity field for *Diaphanoeca grandis*, and velocity field from computational fluid dynamics (CFD) model including a 5-µm-wide flagellar vane. (A) The model morphology shows the cell (orange), the collar filter (green), the flagellum with vane (blue), and the lorica (red). (B) Observed average velocity field. Average velocity field based on particle tracking. (C) The CFD velocity field in the xz-plane is time averaged over the flagellar beat cycle, and the velocity vectors inside filter and chimney are omitted for clarity. The CFD model with a flagellar vane predicts a feeding flow in through the permeable lower part of the lorica and a clearance rate in good agreement with the experimental observations for *D. grandis*. Figure adapted from Nielsen et al. [2017].

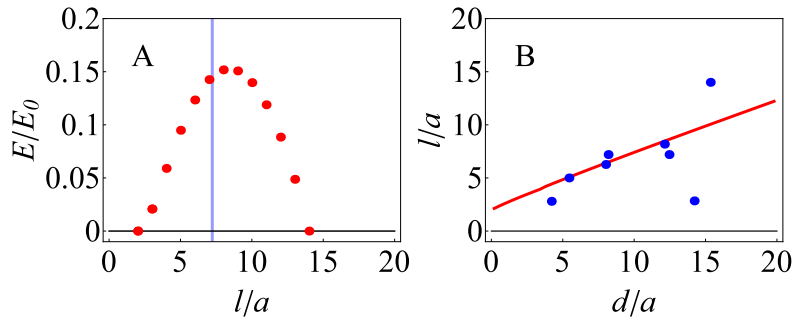

Figure 4.6: Optimum choanoflagellate filters. (A) Encounter rate as a function of filter spacing l scaled with the fibre radius a. The vertical line (blue) indicates the observed average. (B) The theoretical prediction for the optimum filter spacing (solid line, red) and the observed filter spacing for different choanoflagellates (solid circles, blue) as functions of the maximum prey diameter d scaled with the fibre radius a. We have assumed that the maximum prey diameter is equal to 1/3 of the cell radius in each respective choanoflagellate. Figure adapted from Nielsen et al. [2017].

Here C_0 denotes the mass concentration within each decade of particle diameter and a the fibre radius. The optimum filter spacing within the relevant range for choanoflagellates scales approximately linear as about one half the maximum prey size. The observed filter designs in choanoflagellates follow this trend with the assumption that there is a fixed ratio between maximum prey and predator size (figure 4.6 B).

Since biological systems are complex and formed by highly variable selective forces in a changing environment, we acknowledge that even with a certain grade of optimisation we can not say with certainty which parameter should be optimised with respect to which function and to what degree. Thus we do not a priori assume that choanoflagellates with all their elements are designed to optimise a single function [Dudley and Gans, 1991]. Instead we use our analytical and numerical models combined with empirical data to explore possible limiting and optimal design components of microbial filter feeders in a well-defined framework, where we explicitly take into account physical constraints.

4.4 Paper IV: Dense dwarfs versus gelatinous giants

In this manuscript we investigate general trade-offs of the filter-feeding strategy in planktonic organisms. We are especially interested in the effect of the body composition of filter feeders on their fitness and the constraints that lead to body dilution, since gelatinous, dilute organisms form an important group of filter feeders and other, but more dense organisms with similar biomass often have the possibility of additional sensing apparatus. Gelatinous species in general do not use remote senses like vision or flow-sensing, unlike fish and copepods, and thus fully rely on prey physically intercepting their body, mainly through feeding currents. This makes their strategy more similar to much smaller species, such as choanoflagellates.

We use the scope for growth as the energy gain minus the energy investment per time as a proxy for the instantaneous fitness of active planktonic filter feeders, which actively create a flow through an internal, fine-meshed filter. In order to compare organisms with different size and body composition we model the energy-specific scope for growth. The basic equation that we use for the scope for growth is

$$H = Auc - kAu^2 - R_\mathrm{b} \tag{4.2}$$

with the energy-specific filter area A, the filter flow speed u, the prey concentration c in energy per volume, the filter resistance coefficient k, and the energy-specific basal respiration rate R_b. Filter feeders generally invest energy in the motor that is used to create the feeding current, i.e. $R_\mathrm{f} = kAu^2$, as well as in basic maintenance, i.e. R_b. Both investments can be measured in the form of the respiration rate of the organism. The gained energy is given by the energy of the encountered prey with characteristic abundance that is collected through the feeding flow, i.e. $G = Auc$, where Au is the energy-specific clearance rate.

From our simple model we can predict optimal strategies that balance the trade-off between gain and investment which are connected through the filter flow (figure 4.7 A).

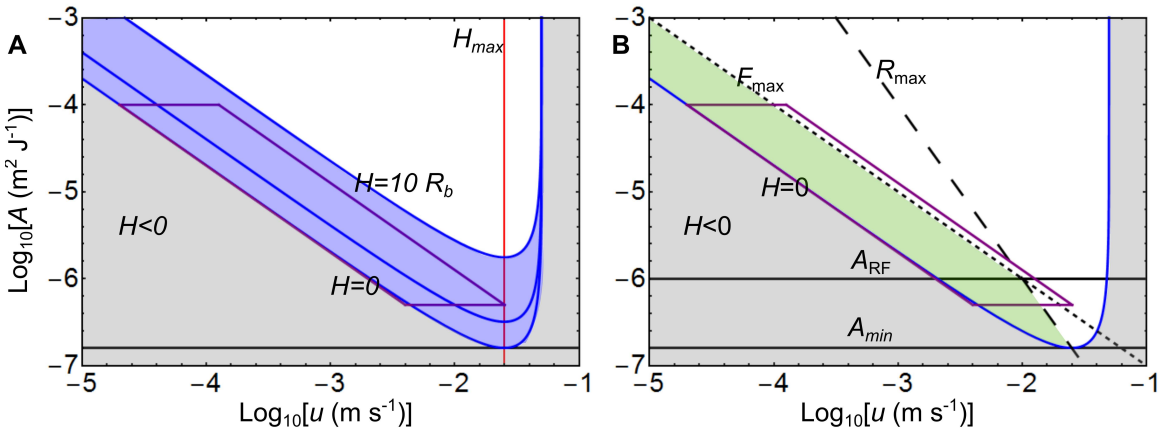

Figure 4.7: Filter-feeding strategies with optima and constraints. Scope for growth H as a function of filter flow speed u and energy-specific filter area A of general filter feeders with constant filter ultra structure at a characteristic prey concentration $c = 5 \cdot 10^3\,\mathrm{J\,m^{-3}}$. Infeasible trait combinations leading to negative growth rate (grey). Above the contour line for $H = 0$ growth is positive. (A) The range of trait combinations in planktonic filter feeders is marked (purple box) as well as the range of positive growth rates up to ten times the basal respiration rate R_b (blue). Most of the found flow speeds lead to growth rates that are well below the maximum H_max (red line). (B) The allowed strategies (green) are additionally limited by the maximum power R_max and the maximum force F_max of the respective motor. The trait combinations and the scaling of the clearance rates in planktonic filter feeders (purple box) suggest that they are mainly limited by a maximum force. One can define several minimum limits to the filter area. Below A_min the growth rate becomes negative for all flow speeds and below A_RF the force, clearance rate, and growth rate decrease, being constrained by the maximum motor power R_max.

One strategy is to maximise the specific scope for growth at a certain (characteristic) prey concentration ($H_{\max}$) and another is to minimise the prey concentration that the organism is able to survive at and each strategy leads to a different optimum filter flow speed. Both fast growth and prevention of starvation at low prey abundance are essential for successful strategies in marine pelagic organisms, but the measured flow speeds in choanoflagellates as well as salps are lower than what is expected from the described optimum strategies.

Thus we consider the motor performance limits that depend on the motor size (energy content) and which determine maximum feasible filter flow speeds (figure 4.7 B). Both a maximum motor power and a maximum motor force are considered and we assume that either can ultimately limit the filter-feeding performance. We find the force limit dominating in most of the feasible range, where the scope for growth is positive at realistic prey concentrations. This leads to constant specific clearance rates across size classes as optimum within the force constraint and we find that this trend is confirmed by species-overarching data on clearance rates.

The specific scope for growth decreases linearly with the energy-specific filter area and becomes negative below a certain minimum energy-specific area at characteristic prey concentrations. With a typical body energy density the surface area and thus the filter area for small organisms is naturally large compared to their volume and energy content and thus they will as filter feeders have large enough scopes for growth to survive. This is what we call the *dense dwarf strategy*. However, with increasing energy content the area to volume ratio and thus the energy-specific filter area decrease and can only be increased by changing the body composition, leading to large gelatinous bodies (*gelatinous giant strategy*). We can generally predict the existence of a maximum energy density that decreases with body energy content (figure 4.8). Organisms that rely on actively created flows through internal, fine-meshed filters are not able to survive with higher densities. Thus, with a high energy content those low Reynolds number filter feeders, that cannot find dense patches of prey or switch to raptorial feeding, can only capture enough food in dilute environments, if they are gelatinous.

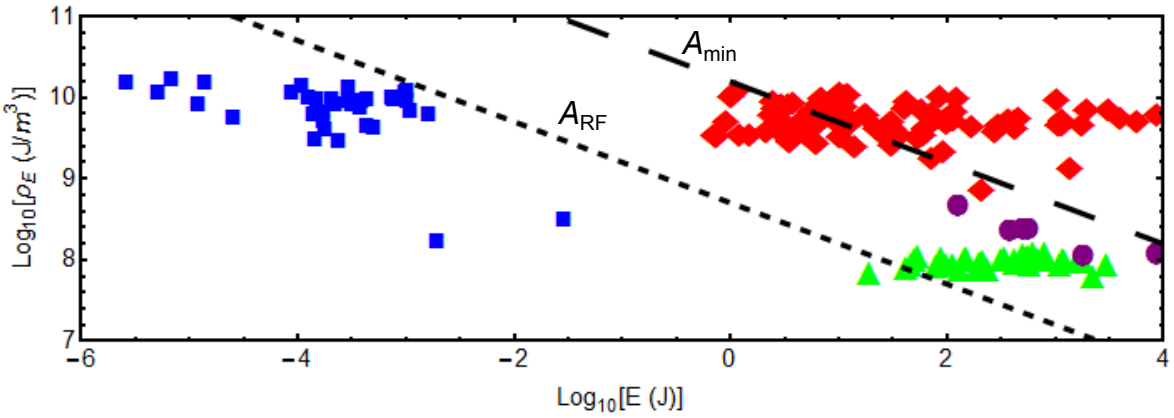

Figure 4.8: Energy density as a function of body energy content for protozoans (squares, blue), tunicates (triangles, green), jellyfish (circles, purple), and other zooplankton that are mainly copepods (diamonds, red) with data from Kiørboe [2013]. The black lines indicate energy densities, above which filter feeding becomes infeasible. They are calculated from minimum energy-specific surface areas using A_{RF} (black, dotted) or A_{min} at low observed prey concentration $5 \cdot 10^2\,\mathrm{J\,m^{-3}}$ (black, dashed) (cf. figure 4.7).

4.5 Paper V: Capture of finite-sized prey

In the last manuscript we consider the capture of finite-sized prey by direct interception feeders such as flagellates. Our focus here is the effect of prey size and non-perfect absorption (sloppy feeding) on prey clearance rates.

I started to work on this project during my external stay of two months in spring 2017 at the University of Warwick and we plan to complete this collaborative study in the next few months, during which I will be employed as a post-doctoral researcher at DTU Physics.

Our model considers a towed sphere with constant velocity that intercepts with prey particles of different size, which are advected with the flow and additionally move by Brownian diffusion. We chose this simple model flow, since the no-slip condition on the cell surface has a big contribution to the near-field flows of most direct interception feeders, independent of specific flagellar arrangements and beat patterns.

We numerically calculate the clearance rate for a realistic prey size range and compare the results to analytical calculations that for a perfect absorber can estimate the capture over the whole prey size range with good agreement (figure 4.9 A). For a perfect absorber there is an equally large clearance rate for the smallest diffusing particles as for the largest advected prey with the lowest clearance at intermediate-sized prey.

When considering a finite rate κ, at which prey is captured when in contact with the cell (foraging rate), the model predator becomes sloppy and loses prey that has a short time of residence close to the predator. We find that the non-monotonic form of the clearance rate with minimum at intermediate prey sizes flattens at low foraging rates.

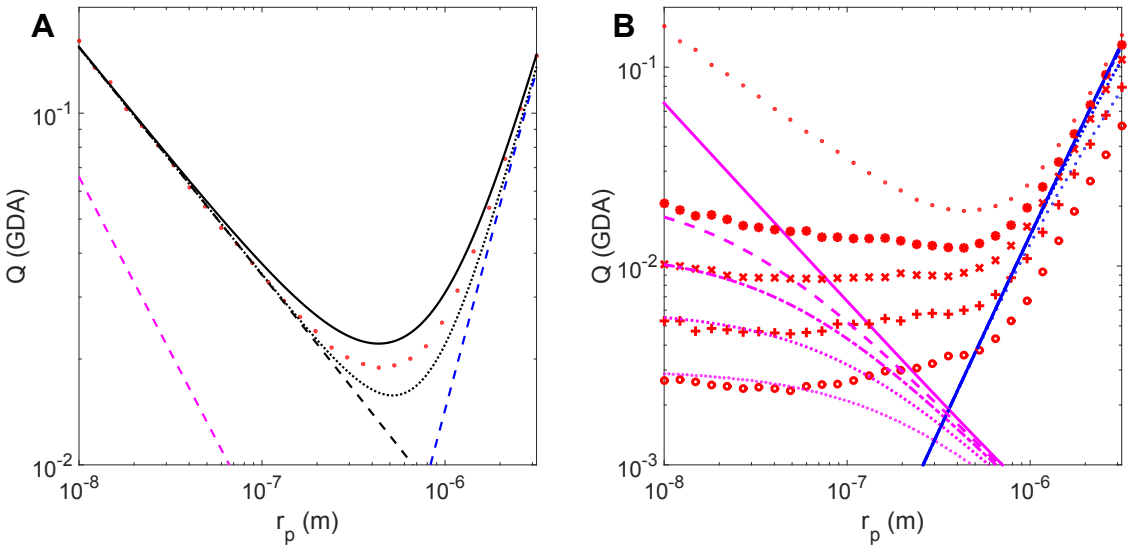

Figure 4.9: Clearance rates for a perfect absorber and sloppy feeders of radius $a = 10$ µm as a function of prey radius r_p. The predator translates with speed $U = 100\,\mu\mathrm{m\,s^{-1}}$. 1 GDA (guideline daily amount) corresponds to 10 cell volumes per second and estimates a typical clearance rate requirement. (A) Perfect absorber. Simulations (red filled circles) and analytical formulas for pure diffusion (magenta line, dashed), advection-diffusion of point particles with $r_\mathrm{p} = 0$ (black line, dashed), advection of finite-sized particles including Faxén correction (blue line, dashed), and the sum of advection-diffusion (with $r_\mathrm{p} = 0$) and advection (black line, dotted). The black solid line shows a boundary layer estimate that includes advection and diffusion of finite-sized particles with steric interaction as well as the hydrodynamic interaction through Faxén forces on the prey. (B) Sloppy feeders with different foraging rates. The simulated foraging rates (red) are $\kappa = 1\,\mathrm{s^{-1}}$ ('o'), $\kappa = 2\,\mathrm{s^{-1}}$ ('+'), $\kappa = 4\,\mathrm{s^{-1}}$ ('x'), $\kappa = 8\,\mathrm{s^{-1}}$ ('*') and $\kappa \to \infty$ (filled circles). Analytical estimates for pure diffusion (magenta) and pure advection (blue) (lines with decreasing dash length for decreasing rate κ). Sloppy feeders are found to predominantly encounter large prey. The clearance rates for the smallest prey are drastically reduced and the minimum is flattened out. The purely diffusive estimates fit well for small prey sizes and small foraging rates, while the advective estimates only match for the largest prey and high foraging rates.

Sloppy feeders capture large prey with much higher clearance rates than small prey (figure 4.9 B), shifting their physically selected prey size spectrum towards larger particles.

We further find, with an analytical calculation for advective capture, that the clearance rate is increased by about 30% due to the hydrodynamic interaction between a large predator with small finite-sized spherical prey. The resulting approximate formula for small prey is $Q \approx 2\,\pi\,U\,r_\mathrm{p}^2$ with the predator speed U and the prey radius r_p. For this the hydrodynamic interaction is estimated with Faxén forces, due to which the prey trajectories differ from the flow streamlines before contact.

Direct interception feeders, which do not create enhancing feeding currents with flagella, seem not able to capture as much prey as filter-feeding microbes can collect purely by sieving and as is required for the survival as an animal without additional resources (light, dissolved nutrients). Capture rates for such direct interception feeders are consistently low, even though the organisms can feed on a large prey size range, that spans at least two orders of magnitude in prey length.

5 Original papers

5.1 An analytical model of flagellate hydrodynamics

Paper published in Physica Scripta (2017).

An analytical model of flagellate hydrodynamics

2017 Phys. Scr. 92 044003

(http://iopscience.iop.org/1402-4896/92/4/044003)

IOP Publishing | Royal Swedish Academy of Sciences Physica Scripta

Phys. Scr. **92** (2017) 044003 (9pp) https://doi.org/10.1088/1402-4896/aa6164

An analytical model of flagellate hydrodynamics

Julia Dölger, Tomas Bohr and Anders Andersen

Department of Physics and Centre for Ocean Life, Technical University of Denmark, DK-2800 Kgs. Lyngby, Denmark

E-mail: aanders@fysik.dtu.dk

Received 30 September 2016, revised 2 February 2017
Accepted for publication 20 February 2017
Published 10 March 2017

Abstract

Flagellates are unicellular microswimmers that propel themselves using one or several beating flagella. We consider a hydrodynamic model of flagellates and explore the effect of flagellar arrangement and beat pattern on swimming kinematics and near-cell flow. The model is based on the analytical solution by Oseen for the low Reynolds number flow due to a point force outside a no-slip sphere. The no-slip sphere represents the cell and the point force a single flagellum. By superposition we are able to model a freely swimming flagellate with several flagella. For biflagellates with left–right symmetric flagellar arrangements we determine the swimming velocity, and we show that transversal forces due to the periodic movements of the flagella can promote swimming. For a model flagellate with both a longitudinal and a transversal flagellum we determine radius and pitch of the helical swimming trajectory. We find that the longitudinal flagellum is responsible for the average translational motion whereas the transversal flagellum governs the rotational motion. Finally, we show that the transversal flagellum can lead to strong feeding currents to localized capture sites on the cell surface.

Keywords: low Reynolds number flows, microswimmers, flagellates

(Some figures may appear in colour only in the online journal)

1. Introduction

Unicellular plankton play an essential role in aquatic ecosystems and their survival functions depend crucially on their flow environment and the flows that they generate (Guasto *et al* 2012, Pécseli *et al* 2014). The flow fields due to freely swimming plankton contain information on the extent of flow disturbances that attract flow sensing predators, feeding currents that enhance prey capture and nutrient uptake, and the power at which energy is dissipated in the water (Guasto *et al* 2012, Kiørboe 2016). Many unicellular organisms use flagella (actuated filaments) to swim (Gibbons 1981, Fenchel 1986). The bacterium *Escherichia coli* and the alga *Chlamydomonas reinhardtii* have been investigated extensively as representatives of flagellated microswimmers (Berg 2008, Goldstein 2015, Lauga 2016). However, those two model organisms do not represent the diversity of flagellar arrangements and beat patterns of the large group of flagellated microswimmers in the aquatic environment (Lighthill 1976, Sleigh 1981, Inouye and Hori 1991).

In this article we present a hydrodynamic model of eukaryotic flagellates with focus on swimming kinematics and near-cell flows (figure 1). It is largely unknown what the flagellar characteristics are optimized for and which strategies and functions they reflect. Our model has the potential to address these questions. The Reynolds number that gives the ratio between inertial and viscous forces is much less than unity for microswimmers (Purcell 1977). Flagellate hydrodynamics is therefore governed by the time-independent Stokes equation and the equation of continuity for incompressible flows

$$\nabla p = \mu \nabla^2 \mathbf{v}, \tag{1}$$

$$\nabla \cdot \mathbf{v} = 0, \tag{2}$$

where p is the pressure, $\mathbf{v}$ the flow velocity, and μ the dynamic viscosity. Both analytical and numerical models have been developed to study such creeping flows.

Point force models based on the Stokeslet, i.e., the fundamental Green function solution of the creeping flow due to a single point force, are able to represent the far field around different microswimmers (Lauga and Powers 2009, Drescher

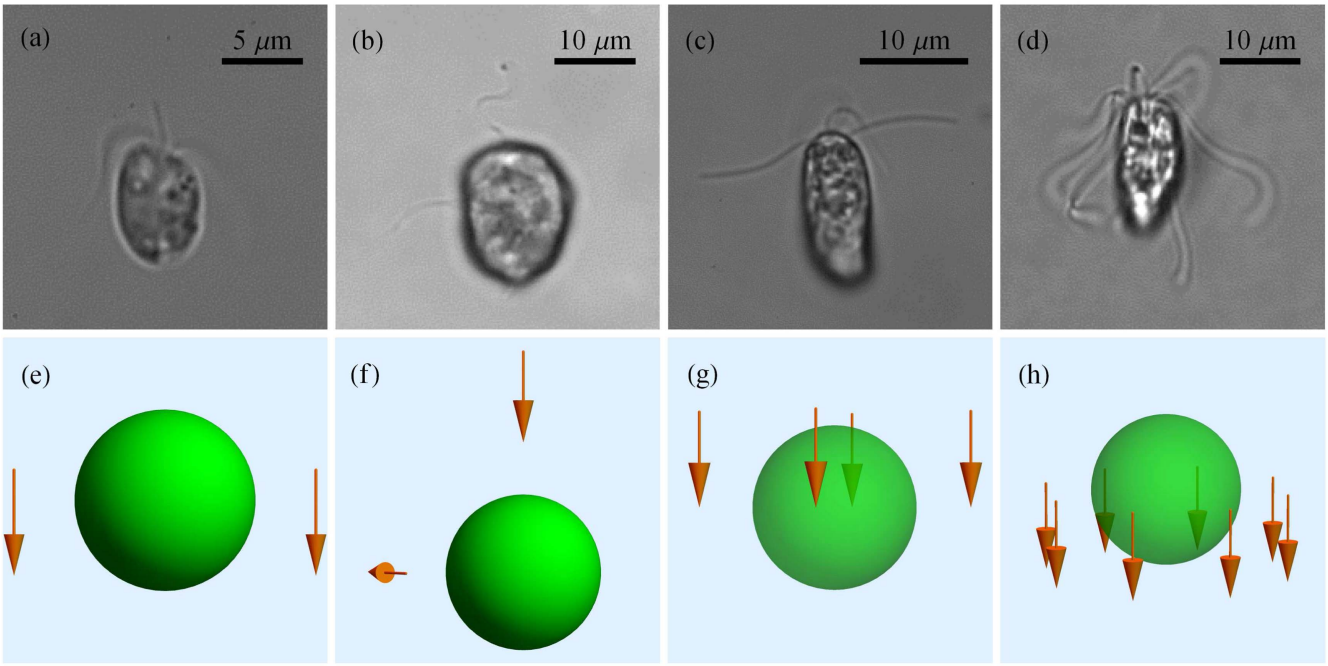

Figure 1. Flagellates with different flagellar arrangements and beat patterns. (a)–(d) Microscope images of freely swimming individuals. (e)–(h) Model descriptions with vectors (orange) indicating the flagellar forces on the water. (a) and (e) *Prymnesium parvum*, a left–right symmetric biflagellate (haptophyte) with a haptonema at the front. (b) and (f) *Heterosigma akashiwo* with a longitudinal (puller) flagellum and a transversal flagellum. (c) and (g) *Tetraselmis sp.* with two pairs of flagella that beat in anti-phase. (d) and (h) *Pyramimonas octopus* with eight flagella. The microscope images are reproduced with permission from Lasse Tor Nielsen.

et al 2010, 2011, Pak and Lauga 2016). A neutrally buoyant microswimmer experiences negligible net force and torque. The most basic point force model of freely swimming microorganisms is thus the stresslet that models two counteracting forces that act on the water and are related to the thrust due to the swimming appendages and the drag on the body, respectively (Lauga and Powers 2009). The stresslet represents the far field around *E. coli* (Drescher *et al* 2011). A model consisting of three point forces has successfully been used for biflagellates with two left–right symmetric flagella, and it represents well the main flow patterns around *C. reinhardtii* (Drescher *et al* 2010). With this model the far field decay of flow disturbances has been studied and equatorial force arrangements were shown to be the most 'quiet', i.e., leading to the least flow disturbances (Kiørboe *et al* 2014, Andersen *et al* 2015).

However, point force models completely disregard the presence of the cell, which is essential for the study of swimming kinematics and near-cell flows. One model that can be used for such studies is the squirmer model of ciliates covered with cilia that create a net flow close to the cell surface (Lighthill 1952, Blake 1971, Pak and Lauga 2016). However, other types of models that take the hydrodynamic interaction between flagella and cell into account are needed to describe swimming kinematics and near-cell flows in flagellates (Kurtuldu *et al* 2013, Polotzek and Friedrich 2013). An analytical three-sphere model has been used, e.g., to study flagellar synchronization and swimming kinematics in biflagellates (Friedrich and Jülicher 2012, Polotzek and Friedrich 2013). Another possible approach for representing near fields is to build on the solution derived by Oseen for the flow due to a point force in proximity of a sphere with no-slip boundary (Oseen 1927, Pozrikidis 1992). This solution forms the basis of analytical models that have been used to describe freely swimming copepods (Jiang *et al* 2002) and to investigate the swimming and feeding of uniflagellates (Higdon 1979a, 1979b, Langlois *et al* 2009). Such a model for freely swimming biflagellates with two left–right symmetric forces was also recently used to represent near-cell flows around biflagellated haptophytes with focus on swimming and feeding (Dölger *et al* 2017). Also for computational fluid dynamics models of flagellated microswimmers a similar flow solution with regularized Stokeslets next to a sphere has been proven to be useful (Wrobel *et al* 2016).

We here establish a general analytical model of freely swimming flagellates, which is based on the Oseen solution and has the potential to represent swimming kinematics and near-cell flows. We present the basic building block giving the flow for an arbitrary point force representing one flagellum of a freely swimming spherical cell. The flow field of a flagellate propelled by several flagella can be obtained by linear flow superposition of such basic flows. As illustrative examples we consider a flagellate with two left–right symmetric forces that by construction swims on a straight path (figures 1(a) and (e)) and a flagellate propelled by two point forces that produce a helical trajectory (figures 1(b) and (f)). For the different cases we show how swimming characteristics and flow properties depend on flagellar arrangement and beat pattern.

2. General model framework

The basic building block of the flagellate model is the flow around a freely translating and rotating sphere propelled by a

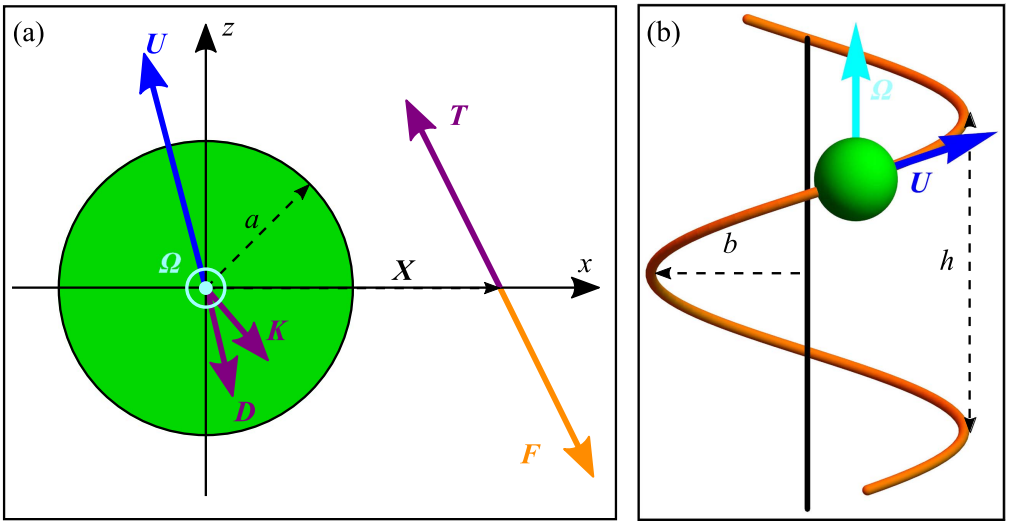

Figure 2. Flagellate model and swimming kinematics. (a) Basic building block with one point force. Sphere (green), point force **F** acting on the fluid (orange), forces acting on the organism (purple), i.e., the thrust force **T**, the force **K** due to the flow produced by the point force, and the Stokes drag $\mathbf{D} = -6\,\pi\,\mu\,a\,\mathbf{U}$ due to the translational motion with velocity **U** (blue). The angular velocity $\boldsymbol{\Omega}$ (light blue) is directed out of the plane in the negative *y*-direction. (b) Helical trajectory with radius *b* and pitch *h* for a sphere translating with velocity **U** and rotating with angular velocity $\boldsymbol{\Omega}$ due to several point forces.

single point force (figure 2(a)). To establish the model we build on the solution by Oseen for the creeping flow due to a point force **F** that is acting on the water in proximity of a fixed no-slip sphere (Oseen 1927, Pozrikidis 1992). The flow field can be written

$$v_{\mathrm{O},j}(\mathbf{x}) = \frac{1}{8\pi\mu}\, G_{jk}(\mathbf{x}, \mathbf{X})\, F_k, \tag{3}$$

where the Green function G_{jk} depends on the field vector **x** and the point force location **X** (appendix). The flow created by the point force results in a force **K** and a torque **L** on the sphere that depend on the radial force component $\mathbf{F}_\mathrm{r} = (\mathbf{F}\cdot\mathbf{X})\mathbf{X}/R^2$, the tangential force component $\mathbf{F}_\mathrm{t} = \mathbf{F} - \mathbf{F}_\mathrm{r}$, and the force distance $R = |\mathbf{X}|$, i.e.,

$$\mathbf{K} = \frac{1}{2}\left[\frac{3}{R/a} - \frac{1}{(R/a)^3}\right]\mathbf{F}_\mathrm{r} + \frac{1}{4}\left[\frac{3}{R/a} + \frac{1}{(R/a)^3}\right]\mathbf{F}_\mathrm{t}, \tag{4}$$

$$\mathbf{L} = \frac{1}{(R/a)^3}\,\mathbf{X}\times\mathbf{F}, \tag{5}$$

where *a* is the radius of the sphere (Pozrikidis 1992, equations (3.3.26) and (3.3.27)). Equations (4) and (5) can be derived using the Faxén relations and the Stokeslet flow solution in an infinite domain without knowledge of the flow solution (3).

If the model flagellate is free to translate and rotate, the net force and torque on it in the creeping flow are zero. We assume a rigid and frictionless connection between the sphere and the point where the force is produced, so that the thrust force $\mathbf{T} = -\mathbf{F}$ is transferred directly to the cell (figure 2(a)). At equilibrium there is balance between the thrust force **T**, the force **K**, and the drag $\mathbf{D} = -6\pi\mu a\mathbf{U}$ due to the translational motion of the sphere, and thus its velocity **U** is determined by

$$\begin{aligned} 6\,\pi\,\mu\,a\,\mathbf{U} &= \mathbf{T} + \mathbf{K} \\ &= f_1(R/a)\,\mathbf{T} + f_2(R/a)\,\frac{(\mathbf{X}\cdot\mathbf{T})\,\mathbf{X}}{R^2}. \end{aligned} \tag{6}$$

Similarly there is balance between the torque $\mathbf{X}\times\mathbf{T}$ due to the thrust force **T**, the torque **L**, and the resistive torque $\mathbf{M} = -8\pi\mu a^3\boldsymbol{\Omega}$ on the sphere due to its rotational motion, and thus the angular velocity $\boldsymbol{\Omega}$ is determined by

$$\begin{aligned} 8\,\pi\,\mu\,a^3\,\boldsymbol{\Omega} &= \mathbf{X}\times\mathbf{T} + \mathbf{L} \\ &= f_3(R/a)\,\mathbf{X}\times\mathbf{T}. \end{aligned} \tag{7}$$

The dimensionless coefficients f_1, f_2, and f_3 depend only on the dimensionless force distance R/a and they turn out to be

$$f_1 = 1 - \frac{3}{4\,R/a} - \frac{1}{4\,(R/a)^3}, \tag{8}$$

$$f_2 = -\frac{3}{4\,R/a} + \frac{3}{4\,(R/a)^3}, \tag{9}$$

$$f_3 = 1 - \frac{1}{(R/a)^3}. \tag{10}$$

To model flagellates with several flagella or several thrust force locations per flagellum, each flow solution representing one point force $\mathbf{F}_i$ at position $\mathbf{X}_i$ can be calculated separately from equation (3) and superposed with the flow fields due to the forces created by the other flagella to obtain the total flow $\mathbf{v}_\mathrm{O} = \sum_i \mathbf{v}_{\mathrm{O},i}$. The translational and the angular velocity can be obtained by superposition of the velocities due to each flagellum, i.e., $\mathbf{U} = \sum_i \mathbf{U}_i$ and $\boldsymbol{\Omega} = \sum_i \boldsymbol{\Omega}_i$.

To calculate the flow around the freely swimming model organism (Jiang *et al* 2002), the Oseen solution $\mathbf{v}_\mathrm{O}$ is

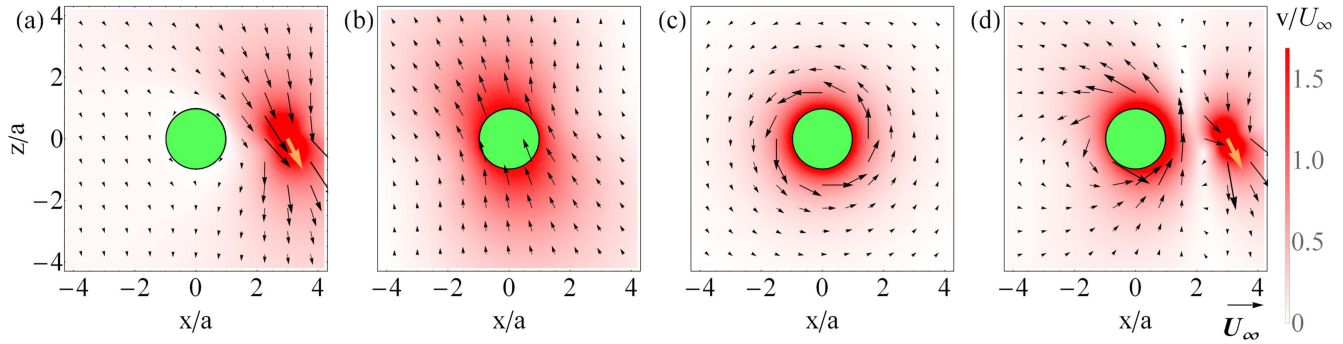

Figure 3. Superposition of creeping flows to calculate the flow around a freely swimming model flagellate. (a) Flow due to a point force (vector, orange) outside a sphere. (b) Flow due to a translating sphere. (c) Flow due to a rotating sphere. (d) Superposition of the flows shown in (a)–(c) resulting in the flow around the freely swimming model flagellate. The color maps show the normalized velocity magnitude v/U_∞ with the velocity scale $U_\infty = F/(6\,\pi\,\mu\,a)$.

superposed with the flow

$$\mathbf{v}_\mathrm{T} = \left[\frac{3}{4\,r/a} + \frac{1}{4\,(r/a)^3}\right]\mathbf{U} + \left[\frac{3}{4\,r/a} - \frac{3}{4\,(r/a)^3}\right]\frac{(\mathbf{x}\cdot\mathbf{U})\,\mathbf{x}}{r^2} \tag{11}$$

due to translation with velocity $\mathbf{U}$ and the flow

$$\mathbf{v}_\mathrm{R} = \frac{1}{(r/a)^3}\,\boldsymbol{\Omega}\times\mathbf{x} \tag{12}$$

due to rotation with angular velocity $\boldsymbol{\Omega}$ (Stone and Duprat 2016). The complete velocity field becomes

$$\mathbf{v} = \mathbf{v}_\mathrm{O} + \mathbf{v}_\mathrm{T} + \mathbf{v}_\mathrm{R}. \tag{13}$$

Superposition of the three flow field contributions leads in general to a complex flow field with both translational and rotational components near the cell and intense singular flow in the vicinity of the point force (figure 3).

3. Straight, circular, and helical trajectories

The vectors $\mathbf{U}$ and $\boldsymbol{\Omega}$ together determine the trajectory of the microswimmer. A model flagellate propelled by a single constant point force swims in the symmetry plane spanned by $\mathbf{X}$ and $\mathbf{T}$. Formally, looking at the expressions (6) and (7) and using that $\mathbf{X}\times\mathbf{T}$ is perpendicular to the plane spanned by $\mathbf{X}$ and $\mathbf{T}$, we see that $\mathbf{U}$ is perpendicular to $\boldsymbol{\Omega}$. The trajectory is thus in this case restricted to a circle, or a straight line when $\boldsymbol{\Omega} = \mathbf{0}$.

For a general model flagellate propelled by several constant point forces, $\mathbf{U}$ and $\boldsymbol{\Omega}$ are neither parallel nor perpendicular to each other and the swimming trajectory is helical (figure 2(b)). The velocity $\mathbf{U}$ is constant in the co-rotating coordinate system with axes that follow the rotation of the microswimmer, and without loss of generality we define $\mathbf{e}_z = \boldsymbol{\Omega}/\Omega$ and decompose $\mathbf{U} = U_\perp\mathbf{e}_y + U_\parallel\mathbf{e}_z$ with

$$U_\parallel = \mathbf{U}\cdot\mathbf{e}_z, \tag{14}$$

$$U_\perp = \sqrt{U^2 - (\mathbf{U}\cdot\mathbf{e}_z)^2}. \tag{15}$$

The velocity $\mathbf{U}'$ of the cell center in the stationary coordinate system with axes that are fixed is calculated by rotating the velocity vector $\mathbf{U}$ around the z-axis as

$$\begin{bmatrix}U_{x'}\\U_{y'}\\U_{z'}\end{bmatrix} = \begin{bmatrix}\cos\Omega\,t & -\sin\Omega\,t & 0\\ \sin\Omega\,t & \cos\Omega\,t & 0\\ 0 & 0 & 1\end{bmatrix}\begin{bmatrix}0\\U_\perp\\U_\parallel\end{bmatrix}. \tag{16}$$

Integration yields the trajectory $\mathbf{s}'(t)$ of the cell center in the stationary coordinate system as

$$\mathbf{s}'(t) = \int\mathbf{U}'\mathrm{d}t = \frac{U_\perp}{\Omega}(\cos\Omega\,t\;\mathbf{e}_{x'} + \sin\Omega\,t\;\mathbf{e}_{y'}) + U_\parallel\,t\;\mathbf{e}_{z'}, \tag{17}$$

which describes a helical trajectory around the z'-axis (figure 2(b)). We can identify the helix radius

$$b = \frac{U_\perp}{\Omega} \tag{18}$$

and the pitch

$$h = \frac{2\,\pi\,U_\parallel}{\Omega}. \tag{19}$$

For constant $\mathbf{U}$ and $\boldsymbol{\Omega}$ the orientation of the flagellate is constant with respect to the locally defined Frenet–Serret basis for the helical trajectory such that some points on the cell surface are always on the 'outside' and some on the 'inside' of the trajectory (Crenshaw 1993a).

4. Flagellate propelled by two left–right symmetric forces

As a special case we look at a left–right symmetric model flagellate propelled by two constant point forces. This model can represent common biflagellates such as *C. reinhardtii* and some species of haptophytes such as *Prymnesium parvum* (figures 1(a) and (e)) (Dölger *et al* 2017). The two point forces $\mathbf{F}_1$ and $\mathbf{F}_2$ of equal magnitude F are assumed to lie in the xz-plane with radial and angular force positions R and θ, and force direction α (figure 4(a)).

Since the transversal force components towards and away from the symmetry axis cancel due to the left–right symmetry, the swimming velocity will point along the symmetry axis. Also, the torques due to the two point forces fully cancel each

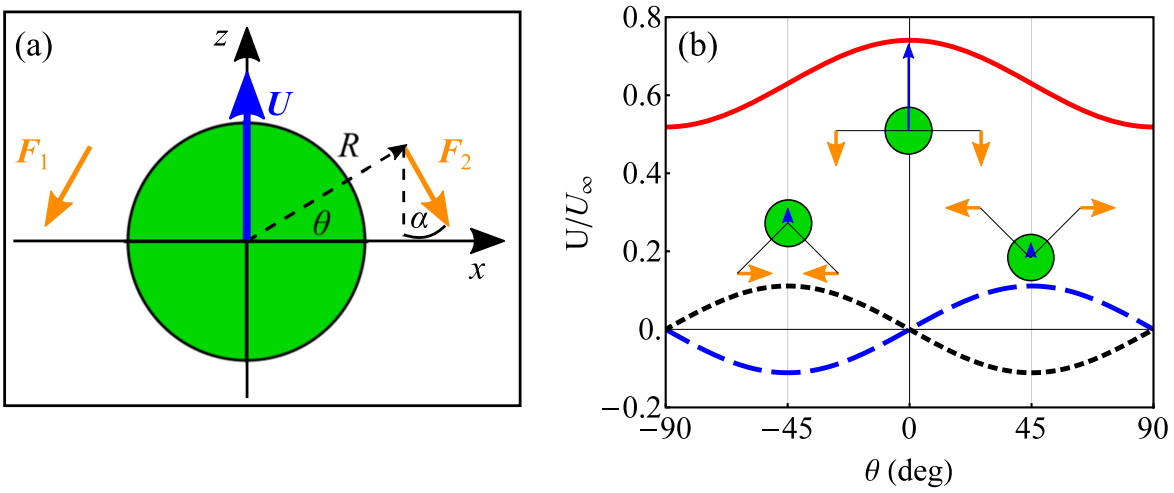

Figure 4. Model and swimming velocity for a left–right symmetric biflagellate. (a) Model microswimmer with fixed point forces $\mathbf{F}_l$ and $\mathbf{F}_2$ (orange) and translational velocity $\mathbf{U}$ (blue). Radial and angular force positions R and θ, and force direction α. (b) Normalized swimming velocity in the z-direction for the force distance $R = 3\,a$ as function of the angular force position θ for backwards pointing forces, i.e., $\alpha = 0$ (red line, solid) and transversely directed forces with $\alpha = 90°$ (blue line, dashed) and $\alpha = 270°$ (black line, dotted). The swimming velocity is maximal for equatorially placed, backwards pointing forces.

other and thus the model microswimmer does not rotate. The thrust force $\mathbf{T} = 2F\cos\alpha\,\mathbf{e}_z$ is proportional to the force components along the symmetry axis. As function of force position and orientation the swimming velocity can be calculated using equation (6) as

$$\frac{U}{U_\infty} = \cos\alpha\left[1 - \frac{3\,(1+\sin^2\theta)}{4\,R/a} - \frac{1-3\sin^2\theta}{4\,(R/a)^3}\right] + \frac{3}{8}\sin\alpha\,\sin 2\,\theta\left[\frac{1}{R/a} - \frac{1}{(R/a)^3}\right], \tag{20}$$

where

$$U_\infty = \frac{F}{3\,\pi\,\mu\,a}. \tag{21}$$

The highest swimming velocity U_∞ is obtained when the forces are pointing backwards ($\alpha = 0$) and are placed far away from the cell. In this case the model reduces to that of a towed sphere. With a fixed point force magnitude F and distance R, the fastest swimming is obtained for an equatorial force arrangement with $\theta = 0$ and $\alpha = 0$ (figure 4(b)). The biflagellated haptophyte *P. parvum* has a cell radius of $a = 3\,\mu$m and an average swimming speed of $U = 30\,\mu\text{m s}^{-1}$ (Dölger *et al* 2017). Using equation (20) for forces with $R = 8\,\mu$m, $\theta = 0$, and $\alpha = 0$ we estimate that $U = 0.7\,U_\infty$, and using equation (21) with $\mu = 1\times10^{-3}$ Pa s we find that each flagellum of *P. parvum* exerts an average force of $F = 1$ pN on the water. A model swimmer with the above-mentioned force configuration produces a flow field that compares well with the measured time-averaged flow field around the biflagellate *P. parvum* (Dölger *et al* 2017). Our force estimate is comparable to the estimated average force per flagellum of approximately 5 pN for the larger *C. reinhardtii* (Drescher *et al* 2010, Goldstein 2015).

So far we have looked at models for steady microswimmers with constant point forces that represent time-averaged flow fields. In reality the periodic shape change of the beating flagella leads to periodically varying forces on the water (Purcell 1977). If the point forces simply rotate at fixed locations relative to the cell and the time-average of each point force vanishes, there is no net propulsion. However, if the forces additionally move on closed trajectories relative to the cell, the model organism can swim due to the drag difference between different force positions. This mechanism of force variation can model the breast-stroke beat of biflagellates with short flagella, and has been shown to capture measured time-resolved near-cell flow fields around *P. parvum* (Dölger *et al* 2017). Here we ask which periodic force variation leads to the highest average swimming velocity, and what the effect is of the transversal forces.

As a schematic model we approximate the breast-stroke beat by four pairs of point forces of constant magnitude F that each act during one fourth of the beat period (figure 5(a)). The optimal angular arrangement for the power stroke is according to equation (20) at the equator at $\theta_p = 0$. The further away from the cell the power stroke acts, the faster the model organism swims. Thus we assume that the distance R_p of the power stroke is set by the flagella length to a maximum feasible value. The return stroke is assumed to be positioned at the equator as well with $\theta_r = 0$. It will lead to propulsion in the opposite direction to the power stroke. The velocity contribution due to the power and the return stroke is then calculated as

$$\frac{U_{pr}}{U_\infty} = \frac{1}{8}\left[\frac{3}{R_r/a} - \frac{3}{R_p/a} + \frac{1}{(R_r/a)^3} - \frac{1}{(R_p/a)^3}\right], \tag{22}$$

which is positive for $R_r < R_p$ (figure 5(b)). Also the purely transversal forces can lead to propulsion due to the force $\mathbf{K}$ when located below or above the equator, although their direct thrust $\mathbf{T}_l + \mathbf{T}_2 = \mathbf{0}$ vanishes. The transversal forces are assumed to be symmetrically arranged at $\pm\theta_t$ and at equal distance R_t. They both lead to swimming in the positive z-

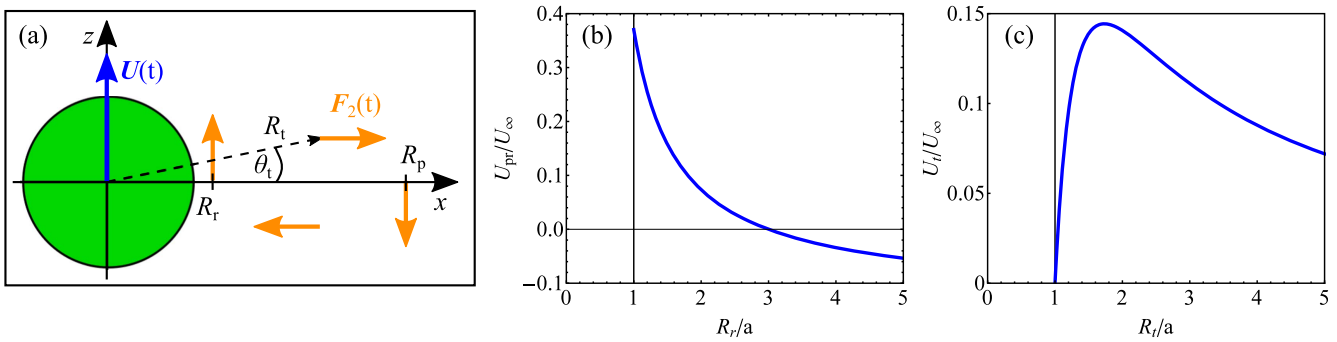

Figure 5. Time-dependent model and normalized swimming velocity for a left–right symmetric biflagellate. (a) Right half of model microswimmer with point force $\mathbf{F}_2(t)$ varying during the beat cycle. Forces for power and return strokes are placed equatorially, i.e., $\theta_p = \theta_r = 0$ with radial positions R_p and R_r. The transversal forces are placed symmetrically at $\pm\theta_t$ with radial position R_t. (b) Average swimming velocity in the z-direction due to power and return stroke as function of return stroke distance R_r/a for $R_p = 3\,a$. (c) Average swimming velocity in the z-direction due to transversal strokes as function of transversal force distance R_t/a for $\theta_t = \theta_{opt} = 45°$. The swimming velocity is highest for return strokes close to the cell and transversal strokes with radial position $R_t = R_{opt} = \sqrt{3}\,a$.

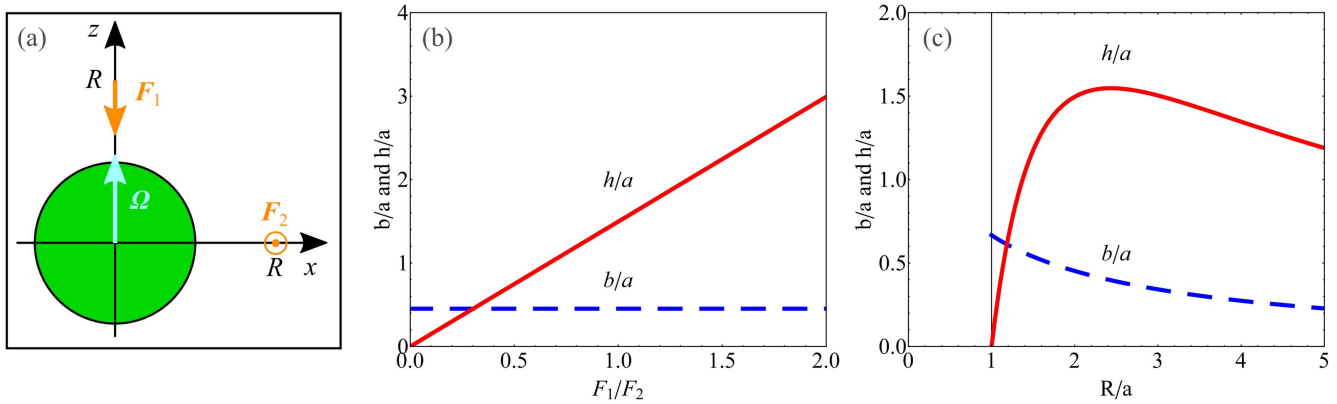

Figure 6. Model flagellate with helical trajectory. (a) Model microswimmer with point forces $\mathbf{F}_1$ and $\mathbf{F}_2$ (orange) and angular velocity $\boldsymbol{\Omega}$ (light blue). (b) and (c) helix radius b/a (dashed line, blue) and helix pitch h/a (solid line, red) as functions of the force ratio F_1/F_2 for $R = 2\,a$ (b) and as functions of the force distance R/a for $F_1 = F_2$ (c). The radius decreases for increasing force distance from a maximum $b = b_{max} = (2/3)\,a$. The pitch increases linearly with the force ratio F_1/F_2 and has a maximum at a force distance of $R = R_{opt} \approx 2.4\,a$.

direction with the velocity contribution

$$\frac{U_t}{U_\infty} = \frac{3}{8}\sin 2\,\theta_t\left[\frac{1}{R_t/a} - \frac{1}{(R_t/a)^3}\right]. \tag{23}$$

For any force distance R_t the highest velocity can be obtained for transversal forces located at the angular positions $\pm\theta_{opt} = \pm 45°$. The optimum distance of the transversal forces is $R_{opt} = \sqrt{3}\,a$ (figure 5(c)), so that the maximum velocity that can be obtained from the transversal forces is $U_t(R_{opt}, \theta_{opt}) = 0.14\,U_\infty$. Correspondingly for a combined power and return stroke in an equatorial arrangement with $R_p = 3\,a$ and $R_r = 1.1\,a$ we find the swimming velocity $U_{pr} = 0.30\,U_\infty$, and we conclude that the transversal forces can contribute significantly to facilitate swimming in biflagellates.

5. Simple flagellate model with helical trajectory

With more than one constant point force a model flagellate generally swims with a helical trajectory if the forces are not symmetrically arranged to create straight or circular trajectories. Helical trajectories are common among flagellates (Jennings 1901, 1904, Fenchel 2001), and they are useful for helical klinotaxis, i.e., the movement towards stimuli due to gradients (chemical, light, temperature, magnetic field) (Crenshaw 1993b, 1996, Friedrich and Jülicher 2009). Here we study a flagellate with a longitudinal flagellum that creates a typical puller arrangement with a force $\mathbf{F}_1 = -F_1\mathbf{e}_z$ at $\mathbf{X}_1 = R\,\mathbf{e}_z$, and a transversal flagellum that creates a force tangentially to the surface of the sphere $\mathbf{F}_2 = -F_2\,\mathbf{e}_y$ at $\mathbf{X}_2 = R\,\mathbf{e}_x$ (figure 6(a)). The flagellate *Heterosigma akashiwo* has a flagellar arrangement for which this model can be applied (figures 1(b) and (f)). For simplicity we only explore the effect of the y-component of the force due to the transversal flagellum, and we disregard possible force components in other directions. Such components are most likely also created by the transversal flagellum of *H. akashiwo*.

The translational velocity is calculated with equation (6) as

$$6\,\pi\,\mu\,a\,\mathbf{U} = f_1\,F_2\,\mathbf{e}_y + (f_1 + f_2)\,F_1\,\mathbf{e}_z \tag{24}$$

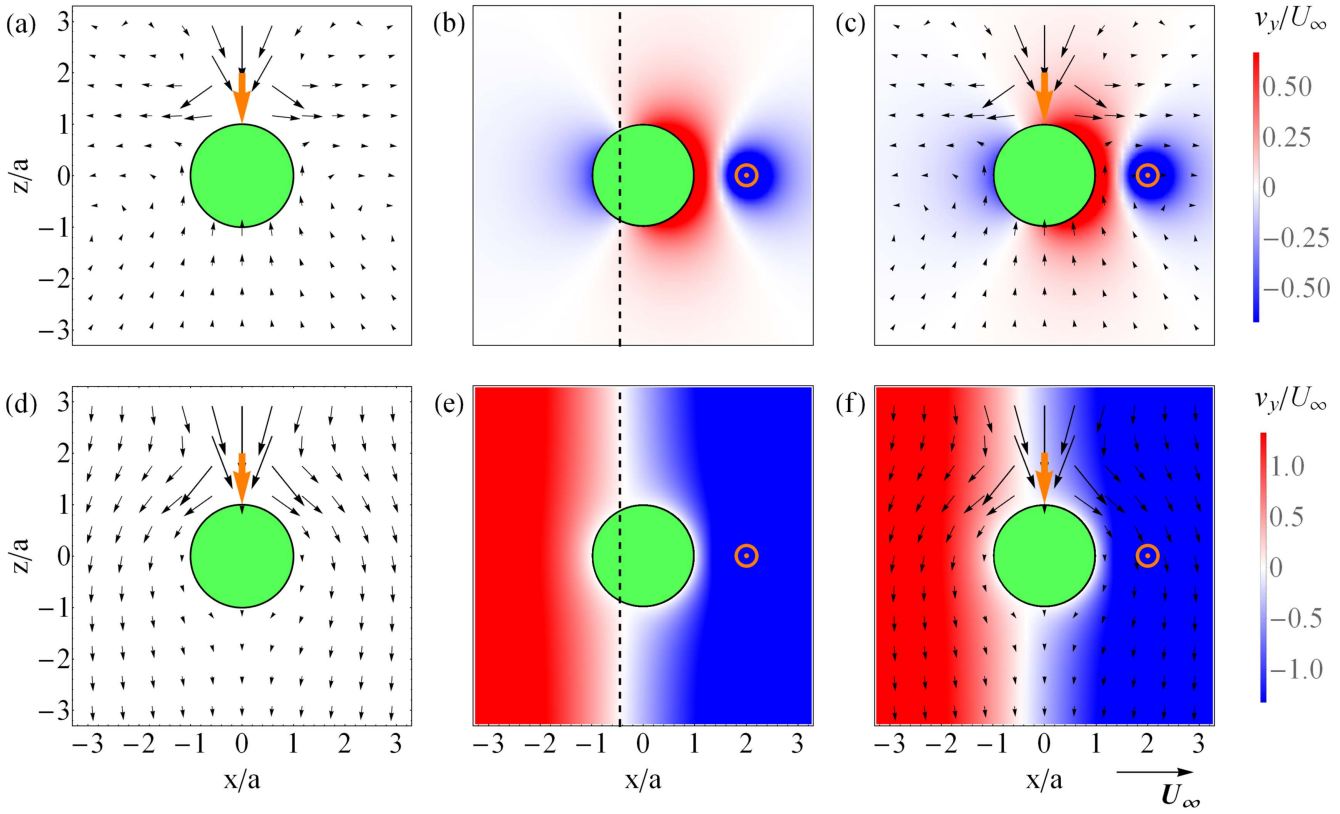

Figure 7. Flow fields for model microswimmer with straight, circular, and helical trajectories, respectively. (a)–(c) Laboratory frame of reference and (d)–(f) co-moving frame of reference. (a) and (d) Purely longitudinal flagellum, (b) and (e) purely transversal flagellum with the axis of rotation (dashed lines) indicated, and (c) and (f) both a longitudinal and a transversal flagellum of equal force magnitude $F_1 = F_2 = F$. Point forces (orange). The color maps show the normalized out-of-plane component v_y/U_∞ with velocity scale $U_\infty = \sqrt{2}\, F/(6\,\pi\,\mu\,a)$.

and the angular velocity with equation (7) as

$$8\,\pi\,\mu\,a^3\,\mathbf{\Omega} = f_3\,R\,F_2\,\mathbf{e}_z. \tag{25}$$

In the resulting helical trajectory the longitudinal force $\mathbf{F}_1$ will always be directed parallel to the helix axis, while the transversal force $\mathbf{F}_2$ will always be positioned on the outside of the helix. The velocity component $U_\parallel$, see equation (14), due to the longitudinal force $\mathbf{F}_1$ leads to forward motion

$$U_\parallel = \frac{(f_1 + f_2)\,F_1}{6\,\pi\,\mu\,a}, \tag{26}$$

while the component $U_\perp$, see equation (15), due to the transversal force $\mathbf{F}_2$ leads to the rotational motion in the helix

$$U_\perp = \frac{f_1\,F_2}{6\,\pi\,\mu\,a}. \tag{27}$$

Thus for a constant longitudinal force $\mathbf{F}_1$ leading to a constant average translational velocity, the shape of the helical trajectory can be tuned by varying the magnitude of the tangential force $\mathbf{F}_2$. The radius is independent of the force ratio F_1/F_2 and depends only on the force distance. It is calculated with equation (18) as

$$\frac{b}{a} = \frac{1 + R/a + 4\,(R/a)^2}{3\,[R/a + (R/a)^2 + (R/a)^3]}. \tag{28}$$

The pitch also depends on the force distance and it is proportional to the force ratio F_1/F_2. It can be written using equation (19) as

$$\frac{h}{a} = 4\,\pi\,\frac{-1 - R/a + 2\,(R/a)^2}{3\,[R/a + (R/a)^2 + (R/a)^3]}\,\frac{F_1}{F_2}. \tag{29}$$

The dependences of the pitch and the radius on the force distance R/a and the force ratio F_1/F_2 show several characteristic features (figures 6(b) and (c)). The radius decreases with force distance from its maximum value $b_{\max} = (2/3)\,a$ to zero at large force distances, while the pitch first increases from zero to a maximum $h_{\max} \approx 1.5\,(F_1/F_2)\,a$ for the force distance $R_{\text{opt}} \approx 2.4\,a$, and subsequently decreases as $(R/a)^{-1}$ for large R/a. A typical individual of *H. akashiwo* with a cell radius of $a = 5\ \mu$m swims with $U_\parallel = 50\ \mu\text{m s}^{-1}$, $U_\perp = 90\ \mu\text{m s}^{-1}$, and $\Omega = 2\ \text{s}^{-1}$ (Gurarie *et al* 2011). From equations (18) and (19) we estimate $b = 40\ \mu$m and $h = 160\ \mu$m. The large radius ($b > (2/3)\,a$) indicates that the transversal flagellum does not only produce a tangential force in the y-direction but also a radial force in the x-direction that allows larger radii of circular motion than in our simplified configuration.

The near-cell flow field can be used to find the optimal place for prey capture on the cell where the clearance rate per unit surface area is highest (figure 7) (Nielsen and Kiørboe 2015). The clearance rate, i.e., the volume flow rate into the capture zone surrounding the cell should be calculated in the co-moving frame of reference in which the cell is at rest. With only the longitudinal flagellum active, the flagellate swims on a straight line and the model reduces to the previously studied

model of copepods and uniflagellates (figures 7(a) and (d)) (Jiang *et al* 2002, Langlois *et al* 2009). The flagellum enhances the flow velocities near the forward half of the cell surface, and it thereby increases the clearance rate for direct capture on the cell relative to the clearance rate for a towed sphere. The closer the point force is to the cell, the larger is the enhancement of the clearance rate (Langlois *et al* 2009). The transversal flagellum results in rotational flows with high velocities relative to the cell surface, in particular in the region nearest to the point force (figures 7(e) and (f)). However, the clearance rate in the region will presumably only be enhanced for the microswimmer with helical trajectory due to prey depletion in the water around the microswimmer with circular trajectory that retraces its path.

6. Conclusions

We have described an analytical model framework based on the exact solution of the creeping flow due to a point force next to a no-slip sphere, and we have illustrated how the model can be used to predict swimming kinematics and near-cell flows of flagellates with different flagellar arrangements and beat patterns. We believe that the model can be useful as a basis for the investigation of swimming velocities, search strategies, flow disturbances, feeding, and energy consumption. Thereby the model can contribute to the trait-based approach to aquatic ecology by providing a framework to investigate the flagellar arrangement as a key trait based on which optima and compromises between essential functions can be explored.

Acknowledgments

We are grateful to Lasse Tor Nielsen for flagellate images, and we thank Lasse Tor Nielsen and Jens Juul Rasmussen for critical reading of the manuscript. The Centre for Ocean Life is a VKR Centre of Excellence supported by the Villum Foundation.

Appendix. The flow due to a point force external to a sphere

Oseen's solution (Oseen 1927, p 108) and (Higdon 1979b, equations (3) and (4)) for the creeping flow due to a point force $\mathbf{F}$ next to a no-slip sphere with radius a is represented by a Green function G_{jk} which depends on the field vector $\mathbf{x}$ with $r = |\mathbf{x}|$, and the positions $\mathbf{X}$ and $\mathbf{X}^* = (a^2/|\mathbf{X}|^2)\mathbf{X}$ of the point force and the inverse point:

$$\begin{aligned} G_{jk} = {} & \frac{\delta_{jk}}{|\mathbf{x}-\mathbf{X}|} + \frac{(x_j - X_j)(x_k - X_k)}{|\mathbf{x}-\mathbf{X}|^3} - \frac{a}{|\mathbf{X}|}\frac{\delta_{jk}}{|\mathbf{x}-\mathbf{X}^*|} \\ & - \frac{a^3}{|\mathbf{X}|^3}\frac{(x_j - X_j^*)(x_k - X_k^*)}{|\mathbf{x}-\mathbf{X}^*|^3} - \frac{|\mathbf{X}|^2 - a^2}{|\mathbf{X}|}\left\{\frac{X_j^* X_k^*}{a^3|\mathbf{x}-\mathbf{X}^*|}\right. \\ & - \frac{a}{|\mathbf{X}|^2|\mathbf{x}-\mathbf{X}^*|^3}[X_j^*(x_k - X_k^*) + X_k^*(x_j - X_j^*)] \\ & \left. + \frac{2X_j^* X_k^*}{a^3}\frac{X_l^*(x_l - X_l^*)}{|\mathbf{x}-\mathbf{X}^*|^3}\right\} - (r^2 - a^2)\frac{\partial \phi_k}{\partial x_j} \end{aligned} \tag{A.1}$$

with

$$\begin{aligned} \frac{\partial \phi_k}{\partial x_j} = {} & \frac{|\mathbf{X}|^2 - a^2}{2\,|\mathbf{X}|^3}\left\{\frac{-3X_k(x_j - X_j^*)}{a\,|\mathbf{x}-\mathbf{X}^*|^3} + \frac{a\delta_{jk}}{|\mathbf{x}-\mathbf{X}^*|^3}\right. \\ & - \frac{3a\,(x_j - X_j^*)(x_k - X_k^*)}{|\mathbf{x}-\mathbf{X}^*|^5} - \frac{2X_k X_j^*}{a\,|\mathbf{x}-\mathbf{X}^*|^3} \\ & + \frac{6X_k}{a\,|\mathbf{x}-\mathbf{X}^*|^5}(x_j - X_j^*)(x_l - X_l^*)X_l^* \\ & + \frac{3a}{|\mathbf{X}^*|}\frac{X_k^*(x_j - X_j^*)\,|\mathbf{x}-\mathbf{X}^*|^2 + (x_j - X_j^*)(x_k - X_k^*)\,|\mathbf{X}^*|^2}{|\mathbf{x}-\mathbf{X}^*|^3|\mathbf{X}^*|(|\mathbf{X}^*||\mathbf{x}-\mathbf{X}^*| + x_l X_l^* - |\mathbf{X}^*|^2)} \\ & + \frac{3a}{|\mathbf{X}^*|}\frac{(|\mathbf{x}-\mathbf{X}^*| - |\mathbf{X}^*|)\,|\mathbf{x}-\mathbf{X}^*|^2|\mathbf{X}^*|\delta_{jk}}{|\mathbf{x}-\mathbf{X}^*|^3|\mathbf{X}^*|(|\mathbf{X}^*||\mathbf{x}-\mathbf{X}^*| + x_l X_l^* - |\mathbf{X}^*|^2)} \\ & - \frac{3a}{|\mathbf{X}^*|}\frac{|\mathbf{X}^*|(x_j - X_j^*) + |\mathbf{x}-\mathbf{X}^*|X_j^*}{|\mathbf{x}-\mathbf{X}^*|^2|\mathbf{X}^*|(|\mathbf{X}^*||\mathbf{x}-\mathbf{X}^*| + x_l X_l^* - |\mathbf{X}^*|^2)^2} \\ & \times (X_k^*\,|\mathbf{x}-\mathbf{X}^*|^2 - (x_k - X_k^*)\,|\mathbf{X}^*|^2 \\ & + (x_k - 2X_k^*)|\mathbf{x}-\mathbf{X}^*||\mathbf{X}^*|) \\ & - \frac{3a}{|\mathbf{X}^*|}\frac{x_j X_k^* + r|\mathbf{X}^*|\delta_{jk}}{r|\mathbf{X}^*|(r|\mathbf{X}^*| + x_l X_l^*)} \\ & \left. + \frac{3a}{|\mathbf{X}^*|}\frac{(|\mathbf{X}^*|x_j + rX_j^*)(|\mathbf{X}^*|x_k + rX_k^*)}{r|\mathbf{X}^*|(r|\mathbf{X}^*| + x_l X_l^*)^2}\right\}. \end{aligned} \tag{A.2}$$

References

Andersen A, Wadhwa N and Kiørboe T 2015 Quiet swimming at low Reynolds number *Phys. Rev.* E **91** 042712

Berg H C 2008 *E. coli in Motion* (Berlin: Springer)

Blake J R 1971 A spherical envelope approach to ciliary propulsion *J. Fluid Mech.* **46** 199–208

Crenshaw H C 1993a Orientation by helical motion—I. Kinematics of the helical motion of organisms with up to six degrees of freedom *Bull. Math. Biol.* **55** 197–212

Crenshaw H C 1993b Orientation by helical motion—III. Microorganisms can orient to stimuli by changing the direction of their rotational velocity *Bull. Math. Biol.* **55** 231–55

Crenshaw H C 1996 A new look at locomotion in microorganisms: rotating and translating *Am. Zool.* **36** 608–18

Dölger J, Nielsen L T, Kiørboe T and Andersen A 2017 Swimming and feeding of mixotrophic biflagellates *Sci. Rep.* **7** 39892

Drescher K, Dunkel J, Cisneros L H, Ganguly S and Goldstein R E 2011 Fluid dynamics and noise in bacterial cell–cell and cell–surface scattering *Proc. Natl Acad. Sci.* **108** 10940–5

Drescher K, Goldstein R E, Michel N, Polin M and Tuval I 2010 Direct measurement of the flow field around swimming microorganisms *Phys. Rev. Lett.* **105** 168101

Fenchel T 1986 The ecology of heterotrophic microflagellates *Advances in Microbial Ecology* ed K C Marshall vol 9 (New York: Springer) ch 2, pp 57–97

Fenchel T 2001 How dinoflagellates swim *Protist* **152** 329–38

Friedrich B M and Jülicher F 2009 Steering chiral swimmers along noisy helical paths *Phys. Rev. Lett.* **103** 068102

Friedrich B M and Jülicher F 2012 Flagellar synchronization independent of hydrodynamic interactions *Phys. Rev. Lett.* **109** 138102

Gibbons I R 1981 Cilia and flagella of eukaryotes *J. Cell Biol.* **19** 107s–124s

Goldstein R E 2015 Green algae as model organisms for biological fluid dynamics *Annu. Rev. Fluid Mech.* **47** 343–75

Guasto J S, Rusconi R and Stocker R 2012 Fluid mechanics of planktonic microorganisms *Annu. Rev. Fluid Mech.* **44** 373–400

Gurarie E, Grünbaum D and Nishizaki M T 2011 Estimating 3D movements from 2D observations using a continuous model of helical swimming *Bull. Math. Biol.* **73** 1358–77

Higdon J J L 1979a The generation of feeding currents by flagellar motion *J. Fluid Mech.* **94** 305–30

Higdon J J L 1979b A hydrodynamic analysis of flagellar propulsion *J. Fluid Mech.* **90** 685–711

Inouye I and Hori T 1991 High-speed video analysis of the flagellar beat and swimming patterns of algae: possible evolutionary trends in green algae *Protoplasma* **164** 54–69

Jennings H S 1901 On the significance of the spiral swimming of organisms *Am. Nat.* **35** 369–78

Jennings H S 1904 *Contributions to the Study of the Behaviour of Lower Organisms* (Washington, DC: Carnegie Institution of Washington Publication)

Jiang H, Osborn T R and Meneveau C 2002 The flow field around a freely swimming copepod in steady motion. Part I: Theoretical analysis *J. Plankton Res.* **24** 167–89

Kiørboe T 2016 Fluid dynamic constraints on resource acquisition in small pelagic organisms *Eur. Phys. J. Spec. Top.* **225** 669–83

Kiørboe T, Jiang H, Gonçalves R J, Nielsen L T and Wadhwa N 2014 Flow disturbances generated by feeding and swimming zooplankton *Proc. Natl Acad. Sci.* **111** 11738–43

Kurtuldu H, Tam D, Hosoi A E, Johnson K A and Gollub J P 2013 Flagellar waveform dynamics of freely swimming algal cells *Phys. Rev.* E **88** 013015

Langlois V J, Andersen A, Bohr T, Visser A W and Kiørboe T 2009 Significance of swimming and feeding currents for nutrient uptake in osmotrophic and interception-feeding flagellates *Aquat. Microb. Ecol.* **54** 35–44

Lauga E 2016 Bacterial hydrodynamics *Annu. Rev. Fluid Mech.* **48** 105–30

Lauga E and Powers T R 2009 The hydrodynamics of swimming microorganisms *Rep. Prog. Phys.* **72** 096601

Lighthill J 1952 On the squirming motion of nearly spherical deformable bodies through liquids at very small Reynolds numbers *Commun. Pure Appl. Math.* **5** 109–18

Lighthill J 1976 Flagellar hydrodynamics *SIAM Rev.* **18** 161–230

Nielsen L T and Kiørboe T 2015 Feeding currents facilitate a mixotrophic way of life *ISME J.* **9** 2117–27

Oseen C W 1927 *Neuere Methoden und Ergebnisse in der Hydrodynamik* (Leipzig: Akademische Verlagsgesellschaft)

Pak O S and Lauga E 2016 Theoretical models of low-Reynolds-number locomotion *Fluid-Structure Interactions in Low-Reynolds-Number Flows* ed C Duprat and H A Stone (Cambridge: Royal Society of Chemistry) ch 4

Pécseli H L, Trulsen J K and Fiksen Ø 2014 Predator–prey encounter and capture rates in turbulent environments *Limnology Oceanogr.: Fluids Environ.* **4** 85–105

Polotzek K and Friedrich B M 2013 A three-sphere swimmer for flagellar synchronization *New J. Phys.* **15** 045005

Pozrikidis C 1992 *Boundary Integral and Singularity Methods for Linearized Viscous Flow* (Cambridge: Cambridge University Press)

Purcell E M 1977 Life at low Reynolds number *Am. J. Phys.* **45** 3–11

Sleigh M A 1981 Flagellar beat patterns and their possible evolution *BioSystems* **14** 423–31

Stone H A and Duprat C 2016 Low-Reynolds-number flows *Fluid-Structure Interactions in Low-Reynolds-Number Flows* ed C Duprat and H A Stone (Cambridge: Royal Society of Chemistry) ch 2

Wrobel J K, Cortez R, Varela D and Fauci L 2016 Regularized image system for Stokes flow outside a solid sphere *J. Comput. Phys.* **317** 165–84

5.2 Swimming and feeding of mixotrophic biflagellates

Paper published in Scientific Reports (2017).

SCIENTIFIC REPORTS

OPEN

Swimming and feeding of mixotrophic biflagellates

Julia Dölger[1], Lasse Tor Nielsen[2], Thomas Kiørboe[2] & Anders Andersen[1]

Received: 05 August 2016
Accepted: 29 November 2016
Published: 05 January 2017

Many unicellular flagellates are mixotrophic and access resources through both photosynthesis and prey capture. Their fitness depends on those processes as well as on swimming and predator avoidance. How does the flagellar arrangement and beat pattern of the flagellate affect swimming speed, predation risk due to flow-sensing predators, and prey capture? Here, we describe measured flows around two species of mixotrophic, biflagellated haptophytes with qualitatively different flagellar arrangements and beat patterns. We model the near cell flows using two symmetrically arranged point forces with variable position next to a no-slip sphere. Utilizing the observations and the model we find that puller force arrangements favour feeding, whereas equatorial force arrangements favour fast and quiet swimming. We determine the capture rates of both passive and motile prey, and we show that the flow facilitates transport of captured prey along the haptonema structure. We argue that prey capture alone cannot fulfil the energy needs of the observed species, and that the mixotrophic life strategy is essential for survival.

Small plankton form an essential part of the marine ecosystem. Such organisms face the challenge of living in a light- and nutrient-limited environment, while being exposed to flow-sensing predators. Many unicellular flagellates in the size range from 2 to 50 micrometer are mixotrophic and use a combination of photosynthesis, dissolved nutrient uptake, and prey capture to access resources[1,2]. Despite the increase in predation risk due to the induced flow disturbances, they must swim to reach light and food and create feeding currents that enhance prey capture and nutrient uptake. They do so by means of cilia and flagella in different numbers and with different positions, lengths, and dynamics[3–5]. This diversity in flagellar arrangements suggests different strategies with trade-offs, since not all functions can be optimized simultaneously. Biflagellates with two left-right symmetrically arranged flagella, such as the well-studied algae *Chlamydomonas reinhardtii*, are an abundant and successful flagellate form[4,6]. By tuning the flagellar arrangement and beat pattern, biflagellates can arrange the thrust forces in front of the cell (puller), equatorially (neutral), or behind the cell (pusher)[7]. What are the advantages and disadvantages of different flagellar arrangements and beat patterns in mixotrophic biflagellates, and to what extent are these archetypical, multi-functional organisms optimized for swimming, predator avoidance, and prey capture?

To answer these questions we focus on two mixotrophic, biflagellated species of haptophytes with different morphologies, kinematics, and feeding strategies (Methods, Fig. 1, and Supplementary Videos S1 and S2). *Prymnesium polylepis* has long flagella that move in an undulatory fashion and it feeds on small prey captured on the long and slender haptonema that emerges from the cell front. The feeding process involves capture, transport along the haptonema, and delivery of prey to the ingestion site at the opposite end of the cell[8] (Fig. 1c–f). *Prymnesium parvum* feeds on much larger food items, and even performs micropredation on fish using toxins[9,10]. Organisms of this species do not have an apparent use of the haptonema and exhibit a short haptonema and short flagella moving with a ciliary beat.

The flow around an organism produced by its flagellar motion is important for all essential functions[3]. It reveals information about swimming, power consumption, feeding currents, and exposure to flow-sensing predators[11–13]. Idealized viscous flow models can be used to examine the hydrodynamics around a microswimmer[3,14]. Models representing a swimmer just by a few point forces on the fluid are able to describe the flow far from the organism[11,15,16], whereas the flow close to the organism is poorly represented since such models fail to describe the boundary conditions at the cell surface. Examples of models suited for the description of near cell flows are the squirmer model used for ciliates[17,18] and the Oseen model used for copepods and uniflagellates[12,19–21]. The effect of different flagellar arrangements and beat patterns in biflagellates has previously been investigated with

[1]Technical University of Denmark, Department of Physics and Centre for Ocean Life, DK-2800 Kgs. Lyngby, Denmark. [2]Technical University of Denmark, National Institute of Aquatic Resources and Centre for Ocean Life, DK-2920 Charlottenlund, Denmark. Correspondence and requests for materials should be addressed to T.K. (email: tk@aqua.dtu.dk) or A.A. (email: aanders@fysik.dtu.dk).

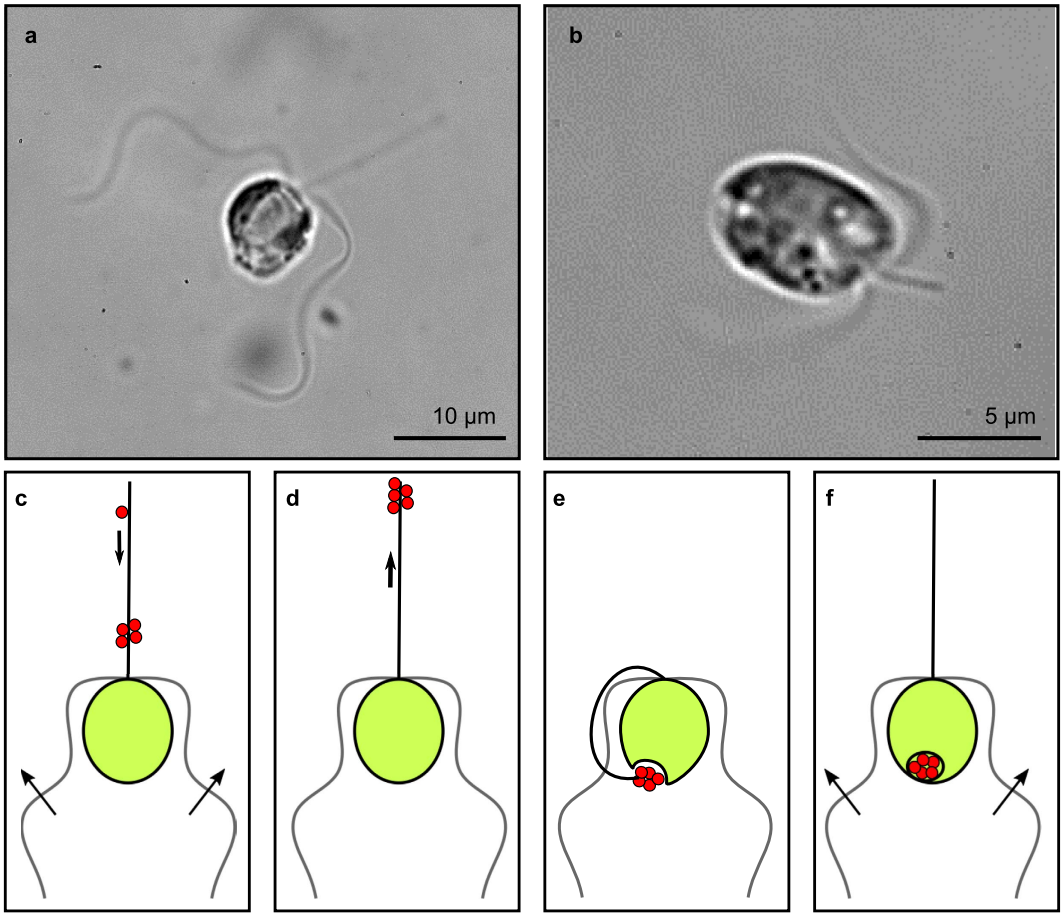

Figure 1. Individuals of the two studied haptophyte species and function of the haptonema. (**a**) *Prymnesium polylepis* and (**b**) *Prymnesium parvum*. (**c**–**f**) Sketch adapted from Kawachi and coworkers[8]. The haptophyte captures prey (red) on its haptonema while swimming and collects them at a specific aggregation point (**c**). While the flagella are paused, the aggregate is actively transported to the tip of the haptonema (**d**), which is bent towards the back of the cell (**e**), where the particles are engulfed (**f**). The purpose and means of the movement of prey towards the aggregation point are unknown.

focus on swimming and nutrient uptake[22], swimming and flagellar synchronization[23,24], and quiet swimming[13]. Hydrodynamic interactions between cell and flagellum play an important role for propulsion, and therefore provide one reason for models to take into account the no-slip boundary condition at the cell surface[25].

Here, we investigate how different flagellar arrangements and beat patterns in biflagellates affect swimming speed, flow disturbance, and prey capture. We examine how far each of these essential functions is optimized in mixotrophs. The flow fields of the two characteristically different haptophyte species are visualized using micro particle image velocimetry (Methods). To explore the influence of the flagellar arrangement, we build on the Oseen model and develop an analytical biflagellate model consisting of two point forces in the vicinity of a spherical body with no-slip boundary. The model captures the essential features of the observed flow. With the model we quantify the time-varying and the time-averaged near cell flows around the two species and we find optima for swimming, predator avoidance, and prey capture.

Results

Flagellar arrangements, beat patterns, and flow fields. The two species show characteristic differences in their flagellar arrangements and beat patterns and in the resulting flow fields. *Prymnesium polylepis* has long flagella that beat in an undulatory mode with travelling waves that move down the flagella (Fig. 2a–d, Table 1, Supplementary Video S3). The phase shift between the two flagella does not show a clear pattern and varies across individuals and over time. The swimming speed is constant. Behind the organism, large, mainly transversal time-varying flows are formed around the beating flagella. The time-dependent flow is qualitatively different for *P. parvum*, that has short flagella and swims with an unsteady ciliary beat pattern leading to large variation in swimming velocity during the beat cycle (Fig. 2e–h, Table 1, Supplementary Video S4). In each beat phase one can note symmetrically arranged patches with high flow speeds, the flow directions and positions of which follow roughly the dynamics of the flagella end segments. *Prymnesium parvum*, as observed, mainly swims with a synchronous beat, which is interrupted by periods of asynchronous "tumbling" motion. The beat pattern, flow fields, and swimming velocity variation during the beat cycle of *P. parvum* resemble roughly those of

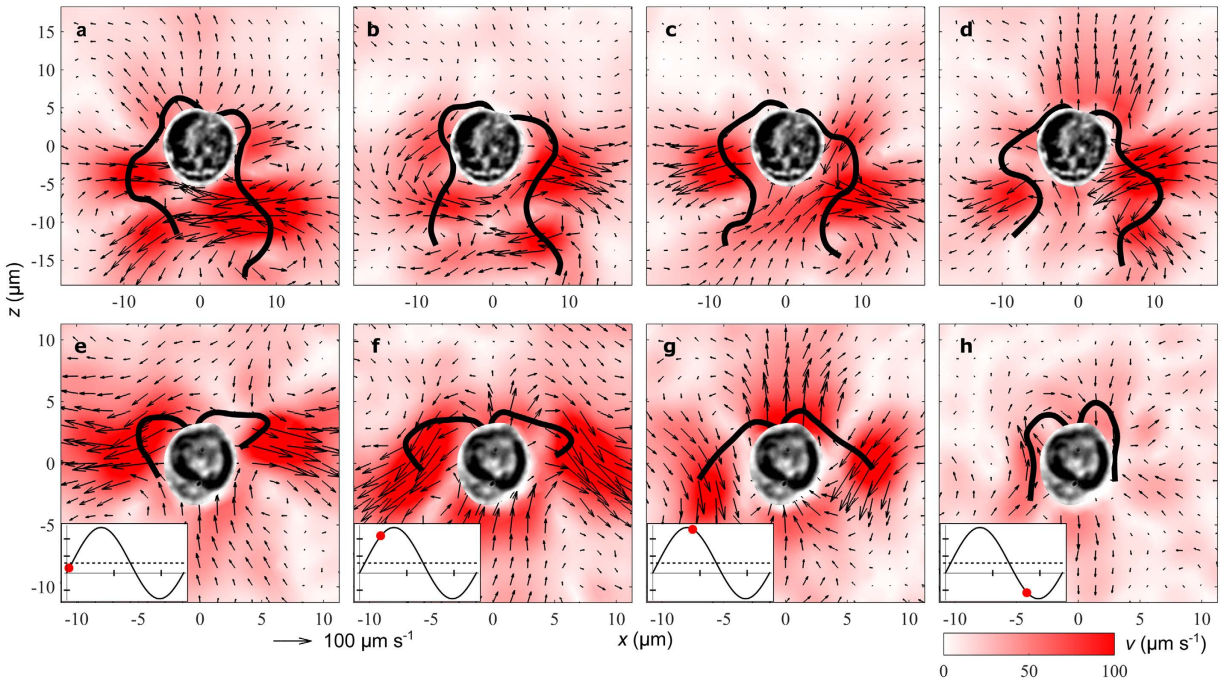

Figure 2. Instantaneous velocity fields measured around freely swimming individuals of the two haptophyte species during their beat cycles. (**a**–**d**) Velocity fields for *Prymnesium polylepis*, averaged over four beat cycles and (**e**–**h**) velocity fields for *Prymnesium parvum*, averaged over three beat cycles. Insets show measured cell velocity (ticks: 50 μm s^{-1}) as function of time (ticks: 10 ms). Instantaneous cell velocity (solid line, black) with beat cycle phase (filled circles, red) and average cell velocity (dashed line, black).

	P. polylepis	P. parvum
Cell length (μm)	9.1 ± 0.8	7.2 ± 0.3
Cell width (μm)	6.8 ± 0.4	5.4 ± 0.5
ESD of cell 2a (μm)	9	6
Haptonema length l_h (μm)	13.5 ± 1.3	3.4 ± 0.6
Length of flagella (μm)	28	10
Beat period of flagella (ms)	30	25
Average swimming speed U (μm s^{-1})	45	30
Average point force magnitude F (pN)	3	1
Radial force position R (μm)	14(=3a)	8(=3a)
Angular force position θ (deg)	−45	0

Table 1. Morphology, flagellar dynamics, and swimming speed of *Prymnesium polylepis* and *Prymnesium parvum*. The values for cell length, cell width, and haptonema length are averages based on five individuals (mean ± SD), and the values for equivalent spherical diameter of the cell (ESD), length and beat period of the flagella, swimming speed, point force magnitude and position are based on two closely studied individuals. The time-averaged force positions were roughly estimated by visual comparison of the time-averaged flow fields from experiment and model, and the point force magnitudes were calculated using equation (3) with the estimated time-averaged force positions and the measured time-averaged swimming velocities.

C. reinhardtii[15,22,26]. However, the beat pattern differs in the characteristic backwards bending of the flagella during the power stroke (Fig. 2e,f).

To explore the effect of the flagellar arrangements and beat patterns we developed a model for freely swimming biflagellates. The cell body, modelled as a no-slip sphere, is propelled by two left-right symmetrically arranged point forces acting on the water (Fig. 3). The model is based on Oseen's solution of the Stokes equation for the flow due to a single point force next to a stationary sphere[27,28]. We neglect the friction on the two flagella compared to the friction on the cell. One can think of the cell and the two point forces as being connected by a thin, rigid, and frictionless scaffold[23,24]. To obtain the flow around the freely swimming model biflagellate we use the linearity of the Stokes equation when superposing the flow due to each of the point forces and the flow due to the sphere towed with the translational velocity calculated from the force balance[19]. The forces on the model flagellate are the

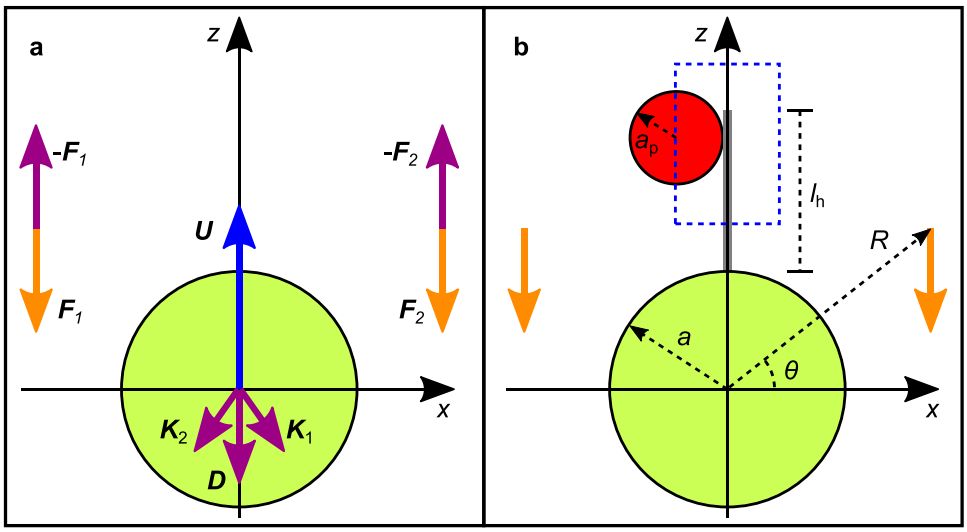

Figure 3. Biflagellate model and capture zone. (**a**) Model with a no-slip sphere (green) and two point forces (orange) representing the cell and the two flagella, respectively. The flagellate swims in the z-direction. The forces on the organism are shown as vectors in purple, i.e., the thrust forces $-\mathbf{F}_1$ and $-\mathbf{F}_2$, the forces $\mathbf{K}_1$ and $\mathbf{K}_2$ due to the flow produced by the point forces, and the Stokes drag $\mathbf{D} = -6\pi\mu a\mathbf{U}$ due to the translational motion of the cell with velocity $\mathbf{U}$ (vector, blue). (**b**) Haptophyte model with capture zone (dashed, blue) around the haptonema (grey) corresponding to a spherical prey (red).

thrust force $-(\mathbf{F}_1 + \mathbf{F}_2)$, the force $\mathbf{K}_1 + \mathbf{K}_2$ due to the flow produced by the two point forces on the water, and the Stokes drag $\mathbf{D} = -6\pi\mu a\mathbf{U}$, where μ is the dynamic viscosity and $\mathbf{U}$ the velocity of the translational motion of the cell[19]. We therefore have the force balance on the flagellate

$$6\pi\mu a\mathbf{U} = -(\mathbf{F}_1 + \mathbf{F}_2) + \mathbf{K}_1 + \mathbf{K}_2, \tag{1}$$

and since the forces $\mathbf{K}_1$ and $\mathbf{K}_2$ are known analytically[28], we can determine the translational velocity of the cell.

The time-averaged flows close to and in front of the cell body are well represented for both haptophyte species by the biflagellate model with backwards directed point forces at characteristic positions, which we roughly estimated by visual comparison of the model flow fields with the measured flow fields around one organism of each species (Fig. 4, Supplementary Fig. S5, and Table 1). The time-resolved flow fields around *P. polylepis* show an extended, time-varying and often asymmetric force distribution along the flagella. This makes the simple biflagellate model for this organism only applicable for the time-averaged flow. To model the time-dependent flow around *P. parvum*, we used the rapidly moving, tracked flagellar ends to model the thrust force positions, since we assume that they contribute significantly to the force production. Also, the flagellar end segments appear to be transversely oriented to the trajectories in the main part of *P. parvum*'s beat cycle, and we therefore applied forces of constant magnitude acting tangentially to the trajectories. We estimated elliptic trajectories with the downwards power stroke further away from the body than the upwards return stroke. The model biflagellate is able to swim due to the difference in the drag on the cell body between the power stroke and the return stroke (Fig. 5). Furthermore the forces in the transverse direction towards and away from the cell contribute more than 20% to the forward drag due to their favourable arrangement below and above the equator. The flow fields of the simple model strongly resemble the measured flow fields of *P. parvum* (Figs 2e–h and 5a–d). We conclude that the variation of the thrust force position during the beat cycle can play a large role for the swimming of biflagellates. Similar findings on the role of thrust force positions were made on *C. reinhardtii* using a numerical singularity model[25] and a three-sphere model[24].

Swimming speed and flow disturbance. Swimming speed as well as flow disturbance depend characteristically on the flagellar arrangement. The swimming speed U can be determined theoretically from the force balance on the flagellate (1). The force $\mathbf{K}_1 + \mathbf{K}_2$ is proportional to the magnitude of the point forces $F = |\mathbf{F}_1| = |\mathbf{F}_2|$, and it depends strongly on the radial force position R and the angular force position θ (Fig. 3) [28, p. 88, eq. (3.3.26)]. In the biflagellate model with thrust forces in the positive z-direction the force expression simplifies to

$$\mathbf{K}_1 + \mathbf{K}_2 = -\left[\frac{3(1 + \sin^2\theta)}{2R/a} + \frac{1 - 3\sin^2\theta}{2(R/a)^3}\right]F\mathbf{e}_z. \tag{2}$$

We therefore analytically obtain the swimming speed as

$$U = \left[1 - \frac{3(1 + \sin^2\theta)}{4R/a} - \frac{1 - 3\sin^2\theta}{4(R/a)^3}\right]\frac{F}{3\pi\mu a}, \tag{3}$$

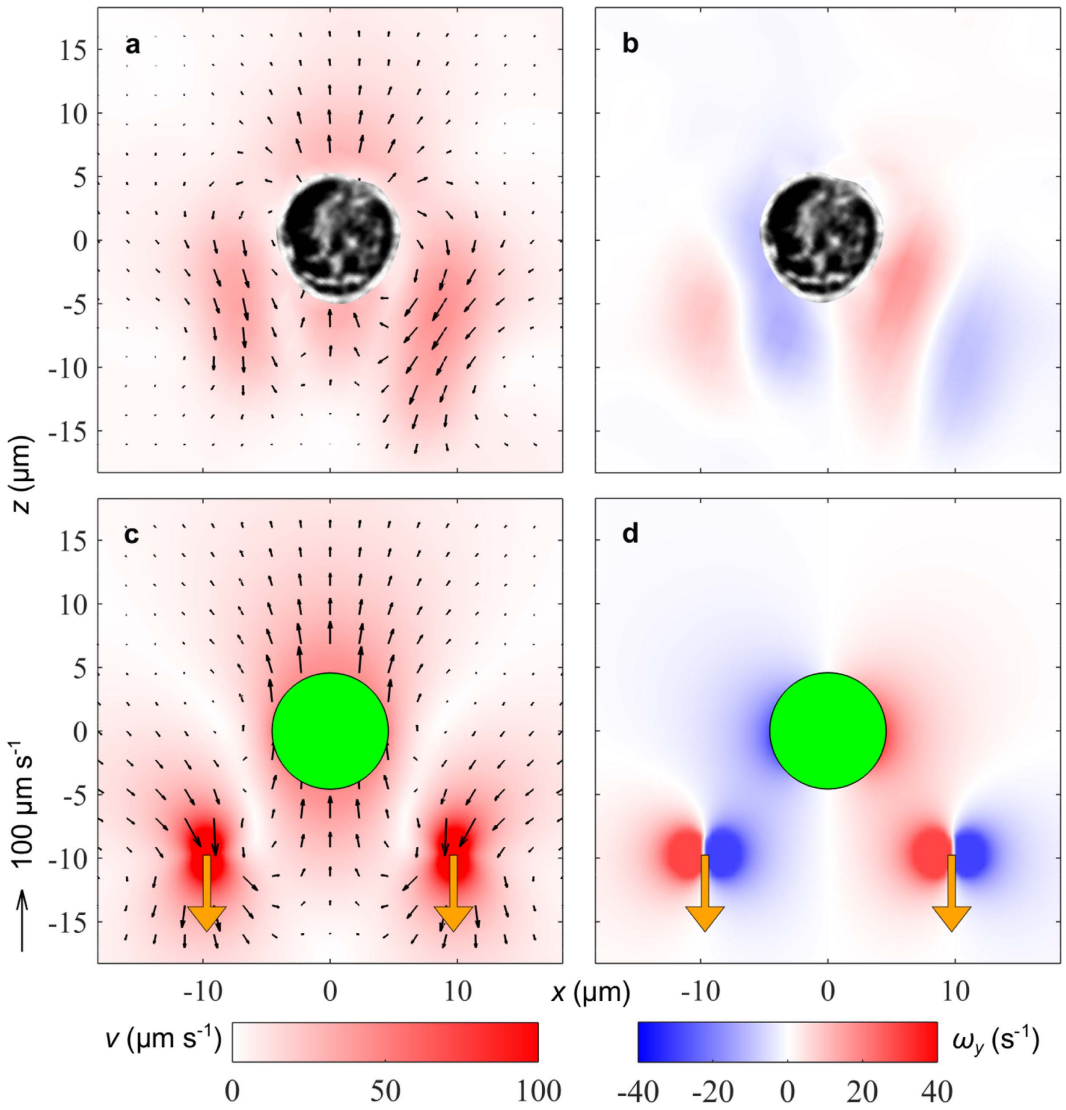

Figure 4. Measurements and biflagellate model results for the average velocity field and vorticity field for *Prymnesium polylepis*. (**a**,**b**) Measured velocity and vorticity, respectively, averaged over all frames in four beat cycles. (**c**,**d**) Modelled velocity and vorticity, respectively. The orange vectors show the location and the direction of the point forces on the water. The colour maps show the velocity magnitude v (**a**,**c**) and the vorticity component ω_y (**b**,**d**), i.e., counter-clockwise rotation in blue and clockwise rotation in red.

where the highest swimming speed $U_\infty = F/(3\pi\mu a)$ for constant thrust force magnitude is obtained when the thrust forces are placed far from the cell body and the model reduces to the flow due to a towed sphere. By arranging the thrust forces equatorially the swimming speed reaches a maximum for constant thrust force magnitude and distance. The speed for this arrangement is significantly higher than for the corresponding puller or pusher when the thrust forces are close to the cell body (Fig. 6a). An optimal equatorial flagellar arrangement is found for *P. parvum* in time-average, whereas *P. polylepis* with its estimated angular force position appears to have a flagellar arrangement that is not optimized for fast propulsion.

To reduce the risk of detection by flow-sensing predators the haptophytes should make their disturbance zones as small as possible[11]. How does the size of the disturbance zone vary with force positions for a fixed swimming speed? It has been shown that for detection of prey by a larger predator absolute flow velocities matter as opposed to spatial and temporal derivatives, which in prey can trigger escape from predators[29]. The mean threshold speed was found to be 40–50 μm s^{-1} for prey detection by the ciliate *Mesodinium pulex*, which feeds on similar-sized prey as haptophytes[30], and the threshold value 40 μm s^{-1} has been measured for the copepod *Oithona similis*[29]. Thus we shall use 40 μm s^{-1} as a reasonable threshold speed estimate for the detection of haptophytes. We define the disturbance zone as the volume inside which the flow speed exceeds 40 μm s^{-1}. The maximum disturbance area in the xz-plane during the beat cycle for *P. polylepis* and *P. parvum* is found to be 443 μm^2 and 186 μm^2, respectively. In good agreement the time-dependent model of *P. parvum* gives an area of 158 μm^2 (Fig. 5). From the model we calculate the disturbance distance as the equivalent spherical radius r of the disturbance zone for differently positioned power strokes with backwards pointing forces (Fig. 6b). The swimming speed is fixed to the

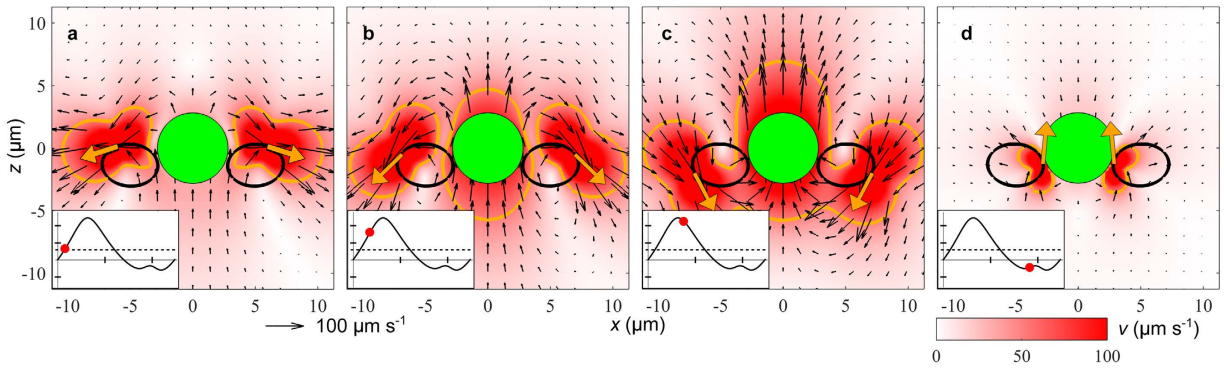

Figure 5. Time sequence of instantaneous velocity fields for the biflagellate model of *Prymnesium parvum*. The left-right symmetrically arranged point forces on the water (vectors, orange) move on elliptic trajectories (solid line, black) following the measured end points of the flagella. Insets show cell velocity (ticks: 50 μm s^{-1}) as function of time (ticks: 10 ms). Instantaneous cell velocity (solid line, black) with beat cycle phase (filled circles, red) and average cell velocity (dashed line, black). The area inside the contour (solid line, orange) is the cross-section in the *xz*-plane of the disturbance zone in which the flow speed exceeds the threshold speed 40 μm s^{-1}.

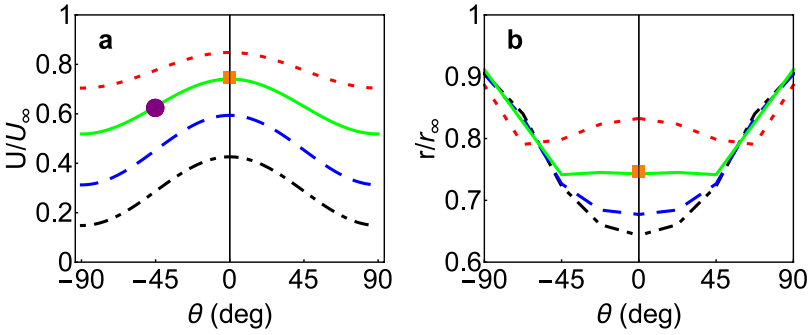

Figure 6. Normalized swimming speed and flow disturbance distance for different flagellar arrangements. Angular force position θ and radial force position: $R = 1.5a$ (dotted-dashed lines, black), $R = 2a$ (dashed lines, blue), $R = 3a$ (solid lines, green), and $R = 5a$ (dotted lines, red). (**a**) Modelled swimming speed (lines) and estimated time-averaged values for *Prymnesium polylepis* (filled circle, purple) and *Prymnesium parvum* (filled square, orange). A maximum of the swimming speed is found for equatorially placed, far-away forces ($\theta = 0$ deg, *R* large). (**b**) The disturbance distance modelled for the maximum thrust force magnitude of *P. parvum* (lines) and the estimated value for the power stroke of *P. parvum* (filled square, orange). Maximum disturbance is found for force arrangements at the poles ($\theta = \pm 90$ deg) and for $R < 3a$ the smallest disturbance distance is found for equatorial arrangements ($\theta = 0$ deg).

maximum speed during the beat cycle of *P. parvum* and the disturbance distance r_∞ for forces far from the cell body is used as reference. The disturbance distance for small force distances, i.e., for $R < 3a$, is found to be lowest for equatorial arrangements. For larger force distances, however, minimum detection risk occurs at angular force positions between the equator and the poles. The equatorial thrust force arrangement of *P. parvum* minimizes the disturbance zone with the intermediate force distance providing a trade-off between fast and quiet swimming.

Prey capture on haptonema and cell. Haptophytes with a long haptonema such as *P. polylepis* use the haptonema for prey capture (Fig. 1c–f). How does the flagellar arrangement support this feeding and is it sufficient to fulfil the energy needs of the organism? The clearance rate is defined as the volume of ambient water cleared for prey per unit time[31]. The maximum clearance rate of eukaryotes that solely live from prey capture (heterotrophy) is found to be of the order of one million cell volumes per day[32,33]. Furthermore typical cell division rates of one per day suggest that at typical concentrations of available prey the empirically found maximum clearance rate is in fact needed in order to survive heterotrophically in the ocean[34]. This applies generally to marine heterotrophic microorganisms, and thus also to haptophytes if they are to survive on heterotrophy alone. Thus we here define the guideline daily amount (GDA) for heterotrophs as one million cell volumes per day. The presence of the haptonema is neglected in the model flow calculations, since an analytical estimate of the flow around the haptonema suggests, that it influences the flow only close to its surface (Methods). The advective clearance rate for capture treats the prey as passive tracers following the ambient flow. In the model it is estimated as the volume flow rate into a cylindrical capture zone with radius equal to the prey radius around the haptonema and into a spherical capture zone with radius equal to the cell radius plus the prey radius surrounding the cell (Fig. 3b). For the calculation, the prey particles are treated as spherical particles with radius $a_p = 1$ μm attaching

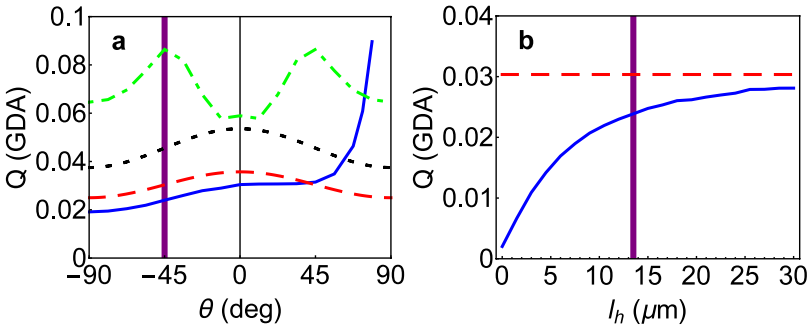

Figure 7. Advective clearance rate on haptonema and cell of *Prymnesium polylepis*. (**a**) The clearance rate on the haptonema (solid line, blue) and cell (dotted-dashed line, green) as function of the angular force position with approximations $Q = \pi a_p^2 U$ from ballistic encounter on the haptonema (dashed line, red) and $Q = (3/2)\pi a_p^2 U$ from capture on a towed sphere (dotted line, black), respectively. The clearance rate on the haptonema is largest for puller arrangements ($\theta = 90$ deg) and on the cell it is maximal for flagellar forces arranged at $\theta = \pm 45$ deg. (**b**) The clearance rate on the haptonema (solid line, blue) as function of haptonema length with ballistic approximation (dashed line, red). Observed force position (a) and haptonema length of (b) *P. polylepis* are indicated (vertical lines, purple). The guideline daily amount (GDA) is defined as one million cell volumes per day.

Encounter model	Example prey	ESD (μm)	u (μm s^{-1})	τ (s)	λ (μm)	Q (*GDA*)
Advective (non-motile prey)	Spherical tracers	2	0	/	0	0.024
Brownian diffusive (non-motile prey)	Spherical tracers	2	0	/	0	0.002
Ballistic (motile prey)	*Microscilla furvescens* (M58792)	1.7	32	1.4	46	0.132
Effective diffusive (motile prey)	Marine bacterium TW-3 (AY028198)	1.2	44	0.04	2	0.151

Table 2. Advective, ballistic, and diffusive clearance rate estimates for non-motile and motile prey of *Prymnesium polylepis*. Equivalent spherical diameter (ESD), swimming speed u, run time τ, and run length λ of the prey[37]. The clearance rate Q on the haptonema in units of the guideline daily amount (GDA), defined as one million cell volumes per day.

with 100% efficiency to the haptonema or cell upon touch. Our choice of prey size is based on the observations on prey selectivity of the related species *Haptolina hirta*, for which prey in the range 0.3–4.1 μm in diameter were ingested with a favoured prey of length 2.5 μm[8]. The thrust force is held constant at the value for the average flow of *P. polylepis* (Fig. 4).

For pusher arrangements the clearance rate on the haptonema follows the estimate of ballistic encounter of passive prey on the moving haptonema, which is calculated as the projected area of the encounter zone on the swimming direction times the swimming speed, i.e., $Q = \pi a_p^2 U$. Thus the advective clearance rate on the haptonema has a local maximum at an equatorial force position due to the maximum in swimming speed (Figs 6a and 7a). For puller arrangements the velocity of the feeding current towards the haptonema exceeds the swimming speed and leads to a high increase of the clearance rate, suggesting an optimum arrangement with forces acting right next to the haptonema. On the other hand, the calculated clearance rate on the cell body does not distinguish between puller and pusher arrangements and has maxima for forces positioned at $\theta = \pm 45$ deg. The approximation $Q = (3/2)\pi a_p^2 U$ for small ($a_p \ll a$) and passive prey is estimated from the creeping flow past a towed sphere as the volume flow rate within a stream-tube that encloses the sphere with the closest distance a_p[31,35,36]. This formula matches only for forces close to the cell equator and does not capture the two maxima. *Prymnesium polylepis* with mean forces positioned approximately 45 deg behind the cell body does not seem to be optimized for advective prey capture on the haptonema, but apparently for capture on the cell body. The cell surface, which is lined with spine scales, has, however, not been confirmed to be able to capture and transport small prey to the ingestion site on the back. The advective clearance rate of *P. polylepis* increases and eventually saturates with increasing haptonema length, and the observed mean haptonema length ensures a clearance rate near the asymptotic value (Fig. 7b and Table 2).

To what extent does the motility of the prey contribute to capture on the haptonema? For the following estimates we focus on encounter purely by random motion without advection. Motile prey such as swimming bacteria are encountered ballistically, if their run length, i.e., the length of their straight trajectory segments, is larger than the size of the capture zone[37]. The ballistic clearance rate for a stationary capture zone of surface area S collecting small randomly moving prey with swimming speed u and uniformly distributed directions can be calculated as $Q = (1/4)Su$ (Methods). This simple formula provides a generalization of the well-known formula, $Q = \pi a^2 u$, for spherical capture zones[38–40]. To calculate the ballistic clearance rate the haptonema surface is calculated as that of a cylinder, i.e., $S = 2\pi a_p(l_h + a_p)$ with the haptonema length l_h and the prey radius a_p. If the run length of the motile prey is smaller than the size of the capture zone, particle capture creates a significant concentration gradient and

encounter is best considered as effective diffusion with the diffusion coefficient $D_{eff} = u^2\tau/3$ depending on u the prey speed and τ the run time[41]. This process is considerably faster than Brownian diffusion of passive particles with $D = k_B T/(6\pi\mu a_p)$, where $k_B T$ is the Boltzmann energy at 16 °C. For both diffusive processes the haptonema is treated as a slender spheroid resulting in the clearance rate $Q = 2\pi D l_h/\ln(l_h/a_p)$ (Table 2)[42]. Our estimates of advective, diffusive, and ballistic clearance rates of *P. polylepis* show that all contributions are considerably lower than the estimated guideline daily amount for heterotrophs. For micrometer-sized prey Brownian diffusion is negligible. Encounters of motile prey, both ballistic and effective diffusive, give the highest estimated clearance rates, however, still ten times lower than the GDA (Table 2).

Discussion

We have shown that our analytical model can be used to represent near cell flows around freely swimming biflagellates with different flagellar arrangements. With the model we identified trade-offs between equatorial flagellar arrangements that favour fast and quiet swimming as opposed to puller arrangements that favour feeding. The optimal force distance is far away to swim fast and close to the cell body in order to create the least flow disturbance. The clearance rate estimates for the example of *P. polylepis* result in values which are too low to ensure survival in the pelagic realm, and we therefore argue that photosynthesis and nutrient uptake are likely to be essential for the survival of this species and potentially other mixotrophic biflagellates.

The time-averaged thrust force magnitudes per unit flagellum length in the two biflagellates were found to be approximately equal (Table 1). *Prymnesium parvum* was shown to have a favourable equatorial beat pattern and intermediate force distances that appear to make a compromise between fast and quiet swimming. *Prymnesium polylepis*, in contrast, was, based on its time-averaged force arrangement, not found to be particularly optimal, neither for swimming nor for advective feeding even though this species is dependent on encountering small prey. The low advective contribution to prey capture is one possible reason why the flagellar arrangement in *P. polylepis* is not defined by the optimum for steady advective feeding. Furthermore, the flagella and the highly time-varying flows around them could hinder prey capture, if the flagella were in a puller arrangement positioned close to the haptonema.

Another aspect of prey capture in *P. polylepis* is the design of the haptonema that is optimized as a long slender structure favourable for prey encounter, but with physical limitations given by the cost of production, stability, flow resistance, and the ability to reach the ingestion site at the back end of the cell. The created feeding flow does not only support the motion of prey towards but also along the haptonema towards the aggregation point close to the cell body (Fig. 1c). The Stokes drag on particles of 1 μm radius moving with the local flow velocity decreases to around 0.4 pN at the distance of 5 μm from the cell body, reported as the typical location of the aggregation point[8]. The transport of captured prey along the haptonema towards the aggregation point can therefore be purely due to the flow created by the flagellar beat if the friction on the haptonema is not larger than this drag. We speculate that the positioning of the prey at the aggregation point allows the haptophyte to hold on to the prey with the least effort without blocking the capture of additional prey.

Some of the above predictions can readily be applied to other biflagellates. For example the 2–3 times speed difference between the two swimming modes of *C. reinhardtii* could, according to our model analysis, be due to the difference in angular force arrangements between the ciliary puller beat and the undulatory pusher beat[22]. Furthermore the time-varying biflagellate model with moving point forces implies that an approximately four times larger force is needed to propel the unsteady swimmer *P. parvum*, than the time-averaged model suggests. A similar numerical factor has earlier been found by comparison of power dissipation in time-resolved and time-averaged flows around *C. reinhardtii*[26]. As an outlook the model can be generalized to fit other microswimmers with different numbers and arrangements of appendages, further taking into account body rotation using the torque balance. It will in particular be relevant to examine how purely heterotrophic flagellates acquire sufficient nutrition[12].

Methods

Cultures and observations. Cultures were grown in B1-medium (non-axenic) with a salinity of 32 at 20 °C. They were subjected to 100 μmol photons $m^{-2} s^{-1}$ on a 12:12 h light:dark cycle. Observations of swimming haptophyte cells were made using an Olympus IX71 inverted microscope equipped with a 100 × DIC objective, and in some cases an additional 2 × magnifying lens. Recordings were made using a Phantom V210 high-speed (1000 fps for *P. polylepis*, 500 fps for *P. parvum*), high-resolution (1280 × 800 pixels) digital video camera. Fields of view were 0.26 mm × 0.16 mm for *P. polylepis* and 0.13 mm × 0.08 mm for *P. parvum*. The organisms swam in 10 mm × 10 mm × 0.5 mm chambers mounted on a microscope slide with silicone grease. The microscope was focused at the full working distance of the lens (150 μm) from the cover glass to limit wall effects. Observations were made in an air-conditioned room set to 16 °C.

Flow measurements. Flow fields were measured with micro particle image velocimetry. The medium was seeded with neutrally buoyant, polymer spheres with diameter $d = 300$ nm. The focal depth of the objective of approximately 1 μm defined the thickness of the observation plane. Organisms were masked using ImageJ 1.46r prior to analysis. We used a multi-pass algorithm in DaVis PIV software 8.0.6 (Lavision GmbH, Göttingen, Germany) with decreasing size of the interrogation windows, with a final window size of 32 × 32 pixels with 75% overlap. There were on average $N_p = 16$ and $N_p = 4$ particles in each interrogation window for *P. polylepis* and *P. parvum*, respectively. The flow speed resolution limit due to Brownian motion of seeding particles was estimated as $v_B = 2\sqrt{D/(N_p N_f \Delta t)}$ with $D = k_B T/(3\pi\mu d)$, the time resolution Δt, and N_f the number of averaged frames[43]. For the time-resolved flow fields we calculated $v_B = 8.8$ μm s^{-1} for *P. polylepis* with $N_f = 4$ and $v_B = 14.4$ μm s^{-1} for *P. parvum* with $N_f = 3$.

Flow profile around the haptonema. To estimate the effect of the haptonema on the flow in front of the cell body of *P. polylepis* we calculated the Stokes flow past a prolate no-slip spheroid with the constant far field flow velocity U in the length direction [44, p. 154f.]. With the half-major axis 6.75 μm and half-minor axis 0.1 μm we found that the flow velocity is decreased by one half on a spheroidal stream surface around the haptonema with a distance 0.17 μm from the tip and 1.41 μm from the middle of the haptonema.

Calculation of ballistic clearance rates. We derived a simple formula that allows immediate calculation of the clearance rate as $Q = (1/4)Su$ for any stationary capture zone with surface area S when the prey are uniformly distributed point particles ballistically moving with speed u with equal probability in all directions [39, p. 179, eq. (5–32)]. We obtained this result by calculating the clearance rate per unit surface area as $q = u/(4\pi) \int_0^{2\pi} \mathrm{d}\phi \int_0^{\pi/2} \mathrm{d}\theta \cos\theta \sin\theta = (1/4)u$ and multiplying by the total surface area, i.e., $Q = Sq$.

References

1. Burkholder, J. M., Glibert, P. M. & Skelton, H. M. Mixotrophy, a major mode of nutrition for harmful algal species in eutrophic waters. *Harmful Algae* **8,** 77–93 (2008).
2. Andersen, K. H. *et al.* Characteristic sizes of life in the oceans, from bacteria to whales. *Ann. Rev. Mar. Sci.* **8,** 217–241 (2016).
3. Lighthill, J. Flagellar hydrodynamics. *SIAM Rev.* **18,** 161–230 (1976).
4. Sleigh, M. A. Flagellar beat patterns and their possible evolution. *BioSystems* **14,** 423–431 (1981).
5. Inouye, I. & Hori, T. High-speed video analysis of the flagellar beat and swimming patterns of algae: possible evolutionary trends in green algae. *Protoplasma* **164,** 54–69 (1991).
6. Harris, E. H., Stern, D. B. & Witman, G. *The Chlamydomonas Sourcebook* vol. 1 (Cambridge University Press, 2009).
7. Klindt, G. S. & Friedrich, B. M. Flagellar swimmers oscillate between pusher- and puller-type swimming. *Phys. Rev. E* **92,** 063019 (2015).
8. Kawachi, M., Inouye, I., Maeda, O. & Chihara, M. The haptonema as a food-capturing device: observations on *Chrysochromulina hirta* (prymnesiophyceae). *Phycologia* **30,** 563–573 (1991).
9. Tillmann, U. Kill and eat your predator: a winning strategy of the planktonic flagellate *Prymnesium parvum*. *Aquat. Microb. Ecol.* **32,** 73–84 (2003).
10. Fistarol, G. O., Legrand, C. & Granéli, E. Allelopathic effect of *Prymnesium parvum* on a natural plankton community. *Mar. Ecol. - Prog. Ser.* **255,** 115–125 (2003).
11. Kiørboe, T., Jiang, H., Goncalves, R. J., Nielsen, L. T. & Wadhwa, N. Flow disturbances generated by feeding and swimming zooplankton. *P. Natl. Acad. Sci. USA* **111,** 11738–11743 (2014).
12. Langlois, V. J., Andersen, A., Bohr, T., Visser, A. W. & Kiørboe, T. Significance of swimming and feeding currents for nutrient uptake in osmotrophic and interception-feeding flagellates. *Aquat. Microb. Ecol.* **54,** 35–44 (2009).
13. Andersen, A., Wadhwa, N. & Kiørboe, T. Quiet swimming at low Reynolds number. *Phys. Rev. E* **91,** 042712 (2015).
14. Lauga, E. & Powers, T. R. The hydrodynamics of swimming microorganisms. *Rep. Prog. Phys.* **72,** 096601 (2009).
15. Drescher, K., Goldstein, R. E., Michel, N., Polin, M. & Tuval, I. Direct measurement of the flow field around swimming microorganisms. *Phys. Rev. Lett.* **105,** 168101 (2010).
16. Drescher, K., Dunkel, J., Cisneros, L. H., Ganguly, S. & Goldstein, R. E. Fluid dynamics and noise in bacterial cell-cell and cell-surface scattering. *P. Natl. Acad. Sci. USA* **108,** 10940–10945 (2011).
17. Lighthill, M. J. On the squirming motion of nearly spherical deformable bodies through liquids at very small Reynolds numbers. *Commun. Pur. Appl. Math.* **5,** 109–118 (1952).
18. Blake, J. R. A spherical envelope approach to ciliary propulsion. *J. Fluid Mech.* **46,** 199–208 (1971).
19. Jiang, H., Osborn, T. R. & Meneveau, C. The flow field around a freely swimming copepod in steady motion. Part I: Theoretical analysis. *J. Plankton Res.* **24,** 167–189 (2002).
20. Higdon, J. J. L. A hydrodynamic analysis of flagellar propulsion. *J. Fluid Mech.* **90,** 685–711 (1979).
21. Higdon, J. J. L. The generation of feeding currents by flagellar motion. *J. Fluid Mech.* **94,** 305–330 (1979).
22. Tam, D. & Hosoi, A. E. Optimal feeding and swimming gaits of biflagellated organisms. *P. Natl. Acad. Sci. USA* **108,** 1001–1006 (2011).
23. Friedrich, B. M. & Jülicher, F. Flagellar synchronization independent of hydrodynamic interactions. *Phys. Rev. Lett.* **109,** 138102 (2012).
24. Polotzek, K. & Friedrich, B. M. A three-sphere swimmer for flagellar synchronization. *New J. Phys.* **15,** 045005 (2013).
25. Kurtuldu, H., Tam, D., Hosoi, A., Johnson, K. A. & Gollub, J. Flagellar waveform dynamics of freely swimming algal cells. *Phys. Rev. E* **88,** 013015 (2013).
26. Guasto, J. S., Johnson, K. A. & Gollub, J. P. Oscillatory flows induced by microorganisms swimming in two dimensions. *Phys. Rev. Lett.* **105,** 168102 (2010).
27. Oseen, C. W. *Neuere Methoden und Ergebnisse in der Hydrodynamik* (Akademische Verlagsgesellschaft Leipzig, 1927).
28. Pozrikidis, C. *Boundary Integral and Singularity Methods for Linearized Viscous Flow* (Cambridge University Press, 1992).
29. Kiørboe, T. & Visser, A. W. Predator and prey perception in copepods due to hydromechanical signals. *Mar. Ecol. - Prog. Ser.* **179,** 81–95 (1999).
30. Jakobsen, H. H., Everett, L. M. & Strom, S. L. Hydromechanical signaling between the ciliate *Mesodinium pulex* and motile protist prey. *Aquat. Microb. Ecol.* **44,** 197–206 (2006).
31. Kiørboe, T. *A mechanistic approach to plankton ecology* (Princeton University Press, 2008).
32. Hansen, P., Bjørnsen, P. & Hansen, B. Zooplankton grazing and growth: Scaling within the 2-2,000-μm body size range. *Limnol. Oceanogr.* **42,** 687–704 (1997).
33. Kiørboe, T. & Hirst, A. Shifts in mass scaling of respiration, feeding, and growth rates across life-form transitions in marine pelagic organisms. *Am. Nat.* **183,** E118–E130 (2014).
34. Kiørboe, T. How zooplankton feed: mechanisms, traits and trade-offs. *Biol. Rev.* **86,** 311–339 (2011).
35. Spielman, L. A. Particle capture from low-speed laminar flows. *Ann. Rev. Fluid Mech.* **9,** 297–319 (1977).
36. Kiørboe, T. & Titelman, J. Feeding, prey selection and prey encounter mechanisms in the heterotrophic dinoflagellate noctiluca scintillans. *J. Plankton Res.* **20,** 1615–1636 (1998).
37. Visser, A. W. & Kiørboe, T. Plankton motility patterns and encounter rates. *Oecologia* **148,** 538–546 (2006).
38. Dusenbery, D. B. *Living at Microscale* (Harvard University Press, 2009).
39. Kauzmann, W. *Kinetic Theory of Gases* (W. A. Benjamin, 1966).
40. Gerritsen, J. & Strickler, J. R. Encounter probabilities and community structure in zooplankton: a mathematical model. *J. Fish. Res. Board Can.* **34,** 73–82 (1977).
41. Lovely, P. S. & Dahlquist, F. W. Statistical measures of bacterial motility and chemotaxis. *J. Theor. Biol.* **50,** 477–496 (1975).
42. Berg, H. C. *Random Walks in Biology* (Princeton University Press, 1993).

43. Raffel, M., Willert, C. E., Wereley, S. T. & Kompenhans, J. *Particle Image Velocimetry* 2nd edn. (Springer Verlag, 2007).
44. Happel, J. & Brenner, H. *Low Reynolds number hydrodynamics: with special applications to particulate media* (Martinus Nijhoff Publishers, 1983).

Acknowledgements
We are thankful to Tomas Bohr for many stimulating discussions. The Centre for Ocean Life is a VKR Centre of Excellence supported by the Villum Foundation.

Author Contributions
J.D., L.T.N., T.K. and A.A. designed research; L.T.N. performed experiments; J.D. and L.T.N. analysed data; J.D. and A.A. developed and applied theory; and J.D. and A.A. wrote the paper. All authors commented on the paper.

Additional Information
Supplementary information accompanies this paper at http://www.nature.com/srep

Competing financial interests: The authors declare no competing financial interests.

How to cite this article: Dölger, J. *et al.* Swimming and feeding of mixotrophic biflagellates. *Sci. Rep.* **7**, 39892; doi: 10.1038/srep39892 (2017).

Publisher's note: Springer Nature remains neutral with regard to jurisdictional claims in published maps and institutional affiliations.

5.3 Hydrodynamics of microbial filter feeding

Paper published in Proceedings of the National Academy of Sciences (2017).

Hydrodynamics of microbial filter feeding

Lasse Tor Nielsen[a,1], Seyed Saeed Asadzadeh[b], Julia Dölger[c], Jens H. Walther[b,d], Thomas Kiørboe[a], and Anders Andersen[c]

[a]National Institute of Aquatic Resources and Centre for Ocean Life, Technical University of Denmark, DK-2800 Kongens Lyngby, Denmark; [b]Department of Mechanical Engineering, Technical University of Denmark, DK-2800 Kongens Lyngby, Denmark; [c]Department of Physics and Centre for Ocean Life, Technical University of Denmark, DK-2800 Kongens Lyngby, Denmark; and [d]Swiss Federal Institute of Technology Zürich, Chair of Computational Science, ETH Zentrum, CH-8092 Zürich, Switzerland

Edited by M. A. R. Koehl, University of California, Berkeley, CA, and approved July 10, 2017 (received for review June 7, 2017)

Microbial filter feeders are an important group of grazers, significant to the microbial loop, aquatic food webs, and biogeochemical cycling. Our understanding of microbial filter feeding is poor, and, importantly, it is unknown what force microbial filter feeders must generate to process adequate amounts of water. Also, the trade-off in the filter spacing remains unexplored, despite its simple formulation: A filter too coarse will allow suitably sized prey to pass unintercepted, whereas a filter too fine will cause strong flow resistance. We quantify the feeding flow of the filter-feeding choanoflagellate *Diaphanoeca grandis* using particle tracking, and demonstrate that the current understanding of microbial filter feeding is inconsistent with computational fluid dynamics (CFD) and analytical estimates. Both approaches underestimate observed filtration rates by more than an order of magnitude; the beating flagellum is simply unable to draw enough water through the fine filter. We find similar discrepancies for other choanoflagellate species, highlighting an apparent paradox. Our observations motivate us to suggest a radically different filtration mechanism that requires a flagellar vane (sheet), something notoriously difficult to visualize but sporadically observed in the related choanocytes (sponges). A CFD model with a flagellar vane correctly predicts the filtration rate of *D. grandis*, and using a simple model we can account for the filtration rates of other microbial filter feeders. We finally predict how optimum filter mesh size increases with cell size in microbial filter feeders, a prediction that accords very well with observations. We expect our results to be of significance for small-scale biophysics and trait-based ecological modeling.

protozoans | choanoflagellates | filter feeding | microswimmers | computational fluid dynamics

Heterotrophic microorganisms in the oceans inhabit a dilute environment and they need efficient feeding mechanisms to acquire enough food to sustain growth (1, 2). At the microscale the Reynolds number is low and viscous forces govern hydrodynamical interactions. This implies extensive, long-range flow disturbances around moving particles and microswimmers, impeding cell–cell contact and prey capture (3, 4). However, to encounter enough food, purely heterotrophic plankton that rely solely on prey capture typically need to clear a volume of water for prey corresponding to 1 million times their own body volume per day (4). Thus, heterotrophic microbes face a difficult challenge, and the prevailing viscous forces must strongly influence prey capture and shape the various feeding modes through evolution.

Many unicellular flagellates as well as colonial sponges and metazoans, e.g., tunicates, use filter feeding to catch bacteria-sized prey (1, 5–7). They establish a feeding current, from which prey particles are sieved using filter structures. Such filter feeders benefit from having filters with small mesh size that allow the organisms to capture small prey (5, 8). However, filter spacing involves a trade-off: The finer the mesh size is, the higher the availability of food but the lower the clearance rate due to a dramatic decrease in filter permeability (9). An optimum mesh size must therefore exist. While microbial filter feeding has been studied regarding the pressure drop across the filter and the observed clearance rates (5), clearance rates have never been related to the force production of the flagellum that drives the feeding current. Can a beating flagellum even produce sufficient force to account for the observed clearance rates through such fine filters?

Choanoflagellates are the prime example of unicellular filter feeders (1, 10, 11). They are equipped with a single flagellum that is surrounded by a funnel-shaped collar filter made up of microvilli extending from the cell. Some species are sessile and attach with a stalk to solid surfaces whereas others are freely swimming and have a basket-like structure (lorica) that surrounds cell, flagellum, and filter (Fig. 1). The beating flagellum creates a feeding current that transports bacteria-sized prey to the outside of the collar filter from where the prey are transported to the cell surface and phagocytosed (10, 12–16). Far-field flows created by choanoflagellates have recently been measured and modeled for the sessile choanoflagellate *Salpingoeca rosetta* (14). However, the essential near-cell feeding flow in choanoflagellates is poorly understood and has not been resolved quantitatively in experiments (10, 11).

As a model organism of microbial filter feeders, we focus on the choanoflagellate *Diaphanoeca grandis* that swims freely and carries a lorica (Fig. 1). The lower part of the lorica has large openings, whereas the upper part is covered by a fine web with small pore sizes (13). The collar filter therefore supposedly functions as an internal filter, and prey particles should not circumvent the filter once inside the lorica.

Using *D. grandis*, we here ask: What are the mechanisms of particle capture in choanoflagellates, and what is the optimum filter spacing? We use high-speed videography and particle tracking to quantify the feeding flow. For comparison, we use

Significance

Microbes compose the majority of life in aquatic ecosystems and are crucial to the transfer of energy to higher trophic levels and to global biogeochemical cycles. They have evolved different foraging mechanisms of which our understanding is poor. Here, we demonstrate for filter-feeding choanoflagellates—the closest relatives to multicellular life—how the observed feeding flow is inconsistent with hydrodynamic theory based on the current understanding of the morphology. Instead, we argue for the widespread presence of flagellar vanes and suggest an alternative pumping mechanism. We also demonstrate a trade-off in filter spacing that allows us to predict choanoflagellate prey sizes. These mechanistic insights are important to correctly understand and model microbial heterotrophs in marine food webs.

Author contributions: L.T.N., T.K., and A.A. designed research; L.T.N. performed experiments; L.T.N. and A.A. analyzed data; S.S.A. and J.H.W. conducted CFD simulations; J.D. and A.A. developed and applied theory; and L.T.N., T.K., and A.A. wrote the paper with comments from S.S.A., J.D., and J.H.W.

The authors declare no conflict of interest.

This article is a PNAS Direct Submission.

[1]To whom correspondence should be addressed. Email: ltor@aqua.dtu.dk.

This article contains supporting information online at www.pnas.org/lookup/suppl/doi:10.1073/pnas.1708873114/-/DCSupplemental.

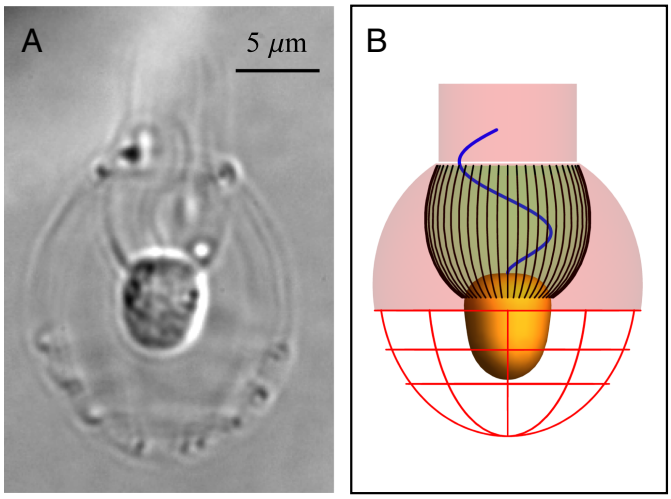

Fig. 1. Morphology of *D. grandis*. (*A*) Microscopic image of freely swimming choanoflagellate. (*B*) Model morphology with cell (orange), collar filter (green surface and black lines), flagellum (blue), and lorica (red). The ribs (costae) in the lower (posterior) part of the lorica are indicated, whereas for clarity the ribs in the finely netted, upper (anterior) part of the lorica are not shown.

computational fluid dynamic (CFD) simulations and simple estimates of the filter resistance and the force production due to the beating flagellum. Our analysis shows that modeling the beating flagellum as a simple, slender structure produces a force that is an order of magnitude too small to account for the observed clearance rate. This demonstrates the strong trade-off in small-scale filter feeding and leads us to suggest an alternative flagellar pumping mechanism.

Results

Observed Feeding Flow and Clearance Rate. We developed a generic model morphology of *D. grandis* to collate particle track observations from individual cells (*Model Morphology and Observed Flow*, Table S1, and Fig. 1). The feeding flow is driven by the beating flagellum. The flow transports particles from the region below the choanoflagellate, in through the large openings in the lower part of the lorica and up toward the collar filter on which the particles are caught (Fig. 2 and Movie S1). The detailed visualization reveals a true filtration flow that undoubtedly passes through the filter, confirming the current understanding of filter feeding in choanoflagellates (11). However, our results are for a loricate species, and it is uncertain whether, and to what extent, nonloricate species can filter the same way, since flow could pass along the filter on the outside and circumvent the filter. From the flow field, one important function of the lorica seems to be the separation of in- and exhalent flow, reducing refiltration. The clearance rate Q can be expressed as the volume flow rate through the filter

$$Q = \int_{A_F} v \, \mathrm{d}A, \qquad [1]$$

where A_F is the surface area of the filter and v is the normal component of the flow velocity. The observed velocity field shows that the water that passes the filter first passes the equator ($z = 0$) in the annular region between the cell and the finely netted part of the lorica. We determine the clearance rate as the volume flow rate upward across the annular region in the equator plane. This procedure is more precise than directly using the flow through the filter. No-slip boundary conditions would suggest reduced flow velocities near the cell and lorica. At the spatial resolution of our experiment, however, the z components of the flow velocities in the annular region do not depend on the distance from the longitudinal axis (Fig. S1*A*). To determine the clearance rate we therefore use the average value $v_z = 7.3 \pm 4.4$ μm·s^{-1} (mean ± SD) times the area of the annular region. We find $Q = (1.22 \pm 0.72) \cdot 10^3$ μm^3·s^{-1}, or 1.20 million cell volumes per day, where the cell volume $V_C = 88$ μm^3. The corresponding flagellar beat frequency is $f = 7.3 \pm 2.6$ Hz (Fig. S1*B*).

Computational Fluid Dynamics and Theoretical Clearance. To explore the feeding flow theoretically we numerically solve the Navier–Stokes equation and the equation of continuity for the incompressible Newtonian flow due to the beating flagellum with the known morphology (*CFD Simulations* and Figs. S2–S5). The collar filter consists of ∼50 evenly distributed microvilli (13), with a fairly uniform filter spacing and permeability along most of their length (Fig. 1). The finely netted upper part of the lorica has pore sizes in the range 0.05−0.5 μm (13), and for simplicity we treat it as an impermeable, rigid surface and neglect the ribs in the lower part of the lorica. *D. grandis* carries a standard eukaryotic flagellum with diameter $b = 0.3$ μm (23), and high-speed videography showed that the flagellum beats, like most other eukaryotic flagella, in a single plane (Movie S2). For computational simplicity we model the flagellum as a thin sheet of width b that is oriented perpendicular to the plane of beating and moving with a simple traveling wave motion in the positive z direction. Based on our validation of the CFD simulations, we estimate that this approach underestimates the flagellar forces by ∼20% (Tables S2 and S3). The time-averaged CFD flow is an order of magnitude weaker than the flow observed experimentally for *D. grandis* (Fig. 2). The model leads to the time-averaged flagellum force in the z-direction $F_{0.3} = 1.1$ pN, the time-averaged power $P_{0.3} = 0.31$ fW, and the clearance rate $Q_{0.3} = 95$ μm^3·s^{-1}, which is ∼13 times lower than the clearance rate based on the observed flow field.

To generalize our CFD results and roughly estimate the clearance rates of other species of choanoflagellates, we model filter resistance and flagellum force. We describe the filter locally as a row of parallel and equidistantly spaced solid cylinders, and we model the flow far from the filter as uniform and perpendicular to the filter plane. For such simple filters we can express the flow speed through the filter

$$v = \kappa \frac{a}{\mu} \Delta p, \qquad [2]$$

where Δp is the pressure drop across the filter, κ the dimensionless permeability of the filter, and μ the dynamic viscosity. The dimensionless permeability κ is a function only of the dimensionless filter spacing l/a. We model κ by combining previous theoretical work on closely and distantly spaced filter structures, respectively (24, 25). The dimensionless permeability κ increases strongly with l/a and contributes to the filter spacing trade-off as discussed above (Fig. S6). For the model morphology we find the average dimensionless permeability $\langle \kappa \rangle = 0.41$. With a flagellum of length L and diameter b we can estimate the flagellum force

$$F_T = C_F \mu L U = 4 C_F \mu L A f, \qquad [3]$$

where C_F is the drag coefficient, $\mu = 1.0 \cdot 10^{-3}$ Pa·s the viscosity, and A the amplitude of the flagellar beat. The average speed of the flagellum is estimated as $U = 4Af$. For simplicity we take C_F to be the drag coefficient of a slender spheroid that is moving sideways, $C_F = 4\pi/(\ln(2L/b) + 1/2)$ (26). The estimate neglects the presence of filter and lorica structures surrounding the flagellum and assumes that all (primarily transversal) drag on the flagellum is converted into longitudinal flow. The corresponding power estimate is $P_T = F_T U = 16 C_F \mu L A^2 f^2$. To estimate the theoretical clearance rate we assume that the pressure drop is $\Delta p = F/A_F$ and we obtain

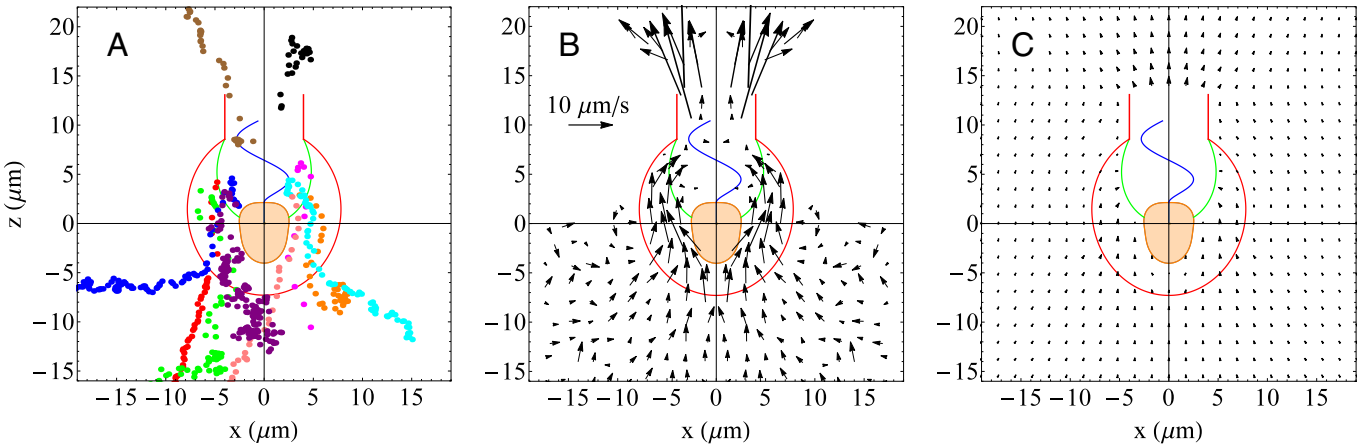

Fig. 2. Observed feeding flow generated by *D. grandis* and velocity field from CFD model based on the standard description of morphology and flagellum. The model morphology shows the cell (orange), the collar filter (green), the flagellum (blue), and the lorica (red). (*A*) Representative particle tracks. The 10 different colors correspond to 10 discrete tracks and the solid circles show particle positions with 0.1-s time intervals. The particles below the choanoflagellate move randomly due to Brownian motion and display a slow net flow toward the lorica openings. (*B*) Average velocity field based on particle tracking. The flow velocities increase dramatically as the particles enter the lorica and approach the collar filter where the particles are eventually caught. The filtered water is expelled in a concentrated jet flow upward and out of the "chimney" of the lorica opposite to and clearly separated from the intake region. (*C*) The CFD velocity field in the *xz* plane is time averaged over the flagellar beat cycle, and the velocity vectors "inside" filter and chimney are omitted for clarity. The CFD model based on the standard description of morphology and flagellum predicts a feeding flow that is more than an order of magnitude weaker than the experimentally observed flow, and it cannot account for the observed clearance rate.

$$Q_T = \langle\kappa\rangle \frac{a}{\mu} F_T = 4\langle\kappa\rangle C_F\, aLAf. \qquad [4]$$

For *D. grandis* the estimate predicts the flagellum force $F_T = 2.5 \pm 0.9$ pN, the power $P_T = 0.20 \pm 0.14$ fW, and the clearance rate $Q_T = 75 \pm 26$ μm^3·s^{-1} in rough agreement with the CFD results.

For other choanoflagellate species we calculate the clearance rate from the analytical estimate (Eq. **4**) and compare it with observations (Table 1). In most species, the theoretical clearance rate grossly underestimates the realized, and only two species seem able to filter significant volumes of water. Of the species listed, only *D. grandis* and *Stephanoeca diplocostata* carry a lorica. The rest are nonloricate and potentially subject to filter circumvention, which we did not account for. Filter circumvention would increase the flow rate, but potentially reduce the clearance rate, since water would not actually be filtered.

Discussion

The Filter-Feeder Paradox. Our results reveal a paradox: The CFD model and the simple estimates underestimate the clearance rate based on the observed flow field by more than an order of magnitude. The flow-field–derived clearance rate seems robust, as it is similar to an earlier observation (13) and at the same time consistent with the general notion that heterotrophic plankton need to daily clear a volume of approximately 1 million times their own body volume (4). Instead, the theory can of course

Table 1. Characteristic morphological and kinematic parameters for selected choanoflagellate and choanocyte species

Species	ESR, μm	*L*, μm	*f*, Hz	*A*, μm	λ, μm	*a*, μm	*l*, μm	*W*, μm	Q_T, μm^3·s^{-1}	Q_V, μm^3·s^{-1}	*Q*, μm^3·s^{-1}	Source
*Codosiga botrytis**	3.75	29.0	30.0	6.4†	17.5	0.088	0.25	10.3†	64	34,600	2,600‡	(17, 18)
*Codosiga gracilis**	1.84	8.3	10.0	1.5§	10.3	0.075	0.54	5.5§	42	850	1,000	(10, 19)
Diaphanoeca grandis¶	2.50	11.0	10.0	4.0	10.0	0.075	0.40	8.0	65	3,200	4,400	(13)
Diaphanoeca grandis¶	2.80	11.7	7.3	2.8	8.6	0.075	0.54	8.0	75	1,410	1,220	This study
*Monosiga brevicollis**	2.00#	13.8#	50.0	2.4	12.2	0.055	0.45	6.6	476	9660	400‡	(20)
*Monosiga ovata**	1.26	6.0	14.4	2.0‖	18.5‖	0.100	0.28	4.4‖	3	2,340	1,800	(21, 22)
*Monosiga sp.**	1.63	5.5	32.5	1.0	6.0	0.100	0.50	2.5	35	490	600	(1)
*Salpingoeca amphoridium**	2.30	20.7	17.0	3.0§	17.9	0.050	0.70	3.8§	716	3,470	600‡	(10)
Stephanoeca diplocostata¶	1.80	8.3	10.0	2.0§	8.6	0.075	0.47	5.4§	40	930	4,400	(10, 19)
*Spongilla lacustris***	2.00‖	10.4	11.0	1.5‖	12.2	0.060	0.18	3.1	2	620	400‡	(20)

ESR, equivalent spherical radius of cell; *L*, flagellum length; *f*, flagellum beat frequency; *A*, amplitude of flagellar beat; λ, flagellar wavelength; *a*, microvillum radius; *l*, distance between centers of neighboring microvilli; *W*, diameter of chimney or anterior filter exhaust opening; Q_T, theoretical estimate of clearance rate based on Eq. **4**; Q_V, clearance rate estimate based on the presence of a vane according to Eq. **5**; and *Q*, observed clearance rate from incubation experiments or similar.

*Sessile.

†Estimated from ref. 18.

‡Data on *Q* were unavailable, and instead *Q* was estimated as 1 million cell volumes per day (4). In species with different morphotypes, data are for single, sessile cells.

§Estimated from ref. 10.

¶Loricate, freely swimming.

#Measured using original videos kindly provided by Mah et al. (20).

‖Estimated from ref. 21.

**Choanocyte.

be questioned, most obviously perhaps through the notion that various types of flagellar hairs often line eukaryotic flagella and could increase the force output of the flagellum (23). However, the force estimate is only weakly influenced by the flagellum diameter (Eq. **3**), as long as we neglect interaction between flagellum and filter, and simple flagellar hairs would have little influence on the clearance rate. It is thus difficult to see how the flagellum would be able to deliver the force required to account for the experimentally observed clearance rate, unless some major aspect of its morphology or function has been overlooked.

Pumping Mechanism Conjecture. A few choanoflagellate species have been shown to have a so-called flagellar vane composed of a sheet-like structure along the length of the flagellum (17, 20, 27). Although a flagellar vane has been observed in a few choanoflagellate species, the structure remains elusive. Leadbeater (27) went so far as to call it a "mystery" because the structure is notoriously difficult to visualize using electron microscopy. While a vane cannot account for the clearance rate due to increased flagellum drag as long as interactions between flagellum and filter are neglected, this structure could still offer a satisfactory solution to the apparent paradox: With a vane, the distance between flagellum and the inside of the collar would be reduced, reducing transversal flow past the beating flagellum inside the collar. Instead, more fluid would be forced upward, and the resulting low pressure would have to be equalized by a flux through the filter. With a flagellar vane nearly as wide as the collar, or even physically attached to the inside of the collar, the pumping mechanism would be radically different. The highly similar choanocytes of aquatic sponges have been shown to have flagellar vanes that indeed are attached to the filter or span its width (20, 28, 29). The flagellum together with its vane would function as a waving wall forming two adjacent peristaltic pumps (30), one on each side of the vane, that draw in water through the filter and expel it out of the chimney of the lorica. To explore such a pumping mechanism we replace the flagellum in the CFD model with a $b = 5$-μm-wide sheet that spans almost the entire width of the filter (Movies S3–S5). The time-averaged CFD flow agrees well with the flow observed for *D. grandis* (Fig. 3). The model leads to the time-averaged flagellum force in the z-direction $F_5 = 12.1$ pN, the time-averaged power $P_5 = 2.20$ fW, and the clearance rate $Q_5 = 898\ \mu m^3 \cdot s^{-1}$, slightly lower than the experimentally observed clearance rate.

To explore the vane-based pumping mechanism conjecture for other choanoflagellates we make a rough estimate of the clearance rate as the volume flow rate given by the simple model

$$Q_V = AW\lambda f, \qquad [5]$$

where W is the diameter of the chimney of the lorica and λ the flagellar wavelength. We assume that the flagellum is moving in the central beat plane with amplitude A and that the flagellar vane is attached to filter and chimney. The average peak-to-peak amplitude of the flagellar vane must therefore be A, and we assume that a water volume $AW\lambda$ is forced through the filter and out of the chimney per flagellar beat period. For *D. grandis* we find the estimate $Q_V = (1.41 \pm 0.50) \cdot 10^3\ \mu m^3 \cdot s^{-1}$ in good agreement with the clearance rate based on the observed flow field (Table 1).

In fact, Q_V provides a solid prediction of the observed clearance rate Q in six of the seven species for which the naked flagellum clearance rate estimate Q_T cannot account for Q (Table 1). Thus, two species seem to use a simple flagellum to drive the feeding current, whereas six choanoflagellate species and the choanocyte rely on a flagellar vane. A narrow vane has been observed in *Monosiga brevicollis*, but a vane this small would have only limited influence on the clearance rate (Fig. S5), and the apparent discrepancy is certainly within estimate uncertainties. Only for *Codosiga botrytis* does neither of the two models adequately predict Q. This species has a long and rapidly beating flagellum that extends far beyond the collar and also the finest of the choanoflagellate filters. Combined, this suggests that this species may not perform actual filter feeding, but instead relies on cross-flow filtration in which the flow passes along and not through the filter. The suggested pumping mechanism would also provide a means to avoid unwanted filter circumvention in loricate as well as nonloricate species. If the vane spans most of the collar width, a flagellum wavelength "traps" a package of water that has to be expelled with the flagellar beat. Furthermore, typical flagellar beat frequencies of eukaryotic organisms are in the range 30–70 Hz (1, 18), and the low beat frequencies found in *D. grandis* and a number of other choanoflagellate species stand out (Table 1). We speculate that the low beat frequencies are the result of extensive flagellar vanes and their high force requirements. While the dynein motor proteins themselves would easily

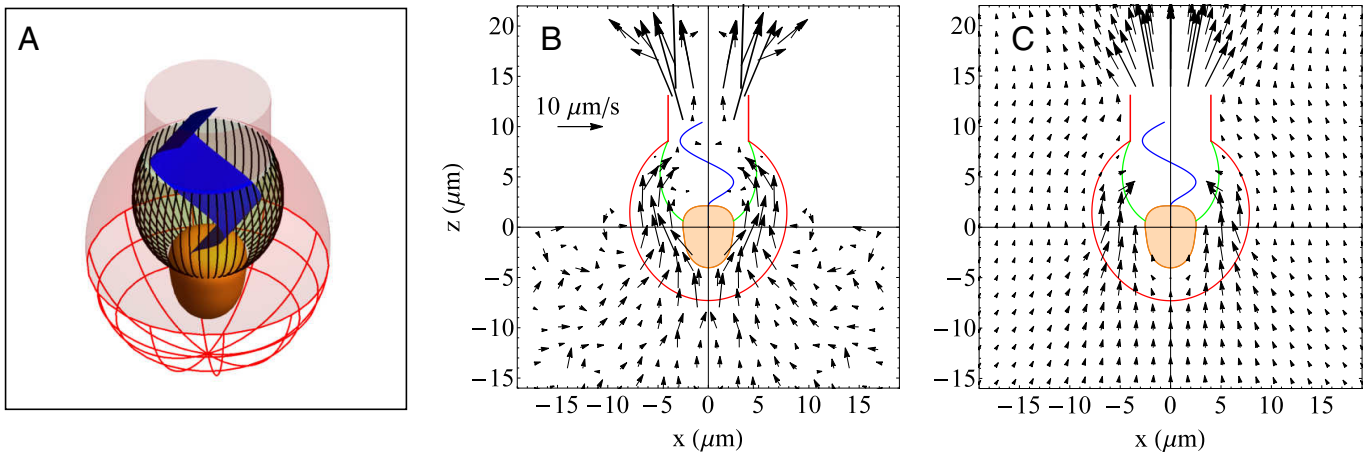

Fig. 3. Model morphology with a flagellar vane, observed average velocity field for *D. grandis*, and velocity field from CFD model including a 5-μm-wide flagellar vane. (*A*) The model morphology shows the cell (orange), the collar filter (green), the flagellum with a 5-μm-wide flagellar vane (blue), and the lorica (red). (*B*) Observed average velocity field. The velocity field is identical to the velocity field in Fig. 2*B*, and it is shown repeatedly to facilitate comparison with the CFD result. (*C*) The CFD velocity field in the *xz* plane is time averaged over the flagellar beat cycle, and the velocity vectors inside filter and chimney are omitted for clarity. The CFD model with a flagellar vane predicts a feeding flow in through the permeable lower part of the lorica and a clearance rate in good agreement with the experimental observations for *D. grandis*.

provide the needed force (31), the shear due to the flagellar beat motion could be too much for delicate vane structures. The presence of a 5-μm-wide vane increases the energetic costs of beating the flagellum by an order of magnitude, making the energetic costs a significant fraction of the total energy budget of the cell, contrary to common belief (32, 33). This is in agreement with results from the similar choanocytes (34) and demonstrates a strong trade-off for microbial filter feeders between acquiring new energy and investing energy to do so.

The Filter-Feeder Trade-Off and the Optimum Filter. The main purpose of the filter is to intercept as much food as possible. The above-mentioned filter trade-off suggests that there is an optimum filter spacing that will maximize the prey encounter rate E in terms of prey biomass per unit time. The encounter rate can be expressed as the integral

$$E = Q \int_0^\infty \beta(s)\, C(s)\, \mathrm{d}s, \qquad [6]$$

where β is the collection efficiency, C the size-specific mass concentration of prey particles, and s the particle diameter. It is generally accepted that logarithmic particle size bins contain approximately equal amounts of biomass (35),

$$C(s) = \frac{C_0/\ln 10}{s}, \qquad [7]$$

where C_0 is the particle mass concentration within each decade in particle diameter. Now, if the particles are captured by sieving, we can assume 100% collection efficiency, $\beta = 1$, for particles with diameter greater than the filter gap $l - 2a$ and smaller than the maximum prey size d. In this case we can write the encounter rate as

$$\begin{aligned} E &= Q \int_{l-2a}^{d} C(s)\mathrm{d}s \\ &= E_0 \langle \kappa \rangle \log \frac{d/a}{l/a - 2}, \end{aligned} \qquad [8]$$

where $E_0 = (a/\mu) F C_0$ is independent of l and d. Independent of the flagellum force F and method of pumping, it is thus possible to predict the optimum filter spacing of aquatic microbial filter feeders. With the maximum prey size $d = (1/3)\,\mathrm{ESR} = 0.93\ \mu\mathrm{m}$ for *D. grandis* (approximately the openings of the coarse outer filter), we obtain the optimum dimensionless filter spacing $l/a = 8.4$ in close agreement with the observed average value (Fig. 4*A*). The optimum filter spacing increases approximately linearly with the maximum prey size in the range relevant for choanoflagellates, and it is consistent with observations (Fig. 4*B*). One species, *C. botrytis*, deviates from this pattern, consistent with our suggestion that this species may not be a true filter feeder. We can approximate the encounter rate when $l/a \gg 1$ as

$$E \approx E_0 \frac{l/a}{8\pi} \left(1 - 2\ln\frac{2\pi}{l/a}\right) \log \frac{d/a}{l/a}, \qquad [9]$$

which allows analytical determination of the optimum filter spacing

$$\frac{l}{a} \approx \exp\left[-1 + \frac{1}{\ln(d/a)} + \frac{\ln(2\pi) - 1/2}{[\ln(d/a)]^2}\right] \frac{d}{a}. \qquad [10]$$

The expression shows that the optimum filter spacing is approximately proportional to the maximum prey size when the filter spacing is large, leading to a relatively small prey size range. Particles smaller than the filter spacing can be collected by direct interception or diffusional deposition, but these effects are estimated to be small compared with sieving for the measured filter spacing of *D. grandis* (36).

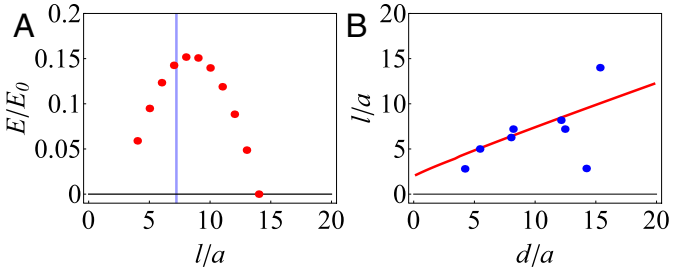

Fig. 4. Optimum choanoflagellate filters. (*A*) Encounter rate as function of dimensionless filter spacing (Eq. **8**). The vertical line (blue) indicates the observed average of the dimensionless filter spacing. (*B*) The theoretical prediction for the optimum dimensionless filter spacing (solid line, red) and the observed dimensionless filter spacing for the choanoflagellates in Table 1 (solid circles, blue) as functions of the maximum dimensionless prey diameter. We have assumed that the maximum prey diameter is equal to (1/3) ESR. The outlier below the predicted line is *C. botrytis*, speculated to rely on cross-flow filtration rather than true filtration.

Conclusion

We have shown that a simple, naked flagellum cannot account for the clearance rates observed in many choanoflagellate species. Instead, we suggest a widespread presence of the sporadically observed flagellar vane. The proposed pumping mechanism is radically different and can explain how choanoflagellates can perform efficient small-scale filter feeding. The explored problems and our model estimates are relevant to the understanding of small-scale filtering in general, and the mechanistic insights allow quantification of the trade-offs involved in various microbial feeding modes. We have, for instance, demonstrated that microbial filter feeding is an energetically costly process that takes up much more than a few percent of the total energy budget of the cell as otherwise typically believed.

Materials and Methods

Experimental Organisms. The choanoflagellate *D. grandis* (American Type Culture Collection no. 50111) was grown nonaxenically in the dark in B1 medium (salinity 32) at 10 °C. The culture was diluted once every 2–3 wk, and a few organically grown, autoclaved, rice grains were added per 65-mL flask to serve as bacterial substrate.

Videography of Flagellum Motion and Feeding Flow. To explore the near-cell flow field and the motion of the beating flagellum, cells were observed at high magnification, using a high-speed digital video. An Olympus IX-71 inverted microscope equipped with a UPLSAPO60XO/1.35 oil-immersion objective and a U-ECA magnifying lens provided a total of 1,920× magnification. Video sequences were obtained using a Phantom v210 high-speed digital video system. Videos were recorded at a frame rate of 100 fps and a resolution of 1,024 pixels × 800 pixels. This provided 10 pixels/μm. Observations were done in an ≈1-mL chamber, constructed as a 5-mm-high polycarbonate ring (diameter 2 cm) mounted with silicone between an objective slide and a cover glass. Cells either were free swimming or settled onto the slide. Flagellum length and average amplitude of the flagellar beat were estimated on five individuals that were oriented with the flagellum beat plane aligned with the focal plane of the microscope. For each frame in a single beat cycle, the flagellum position was digitized manually using ImageJ by identifying approximately 15 points along the flagellum. Neutrally buoyant, 300-nm polystyrene beads were added to a concentration of $\sim 1 \cdot 10^6$ mL^{-1} to visualize the water flow. The particles were pretreated with BSA and sonicated before use to avoid clumping.

Flow-Field Analysis. Based on cell alignment, a total of 19 video sequences, each fielding a unique individual, were selected for use in the flow-field analysis. The frequency of the flagellar beat was noted at 1-s intervals, by manual, visual inspection of the slowed-down 100-fps video sequences. Two-dimensional particle tracks were resolved on reduced–frame-rate video sequences (10 fps), using the manual tracking plugin for ImageJ. A total of 73 tracks were used to construct the velocity field. Each particle track was associated with the frequency of the flagellar beat at the corresponding time. All particle tracks were collated using the average model morphology,

and the velocity field in the *xz* plane was constructed using a square grid with 2-μm $\times$ 2-μm spatial resolution. The velocity field was assumed to have rotational symmetry about the longitudinal axis of the cell, and the observed velocity field in the *xz* plane was therefore correspondingly assumed to have left–right reflection symmetry with respect to the longitudinal axis. Within each grid window the manually detected particle positions were selected and for each particle track the average particle position and velocity were determined. Position and velocity associated with a given grid window were subsequently determined as the equally weighted average over all particle tracks within the window.

ACKNOWLEDGMENTS. We thank Jasmine Mah for providing videos of *M. brevicollis* and Øjvind Moestrup and Helge Abildhauge Thomsen for helpful discussions. The Centre for Ocean Life is a Villum Kann Rasmussen Centre of Excellence supported by the Villum Foundation, and S.S.A. and J.H.W. were supported by a research grant (9278) from the Villum Foundation.

1. Fenchel T (1982) Ecology of heterotrophic microflagellates. I. Some important forms and their functional morphology. *Mar Ecol Prog Ser* 8:211–223.
2. Fenchel T (1984) Suspended marine bacteria as a food Source. *Flows of Energy and Materials in Marine Ecosystems*, ed Fasham MJR (Plenum, New York), pp 301–315.
3. Kiørboe T, Plough H, Thygesen UH (2001) Fluid motion and solute distribution around sinking aggregates. I. Small-scale fluxes and heterogeneity of nutrients in the pelagic environment. *Mar Ecol Prog Ser* 211:1–13.
4. Kiørboe T (2011) How zooplankton feed: Mechanisms, traits and trade-offs. *Biol Rev* 86:311–339.
5. Fenchel T (1986) Protozoan filter feeding. *Prog Protistology* 1:65–113.
6. Larsen PS, Riisgård HU (1994) The sponge pump. *J Theor Biol* 168:53–63.
7. Riisgård HU, Larsen PS (2010) Particle capture mechanisms in suspension-feeding invertebrates. *Mar Ecol Prog Ser* 418:255–293.
8. Fenchel T (1980) Relation between particle size selection and clearance in suspension-feeding ciliates. *Limnol Oceanogr* 25:733–738.
9. Ayaz F, Pedley TJ (1999) Flow through and particle interception by an array of closely-spaced circular cylinders. *Eur J Mech B Fluids* 18:173–196.
10. Pettitt ME, Orme BAA, Blake JR, Leadbeater BSC (2002) The hydrodynamics of filter feeding in choanoflagellates. *Eur J Protistol* 38:313–332.
11. Leadbeater BSC (2015) *The Choanoflagellates: Evolution, Biology and Ecology*. (Cambridge Univ Press, Cambridge, UK).
12. Lapage G (1925) Notes on the choanoflagellate, *Codosiga botrytis*, ehrbg. *J Cell Sci* 69:471–508.
13. Andersen P (1988/1989) Functional biology of the choanoflagellate *Diaphanoeca grandis* Ellis. *Mar Microb Food Webs* 3:35–50.
14. Roper M, Dayel MJ, Pepper RE, Koehl MAR (2013) Cooperatively generated stresslet flows supply fresh fluid to multicellular choanoflagellate colonies. *Phys Rev Lett* 110:228104.
15. Dayel MJ, King N (2014) Prey capture and phagocytosis in the choanoflagellate *Salpingoeca rosetta. PLoS One* 9:e95577.
16. Kirkegaard JB, Goldstein RE (2016) Filter-feeding, near-field flows, and the morphologies of colonial choanoflagellates. *Phys Rev E* 94:052401.
17. Hibbert DJ (1975) Observations on the ultrastructure of the choanoflagellate *Codosiga botrytis* (ehr.) Saville-Kent with special reference to the flagellar apparatus. *J Cell Sci* 17:191–219.
18. Sleigh MA (1964) Flagellar movement of the sessile flagellates *Actinomonas, Codonosiga, Monas*. *J Cell Sci* 105:405–414.
19. Eccleston PJD, Leadbeater BSC (1994) A comparison of the growth kinetics of 6 marine heterotrophic nanoflagellates fed with one bacterial species. *Mar Ecol Prog Ser* 105:167–178.
20. Mah JL, Christensen-Dalsgaard KK, Leys SP (2014) Choanoflagellate and choanocyte collar-flagellar systems and the assumption of homology. *Evol Dev* 16:25–37.
21. Boenigk J, Arndt H (2000) Comparative studies on the feeding behavior of two heterotrophic nanoflagellates: The filter-feeding choanoflagellate *Monosiga ovata* and the raptorial-feeding kinetoplastid *Rhynchomonas nasuta*. *Aquat Microb Ecol* 22:243–249.
22. Leadbeater BSC (1972) Fine-structural observations on some marine choanoflagellates from the coast of Norway. *J Mar Biol Assoc UK* 52:67–79.
23. Moestrup Ø (1982) Flagellar structure in algae: A review, with new observations particularly on the Chrysophyceae, Phaeophyceae (Fucophyceae), Euglenophyceae, and *Reckertia*. *Phycologia* 21:427–528.
24. Keller JB (1964) Viscous flow through a grating or lattice of circular cylinders. *J Fluid Mech* 18:94–96.
25. Tamada K, Fujikawa H (1957) The steady two-dimensional flow of viscous fluid at low Reynolds numbers passing through an infinite row of equal parallel circular cylinders. *Q J Mech Appl Math* 10:425–432.
26. Berg HC (1993) *Random Walks in Biology* (Princeton Univ Press, Princeton).
27. Leadbeater BSC (2006) The 'mystery' of the flagellar vane in choanoflagellates. *Nova Hedwigia Beiheft* 130:213–223.
28. Mehl D, Reiswig HM (1991) The presence of flagellar vanes in choanomeres of Porifera and their possible phylogenetic implications. *J Zool Syst Evol Res* 29:312–319.
29. Weissenfels N (1992) The filtration apparatus for food collection in freshwater sponges (Porifera, Spongillidae). *Zoomorphology* 112:51–55.
30. Jaffrin MY, Shapiro AH (1971) Peristaltic pumping. *Ann Rev Fluid Mech* 3:13–37.
31. Lindemann CB (2003) Structural-functional relationships of the dynein, spokes, and central-pair projections predicted from an analysis of the forces acting within a flagellum. *Biophys J* 84:4115–4126.
32. Purcell EM (1977) Life at low Reynolds number. *Am J Phys* 45:3–11.
33. Guasto JS, Rusconi R, Stocker R (2012) Fluid mechanics of planktonic microorganisms. *Annu Rev Fluid Mech* 44:373–400.
34. Leys SP, et al. (2011) The sponge pump: The role of current induced flow in the design of the sponge body plan. *PLoS One* 6:e27787.
35. Sheldon RW, Prakash A, Sutcliffe Jr. WH (1972) The size distribution of particles in the ocean. *Limnol Oceanogr* 17:327–340.
36. Spielman LA (1977) Particle capture from low-speed laminar flows. *Ann Rev Fluid Mech* 9:297–319.
37. Pozrikidis C (2011) *Introduction to Theoretical and Computational Fluid Dynamics* (Oxford Univ Press, Oxford), 2nd Ed.
38. Happel J, Brenner H (1983) *Low Reynolds Number Hydrodynamics: With Special Applications to Particulate Media* (Martinus Nijhoff, The Hague, The Netherlands).

Supporting Information

Nielsen et al. 10.1073/pnas.1708873114

The *Supporting Information* is mainly devoted to our CFD simulations, including verification, validation, results, and movies with flow animations. Additionally, we present movies of observed particle tracks and flagellar beats, details of the model morphology, and details of the analytical modeling of the filter resistance.

Model Morphology and Observed Flow

To collate particle tracks from the different individuals and to set up the CFD simulation geometry, we construct a generic morphology model to which all observations are scaled. We focus on six individuals that are viewed from the side with the longitudinal axis of the cell in the focal plane. To good approximation the cell surface and the outline of the lorica have rotational symmetry about the longitudinal axis, and we therefore describe them as surfaces of revolution. In spherical polar coordinates we write

$$R(\theta) = R_0\,(1 + \alpha_1 \cos\theta + \alpha_2 \cos 2\,\theta + \alpha_3 \cos 3\,\theta), \quad \textbf{[S1]}$$

where R_0, α_1, α_2, and α_3 are morphology parameters. The polar angle θ is defined relative to the longitudinal axis of the cell, and the location of the flagellum, i.e., the flagellar basal body, is used to define the north (anterior) pole of the cell. For both the cell surface and the outline of the lorica we list the morphology parameters (Table S1).

To model the outline of the filter we use the interpolation

$$R_F(\theta) = R_C(\theta_C) + [R_L(\theta_L) - R_C(\theta_C)]\,\frac{\theta - \theta_C}{\theta_L - \theta_C}, \quad \textbf{[S2]}$$

where $\theta_C = 76^\circ$ and $\theta_L = 25^\circ$ are the polar angles where the filter connects to cell R_C and lorica R_L, respectively. The average dimensionless filter spacing is $\langle l/a \rangle = 7.2$, where l denotes the distance between the centers of neighboring microvilli and $a = 0.075$ μm the radius of an individual microvillum (13). The flagellum length and the average amplitude of the flagellar beat are $L = 11.7 \pm 1.5$ μm and $A = 2.8 \pm 0.2$ μm, respectively.

CFD Simulations

Simulation Setup. We apply the commercial CFD program STAR-CCM+ (12.02.010-R8) to numerically solve the Navier–Stokes equation and the equation of continuity for incompressible Newtonian flow using the finite-volume approach. Both the frequency parameter and the Reynolds number are much smaller than unity, and the flow is therefore a quasi-steady Stokes flow (37). We use the model morphology and a spherical computational domain with the model cell held stationary at the center (Fig. S2). With this approach we disregard the slow swimming motion and the periodic rocking motion of the cell during the flagellar beat, which we presume to have negligible effect on the feeding flow. The no-slip boundary condition is applied at the surfaces of the cell and the microvilli. The upper part of the lorica and the chimney of height 5 μm are treated as impermeable surfaces with no-slip boundary condition, and the lower part of the lorica is disregarded (Fig. S2*A*).

We treat the beating flagellum as a thin sheet of width b that is moved in the xz plane with prescribed kinematics and on which the no-slip boundary condition is satisfied with the prescribed velocity. We model the displacement of the flagellum in the x direction as the simple traveling wave,

$$h(z,t) = A\left[1 - e^{-(z-z_B)/\delta}\right]\sin[k(z - z_B) - \omega t], \quad \textbf{[S3]}$$

where z_B is the z coordinate of the flagellar basal body at the cell surface, $\delta = 1.0$ μm the characteristic length scale of the amplitude modulation, $k = 2\pi/\lambda$ the wave number, and $\omega = 2\pi f$ the angular frequency. At the exterior boundary of the computational domain we apply a constant pressure boundary condition (Fig. S2*B*).

We take advantage of mesh morphing to avoid reconstructing the mesh geometry at the different flagellum positions during the flagellar beat. The morphing motion redistributes mesh vertices in response to the movement of the flagellum at each time step. Therefore, between two time steps, the mesh is morphed in response to the flagellar movement and at each time step, the discretized forms of the governing equations are solved inside the entire computational domain. We use polyhedral cells for the discretization since they allow mesh morphing and flexibility when representing the complex geometry of the model organism (Fig. S3).

Verification. We make sure that the four governing equations are satisfied with negligible error and that the flagellum force converges for each time step during the computational iteration process. To verify that the solutions for the time-averaged flagellum force and the time-averaged clearance rate do not depend on the mesh size, we discretize the computational domain with different mesh sizes. For meshes with more than 4 million computational cells we find ∼1% variation, and in the result simulations we use 4.8 million computational cells (Fig. S4). We use two different time steps to check the time-step independence, and we conclude that 24 time steps per flagellar beat period are sufficient (Table S2). To make sure that the solution is independent of the size of the computational domain, we solve the governing equations inside domains with different sizes. We find minute differences between domains with radii 30 μm and 40 μm, respectively, and in the result simulations we therefore use domains with radius 30 μm (Table S2).

Validation. To validate the computational approach we use it to numerically calculate the drag forces on a slender cylinder and a slender thin sheet in steady flow at Reynolds numbers comparable to the low Reynolds number for the flagellar motion. Our goal is both to validate the results for the slender cylinder against known analytical theory and to validate the approximation of a beating cylindrical flagellum using a thin sheet. We consider the drag force components F_s and F_n in the lengthwise and the sidewise directions

$$F_s = C_s \mu L U, \quad \textbf{[S4]}$$

$$F_n = C_n \mu L U, \quad \textbf{[S5]}$$

where we define the drag coefficients C_s and C_n in the lengthwise and the sidewise directions, respectively, and where L denotes the length of the slender object and U the speed of the steady far-field flow relative to the object. For the slender cylinder we use the analytical approximations

$$C_s \approx \frac{2\pi}{\ln(2L/b) - 0.72}, \quad \textbf{[S6]}$$

$$C_n \approx \frac{4\pi}{\ln(2L/b) + 0.50}, \quad \textbf{[S7]}$$

that were derived by Burgers (ref. 38, equations 5-11.52 and 5-11.54). In the numerical simulations we apply a cylindrical computational domain that in extension is an order of magnitude

larger than the length of the cylinder or plate. The object is held stationary at the center of the domain, and the no-slip boundary condition is applied at the surface of the object. A flow inlet boundary condition is applied on one end face of the computational domain, and a pressure boundary condition is used on the other external boundaries. The CFD results and the approximate theoretical results agree within the expected accuracy, and the CFD results for the thin plate are roughly 20% smaller than the CFD results for the cylinder (Table S3). We therefore expect the CFD simulation using the thin-plate model to underestimate the force due to the cylindrical flagellum by roughly 20%.

Results. The main simulation results are the time-averaged flagellum forces in the z-direction F_z and the time-averaged clearance rates Q for different widths of the flagellum b. In addition to the simulation data for the narrow flagellum with $b = 0.3$ μm and the wide flagellum with $b = 5.0$ μm that we discuss in the main text, we show results for intermediate b values (Fig. S5). Both F_z and Q increase with b, and they are roughly proportional.

Filter Resistance

For the drag force per unit length D on a single cylinder in the filter we introduce a dimensionless drag coefficient C_D. We write it in the form $D = C_D \mu v$, since we consider low Reynolds number flows. The relationship between the dimensionless permeability and the drag coefficient becomes $\kappa = (l/a)/C_D$. Simple filter flows with closely spaced cylinders were modeled by Keller using lubrication theory (24). In this approximation,

$$C_D = \frac{9\pi}{2^{3/2}}\left(1 - \frac{2}{l/a}\right)^{-5/2}. \qquad \textbf{[S8]}$$

The flow can also be analyzed for a filter with widely spaced cylinders, and this was done using the Oseen equation by Tamada and Fujikawa (25). In this case it is convenient to introduce the parameter $\tau = 2\pi/(l/a)$ and to write the drag coefficient $C_D = 8\pi/\Lambda$, where Λ has the form

$$\Lambda = 1 - 2\ln\tau + \frac{1}{6}\tau^2 - \frac{1}{144}\tau^4 + \frac{1}{1{,}080}\tau^6 - \frac{53}{345{,}600}\tau^8 + \frac{139}{5{,}443{,}200}\tau^{10} + \mathcal{O}(\tau^{12}). \qquad \textbf{[S9]}$$

It is not clear a priori how well the two models work for intermediate filter spacing, and we therefore follow Ayaz and Pedley (9) and compare the two models with numerical results. Keller's model is qualitatively correct for both closely and widely spaced cylinders, but it is only quantitatively correct when $l/a < 4$ (Fig. S6*A*). In contrast, the model by Tamada and Fujikawa (25) works well when $l/a > 4$, and it breaks down for closely spaced cylinders. Thus, we estimate κ following Keller's model when $l/a < 4$ and using Tamada and Fujikawa's work when $l/a \geq 4$ (Fig. S6*B*).

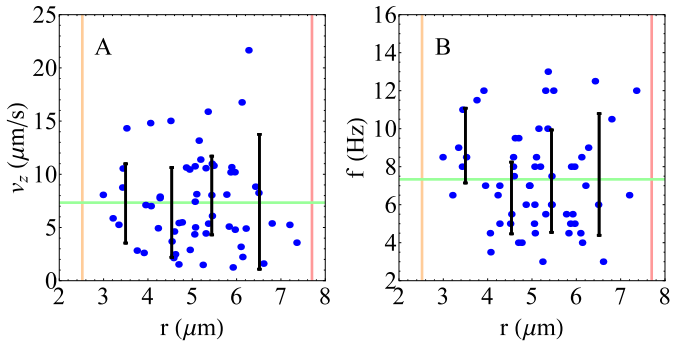

Fig. S1. Flow velocities as function of the distance r from the longitudinal axis and corresponding flagellar beat frequencies used for the clearance rate calculation. The cell surface (orange) and the lorica (red) at the equator are indicated by the vertical lines. The average values are shown as the horizontal lines (green). (*A*) The z components of the particle velocities in the equatorial region between $z = \pm 1$ μm (solid circles, blue) and the z components of the flow velocities obtained by binning (solid circles and error bars, black). (*B*) The corresponding flagellar beat frequencies.

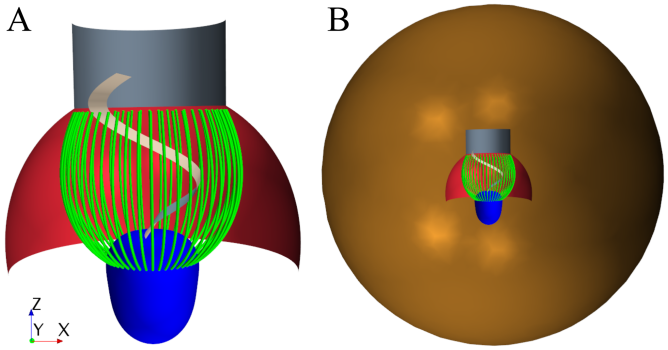

Fig. S2. Model geometry and computational domain. (*A*) The model organism consisting of cell (blue), flagellum (light gray), filter (green), upper part of lorica (red), and chimney (dark gray). The coordinate system is defined so that the flagellum is beating in the *xz* plane. (*B*) The model organism at the center of the spherical computational domain (brown).

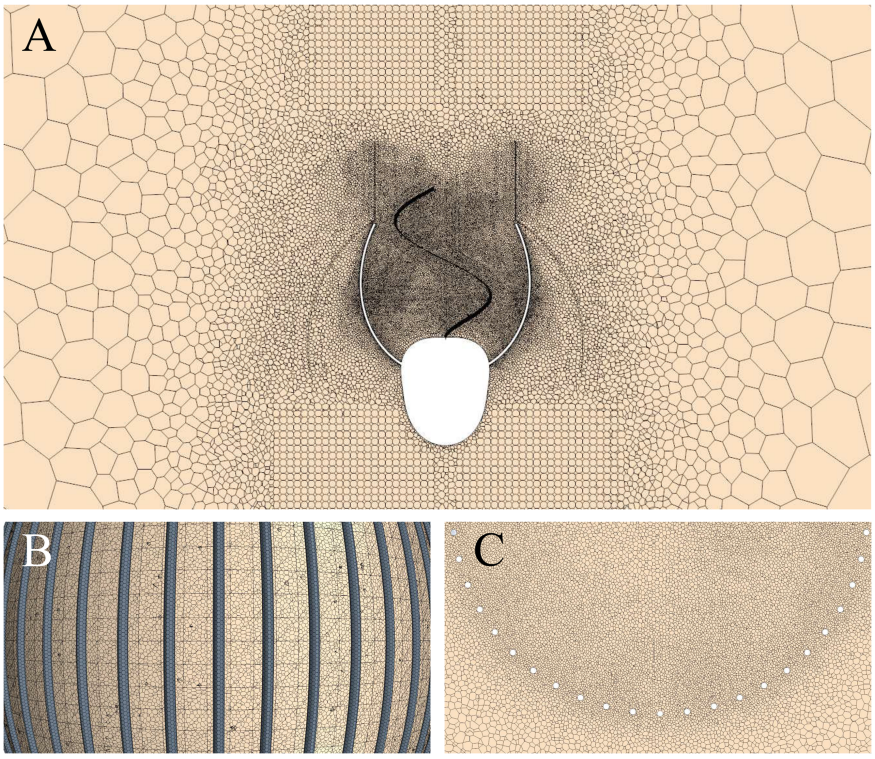

Fig. S3. The computational cells in the discretized computational domain with 4.8 million computational cells for a flagellum of width 5 μm. (*A*) The mesh is chosen very fine around the flagellum and in between the microvilli to resolve the flow structures, whereas a coarse mesh is sufficient to resolve the flow in the far field. (*B* and *C*) Details of the mesh between the microvilli seen from the side and in the *z* direction.

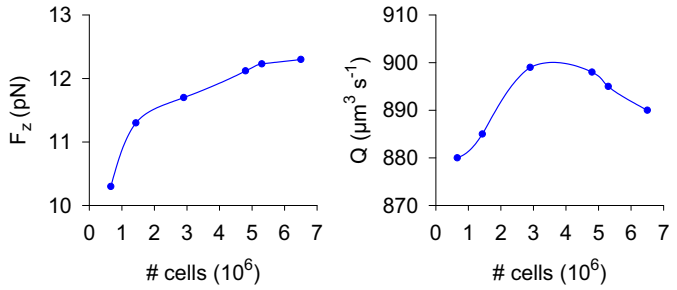

Fig. S4. Mesh size independence of the time-averaged force F_z and the time-averaged clearance rate Q with a flagellum of width 5 μm.

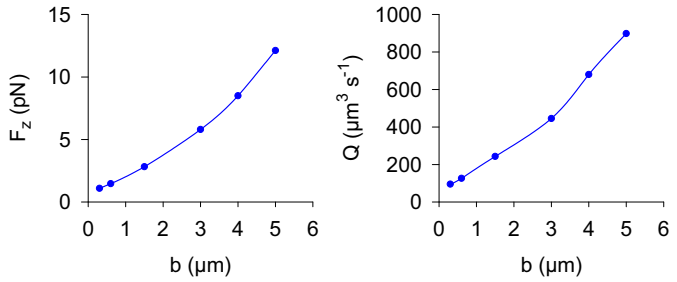

Fig. S5. Time-averaged flagellum force in the *z*-direction F_z and time-averaged clearance rate Q for different widths of the flagellum b.

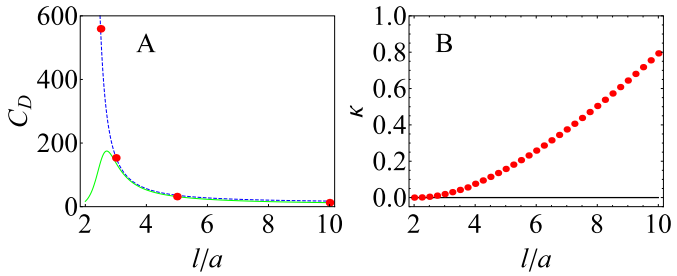

Fig. S6. Filter characteristics. (*A*) The drag coefficient C_D as function of l/a in Keller's model (dashed line, blue), in the model by Tamada and Fujikawa (25) (solid line, green) and in the simulations by Ayaz and Pedley (9) (solid circles, red). (*B*) The dimensionless filter permeability κ using Keller's model when $l/a < 4$ and the model by Tamada and Fujikawa when $l/a \geq 4$.

Table S1. Average morphology parameters that describe both size R_0 and shape α_1, α_2, and α_3 of the cell and the outline of the lorica

Object	R_0, μm	α_1, rad	α_2, rad	α_3, rad
Cell	2.8 ± 0.3	−0.24	0.10	−0.10
Lorica	8.1 ± 0.4	0.15	0.05	0.00

Table S2. Independence of the time-averaged force F_z and the time-averaged clearance rate Q on the number of time steps per beat cycle and the size of the computational domain

Case	F_z, pN	Q, μm^3/s
No. time steps per beat cycle		
24	12.1	898
48	12.2	895
Domain radius, μm		
30	12.1	898
40	12.2	909

Table S3. Drag coefficients C_s and C_n for steady flow past a cylinder and a thin plate and the differences relative to the CFD results for the cylinder

Case	C_s	C_n	Δ_s, %	Δ_n, %
Cylinder, theory	1.81	2.67	0.0	−5.0
Cylinder, CFD	1.81	2.81	—	—
Plate, CFD	1.35	2.35	−25.4	−16.4

All objects are slender with $b/L = 0.03$, where b denotes the cylinder diameter and the plate width, respectively, and L the object length.

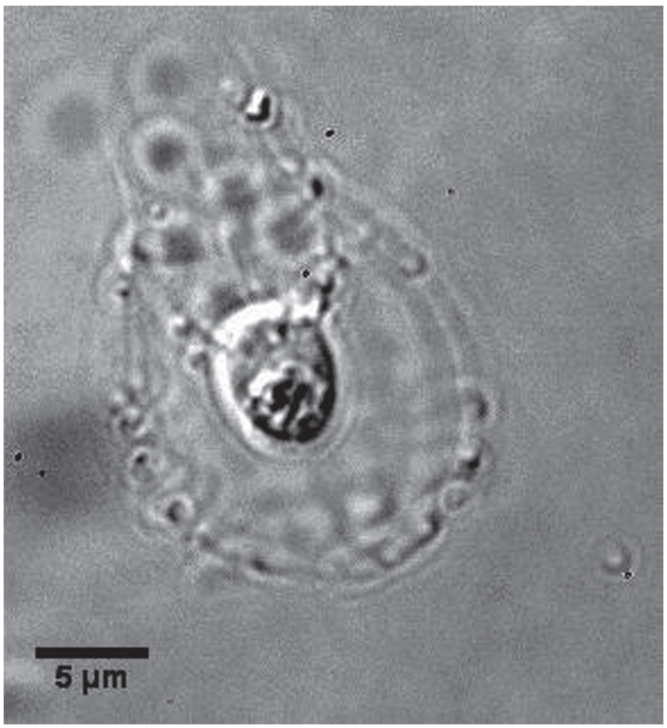

Movie S1. *D. grandis* capturing several 300-nm polystyrene tracer particles. Movies like this were used to construct the flow field (Fig. 2) by manually tracking the tracer particles over time. Displayed in real time.

Movie S1

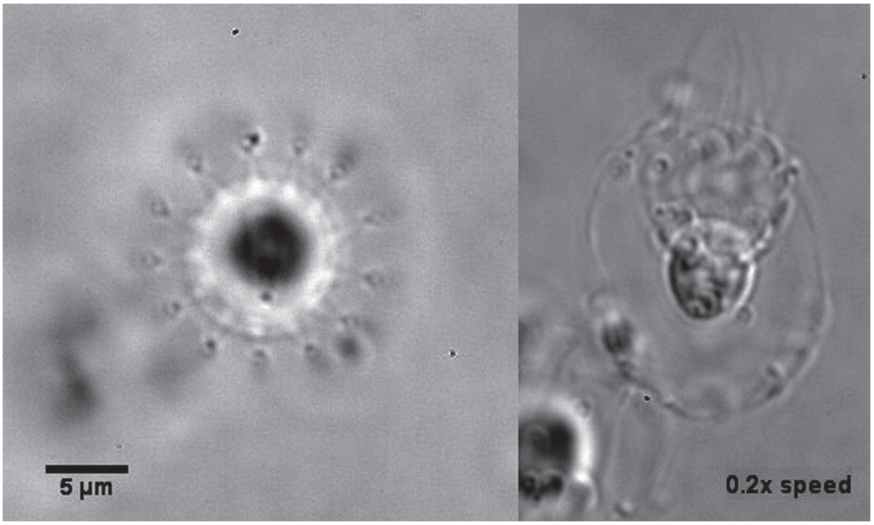

Movie S2. Flagellar beat pattern of *D. grandis*. (*Left*) Cell viewed from the top (apex). The symmetrical pattern surrounding the dark cell is the costae that make up the lorica. (*Right*) Cell seen from the side with the outline of cell, flagellum, lorica, collar, and chimney all visible. Shown is the planar beat pattern of *D. grandis*.

Movie S2

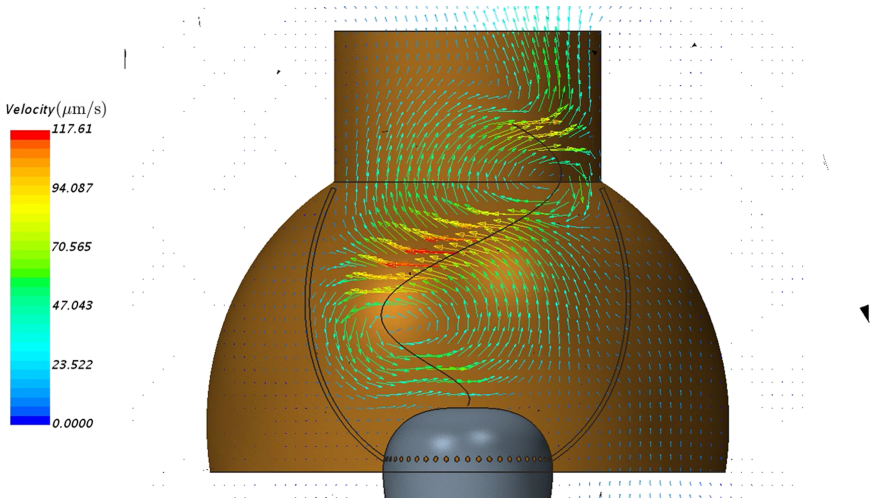

Movie S3. *D. grandis* CFD simulation with a 5-μm-wide vane and 1.5 million computational cells. Shown is lateral view as observed perpendicular to the *xz* plane of the flagellar beat. Note how the flux through the filter is highly time dependent. Fig. 3*C* of the main text presents the time-averaged data from this movie.

Movie S3

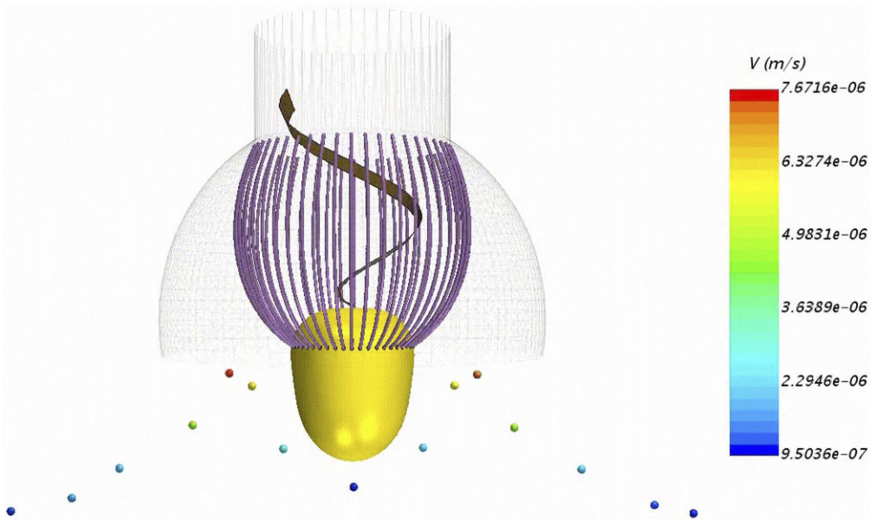

Movie S4. *D. grandis* CFD simulation with a 5-μm-wide vane (brown) and 1.1 million computational cells. Shown are passive tracer particle trajectories in the *xz* plane of the flagellar beat. The vane extends toward and away from the observer. Note how particle velocities are highly time dependent in this plane.

Movie S4

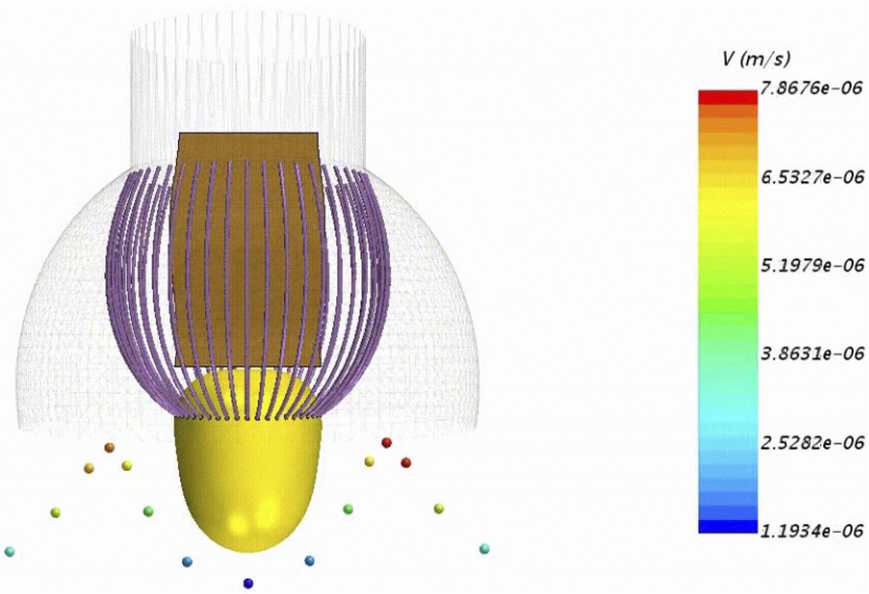

Movie S5. *D. grandis* CFD simulation with a 5-μm-wide vane (brown) and 1.1 million computational cells. Shown are passive tracer particle trajectories in the *yz* plane perpendicular to the flagellar plane of beat. Particle velocities are much less time dependent in this plane compared with the plane parallel to this (Movie S4).

Movie S5

5.4 Dense dwarfs versus gelatinous giants

Manuscript in preparation.

Dense dwarfs versus gelatinous giants: The trade-offs determining the body composition of planktonic filter feeders

Julia Dölger[1,†], Thomas Kiørboe[2,†], and Anders Andersen[1,*,†]

2 March 2018

1. Department of Physics and Centre for Ocean Life, Technical University of Denmark, DK-2800 Kgs. Lyngby, Denmark;

2. National Institute of Aquatic Resources and Centre for Ocean Life, Technical University of Denmark, DK-2800 Kgs. Lyngby, Denmark;

∗ Corresponding author; e-mail: aanders@fysik.dtu.dk.

† ORCIDs: Dölger, 0000-0003-4667-4716; Kiørboe, 0000-0002-3265-336X; Andersen, 0000-0002-3831-1707.

Manuscript elements: Figure 1, figure 2, figure 3, figure 4, table 1, table 2

Keywords: Gelatinous zooplankton, filter feeding, low-Reynolds number fluid dynamics, salps, choanoflagellates.

Manuscript type: E-Article.

Prepared using the suggested LaTeX template for *Am. Nat.*

Abstract

Most marine plankton have a high energy (biomass) density, while some others, although functionally similar, are gelatinous with 100 times more watery bodies. How do those distinctly different body compositions emerge and what are the limitations? We address this fundamental question by investigating the trade-offs and physiological limits in dense and gelatinous filter feeders. Planktonic filter feeders create flow through fibrous structures to collect prey without the use of remote prey sensing. They all feed on micron-sized prey and range in size and body composition from unicellular microbes like choanoflagellates to centimeter-sized gelatinous tunicates such as salps. We formulate a model for the energy budget of an individual active filter feeder, based on which we can compare organisms with different body plans. With the model we find two equally successful strategies, one being small with high energy density (dense dwarf), and the other being large with low energy density (gelatinous giant). We identify a lower limit to the ratio of surface area to energy content, below which the energetic costs lead to starvation, and we show that this constraint forces large filter feeders to be gelatinous. The available strategies are found to be limited by the maximum energy-specific motor force, which leads to constant energy-specific clearance rates across species. These limitations restrict the access to optimum strategies. Alternative strategies for large organisms are to remotely sense and capture individual prey or to seek out patches of high prey concentration and these do not require gelatinous body plans. We further discuss the possibility to generalize the quantified trade-offs to other resource acquisition strategies in the plankton. The option of becoming gelatinous can make strategies available for large organisms, which else are only feasible for smaller ones.

Introduction

Gelatinous organisms that comprise pelagic tunicates such as salps, but also jellyfish and comb jellies, are characterized by a watery body with an energy (biomass) density that is about hundred times lower than that found in non-gelatinous forms (Kiørboe 2013; Lucas and Dawson 2014). Such organisms have become increasingly recognized for their important roles in the oceanic food web (Alldredge and Madin 1982; Arai 2001; Bone 1998; Condon et al. 2012; Harbison 1992), and it has been noted that the watery body makes them capable of surviving in the most dilute environments, which is seen as one of the main advantages of the gelatinous trait (Acuna 2001; Acuna et al. 2011; Harbison 1992). Gelatinous organisms are distinguished from many non-gelatinous organisms of similar energy content by the lack of remote sensing apparatus (Bone 1998; Kiørboe 2011; Martens et al. 2015; Sørnes and Aksnes 2004). With a model analysis of filter feeders across life forms, we aim to explore the gelatinous trait and the conditions under which gelatinous and dense body compositions emerge.

We identify optimal and physically possible combinations of key traits in individuals under different environmental conditions. Our results can be used for the construction and validation of predictive trait-based ecosystem models (Follows and Dutkiewicz 2011; Franks 2009; Smith et al. 2014).

Planktonic interception feeders create a feeding flow past themselves and directly intercept prey particles rather than using remote perception. The strategy is widespread among the plankton, but it is demanding since such organisms need to process huge amounts of ocean water to survive in the dilute oceanic environment (Kiørboe 2011). Interception feeding involves a fundamental trade-off: the flow is crucial to collect prey, but energy is required to create the flow.

Filter feeders are a special group of interception feeders that pass the feeding flow through a water-permeable structure where prey is retained. The main components of a filter feeder are the body, the filter, and the motor, i.e., flagella, cilia, or muscles that drive the feeding flow. The two dominant groups of planktonic filter feeders that we here investigate as examples are

choanoflagellates and salps (figure 1). They are in contrasting ends of the planktonic size spectrum: choanoflagellates are unicellular and use a single flagellum to create a feeding current through a collar-shaped filter made of microvilli that extend from the cell (Leadbeater 2015). The here modeled example species has an additional basket-like lorica, which surrounds the filter and directs the flow, but also aloricate species with efficient pumping mechanisms are shown to experience negligible flow circumvention (Nielsen et al. 2017). Salps are gelatinous pelagic tunicates that are up to several centimeters long and use muscle rings in a barrel-shaped body to drive flow through a filter made of sub-micron thick mucus strands (Bone 1998). The filter spacing varies surprisingly little from choanoflagellates to salps, and they thus compete for a common source of micron-sized prey in the plankton (Hansen et al. 1994; Lombard et al. 2011; Nielsen et al. 2017; Sutherland et al. 2010). Here we ask what the mechanisms are that allow the evolution of these contrasting strategies. We use the overarching similarities to set up a general energetics model of filter feeding to quantify trade-offs and physiological limits. Further similarities that have been found not only for filter feeders but also in comparison to other aquatic and terrestrial organisms are the species-transcending magnitudes of energy-specific respiration and prey clearance rates, while the size scalings are more variable within species groups (Kiørboe and Hirst 2014; Makarieva et al. 2008).

Acuna and collaborators have developed energetics models to explore the fitness of gelatinous species such as salps (filter feeders) and jellyfish (cruising feeders) and through fitness optimization they have estimated optimal filtration or cruising speeds using different fitness measures (Acuna 2001; Acuna et al. 2011). Acuna (2001) estimated the filtration speed for salps that would maximize growth, while Acuna et al. (2011) estimated the cruising speed for jellyfish that would optimize survival at low food concentrations. We here argue that either of these optimal velocity adaptations is often unfeasible, since the flow-creating motor of the organism is not capable of producing sufficiently high flow speeds.

We explore the filter feeding strategy across life forms to determine trait combinations that make the strategy feasible and successful in the marine pelagic zone. Such an approach can potentially increase our understanding of emerging life forms better than the study of single species

in the context of optimal foraging theory (Parker and Smith 1990; Werner and Hall 1974), where often single optimal strategies have been in focus and strong species-specific assumptions are made (Lehman 1976; Smith et al. 2011). With our model of the individual energy budget we show that motor performance constrains optimality of flow speeds and body plan and we predict scalings of clearance rates. We demonstrate that small pelagic filter feeders can have dense body compositions, while larger organisms must either be gelatinous to ensure a sufficient energy-specific filter area or able to remotely perceive prey in order to survive in the pelagic realm.

Model of active planktonic filter feeders

The scope for growth of an individual, i.e., the total energy available for individual growth and reproduction is the energy gain (prey ingestion rate) minus the energy investment (respiration rate). We use energy-specific quantities, i.e., quantities that are defined per energy content of the organism, and the energy-specific scope for growth H is then

$$H = G - R_\mathrm{f} - R_\mathrm{b}, \tag{1}$$

where G is the energy-specific prey ingestion rate. The energy-specific respiration rate is divided into a dynamic part R_f, the cost of flow creation, and a basal part R_b for maintenance. The body energy content is defined as the energy that can be produced by metabolising the biomass content and it is assumed proportional to the body carbon mass (Acuna 2001; Schmidt-Nielsen 2007). Using energy-specific quantities we are able to compare filter feeders with different energy contents. Both G and R_f depend on the filter flow speed u and we can write

$$H = A\,u\,c - k\,A\,u^2 - R_\mathrm{b}, \tag{2}$$

where A is the energy-specific filter area, c the environmental prey concentration in energy per unit volume, and k the filter resistance. For the ingestion we have assumed that the assimilation

efficiency, i.e., the assimilated fraction of the ingested energy, is 100% and that the clearance rate is independent of prey concentration and can be expressed as the volume flow rate $A\,u$ through the filter. A precondition for this is that functions other than prey capture, e.g., prey-size dependent digestion speed and efficiency, play a negligible role. This is expected to be only valid for filter feeders that capture favorable prey at low concentration (Jeschke et al. 2004; Lehman 1976; Wirtz 2012). Realistic assimilation efficiencies, even at optimal temperature and food quality, are lower than 100% due to various energy losses during digestion, but can easily be higher than 50% (Andersen 1986; López-Urrutia et al. 2003; Makarieva et al. 1992; Winter 1978). With the assumption that the assimilation efficiency does not vary across size classes it can be included in an effectively lowered available prey concentration. This would make the challenges of a dilute environment even more pronounced.

The dynamic part, R_f, of the respiration rate is estimated as the energy-specific motor force $F = k\,A\,u$ times the cross-filter flow speed u (Acuna 2001; Vogel 1994). Additional energy conversion efficiencies are assumed to be 100% for simplicity. Observations show that the filter spacing l and the fiber radius a and consequently the filter resistance k vary little across species of planktonic filter feeders (Bone et al. 1991; Leadbeater 2015). We define k as the resistance of an infinite mesh of parallel and equidistant cylinders, which dramatically increases with a/l, the ratio of fiber radius to filter spacing (table 1) (Ayaz and Pedley 1999; Nielsen et al. 2017; Tamada and Fujikawa 1957).

The basal part of the energy-specific respiration rate, R_b, is considered to be constant, since the total energy-specific respiration rate is approximately constant when considered across planktonic life forms (Kiørboe and Hirst 2014; Makarieva et al. 2008). In experiments total respiration rates are usually recorded, and no distinction between basal and dynamic respiration is made. The dynamic respiration rate depends on the behavior of the organism and the cost for continuous flow creation by small plankton is found to be well below 10% of the total respiration rate (Crawford 1992; Svetlichny and Hubareva 2005). We here assume that R_f is maximally equal to the basal respiration R_b, and thus we use the observed value for total respiration rates to estimate R_b.

Assuming a fixed filter resistance k and a basal respiration rate R_b we have three main variables

in our model: the prey concentration, c, the energy-specific filter area, A, and the filter flow speed u. The prey availability c is determined by the environment, whereas A and u define physiological and behavioral key traits of the filter feeder.

Optimal filter feeding

If we imagine that an individual can freely vary its body composition and motor power to vary A and u independently, one can explore what combinations would be favorable (Acuna 2001; Acuna et al. 2011). An optimal strategy in a stable environment is to maximize the scope for growth (Acuna 2001). The flow speed that maximizes the energy-specific scope for growth (2) with the other parameters fixed is given as

$$u_H = \frac{c}{2\,k}, \tag{3}$$

and with this strategy we obtain the maximum scope for growth as

$$H_{\max} = \frac{A\,c^2}{4\,k} - R_{\mathrm{b}}. \tag{4}$$

Thus for a high maximum growth rate, the energy-specific filter area A should be large.

An alternative optimization strategy, which is especially valuable in a changing environment with competitors for food, is to be capable of surviving at low environmental prey concentrations (Acuna et al. 2011; Tilman 1982). The concentration at which the organism can just sustain itself follows from setting H equal to zero in equation (2):

$$c(H=0) = k\,u + \frac{R_{\mathrm{b}}}{A\,u}. \tag{5}$$

Minimization of the function (5) with respect to u results in the flow speed

$$u_{\mathrm{c}} = \sqrt{\frac{R_{\mathrm{b}}}{A\,k}}, \tag{6}$$

leading to a limiting concentration

$$c_{\min}(H=0) = 2\sqrt{\frac{k\,R_{\mathrm{b}}}{A}}, \tag{7}$$

which decreases with increasing A, thus a high energy-specific filter area also favors this strategy.

In figure 2 we compare the filter flow speeds of the choanoflagellate *Diaphanoeca grandis* and the salp *Pegea confoederata* at different prey concentrations to the two optimum strategies. Each organism is characterized by fixed A and k, which we obtain from measured energy-specific filter areas and filter characteristics (table 1). The contour line $H = 0$ divides feasible and unfeasible strategies and it is given by the function $c(H = 0)$ defined in equation (5). For small flow speeds where the basal respiration dominates, it decreases with $c(H = 0) \approx R_\mathrm{b}/(A\,u)$, while at high flow speeds, where the filter resistance comes into play, it increases as $c(H = 0) \approx k\,u$. Both organisms produce flow speeds that are substantially lower than the optimum speeds for maximization of the growth rate at typical concentrations (3) and for survival at the lowest concentrations and (6). The observed low flow speeds can maximize H at very low concentrations (Acuna 2001), but the strategy is not feasible when the resulting growth rate is negative (figure 2).

Figure 3A shows filter feeding strategies at an average observed prey concentration. The strategies are defined as combinations of the traits u and A, where we assume a constant filter resistance k (table 2). Here the contour $H = 0$, which again separates feasible and unfeasible strategies, is characterized by the curve

$$A(H = 0) = \frac{R_\mathrm{b}}{u\,c - k\,u^2}. \tag{8}$$

At low flow speeds we find the decreasing function $A(H = 0) \approx R_\mathrm{b}/(u\,c)$, and $A(H = 0)$ diverges when $u = c/k$. The maximum flow speed c/k, above which we have $G - R_\mathrm{f} < 0$ and thus negative scope for growth, defines a general limit for all filter feeding strategies. However, most observed filter feeders are far from reaching this maximum flow speed. A limitation to feasible strategies is given as the energy-specific filter area that is the minimum of $A(H = 0)$, i.e.,

$$A_\mathrm{min}(H = 0) = \frac{4\,k\,R_\mathrm{b}}{c^2}. \tag{9}$$

Planktonic filter feeders often exhibit low flow speeds, where the dynamic loss kAu^2 can be neglected compared to the constant basal respiration rate (Alldredge and Madin 1982; Kiørboe and Hirst

2014). Thus the growth rate $H \approx A\,u\,c - R_\mathrm{b}$ is approximately equal for the observed strategies that have approximately constant energy-specific clearance rates $A\,u$.

The observations here illustrate that filter feeding strategies are characterized by combinations of physiological and behavioral traits that are defined by a constant energy-specific clearance rate. Flow speeds, however, are found to be insufficient to utilize either of the two optimum strategies, thus we cannot explain the observed trait combinations by global optimization. This suggests physical constraints on the flow speeds that the organisms can produce.

Limitations on body plan and flow speed

There are of course limits to the power and force that the flow-creating motor can generate and these limits depend on the body plan. One natural constraint is found by assuming that the maximum motor power scales linearly with the energy content of the organism. Such a scaling is suggested by several studies on metabolic rates at high activity that found close to linear scaling relations (Glazier 2014; Meyer-Vernet and Rospars 2016; Weibel and Hoppeler 2005). From this we obtain a constant maximum limit R_max to the energy-specific dynamic respiration rate R_f, as has also been found for the energy-specific total respiration rate (Kiørboe and Hirst 2014). We make the simplifying assumption that the maximum motor power is equal to the basal respiration rate, i.e., in the extreme case the total consumption is divided equally into flow creation and basic investment. Thus we have

$$k\,A\,u^2 \;=\; R_\mathrm{f} < R_\mathrm{max} \;=\; R_\mathrm{b}. \tag{10}$$

The larger the energy-specific filter area of an organism, the lower is the flow speed that the motor can generate. With the power limit R_max the flow speed is limited by a maximum

$$u_R = \sqrt{\frac{R_\mathrm{max}}{k\,A}}. \tag{11}$$

We further consider a maximum motor force. For complex motors of multicellular organisms Marden and Allen (2002) have found that the maximum force scales linearly with the motor mass

with a universal constant of proportionality. In our model we can define such a limit as a constant maximum energy-specific force $F_{\max}$ from which we obtain the constraint

$$A\,\Delta p = k\,A\,u < F_{\max}. \tag{12}$$

Due to the force limit $F_{\max}$ the flow speed is limited by a maximum

$$u_F = \frac{F_{\max}}{k\,A}. \tag{13}$$

If both power and force limits are valid as general constraints, the limit to motor performance is ultimately determined by the lower of the two, i.e., if the maximum force limit leads to a higher power than feasible, the motor switches from being force-limited to being power-limited.

Figure 3 B shows for typical observed environmental prey concentrations the feasible combinations of body plans A and filter speeds u, which are restricted by the growth limit $H = 0$ (8) and the motor performance limits $R_{\max}$ (11) and $F_{\max}$ (13) (table 2). Now consider the strategies that achieve maximum growth rate within the limits. At low flow speeds and large filter areas, the force limit $F_{\max}$ (12) dominates. Due to the low speeds we can approximate $H \approx A\,u\,c - R_{\mathrm{b}} = F\,c/k - R_{\mathrm{b}}$. Growth is then maximized at the largest possible force $F = F_{\max}$. Note that here a constant growth rate not only coincides with constant force but also constant clearance rate. Thus, assuming maximum growth strategies, we define the maximum force $F_{\max} = k\,(A\,u)_{\max}$ from the maximum observed clearance rates. On the other hand, when the filter area is smaller, the power limit $R_{\max}$ (10) takes over, which forces the force below $F_{\max}$, thus leading to lower clearance and a growth rate that decrease with decreasing A until $H = 0$ at $A_{\min}$ (9).

If the energy-specific force of filter feeders is constant, the filter area is limited by the minimum

$$A_{\mathrm{F}} = \frac{F^2}{cF - R_{\mathrm{b}}k}, \tag{14}$$

below which the growth rate becomes negative. However, the transition between force and power limit occurs at

$$A_{\mathrm{RF}} = \frac{F_{\max}^2}{k\,R_{\max}}. \tag{15}$$

Thus in the case of constant energy-specific force, the larger limit A_{F} or A_{RF} determines the
168 minimum feasible filter area. Our model places most observed filter feeders in the force-limited regime in typical oceanic environments with large energy-specific areas $A > A_{RF} > A_{\mathrm{F}} > A_{\mathrm{min}}$
170 (figure 3).

If we assume a smaller maximum investment $R_{\mathrm{max}} < R_{\mathrm{b}}$ in flow creation, the feasible range
172 of trait combinations would shrink and A_{RF} as well as A_{min} would become larger and thus more strict. A larger R_{max}, on the other hand, would not increase the feasible range significantly, due to
174 the force limitation.

Discussion

176 We used an energy-budget model to determine optima and limits to body composition and kinematics in active planktonic filter feeders. The available strategies are found to be limited mainly by
178 a universal maximum energy-specific motor force which leads to constant energy-specific clearance rates across species groups. This is confirmed by empirical findings on clearance as well as filtra-
180 tion rates (Alldredge and Madin 1982; Kiørboe and Hirst 2014). The limits to motor performance restrict the access to optimum strategies.

When representing the observed energy densities for small plankton as a function of their energy content, we observe three distinct groups (figure 4) (Kiørboe 2013). Unicellular organisms with a 'natural' dense body composition and a small energy content, pelagic tunicates and jelly fish with a large energy content but low energy density, and other zooplankton with a 'natural' dense body composition and high energy content. We here argue that distinct body plans are a consequence of foraging strategy. The argument for filter feeders is that there exists a minimum energy-specific filter area, below which the filter feeding strategy becomes unfeasible. From this minimum, A, we can determine a maximum energy density as a function of body energy content E as

$$\rho_{\mathrm{max}} = \frac{E}{V} = \frac{1}{A^{3/2}\, E^{1/2}}. \tag{16}$$

182 We have determined different characteristic values for the minimum A, the transition A_{RF} (15),

below which the power limit dominates and the observed constant energy-specific clearance rates
184 can no longer be achieved. A more strict limit is given by the minimum energy-specific area $A_{\min}$ (9), below which no positive growth rates can be achieved at a given prey concentration (figure
186 4). The typical body composition with an energy density around $10^{10}\,\mathrm{J\,m^{-3}}$ is feasible for small unicellular filter feeders which have a low energy content. Their small size allows them a sufficiently
188 large relative filter area with no need to be gelatinous (dwarf strategy). Larger organisms with a high energy content, however, are forced by (16) to have a lower energy density, i.e., a larger wet
190 volume, in order to sustain a large enough encounter surface. This leads to the emergence of what we call gelatinous giants (Acuna 2001).

To what extent can our arguments be generalized to other interception feeders that do not possess a filter? For large interception feeders that cruise through the water and directly intercept prey on their body, such as jellyfish, Acuna et al. (2011) developed a model for the scope for growth. With Acuna's assumption that the main energy cost for those organisms is due to the drag force on the swimming body, we can write their energy-specific scope for growth analogous to the filter feeder model (equation (2)) as

$$H = S\,v\,c - D\,S\,v^3 - R_\mathrm{b}, \tag{17}$$

where S is the energy-specific projected body area in the flow direction, D a constant proportional to the drag coefficient and v the swimming speed. The main difference to the filter feeders is contained in the scaling of the flow producing power with v^3 instead of with v^2 due to the higher Reynolds number of the feeding flow. However, we obtain very similar qualitative features of the model and can determine a minimum energy-specific area as

$$S_\mathrm{min} = \frac{3}{2}\sqrt{\frac{3\,D\,R_\mathrm{b}^2}{c^3}}, \tag{18}$$

192 below which the scope for growth will always be negative. Limits to the body composition, as in filter feeders, follow from equation (16) with S instead of A, and thus large interception feeders,
194 that actively create the feeding current, seem generally restricted by a maximum feasible energy density at high energy content, which decreases as $E^{-1/2}$ (cf. figure 4).

For the third large-sized group in figure 4, 'other zooplankton', interception feeding in the pelagic zone is not feasible. Most other pelagic organisms including fish would fall in the same category (Acuna et al. 2011). Rather than compensating for their otherwise declining energy-specific prey encounter surface by being gelatinous, these organisms have evolved advanced sensing capabilities and perceive their prey individually and from a distance. Remote prey sensing can be hydrodynamic, as in copepods, or visual, as in fish (Martens et al. 2015).

Observations suggest that organisms are either gelatinous or dense, with few intermediate species (figure 4)(Kiørboe 2013). Our arguments here and the suggested scaling would suggest the existence of organisms with intermediate energy densities in the range of body energy contents between 10^{-2} and 10^{0} J. However, this two order of magnitude size range with no observations marks the transition between unicellular and multicellular species, with the latter typically consisting of 100 or more cells, hence the gap in figure 4.

We have demonstrated that physiological constraints ultimately limit the motor performance and, hence, the ability of filter feeders to perform optimally. We now compare the observed energy-specific forces of filter feeders to constant motor mass specific forces, observed by Marden and Allen (2002) for a group of cyclical motors that are subject to multi-axial stress. With the measured average energy-specific filtration rate $A\,u = 5 \cdot 10^{-9}\,\mathrm{m^3\,s^{-1}\,J^{-1}}$ and a typical filter resistance $k = 10^{4}\,\mathrm{kg\,m^{-2}\,s^{-1}}$ (table 2) we can calculate the energy-specific forces used to create the feeding current to approximately $F = 5 \cdot 10^{-5}\,\mathrm{N\,J^{-1}}$ for planktonic filter feeders. In order to convert to forces per motor mass we multiply with the ratio of motor energy density to mass density. The motor mass density is estimated with the density of water as $\rho_{\mathrm{w}} \approx 10^{3}$ kg m^{-3}. The motor energy density is determined as the largest observed body energy density ($\rho_{\mathrm{E}} \approx 10^{10}$ J m^{-3}), which will generally underestimate the mass-specific force, as it includes the entire body, not only the (more dense) motor (Acuna 2001; Kiørboe 2013). Using the above estimated average energy-specific force, we get a motor mass specific force of around 500 N kg^{-1} for planktonic filter feeders. Marden and Allen (2002) found a universal much smaller 57 N kg^{-1}, around which a wide range of motors cluster tightly, including biological motors such as swimming fish. However, in their sample of

specific force-limited motors, biological motors acting in the low Reynolds number regime are not represented. The mass-specific forces produced by copepods during escape jumps (Kiørboe et al. 2010) are similarly an order of magnitude larger than the universal value proposed by Marden and Allen (2002). This suggests special circumstances for motors which create flows at low Reynolds number (here: $Re \lesssim 10^{-3}$ (Sutherland et al. 2010)), while the motor with lowest Reynolds number that exhibits the specific force scaling proposed by Marden and Allen has $Re \approx 10^2$ (Marden 2005; Marden and Allen 2002).

The simplifying assumptions make the model only directly applicable to a subset of the organisms that are typically classified as filter feeders. First of all the model applies to low Reynolds number filter feeders that actively create a feeding flow through fine-meshed filters. The filter modeled as an infinite array is assumed to be prevented from flow circumvention, e.g., by a surrounding channel structure. The additional resistance due to surrounding walls and channel ends is neglected, which is reasonable for fine-meshed filters inside a wide cavity, where the filter resistance due to the mesh dominates. Further the flow-creating motor is assumed to be separate from the filter unlike in ciliated filters where pump elements on the fibers themselves create an effective slip velocity such as in bivalves, brachiopods, or bryozoans (Riisgård and Larsen 2010). Most of those ciliary suspension feeders, however, live in the benthic zone where more prey is available, while our predictions are focused on pelagic plankton that live in a very dilute environment. The model applies to typical planktonic filter feeders in the pelagic zone, such as the specifically modeled salps and choanoflagellates (Nielsen et al. 2017), but it does not apply to organisms with flapping bristles, where flow circumvention plays a significant role (Cheer and Koehl 1987). Filter feeding baleen whales, manta rays, or anchovies, which are not gelatinous, can survive in the pelagic zone by using sensory apparatus to switch to raptorial feeding or to seek out patches of high prey concentration and furthermore those large organisms feed at higher Reynolds numbers than planktonic filter feeders (Burgess et al. 2016; Goldbogen et al. 2013; Hunter and Dorr 1982; Nonacs et al. 1998).

With our study we do not attempt to explain the detailed design and behavior of different planktonic filter feeders with optimality theory (Dudley and Gans 1991; Koehl 1989). Instead

we use a model framework with a minimal number of traits that can constitute a generic filter feeder to investigate optima and limitations of those traits in the pelagic realm. We identify a range of trait combinations that are physically possible or that give an evolutionary advantage to filter feeders under specific conditions. We focus on a mechanistic understanding of the important parameters and their various effects to investigate species-overarching trends rather than making precise quantitative predictions for one unique optimal design and behavior of a single species.

Acknowledgments

We are thankful to Friederike Prowe and Tomas Bohr for stimulating discussions during the development of this model study. The Centre for Ocean Life is a VKR Centre of Excellence supported by the Villum Foundation.

References

Acuna, J. L. 2001. Pelagic Tunicates: Why Gelatinous? American Naturalist 158:100–107.

Acuna, J. L., A. Lopez-Urrutia, and S. Colin. 2011. Faking giants: the evolution of high prey clearance rates in jellyfishes. Science 333:1627–1629.

Alldredge, A. L., and L. P. Madin. 1982. Pelagic tunicates: unique herbivores in the marine plankton. Bioscience 32:655–663.

Andersen, V. 1986. Effect of temperature on the filtration rate and percentage of assimilation of *Salpa fusiformis* cuvier (tunicata: thaliacea). Hydrobiologia 137:135–140.

Arai, M. N. 2001. Pelagic coelenterates and eutrophication: a review. Hydrobiologia 451:69–87.

Ayaz, F., and T. J. Pedley. 1999. Flow through and particle interception by an array of closely-spaced circular cylinders. Eur. J. Mech. B/Fluids 18:173–196.

Bone, Q. 1998. The biology of pelagic tunicates. Oxford University Press.

Bone, Q., J. C. Braconnot, and K. P. Ryan. 1991. On the Pharyngeal Feeding Filter of the Salp *Pegea confoederata* (Tunicata: Thaliacea). Acta Zoologica 72:55–60.

Buck, K. R., F. P. Chavez, and L. Campbell. 1996. Basin-wide distributions of living carbon components and the inverted trophic pyramid of the central gyre of the North Atlantic Ocean. Aquatic Microbial Ecology 10:283–298.

Burgess, K. B., L. I. E. Couturier, A. D. Marshall, A. J. Richardson, S. J. Weeks, and M. B. Bennett. 2016. *Manta birostris*, predator of the deep? Insight into the diet of the giant manta ray through stable isotope analysis. Royal Society Open Science 3:1–10.

Cheer, A. Y. L., and M. A. R. Koehl. 1987. Paddles and rakes: fluid flow through bristled appendages of small organisms. Journal of Theoretical Biology 129:17–39.

Condon, R. H., W. M. Graham, C. M. Duarte, K. A. Pitt, C. H. Lucas, S. H. D. Haddock, K. R. Sutherland, K. L. Robinson, M. N. Dawson, M. B. Decker, C. E. Mills, J. E. Purcell, A. Hermes, Milaj, H. Mianzan, S. I. Uye, S. Gelcich, and L. P. Madin. 2012. Questioning the rise of gelatinous zooplankton in the world's oceans. Bioscience 62:160–169.

Crawford, D. W. 1992. Metabolic cost of motility in planktonic protists: Theoretical considerations on size scaling and swimming speed. Microbial Ecology 24:1–10.

Dudley, R., and C. Gans. 1991. A critique of symmorphosis and optimality models in physiology. Physiological Zoology 64:627–637.

Follows, M. J., and S. Dutkiewicz. 2011. Modeling diverse communities of marine microbes. Annual Review of Marine Science 3:427–451.

Franks, P. J. S. 2009. Planktonic ecosystem models: perplexing parameterizations and a failure to fail. Journal of Plankton Research 31:1299–1306.

Glazier, D. S. 2014. Scaling of metabolic scaling within physical limits. Systems 2:425–450.

Goldbogen, J. A., A. S. Friedlaender, J. Calambokidis, M. F. McKenna, M. Simon, and D. P. Nowacek. 2013. Integrative approaches to the study of baleen whale diving behavior, feeding performance, and foraging ecology. BioScience 63:90–100.

Hansen, B., P. K. Bjornsen, and P. J. Hansen. 1994. The size ratio between planktonic predators and their prey. Limnology and Oceanography 39:395–403.

Harbison, G. R. 1992. The gelatinous inhabitants of the ocean interior. Oceanus 35:18–23.

Hunter, J. R., and H. Dorr. 1982. Thresholds for filter feeding in northern anchovy *Engraulis mordax*. CalCOFI Reports 23:198–204.

Jeschke, J. M., M. Kopp, and R. Tollrian. 2004. Consumer-food systems: why type I functional responses are exclusive to filter feeders. Biological Reviews 79:337–349.

Kiørboe, T. 2011. How zooplankton feed: mechanisms, traits and trade-offs. Biological Reviews 86:311–339.

———. 2013. Zooplankton body composition. Limnology and Oceanography 58:1843–1850.

Kiørboe, T., A. Andersen, V. J. Langlois, and H. H. Jakobsen. 2010. Unsteady motion: escape jumps in planktonic copepods, their kinematics and energetics. Journal of the Royal Society Interface 7:1591–1602.

Kiørboe, T., and A. G. Hirst. 2014. Shifts in mass scaling of respiration, feeding, and growth rates across life-form transitions in marine pelagic organisms. American Naturalist 183:E119–E130.

Koehl, M. A. R. 1989. Discussion: from individuals to populations. *In* R. M. May and S. A. Levin, eds., Perspectives in ecological theory. Princeton University Press.

Leadbeater, B. S. C. 2015. The Choanoflagellates: Evolution, Biology and Ecology. Cambridge University Press.

Lehman, J. T. 1976. The filter-feeder as an optimal forager, and the predicted shapes of feeding curves. Limnology and Oceanography 21:501–516.

Lombard, F., E. Selander, and T. Kiørboe. 2011. Active prey rejection in the filter-feeding appendicularian *Oikopleura dioica*. Limnology and Oceanography 56:1504–1512.

López-Urrutia, Á., J. L. Acuña, X. Irigoien, and R. Harris. 2003. Food limitation and growth in temperate epipelagic appendicularians (tunicata). Marine Ecology Progress Series 252:143–157.

Lucas, C. H., and M. N. Dawson. 2014. What are jellyfishes and thaliaceans and why do they bloom? *In* Jellyfish blooms. Springer Netherlands.

Makarieva, A. M., V. G. Gorshkov, B.-L. Li, S. L. Chown, P. B. Reich, and V. M. Gavrilov. 1992. Feeding, metabolism, and growth of *Cyclosalpa bakeri* in the subarctic pacific. Limnology and Oceanography 37:1236–1251.

———. 2008. Mean mass-specific metabolic rates are strikingly similar across life's major domains: Evidence for life's metabolic optimum. Proceedings of the National Academy of Sciences 105:16994–16999.

Marden, J. H. 2005. Scaling of the maximum net force output by motors used for locomotion. Journal of Experimental Biology 208:1653–1664.

Marden, J. H., and L. R. Allen. 2002. Molecules, muscles, and machines: universal performance characteristics of motors. Proceedings of the National Academy of Sciences 99:4161–4166.

Martens, E. A., N. Wadhwa, N. S. Jacobsen, C. Lindemann, K. H. Andersen, and A. Visser. 2015. Size structures sensory hierarchy in ocean life. Proceedings of the Royal Society B 282:20151346.

Meyer-Vernet, N., and J. P. Rospars. 2016. Maximum relative speeds of living organisms: Why do bacteria perform as fast as ostriches? Physical Biology 13:066006.

Nielsen, L. T., S. S. Asadzadeh, J. Dölger, J. H. Walther, T. Kiørboe, and A. Andersen. 2017. Hydrodynamics of microbial filter feeding. Proceedings of the National Academy of Sciences 114:9373–9378.

Nonacs, P., P. E. Smith, and M. Mangel. 1998. Modeling foraging in the northern anchovy (*Engraulis mordax*): individual behavior can predict school dynamics and population biology. Canadian Journal of Fisheries and Aquatic Sciences 55:1179–1188.

Parker, G. A., and J. M. Smith. 1990. Optimality theory in evolutionary biology. Nature 348:27–33.

Riisgård, H. U., and P. S. Larsen. 2010. Particle capture mechanisms in suspension-feeding invertebrates. Marine Ecology Progress Series 418:255–293.

Schmidt-Nielsen, K. 2007. Animal Physiology - Adaptation and environment. Cambridge University Press.

Smith, S. L., A. Merico, K. W. Wirtz, and M. Pahlow. 2014. Leaving misleading legacies behind in plankton ecosystem modelling. Journal of Plankton Research 36:613–620.

352 Smith, S. L., M. Pahlow, A. Merico, and K. W. Wirtz. 2011. Optimality-based modeling of planktonic organisms. Limnology and Oceanography 56:2080–2094.

354 Sørnes, T. A., and D. L. Aksnes. 2004. Predation efficiency in visual and tactile zooplanktivores. Limnology and Oceanography 49:69–75.

356 Sutherland, K. R., L. P. Madin, and R. Stocker. 2010. Filtration of submicrometer particles by pelagic tunicates. Proceedings of the National Academy of Sciences 107:15129–15134.

358 Svetlichny, L. S., and E. Hubareva. 2005. The energetics of *Calanus euxinus*: locomotion, filtration of food and specific dynamic action. Journal of Plankton Research 27:671–682.

360 Tamada, K., and H. Fujikawa. 1957. The steady two-dimensional flow of viscous fluid at low reynolds numbers passing through an infinite row of equal parallel circular cylinders. The Quarterly
362 Journal of Mechanics and Applied Mathematics 10:425–432.

Tilman, D. 1982. Competition for a single resource. *In* Resource competition and community
364 structure. Princeton University Press.

Vogel, S. 1994. Life in moving fluids: the physical biology of flow. Princeton University Press.

366 Weibel, E. R., and H. Hoppeler. 2005. Exercise-induced maximal metabolic rate scales with muscle aerobic capacity. Journal of Experimental Biology 208:1635–1644.

368 Werner, E. E., and D. J. Hall. 1974. Optimal foraging and the size selection of prey by the bluegill sunfish (*Lepomis macrochirus*). Ecology 55:1042–1052.

370 Winter, J. E. 1978. A review on the knowledge of suspension-feeding in lamellibranchiate bivalves, with special reference to artificial aquacultural systems. Aquaculture 13:1–33.

372 Wirtz, K. W. 2012. Intermittency in processing explains the diversity and shape of functional grazing responses. Oecologia 169:879–894.

Tables

Table 1: Parameter values for *Diaphanoeca grandis* and *Pegea confoederata*.

Parameter	Description	*D. grandis*	*P. confoederata*
$u\,(\mathrm{m\,s^{-1}})$	filter flow speed	$5 \cdot 10^{-5}$	$2 \cdot 10^{-3}$
$A\,(\mathrm{m^2\,J^{-1}})$	energy-specific filter area	$4 \cdot 10^{-5}$	$6 \cdot 10^{-6}$
$R_\mathrm{b}\,(\mathrm{s^{-1}})$	energy-specific basal respiration rate	$1 \cdot 10^{-6}$	$1 \cdot 10^{-6}$
$k\,(\mathrm{kg\,m^{-2}\,s^{-1}})$	filter resistance	$3 \cdot 10^{4}$	$3 \cdot 10^{3}$

Values were calculated from data on the two example species and, where species-characteristic data were unavailable, from mean values of protozoans and tunicates (Acuna 2001; Alldredge and Madin 1982; Bone et al. 1991; Kiørboe and Hirst 2014; Nielsen et al. 2017; Sutherland et al. 2010). The energy contents used for the energy-specific quantities were converted from the measured carbon masses with the conversion factor $5.5 \cdot 10^7\,\mathrm{J\,kgC^{-1}}$ (Acuna 2001). The respiration rates were converted from oxygen to energy consumption per time with the conversion factor $20\,\mathrm{J\,ml{O_2}^{-1}}$ (Schmidt-Nielsen 2007). The filter resistance coefficient was calculated as $k = \frac{8\,\pi\,\mu}{l}\left(1 - 2\ln\tau + \frac{1}{6}\tau^2 - \frac{1}{144}\tau^4 + \frac{1}{1080}\tau^6 - \frac{53}{345600}\tau^8 + \frac{139}{5443200}\tau^{10}\right)^{-1}$ with $\tau = 2\pi\,a/l$ assuming a parallel-cylinder filter (Tamada and Fujikawa 1957).

Table 2: Estimated parameter values and ranges for a standard planktonic filter feeder.

Parameter	Description	Value/Range
$c_{\min}$ $(\mathrm{J\,m^{-3}})$	minimum prey concentration	$5 \cdot 10^2$
c_{mean} $(\mathrm{J\,m^{-3}})$	mean prey concentration	$5 \cdot 10^3$
l (m)	filter mesh spacing	$1 \cdot 10^{-6}$
a (m)	filter fiber radius	$1 \cdot 10^{-7}$
k $(\mathrm{kg\,m^{-2}\,s^{-1}})$	filter resistance	$1 \cdot 10^4$
R_{b} $(\mathrm{s^{-1}})$	energy-specific basal respiration rate	$1 \cdot 10^{-6}$
$R_{\max}$ $(\mathrm{s^{-1}})$	maximum energy-specific power	$1 \cdot 10^{-6}$
$F_{\max}$ $(\mathrm{N\,J^{-1}})$	maximum energy-specific force	$1 \cdot 10^{-4}$
A $(\mathrm{m^2\,J^{-1}})$	energy-specific filter area	$(0.5; 100) \cdot 10^{-6}$
$\log[A\,u/(\mathrm{m^3\,J^{-1}\,s^{-1}})]$	energy-specific filtration rate	-8.3 ± 0.4

Observed and estimated particulate carbon concentrations in the open ocean were used to calculate energy concentrations with the conversion factor $5.5 \cdot 10^7\,\mathrm{J\,kgC^{-1}}$ (Acuna 2001; Buck et al. 1996; Kiørboe 2011). Mean energy densities and measured filter/surface areas versus energy content for different organisms were used to calculate a range of energy-specific areas (Acuna 2001; Alldredge and Madin 1982; Kiørboe 2013). The energy-specific basal respiration rate (and the maximum energy-specific power) were estimated from average measured carbon-specific rates (Kiørboe and Hirst 2014). The maximum energy-specific force was estimated from the highest energy-specific filtration rate in filter feeders using $F_{\max} = k\,A\,u$. Energy-specific filtration rates were taken from (Alldredge and Madin 1982), together with salp and choanoflagellate data from (Nielsen et al. 2017; Sutherland et al. 2010) to estimate the range for true filter feeders. Values for $A\,u$ represent the mean and standard deviation assuming a log-normal distribution.

Figures

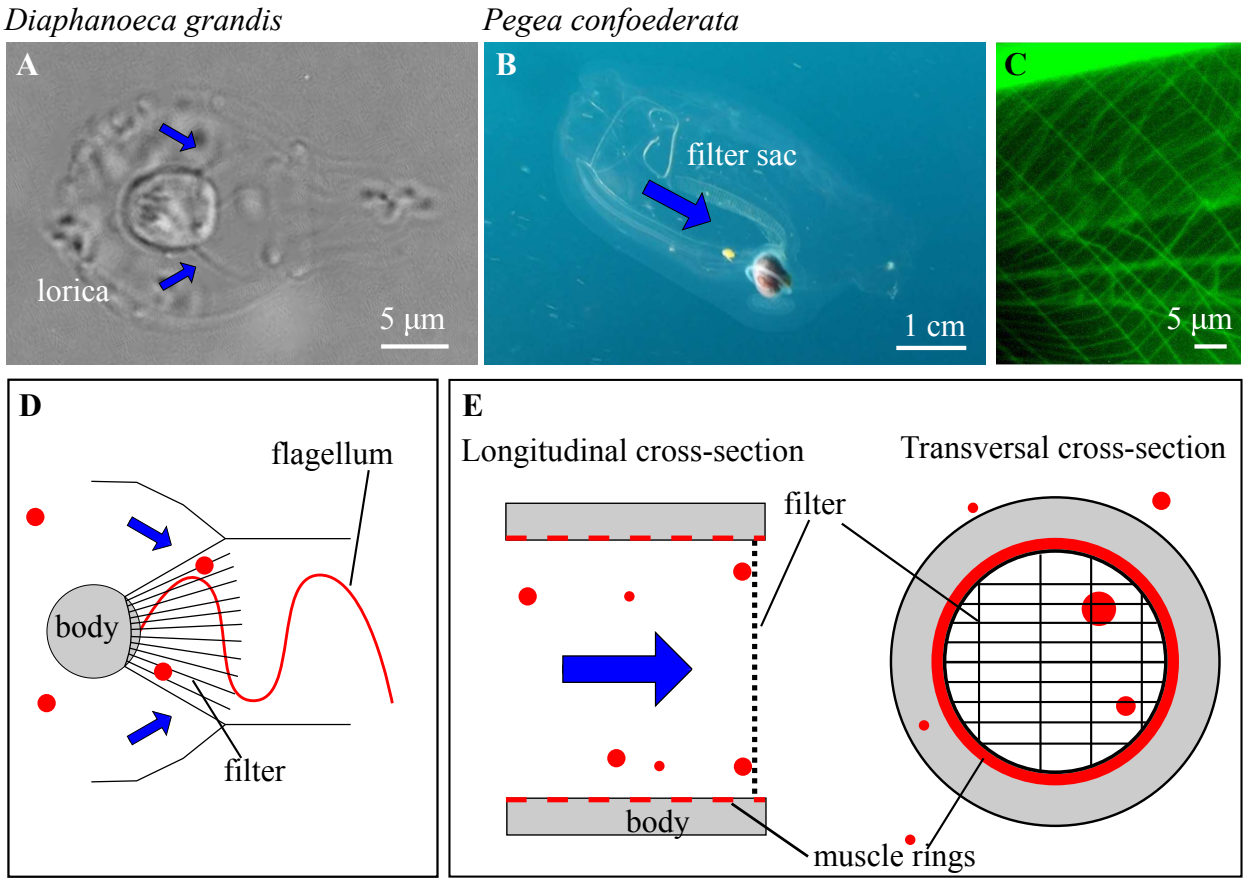

Figure 1: Morphology and models of planktonic filter feeders. (A) Choanoflagellate of species *Diaphanoeca grandis* with cell, collar filter, flagellum, and basket-like lorica structure with particles stuck on it. Image by courtesy of Lasse Tor Nielsen. (B) Salp of species *Pegea confoederata* with gelatinous barrel-shaped body and filter-sac. (C) Mucous filtering mesh of *P. confoederata*. Images (B) and (C) by courtesy of Kelly R. Sutherland. Simplified models of choanoflagellate (D) and salp-type (E) filter feeders, respectively. Blue arrows indicate flow directions.

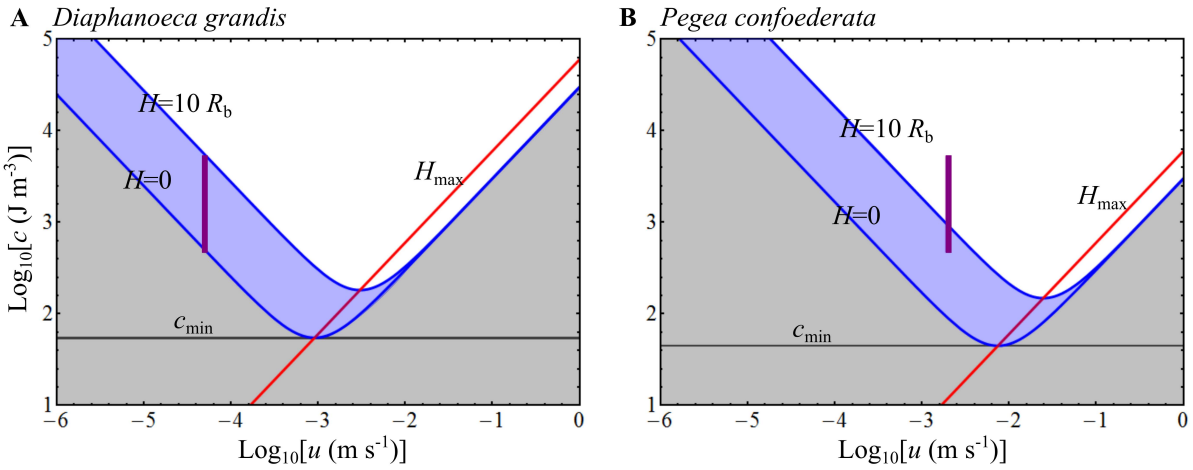

Figure 2: Energy-specific scope for growth H in the parameter space of filter flow speed u and prey concentration c for the choanoflagellate *Diaphanoeca grandis* (A) and the salp *Pegea confoederata* (B). Regions of positive (blue, white) and negative (grey) growth rates are divided by the contour line for $H = 0$, and the growth rates equal to ten times the basic metabolic rate $H = 10\,R_\mathrm{b}$ (blue) are shown. The flow speed that yields the maximum growth rate (H_max) at a given prey concentration is shown by the red line (equation (3)) and the lowest prey concentration $c_\mathrm{min}(H = 0)$, at which the organism can survive, is shown as the black line (equation (7)). Filter flow speeds and a typical range of food concentrations in the ocean are shown by purple bars. The measured flow speeds are in both organisms much smaller than the speeds (3) and (6) needed to maximize a positive growth rate (H_max) or to optimize survival at low prey concentrations ($c_\mathrm{min}(H = 0)$).

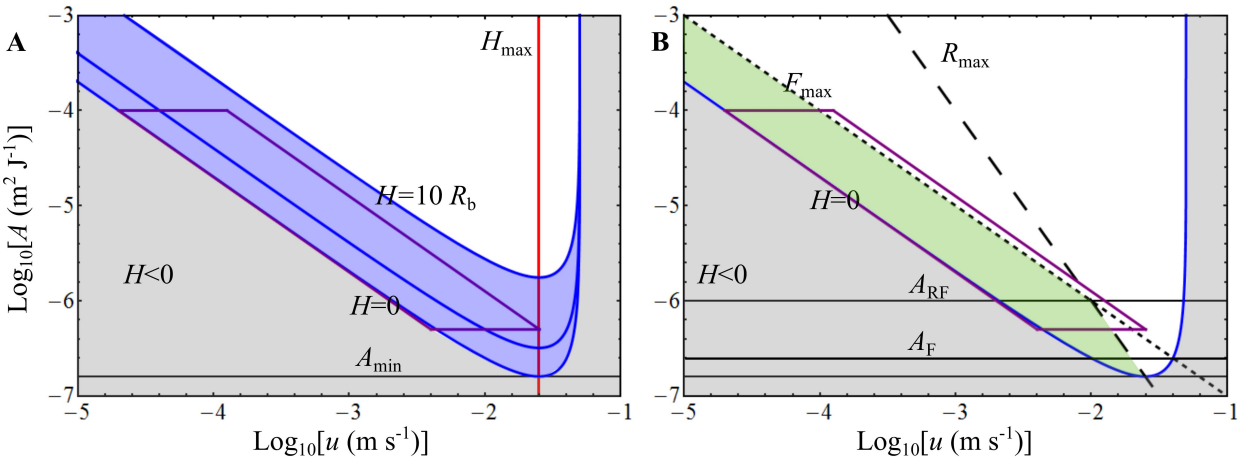

Figure 3: Filter feeding strategies with optima and constraints. Scope for growth H as function of filter flow speed u and energy-specific filter area A of general filter feeders with constant filter resistance at a characteristic prey concentration $c = 5 \cdot 10^3\,\mathrm{J\,m^{-3}}$. Unfeasible trait combinations leading to negative growth rate (grey). Above the contour line for $H = 0$ growth is positive. (A) The range of trait combinations in planktonic filter feeders is marked (purple box) as well as the range of positive growth rates up to ten times the basal respiration rate R_b (blue). Most of the found flow speeds lead to growth rates that are well below the maximum H_max (red line). (B) The allowed strategies (green) are additionally limited by the maximum power R_max and the maximum force F_max of the respective motor. The trait combinations and the scaling of the clearance rates in planktonic filter feeders suggest that they are mainly limited by a maximum force. One can define several minimum limits to the filter area. Below A_min the growth rate becomes negative for all flow speeds and below A_RF the force, clearance rate, and growth rate decrease, being constrained by the maximum motor power R_max. The value A_F describes the minimum feasible filter area, if the motor force $F = F_\mathrm{max}$ is constant.

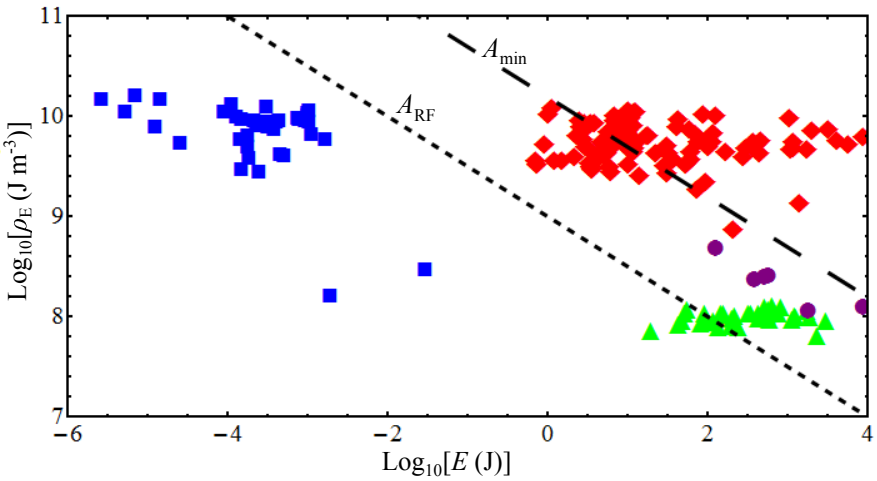

Figure 4: Energy density as function of body energy content for protozoans (squares, blue), tunicates (triangles, green), jellyfish (circles, purple), and other zooplankton that are mainly copepods (diamonds, red) (Kiørboe 2013). The black lines indicate energy densities, above which the model predicts filter feeding to become unfeasible. They are calculated from minimum energy-specific surface areas with equation (16) using A_{RF} from equation (15) (black, dotted) and $A_{\min}$ from equation (9) at low observed prey concentration $c = 5 \cdot 10^2\ \mathrm{J\,m^{-3}}$ (black, dashed) (cf. figure 3 B).

5.5 Capture of finite-sized prey

Manuscript in preparation.

Advective-diffusive capture of finite-sized prey by direct interception feeders

Julia Dölger,[1] Raphaël Jeanneret,[2] Anders Andersen,[1] and Marco Polin[3]

[1]*Department of Physics and Centre for Ocean Life, Technical University of Denmark, DK-2800 Kgs. Lyngby, Denmark*

[2]*Mediterranean Institute for Advanced Studies, IMEDEA (CSIC-UIB), Miquel Marqués 21, 07190 Esporles, Balearic Island*

[3]*Department of Physics, University of Warwick, Gibbet Hill Road, Coventry CV4 7AL, United Kingdom*

(Dated: February 21, 2018)

Abstract

Many aquatic unicellular organisms collect prey by direct interception with their cell from dilute suspensions. The viscous flow environment makes it difficult for such organisms to encounter enough prey. We here study direct interception feeding on the model of a towed sphere that collects Brownian particles of different size by diffusion and advection. Our aim is to elucidate key aspects of feeding strategies in microorganisms, and to understand the conditions under which those organisms are able to survive solely from prey capture. Within this minimal model we calculate the capture rates and their dependence on prey size numerically and compare to analytical estimates to determine the prey size range and composition for direct interception feeders. We find analytically, that the hydrodynamic interaction of predator and prey through Faxén forces can lead to a 30% increase of the advective prey capture rate. We additionally study the effect of contact times on feeding for the case of sloppy feeders, that invest a finite foraging effort in prey capture and thus lose some prey. A perfect absorber can equally well feed on the smallest as on the largest prey, while the clearance rates are lowest for intermediate prey. On the other hand, we find that sloppy feeders lose a large amount of small prey by not instantaneously holding on to it, while much less large prey is lost. The model therefore suggests that sloppy feeders have diets, that are dominated by the largest prey species.

INTRODUCTION

Feeding by direct interception is a common strategy in small marine organisms such as unicellular flagellates that swim and create feeding currents with whip-like appendages [1, 2]. Such organisms rely on direct contact of prey on their cell surface or on attached structures.

Passive prey particles are transported towards the predator by advection as well as by Brownian diffusion. Prey of different sizes are transported and captured differently, since diffusive and advective transport as well as the interaction with the predator vary with prey size. Different capture rates for differently sized prey lead to a physical prey size selection that influences the diet of interception feeders, i.e. their prey size spectrum. If prey is sieved out of the feeding current as in filter feeders [3, 4], the external particle concentrations directly translate into the prey size spectrum of the organism with the mesh size as lower cutoff, while the physical prey size selection for direct interception is more complex. A good measure for physical prey absorption is the size-dependent clearance rate: the number of particles of a given size captured per unit time divided by the external particle concentration [5]. This is equal to the volume of water that is cleared of prey per unit time, when the external particle concentration is sufficiently low.

For different flows around towed and self-propelled organisms and structures, the advective-diffusive uptake of nutrients has been studied with scaling arguments as well as with analytical and numerical calculations [6–9]. Many of these studies focus on purely photosynthetic or osmotrophic organisms, for which light and dissolved nutrients are the only resources, despite the wide-spread ability of unicellular organisms to capture particulate prey [10]. Since dissolved nutrient molecules are much smaller than particulate prey, their size is generally disregarded, when advective-diffusive encounter rates are studied.

For finite-sized prey, however, it has been suggested that the clearance rate for direct interception feeders displays a non-monotonic behaviour as function of prey size with a minimum clearance rate at micrometer-sized prey, when taking into account advection and diffusion as well as the steric interaction between predator and prey [5, 11]. Already simple estimates for purely advective capture rates on a towed sphere predict the clearance rate to increase with prey size for large prey. On the other hand, the estimates of diffusive capture lead to increasing rates towards smaller prey (due to increased diffusion coefficients), which indicate a minimum at intermediate sizes [5]. Continuous formulas that take into account

advective and diffusive effects and the steric interaction for finite sized prey have so far mainly been in use for the particle collection in filters, since the field of aerosol theory that provides those helpful formulas is mainly focused on the retention of particles on collector arrays [11–15]. By comparison of our numerical calculations on a wide range of prey sizes with analytical formulas on the advective-diffusive particle capture we aim to determine the validity and applicability range of different estimates that can be used for the calculation of capture rates in direct interception feeders with spherical body.

Mathijssen *et al.* [16] have recently suggested that prey-size dependent entrainment times might have an additional influence on prey capture in real organisms, meaning the time that predator and prey stay in contact. Intuitively the probability of successful capture should be higher for longer contact times. The highest average contact times were found to occur for micrometer-sized particles, since larger particles due to steric interactions cannot get close to the no-slip surface of the predator, thus passing faster, while small particles, on the other hand, diffuse away more quickly. We here account for the influence of contact times on prey capture by introducing a finite probability to capture prey upon contact with a certain foraging rate. We call the organisms that have such a finite foraging rate sloppy feeders as opposed to perfect absorbers that immediately absorb all prey as soon as it is in contact. To what extent does sloppy feeding influence the capture rates and the prey size range for direct interception feeders and can we use the estimated entrainment times to calculate clearance rates of sloppy feeders?

The flow decay close to the predator cell body with zero velocity at the surface governs the characteristic contact behavior between predator and prey, while flagellar arrangements are often of less importance and can be treated as separate (enhancing) effect to the flow [16–18]. Here we focus on the simple case of a towed solid sphere with constant velocity, which approximates the near-cell flow for most flagellates and disregards additional feeding currents due to specific flagellar arrangements, since we are mainly interested in the effects of prey size.

Physical interactions between predator and prey can be due to different forces, such as van der Waals forces between the particles and hydrodynamic interactions through flows [15, 19, 20]. Here we account for the direct particle-particle interactions only through steric interactions, which simply prevent an overlap of the finite-sized prey with the predator. The hydrodynamic interaction between the particles is here considered with the Faxén forces on

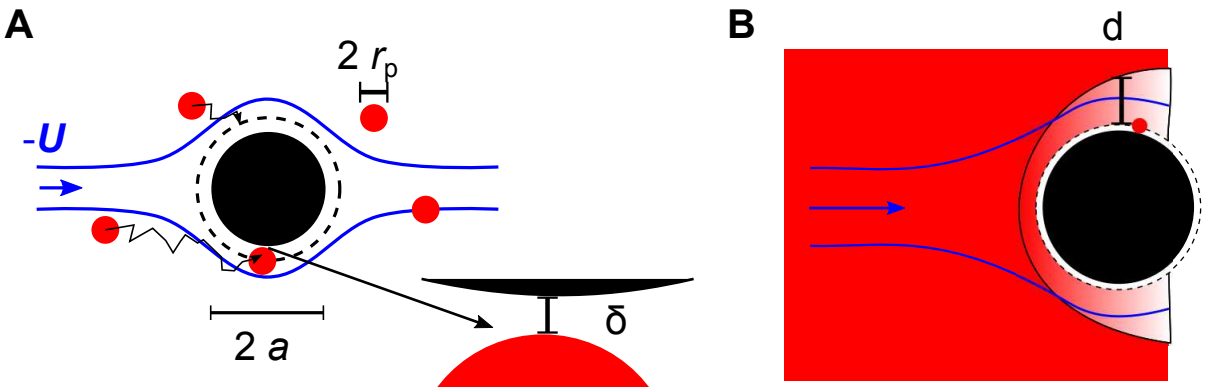

FIG. 1. Model of a direct interception feeder. (A) Prey particles of radius r_p (red) initially arrive (in the co-moving frame) with velocity $-\mathbf{U}$. They follow the flow (blue) and additionally move randomly with Brownian diffusion. The prey are captured by the predator of radius a (black filled circle), when coming within a close distance δ. The encounter surface is shown as dashed circle. (B) In the advective-diffusive case, at large Péclet number, we consider a concentration field (red) that is only depleted in a thin boundary layer around the absorber, the thickness d of which can be estimated. Sketch in (B) adapted from Friedlander [23].

the prey, that can be analytically treated and that account for the modified trajectories of small spherical particles in an external flow that here is provided by the moving predator [21, 22].

In this study we simulate the advective-diffusive capture of finite-sized prey on an interception feeder that we approximate as a towed sphere in Stokes flow. The clearance rate is numerically calculated as function of prey size, which determines the physical prey size selection of the organism. We compare the results to analytical formulas and for sloppy feeders we extract characteristic contact times that we compare to analytical formulas for entrainment times. With a typical marine particle size spectrum we calculate total capture rates and compare to the feeding rates of filter feeding microbes. We further discuss trade-offs and optimum foraging strategies of sloppy feeders.

MODEL OF DIRECT INTERCEPTION FEEDERS

Our model of a direct interception feeder consists of a spherical body of radius a, that moves with constant velocity $\mathbf{U}$. The swimming speed is assumed to scale linearly with the

body radius as $U = q\,a$ with $q = 10\,\mathrm{s}^{-1}$ [24, 25]. Prey are modelled as Brownian spherical particles with radius r_p, that are advected and diffusively transported towards the predator (figure 1 A). The advection is governed by the incompressible Stokes equations and the Einstein-Smoluchowski diffusion coefficient for Brownian motion is calculated as

$$D = \frac{k_\mathrm{B} T}{6\pi\mu r_\mathrm{p}} \tag{1}$$

with the Boltzmann constant $k_\mathrm{B} = 1.38{\cdot}10^{-23}\,\mathrm{J\,K}^{-1}$ and the absolute temperature $T = 300\,\mathrm{K}$ as well as the viscosity $\mu = 10^{-3}\,\mathrm{Pa\,s}$ of water. The parameters of the problem are a, r_p, q, T, and μ, and the thickness δ of the contact zone, i.e., the distance at which prey is captured. For sloppy feeders we additionally consider a finite foraging rate κ that determines the probability P of capture, when prey comes in contact with the predator, i.e.,

$$P = 1 - \exp(-\kappa\, t) \tag{2}$$

during the time step t. Contact occurs when prey is found in close vicinity $r < a + r_\mathrm{p} + \delta$ of the predator. In this study we consider the effects of varying prey size r_p, foraging rate κ, and thickness δ of the contact zone on the clearance rate. All other parameters are fixed.

Since for capture we are interested in the relative predator-prey velocities, we will represent the flow in the co-moving frame of the predator. The flow velocity at large distance is thus $\mathbf{v}|_{r\to\infty} = -\mathbf{U}$ and we have no-slip, i.e., $\mathbf{v}|_{r=a} = 0$, at the cell surface. For the velocity $\mathbf{u}$ of the advected finite-sized prey particles we take into account the Faxén correction [21, 22], that occurs due to the disturbance of the imposed flow by the finite-sized spherical prey. The particle velocity due to advection in the co-moving frame is thus given as

$$\mathbf{u}(\mathbf{x}) = \mathbf{v}(\mathbf{x}) + \frac{r_\mathrm{p}^2}{6}\nabla^2\mathbf{v} \tag{3}$$

$$\begin{aligned} &= U\,\cos\theta\left(\frac{3}{2r/a} - \frac{1}{2(r/a)^3} - 1 - \frac{(r_\mathrm{p}/a)^2}{2(r/a)^3}\right)\mathbf{e}_r \\ &- U\,\sin\theta\left(\frac{3}{4\,r/a} + \frac{1}{4(r/a)^3} - 1 + \frac{(r_\mathrm{p}/a)^2}{4(r/a)^3}\right)\mathbf{e}_\theta \end{aligned} \tag{4}$$

in spherical coordinates, where $\mathbf{v}$ is the well-known creeping flow past a sphere [26] and the last terms in each component originate from the Faxén correction.

We can define a Stokes stream function for the velocity field (4), since $\mathbf{v}$ as well as $\mathbf{u}$ represent axisymmetric incompressible velocity fields that are solutions to the Stokes

equations. The stream function can be written in spherical coordinates as

$$\Psi(r,\theta) = \frac{U}{2}\left(r^2 + \frac{a(a^2+r_\mathrm{p}^2)}{2\,r} - \frac{3\,a\,r}{2}\right)\sin^2\theta. \tag{5}$$

CAPTURE BY A PERFECT ABSORBER

The clearance rate $Q(r_\mathrm{p})$ describes the volume of water cleared for prey per unit time. We can calculate the clearance rate as the volume flow rate into the capture zone, if the concentration is equal to the bulk concentration everywhere, i.e., if diffusion and finite foraging rates are negligible. The capture zone is spherical with radius $a+r_\mathrm{p}$ accounting for the steric interaction with finite-sized prey. The advective clearance rate is then

$$\begin{aligned} Q_\mathrm{a} &= 2\pi(a+r_\mathrm{p})^2\int_0^{\pi/2} u_\mathrm{r}\sin\theta\mathrm{d}\theta = 2\pi\Psi(a+r_\mathrm{p},\pi/2) \\ &= \frac{U\pi r_\mathrm{p}^2}{1+r_\mathrm{p}/a}\left(2+\frac{r_\mathrm{p}}{a}\right). \end{aligned} \tag{6}$$

For small prey the advective clearance rate can be approximated as $Q_\mathrm{a} \approx 2\,U\pi r_\mathrm{p}^2$. Without Faxén correction the clearance rate is $Q_\mathrm{a} \approx 3U\pi r_\mathrm{p}^2/2$ [15]. Thus the correction contributes as much as 25% to the advective clearance rate on the sphere.

Brownian diffusion with the prey-size dependent diffusion coefficient (1) will lead to a depletion zone around the capture zone and a concentration gradient, which is described with the advection-diffusion equation. Here we only consider the steady state. If the predator is a perfect absorber with infinite foraging rate, the concentration at the capture surface is zero, while some distance away it is equal to the bulk concentration. The extent of the depletion zone decreases with increasing Péclet number

$$Pe = \frac{a\,U}{D} = \frac{6\pi\mu q a^2 r_\mathrm{p}}{k_\mathrm{B}T}. \tag{7}$$

This dimensionless number gives the ratio of the characteristic time scales for diffusion and advection.

For a typical unicellular interception feeder with $a = 10\,\mu$m, which we consider here, even the smallest organic prey of $r_\mathrm{p} = 10^{-2}\mu$m results in a high Péclet number $Pe \approx 50$ such that we can approximate the advective-diffusive capture for direct interception feeders with a thin-boundary approximation. In the thin-boundary approximation we consider the depletion zone to be thin [12, 23, 27, 28]. We can estimate its characteristic thickness d, that

leads to an effective increase of the capture zone such that we can use the advective flow rate (6) with adjusted radius $a + r_\mathrm{p} + d$ of the encounter zone (figure 1 B). Following Langmuir's analysis we equate the time t_D to remove all particles from a region of thickness d with the time t_a to pass the capture zone along a streamline with the narrowest distance $r_\mathrm{p} + d$ from the predator [27]. By this we estimate d as the thickness of the depleted boundary layer, i.e. we have

$$t_\mathrm{D} \approx \frac{d^2\pi}{4\,D} = \frac{2\,\pi a^2}{3U\,(r_\mathrm{p}+d)} \approx t_\mathrm{a} \tag{8}$$

$$\Leftrightarrow d^2 r_\mathrm{p} + d^3 - \frac{4k_\mathrm{B}Ta}{9\,\pi\mu q r_\mathrm{p}} = 0. \tag{9}$$

Here we used an approximation for the flow passing at a small distance $r_\mathrm{p} + d \ll a$ from the sphere. The cubic equation (9) can be solved for the thickness d and the final advective-diffusive clearance rate is estimated as

$$Q_\mathrm{aD} = \quad 2\pi\Psi(a + r_\mathrm{p} + d, \pi/2) = \quad \frac{\pi U(r_\mathrm{p}+d)^2}{1+(r_\mathrm{p}+d)/a}\left(\frac{3}{2} + \frac{1}{2}\left(\frac{r_\mathrm{p}}{r_\mathrm{p}+d}\right)^2 + \frac{r_\mathrm{p}+d}{a}\right) \tag{10}$$

$$\approx \qquad \pi U(r_\mathrm{p}+d)^2\left(\frac{3}{2} + \frac{1}{2}\left(\frac{r_\mathrm{p}}{r_\mathrm{p}+d}\right)^2\right). \tag{11}$$

The corresponding estimate of (11) for point particles with $r_\mathrm{p} = 0$ exhibits the characteristic scaling of advectively enhanced diffusion at high Péclet number with

$$Q_\mathrm{aD} \sim (Pe)^{1/3} Q_\mathrm{D} \sim U^{1/3} D^{2/3} a^{4/3}, \tag{12}$$

where $Q_\mathrm{D} = 4\pi a D$ is the purely diffusive clearance [28, 29].

We numerically calculated prey-size dependent clearance rates for a typical interception feeder of radius $a = 10\mu$m, where we chose the thickness of the contact zone as $\delta = 10^{-1}\mu$m. The clearance rates are scaled with the guide line daily amount (GDA), that is $1\,\mathrm{GDA} = 4\pi a^3\, q/3$, around one million cell volumes per day, which is a guideline for the clearance rate that is needed to survive in a typical marine environment [2]. We simulated a range of prey sizes from the smallest organic prey $r_\mathrm{min} = 10^{-2}\mu$m to a maximum prey size that we set to $r_\mathrm{max} \approx 0.3\,a = 3\,\mu$m.

We observe minimum clearance rates for around micron-sized prey as suggested from the analytical formulas (figure 2). Large prey is mainly captured advectively, thus following the analytical calculation for purely advective capture (equation (6)). The small prey, for which

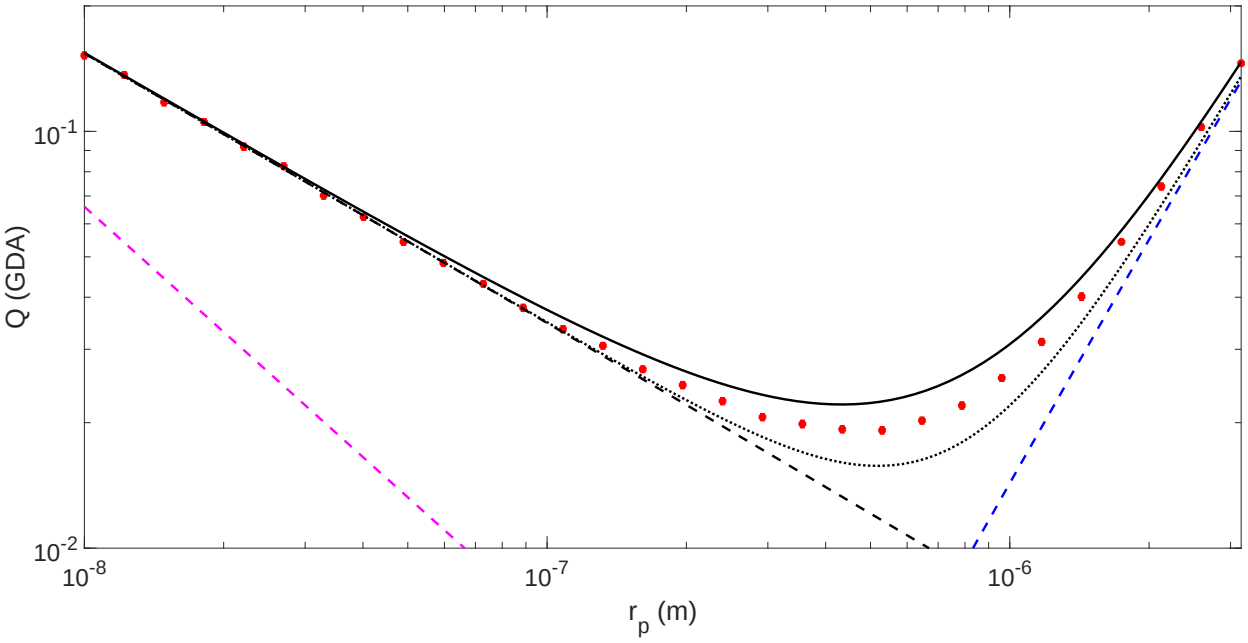

FIG. 2. Clearance rates for a perfect absorber as function of prey size. Numerically calculated clearance rate (red filled circles), where the diameter of the circles indicate the 95 % confidence interval. Analytical formulas for pure diffusion (magenta, dashed), advection-diffusion of point particles (10) with $r_\mathrm{p} = 0$ (black, dashed), advection of finite-sized particles including Faxén correction (6)(blue, dashed), and the sum of advection-diffusion (10) (with $r_\mathrm{p} = 0$) and advection (6) (black, dotted). The black solid line shows the boundary layer estimate (10) that includes advection and diffusion of finite-sized particles with steric interaction as well as the hydrodynamic interaction through the Faxén correction. The general behaviour and the minimum are qualitatively captured by both the sum and the boundary layer estimate. We further have a quantitative match with the sum and boundary layer estimate at small as well as large prey sizes, but the clearance rates for intermediate prey are not exactly captured by either formula, where the numerical values are situated between the sum and the boundary layer estimate.

diffusion plays a more important role, is captured at high Péclet numbers ($Pe \gtrsim 50$). Thus the clearance rates for the smallest prey are as expected much higher than for pure diffusion, but are well represented as advection-diffusion of point particles, since the steric interaction for small highly diffusive prey becomes less important. The numerically calculated clearance rates are for the whole range reasonably well represented by the formula (10), which takes the steric interaction and the Faxén correction into account, while the summation of the

advective-diffusive clearance rate of point particles (10) with $r_\mathrm{p} = 0$ and the purely advective clearance (6) already gives a similarly good despite cruder estimate for the whole range.

SLOPPY FEEDERS

For sloppy feeders with finite foraging rates κ we have at every time step a probability $P < 1$ (2) to capture a prey particle in contact as opposed to the above case of perfect absorption, where $P = 1$. If a particle is in the contact zone for a total time T_C, its capture probability will be

$$P_\mathrm{tot} = 1 - \exp(-\kappa T_\mathrm{C}). \tag{13}$$

Thus if the contact time is large the probability of capture and thus the clearance rate will be large with the maximum clearance rate given with $P_\mathrm{tot} = 1$ as the above discussed clearance rate for a perfect absorber. For pure advection the (maximum) contact time can be approximated with the passing time for particles that follow close streamlines such that predator and prey slide along each other as long as possible [16], i.e.,

$$T_\mathrm{C} = T_\mathrm{a} \approx \frac{2\,\pi a(a + r_\mathrm{p})}{3U\,r_\mathrm{p}}. \tag{14}$$

If the contact time is approximately constant for all impacting particles we can calculate the clearance rate for sloppy feeders as

$$Q = Q_\infty(1 - \exp(-\kappa T_\mathrm{C})) \tag{15}$$

with the maximum advective clearance rate Q_∞ given by equation (6) for a perfect absorber. However, generally the clearance rate needs to be calculated with the average contact time weighted correctly with the likelihood of different impact parameters (initial prey positions).

When considering sloppy feeders with $q = 0$, which only encounter prey by diffusive transport, we can find an analytical solution for a constant flux boundary condition, that relates to the finite foraging rate. In the steady state we have a constant surface concentration $c_\mathrm{S} = c(r = a + r_\mathrm{p}) = \epsilon c_\infty > 0$, that is given as a certain fraction of the bulk concentration $c_\infty = c(r \to \infty)$. The steady state diffusion equation towards the sphere for these concentration boundary conditions has the solution [30]

$$c(r) = c_\infty \left(1 - \frac{a + r_\mathrm{p}}{r}(1 - \epsilon)\right) \tag{16}$$

and the radial flux into the surface is

$$J(r = a + r_\mathrm{p}) = -D \left.\frac{\partial c}{\partial r}\right|_{r=a+r_\mathrm{p}} = -Dc_\infty \frac{1-\epsilon}{a+r_\mathrm{p}}. \tag{17}$$

Due to the given foraging rate κ within a thin contact zone with width δ we can relate the clearance rate to the rate at which the contact zone is emptied, i.e.,

$$Q_\mathrm{D} = 4\pi a^2 \delta \kappa c_\mathrm{S} = 4\pi a^2 \delta \kappa \epsilon \, c_\infty, \tag{18}$$

with the assumption that the concentration within the contact zone is approximately constant and using the volume $4\pi a^2 \delta\kappa$ of the contact zone. This gives us the constant flux condition

$$J(r = a + r_\mathrm{p}) = -\delta\kappa. \tag{19}$$

that we can equate with equation (17) in order to calculate ϵ. We obtain the diffusive clearance rate as

$$Q_\mathrm{D} = Q_\infty \frac{\kappa T_\mathrm{D}}{1 + \kappa T_\mathrm{D}} \tag{20}$$

with the diffusive clearance rate $Q_\infty = 4\pi a D$ for a perfect absorber and the contact time

$$T_\mathrm{D} = \frac{\delta(a + r_\mathrm{p})}{D}. \tag{21}$$

The ratio $\mathcal{K} = \kappa\, T_\mathrm{D}$ between the diffusive and the absorption time scales is the Damköhler number [31]. The growth of the clearance rate for pure diffusion (20) is described with a logistic function different from the exponential estimate (15) for the advective clearance.

We numerically calculated the clearance for sloppy feeders for a range of prey sizes at various finite foraging rates down to $\kappa_\mathrm{min} = 1\,\mathrm{s}^{-1}$ (figure 3). We found that the clearance rates of small prey are much quicker reduced with finite κ than the rates for the capture of large prey, which suggests different characteristic contact times. For small foraging rates the clearance rates become constant at small prey as predicted by the expression (20) for purely diffusive capture, such that the minimum at intermediate prey size disappears.

We fitted the clearance rate as function of foraging rate for each prey size with a logistic function

$$Q = Q_\infty \frac{\kappa T_\mathrm{c}}{1 + \kappa T_\mathrm{c}}. \tag{22}$$

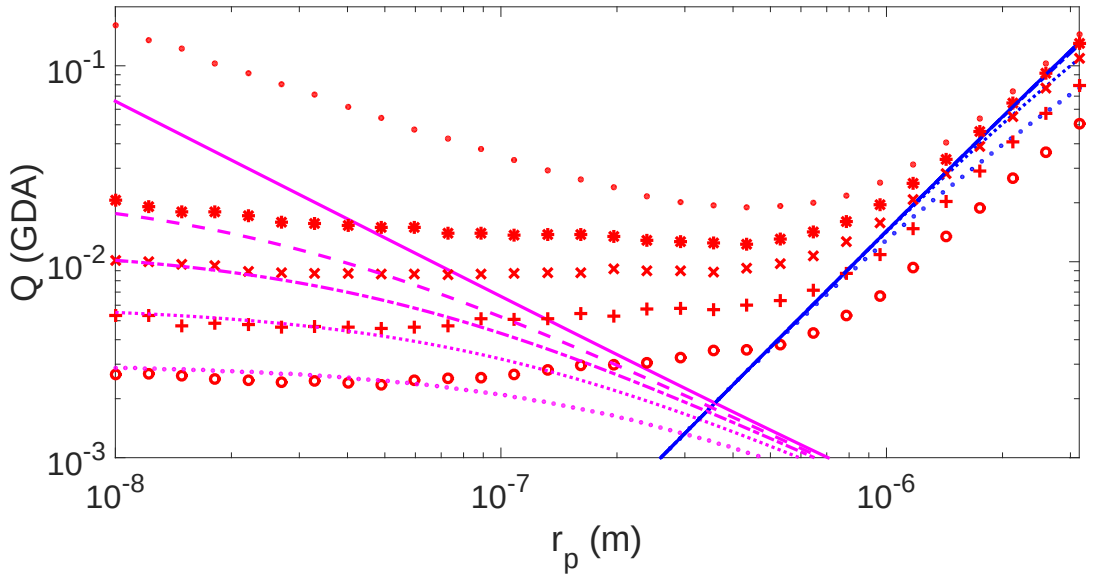

FIG. 3. Numerically calculated clearance rates for a perfect absorber (red, filled circles) and for 4 sloppy feeders as function of prey size. The foraging rates are $\kappa = 1\,\mathrm{s}^{-1}$ ('o'), $\kappa = 2\,\mathrm{s}^{-1}$ ('+'), $\kappa = 4\,\mathrm{s}^{-1}$ ('x'), $\kappa = 8\,\mathrm{s}^{-1}$ ('*'). Analytical estimate for pure diffusion (20) (magenta) and pure advection (15) (blue) (lines with decreasing dash length for decreasing κ). The prey size composition changes for sloppy feeders, which mainly capture large prey. The clearance rates for the smallest prey are drastically reduced. For sloppy feeders the purely diffusive estimates fit well for small prey sizes and small foraging rates, while the advective estimates only match for the largest prey and high foraging rates.

This functional form was found to generally give better fits for all prey sizes. It arises from an exponential distribution of contact times instead of equal contact times for each impacting particle as was assumed for (15).

From the fits we determined a typical contact time T_c, at which half of the maximum amount Q_∞ is reached (figure 4 A). Figure 4 B shows the fitted contact times together with the estimates (14) and (21) for pure advection ($T = 0$) and pure diffusion ($q = 0$) as well as the analytically calculated mean entrainment times from Mathijssen *et al.* [16]. The comparison shows that the fitted contact times are much lower than the mean entrainment times for small prey, while the contact times for large prey match with the purely advective entrainment times. The contact times, however, are expected to increase for diffusive particles, if the size of the contact zone is increased.

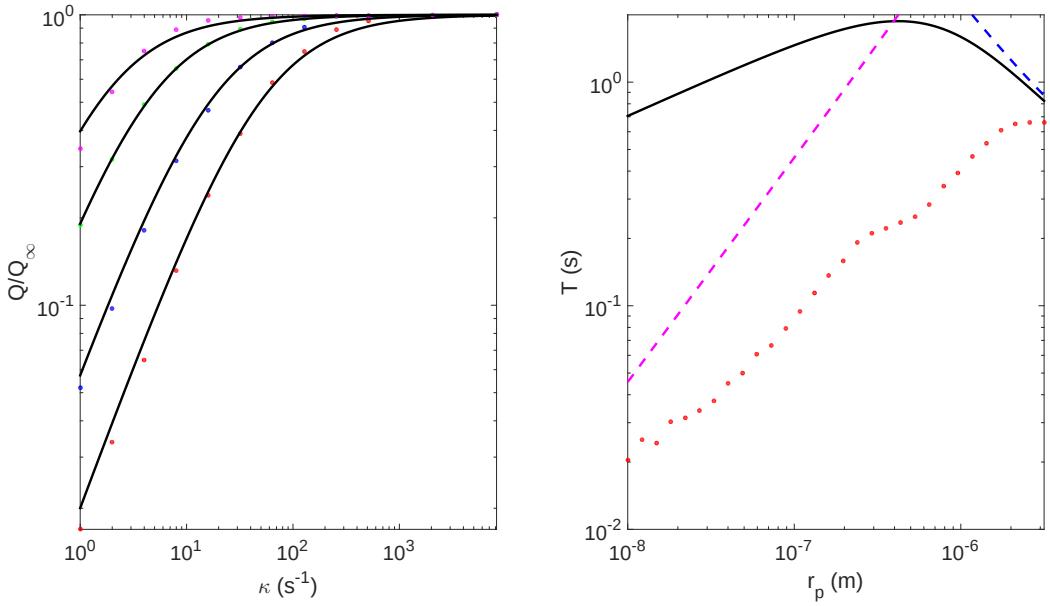

FIG. 4. Clearance rate reduction for sloppy feeders and fitted contact times. (A) The numerically calculated clearance rates as function of the foraging rate κ for different prey sizes (filled circles) with fit (black, solid) for r_p=0.01, 0.06, 0.4 and 3 μm (red, blue, green, magenta). (B) The fitted contact times as function of prey size (red, filled circles) compared to the analytical formula by Mathijssen *et al.* [16] for average entrainment times (black). The fitted contact times are smaller than the average entrainment times, especially for small, highly diffusive particles, that do not stay in very close vicinity for a long time, although being entrained.

DISCUSSION

With the use of our model results we here discuss the applicability of analytical estimates to calculate the prey-size dependent clearance rates for perfect absorbers and sloppy feeders. We use our results to calculate total capture rates using a typical marine particle size spectrum and discuss optimal predation strategies in direct interception feeders. We further summarize the concepts of contact and entrainment and their respective importance for predator-prey interactions.

In order to calculate the total amount of captured prey, we use the Sheldon concentration spectrum

$$C(r_\mathrm{p}) = \frac{c_0}{\ln(10)\, r_\mathrm{p}}, \tag{23}$$

that assumes equal amounts of prey within each logarithmic size class, with the constant biomass concentration c_0 for each decade of particle radius [4, 32]. Thus the total prey encounter rate is calculated as the integral

$$E = \int_{r_{\min}}^{r_{\max}} Q(r_{\mathrm{p}})\, C(r_{\mathrm{p}})\, \mathrm{d}r_{\mathrm{p}} \tag{24}$$

For the simulated parameter values we arrive at

$$E = 0.13\, \mathrm{GDA}\, c_0 \tag{25}$$

for a perfect absorber. The different clearance rates as well as the particle concentration as function of prey size lead to different contributions of differently sized prey to the diet of flagellates. In our model a large contribution for perfect absorbers will come from small bacteria and viruses as well as the largest prey close to the maximum prey size. We can compare the total prey capture (25) to filter-feeding choanoflagellates. The species *Diaphanoeca grandis* for example was estimated to achieve about three times higher capture rates with the sieving of a much more narrow prey size range [4].

SUMMARY AND OUTLOOK

We determined the capture rates and prey size composition for direct interception feeders on the model of a towed sphere. The prey size composition is found to be dominated by large and very small prey, while micrometer-sized prey is captured with the lowest rates by a perfect absorber. The clearance rates are well approximated by a continuous analytical estimate that takes the most important effects into account. The hydrodynamic interaction between predator and prey is modelled in terms of a Faxén correction to the particle velocity and is found to contribute about 25% to the total advective clearance rate. For sloppy feeders we can determine the reduced clearance rates as function of their foraging rate and a typical prey-size dependent contact time. The prey size composition changes and small prey is more easily lost than large prey at finite foraging rates. Direct interception feeders have the ability to feed on a large prey size range. However, even as perfect absorbers, they seem not able to reach the required capture rates for heterotrophic organisms in marine environments and thus typically need to invest in mixotrophic strategies with additional photosynthesis and uptake of dissolved nutrients.

ACKNOWLEDGEMENTS

The Centre for Ocean Life is a Villum Kann Rasmussen Centre of Excellence supported by the Villum Foundation.

[1] T. Fenchel, Marine Ecology Progress Series **8**, 211 (1982).

[2] T. Kiørboe, Biological Reviews **86**, 311 (2011).

[3] T. Fenchel, Progress in Protistology **1**, 65 (1986).

[4] L. T. Nielsen, S. S. Asadzadeh, J. Dölger, J. H. Walther, T. Kiørboe, and A. Andersen, Proceedings of the National Academy of Sciences **114**, 9373 (2017).

[5] J. Shimeta, Limnology and Oceanography **38**, 456 (1993).

[6] H. C. Berg and E. M. Purcell, Biophysical Journal **20**, 193 (1977).

[7] D. Tam and A. E. Hosoi, Proceedings of the National Academy of Sciences **108**, 1001 (2011).

[8] T. Kiørboe, H. Ploug, and U. H. Thygesen, Marine Ecology Progress Series **211**, 1 (2001).

[9] S. Michelin and E. Lauga, Physics of Fluids **23**, 101901 (2011).

[10] R. I. Jones, Marine Microbial Food Webs **8**, 87 (1994).

[11] D. I. Rubenstein and M. A. R. Koehl, The American Naturalist **111**, 981 (1977).

[12] S. K. Friedlander, Industrial and Engineering Chemistry **50**, 1161 (1958).

[13] R. G. Dorman, in *Aerosol Science*, edited by C. N. Davies (Academic Press New York, 1966).

[14] J. Pich, in *Aerosol Science*, edited by C. N. Davies (Academic Press New York, 1966).

[15] L. A. Spielman, Annual Review of Fluid Mechanics **9**, 297 (1977).

[16] A. Mathijssen, R. Jeanneret, and M. Polin, arXiv preprint , 1704.05264 (2017).

[17] V. J. Langlois, A. Andersen, T. Bohr, A. W. Visser, and T. Kiørboe, Aquatic Microbial Ecology **54**, 35 (2009).

[18] J. Dölger, L. T. Nielsen, T. Kiørboe, and A. Andersen, Scientific Reports **7**, 39892 (2017).

[19] L. A. Spielman and S. L. Goren, Environmental Science and Technology **4**, 135 (1970).

[20] B. C. Monger and M. R. Landry, Marine Ecology Progress Series **65**, 123 (1990).

[21] H. Faxén, Annalen der Physik **4**, 89 (1922).

[22] H. Faxén, Arkiv der Matematik **18**, 1 (1924).

[23] S. K. Friedlander, Journal of Colloid and Interface Science **23**, 157 (1967).

[24] N. Meyer-Vernet and J.-P. Rospars, American Journal of Physics **83**, 719 (2015).

[25] M. E. Huntley and M. Zhou, Marine Ecology Progress Series **273**, 65 (2004).

[26] J. Happel and H. Brenner, *Low Reynolds number hydrodynamics* (Martinus Nijhoff Publishers, 1983).

[27] I. Langmuir, in *The collected works by Irving Langmuir – Volume 10: atmospheric phenomena*, edited by G. Suits (Pergamon Press, 1961).

[28] V. G. Levich, *Physicochemical Hydrodynamics* (Prentice Hall, 1962).

[29] W. F. Pickard, Journal of Theoretical Biology **240**, 288 (2006).

[30] J. Crank, *The Mathematics of Diffusion* (Oxford University Press, 1975).

[31] S. Michelin and E. Lauga, Journal of Fluid Mechanics **747**, 572 (2014).

[32] R. W. Sheldon, A. Prakash, and W. H. Sutcliffe, Limnology and Oceanography **17**, 327 (1972).

6 Summary and outlook

6.1 Explored traits

Within the framework of this thesis we identified, quantified and explored physical and behavioural functional traits of flagellates and filter feeders. In the following I will summarise the essential traits that we worked with, before discussing the related trade-offs in the next section.

For flagellates we used an analytical hydrodynamics model to quantify flagellar arrangements and beat patterns through characteristic distributions and movements of forces (paper I and II). The angular force arrangement is one relevant trait that can influence swimming speed, stealth and prey clearance rates in mixotrophic biflagellates (paper II), while for helical swimmers such as *Heterosigma akashiwo* the force distance and relative magnitudes of longitudinal and transversal flagellum can be of importance to shape swimming trajectories and flows.

For filter feeders we considered traits describing the morphology, kinematics and body composition of individual organisms from choanoflagellates to centimetre-sized tunicates (paper III and IV). The feeding flow for choanoflagellates in relation to the design and kinematics of flagellum, filter, and lorica was considered in depth in paper III, where we propose a flagellar vane attached to the slender flagellum to drive the feeding flow. The modelled traits include cell size, length, frequency, amplitude, and wavelength of the flagellum, filter spacing and width of the microvilli as well as the diameter of the lorica chimney related to the width of the vane.

The general filter feeder model in paper IV relates the maximum clearance rate in filter feeders to a motor force limit and predicts gelatinous life forms to emerge within large suspension-feeding plankton. The filter area per energy content (relating energy density and content) as well as the filter speed are considered as the most important traits in this model.

We further began to explore the sloppiness of direct-interception feeders and the relation to capture rates and physical prey size selection (paper V). Obvious traits of such predators are body size, which the prey size range and the characteristic flow speed depend on, while the foraging rate can be a behavioural trait (foraging effort) that is also limited by physical constraints such as stickiness or the number and spatial extent of prey capture sites.

6.2 Trade-offs

In relation to the investigated traits we identified several trade-offs that provide insight into the variety of survival strategies. The flagellar force arrangement in biflagellates was related to a trade-off between swimming speed and hydrodynamic stealth on one side and advective prey capture on the other, which demand different force arrangements to be optimised (paper II). For a swimmer like *Heterosigma akashiwo* with one transverse and one longitudinal flagellum we can think of a trade-off between net translational and rotational velocity depending on the distribution of forces between the two flagella, where the translational velocity can be related to propulsion, while the rotational velocity might have different purposes and advantages for prey search and capture that still need to be explored (paper I).

Filter feeders with constant driving forces seem to have developed filter spacings that balance the filter permeability and the prey size range to optimise feeding rates (paper III). Another general trade-off seems to exist between maximum force and maximum power, or between maximum tension and maximum frequency of biological motors. In filter feeders a force limit seems to dominate the overall scaling of clearance rates. On the other hand, many choanoflagellates seem to use vane-like structures on the flagellum, thus investing more force in slow motion, instead of moving a naked flagellum with less force, but higher frequencies to produce the needed clearance rate. An important physical trade-off for planktonic filter feeders is the one between biomass density and body size (paper IV). Large organisms need to be gelatinous, or dense organisms should be small to filter-feed efficiently.

For interception feeders we relate sloppiness, which comes with a decreased foraging effort, to the reduction of capture rates. Organisms with a higher foraging rate capture larger amounts of prey. However, even with infinite effort in total absorption, the prey encounter rate is limited by the physical prey transport and thus makes very high absorption efficiencies less lucrative.

6.3 Outlook

The goal is to include the identified traits and trade-offs into the research scheme of the Centre for Ocean Life, i.e., we would like to connect to the Models, Nature and Function themes in order to properly contribute to the predictive trait-based approach discussed in section 1.1.

In order to relate flagellate swimming modes to different trophic strategies one could use grazing experiments together with kinematic and morphological observations. Are biflagellates with equatorial force arrangements specialised in photosynthesis or non-advective prey capture and thus focus on swimming and stealth as proposed? It is hypothesised that prey capture is often only used to supplement additional nutrients instead of carbon [Nygaard and Tobiesen, 1993]. Under which circumstances do haptophytes and other mixotrophic organisms supplement their acquired carbon with carbon from particulate prey? One could test the strategies of different flagellates by grazing

experiments, where the light level, prey and nutrient availability, and predator density can be varied independently, so that the model predictions can be tested. Did we identify the most important traits?

Population dynamics models can be used to implement different strategies of unicellular plankton through the characteristic swimming modes that define and constrain the available mixotrophic strategies. Researchers at the Centre for Ocean Life have recently developed a new model approach to mixotrophic strategies, in which the optimum investments in the collection of different resources are investigated under different external conditions [Andersen et al., 2015b; Chakraborty et al., 2017]. Can those affinities be linked and constrained through physically possible swimming modes? Can one predict with such a model a characteristic blooming pattern of flagellates with different motility modes in different seasons, or in different environments? In connection with this it would be interesting to sample the natural occurrences of flagellate swimming modes with respect to their characteristic force arrangements to find spatio-temporal patterns that can be compared to results from population dynamics and to fundamental predictions from the identified trade-offs.

Since large and small planktonic filter feeders, due to similar filter spacings, feed on the same resource, it would be worthwhile to model their competition directly while taking into account their fundamental trade-offs that connect force and body composition. Who is superior in which environment, tunicates or microbes? Although the emergence of gelatinous species can now be better understood, there are still several factors that are unclear. How do large blooms of gelatinous species occur and under which conditions? This question is currently being studied with great effort due to the possibly big ecological and especially economic impacts that are observed and expected [Condon et al., 2012]. Can gelatinous species be kept in check by smaller competitors?

We concluded in paper IV that gelatinous bodies allow organisms to be large with the feeding mode of microbes. But what are the additional advantages and disadvantages of being large and gelatinous? It has long been thought that gelatinous bodies are less attractive or less visible to predators, but predation risk is still difficult to quantify, since gelatinous organisms are easily degraded and difficult to observe, e.g. in gut content studies [Harbison, 1998]. A recent Ph.D. study by Nicolas Schnedler-Meyer [2017] at DTU Aqua investigated the competitive ability and life history strategies of jellyfish to understand the traits and success of this gelatinous group. Not only the gelatinous body, but also complicated and diverse life history strategies are used by most gelatinous organisms [Bone et al., 1998]. How do life history traits connect to the gelatinous body plan? Are gelatinous organisms generally optimized for quick and flexible adaptation to react to changes and to seize opportunities? Salps and their packaging of small prey into dense, fast-sinking fecal pellets are furthermore proposed to play an important role for carbon sequestration, which is an essential function of marine ecosystems [Bruland and Silver, 1981; Sutherland et al., 2010]. How does the filter-feeding strategy and its key traits and trade-offs relate to carbon export rates?

I hope that the investigations that I conducted in the course of my Ph.D project helped to better understand the complex strategies of flagellates and filter feeders and that the mechanistic studies will motivate further research.

Bibliography

J. L. Acuña. Pelagic tunicates: Why gelatinous? *The American Naturalist*, 158(1): 100–107, 2001.

J. L. Acuña, Á. López-Urrutia, and S. Colin. Faking giants: The evolution of high prey clearance rates in jellyfishes. *Science*, 333:1627–1629, 2011.

J. Adler. Chemotaxis in Bacteria. *Science*, 153:708–716, 1966.

R. M. Alexander. *Principles of Animal Locomotion*. Princeton University Press, 2003.

R. Almeda, H. van Someren Greve, and T. Kiørboe. Behavior is a major determinant of predation risk in zooplankton. *Ecosphere*, 8(2):e01668, 2017.

A. Andersen, N. Wadhwa, and T. Kiørboe. Quiet swimming at low Reynolds number. *Physical Review E*, 91:042712, 2015a.

K. H. Andersen. Fish and Fisheries – The size- and trait-based approach, 2017.

K. H. Andersen and J. E. Beyer. Asymptotic Size Determines Species Abundance in the Marine Size Spectrum. *The American Naturalist*, 168(1):54–61, 2006.

K. H. Andersen, D. L. Aksnes, T. Berge, Ø. Fiksen, and A. Visser. Modelling emergent trophic strategies in plankton. *Journal of Plankton Research*, 37(37):862–868, 2015b.

K. H. Andersen, T. Berge, R. J. Gonçcalves, M. Hartvig, J. Heuschele, S. Hylander, N. S. Jacobsen, C. Lindemann, E. A. Martens, A. B. Neuheimer, K. Olsson, A. Palacz, A. E. F. Prowe, J. Sainmont, S. J. Traving, A. W. Visser, N. Wadhwa, and T. Kiørboe. Characteristic Sizes of Life in the Oceans, from Bacteria to Whales. *Annual Review of Marine Science*, 8:217–241, 2016.

P. Andersen. Functional biology of the Choanoflagellate *Diaphanoeca grandis* ellis. *Marine Microbial Food Webs*, 3(2):35–50, 1988/1989.

T. R. Anderson. Plankton functional type modelling: Running before we can walk? *Journal of Plankton Research*, 27(11):1073–1081, 2005.

F. Ayaz and T. J. Pedley. Flow through and particle interception by an infinite array of closely-spaced circular cylinders. *European Journal of Fluid Mechanics – B/Fluids*, 18(2):173–196, 1999.

G. I. Barenblatt. *Scaling*. Cambridge University Press, 2003.

G. K. Batchelor. *An introduction to fluid dynamics*. Cambridge University Press, 2000.

G. K. Batchelor and J. T. Green. The hydrodynamic interaction of two small freely-moving spheres in a linear flow field. *Journal of Fluid Mechanics*, 56(2):375–400, 1972.

L. E. Becker, S. A. Koehler, and H. A. Stone. On self-propulsion of micro-machines at low Reynolds number: Purcell's three-link swimmer. *Journal of Fluid Mechanics*, 490:15–35, 2003.

H. C. Berg. How to Track Bacteria. *The Review of Scientific Instruments*, 42(6): 868–871, 1971.

H. C. Berg. *Random Walks on Biology*. Princeton University Press, 1972.

H. C. Berg. Chemotaxis in bacteria. *Annual Review of Biophysics and Bioengineering*, 4:119–136, 1975.

H. C. Berg. *E. coli in Motion*. Springer Verlag, 2004.

H. C. Berg and D. A. Brown. Chemotaxis in *Escherichia coli* analysed by Three-dimensional Tracking. *Nature*, 239:500–504, 1972.

H. C. Berg and E. M. Purcell. Physics of chemoreception. *Biophysical Journal*, 20: 193–219, 1977.

T. Berge, S. Chakraborty, P. J. Hansen, and K. H. Andersen. Modeling succession of key resource-harvesting traits of mixotrophic plankton. *The ISME Journal*, 11: 212–223, 2016.

J. R. Blake. A spherical envelope approach to ciliary propulsion. *Journal of Fluid Mechanics*, 46:199–208, 1971.

Q. Bone, J. Godeaux, J.-C. Braconnot, R. Fenaux, L. P. Madin, D. Deibel, P. R. Flood, V. Andersen, G. Gorsky, G. R. Harbison, C. P. Galt, R. W. M. Van Soest, and R. Christen. *The Biology of Pelagic Tunicates*. Oxford University Press, 1998.

C. Brennen and H. Winet. Fluid mechanics of propulsion by cilia and flagella. *Annual Review of Fluid Mechanics*, 9:339–398, 1977.

C. J. Brokaw. Flagellar Movement: A Sliding Filament Model. *Science*, 178(4060): 455–462, 1972.

J. H. Brown, J. F. Gillooly, A. P. Allen, V. M. Savage, and G. B. West. Toward a metabolic theory of ecology. *Ecology*, 85(7):1771–1789, 2004.

K. W. Bruland and M. W. Silver. Sinking Rates of Fecal Pellets from Gelatinous Zooplankton (Salps, Pteropods, Doliolids). *Marine Biology*, 63:295–300, 1981.

T. Brunet and N. King. The Origin of Animal Multicellularity and Cell Differentiation. *Developmental Cell*, 43:124–140, 2017.

H. Bruus. *Theoretical Microfluidics*. Oxford University Press, 2008.

S. Chakraborty, L. T. Nielsen, and K. H. Andersen. Trophic Strategies of Unicellular Plankton. *The American Naturalist*, 189(4):E77–E90, 2017.

R. H. Condon, W. M. Graham, C. M. Duarte, K. A. Pitt, C. H. Lucas, S. H. D. Haddock, K. R. Sutherland, K. L. Robinson, M. N. Dawson, M. B. Decker, C. E. Mills, J. E. Purcell, M. A. Hermes, H. Mianzan, S. I. Uye, S. Gelcich, and L. P. Madin. Questioning the rise of gelatinous zooplankton in the world's oceans. *Bioscience*, 62: 160–169, 2012.

R. Cortez, L. Fauci, and A. Medovikov. The method of regularized Stokeslets. *Physics of Fluids*, 17:031504, 2005.

J. Crank. *The Mathematics of Diffusion*. Oxford University Press, 1975.

J. C. Crocker and D. G. Grier. Methods of Digital Video Microscopy for Colloidal Studies. *Journal of Colloid and Interface Science*, 179:298–310, 1996.

J. C. Crocker and E. R. Weeks. Particle tracking using IDL. URL `http://www.physics.emory.edu/faculty/weeks//idl/`.

S. Dijkgraaf. The functioning and significance of the lateral-line organs. *Biological Reviews*, 38:51–105, 1962.

J. Dölger, T. Bohr, and A. Andersen. An analytical model of flagellate hydrodynamics. *Physica Scripta*, 92:044003, 2017a.

J. Dölger, L. T. Nielsen, T. Kiørboe, and A. Andersen. Swimming and feeding of mixotrophic biflagellates. *Scientific Reports*, 7:39892, 2017b.

R. G. Dorman. Filtration. In C. N. Davies, editor, *Aerosol Science*. Academic Press New York, 1966.

K. Drescher, K. C. Leptos, and R. E. Goldstein. How to track protists in three dimensions. *Review of Scientific Instruments*, 80:014301, 2009.

K. Drescher, R. E. Goldstein, N. Michel, M. Polin, and I. Tuval. Direct Measurement of the Flow Field around Swimming Microorganisms. *Physical Review Letters*, 105: 168101, 2010.

K. Drescher, J. Dunkel, L. H. Cisneros, S. Ganguly, and R. E. Goldstein. Fluid dynamics and noise in bacterial cell–cell and cell–surface scattering. *Proceedings of the National Academy of Sciences*, 108:10940–10945, 2011.

R. Dudley and C. Gans. A Critique of Symmorphosis and Optimality Models in Physiology. *Physiological Zoology*, 64(3):627–637, 1991.

J. Elgeti, R. G. Winkler, and G. Gompper. Physics of microswimmers—single particle motion and collective behavior: a review. *Report of Progress in Physics*, 78:056601 (50pp), 2011.

H. Faxén. Der Widerstand gegen die Bewegung einer starren Kugel in einer zähen Flüssigkeit, die zwischen zwei parallelen Ebenen Wänden eingeschlossen ist. *Annalen der Physik*, 4(68):89–119, 1922.

H. Faxén. Der Widerstand gegen die Bewegung einer starren Kugel in einer zähen Flüssigkeit, die zwischen zwei parallelen Ebenen Wänden eingeschlossen ist. *Arkiv fur Matematik, Astronomi och Fysik*, 18(29):1–52, 1924.

R. Fenaux. Anatomy and functional morphology of the appendicularia. In Q. Bone, editor, *The Biology of Pelagic Tunicates*. Oxford University Press, 1998.

T. Fenchel. Ecology of Heterotrophic Microflagellates. i. Some Important Forms and Their Functional Morphology. *Marine Ecology Progress Series*, 8:211–223, 1982.

T. Fenchel. Protozoan Filter Feeding. *Progress in Protistology*, 1:65–115, 1986.

T. Fenchel. Marine plankton food chains. *Annual Review of Ecology, Evolution, and Systematics*, 19:19–38, 1988.

G. O. Fistarol, C. Legrand, and E. Granéli. Allelopathic effect of *Prymnesium parvum* on a natural plankton community. *Marine Ecological Progress Series*, 255:115–125, 2003.

K. J. Flynn, D. E. Stoecker, A. Mitra, J. A. Raven, and P. M. Glibert. Misuse of the phytoplankton – zooplankton dichotomy: the need to assign organisms as mixotrophs within plankton functional types. *Journal of Plankton Research Horizons*, 35:5–11, 2013.

M. J. Follows and S. Dutkiewicz. Modeling diverse communities of marine microbes. *Annual Review of Marine Science*, 3:427–451, 2011.

S. K. Friedlander. Particle Diffusion in Low-Speed Flows. *Journal of Colloid and Interface Science*, 23:157–164, 1967.

J. Gerritsen and J. R. Strickler. Encounter Probabilities and Community Structure in Zooplankton: a Mathematical Model. *Journal of the Fisheries Board of Canada*, 34:73–82, 1977.

I. R. Gibbons. Cilia and Flagella of Eukaryotes. *The Journal of Cell Biology*, 91: 107–124, 1981.

J. F. Gilliam and D. F. Fraser. Habitat selection under predation hazard: Test of a model with foraging minnows. *Ecology*, 68:1856–1862, 1987.

J. Godeaux, Q. Bone, and J.-C. Braconnot. Anatomy of Thaliacea. In Q. Bone, editor, *The Biology of Pelagic Tunicates*. Oxford University Press, 1998.

R. E. Goldstein. Green Algae as Model Organisms for Biological Fluid Dynamics. *Annual Review of Fluid Mechanics*, 47:343–75, 2015.

J. M. Gonzalez and C. A. Suttle. Grazing by marine nanoflagellates on viruses and virus-sized particles: ingestion and digestion. *Marine Ecology Progress Series*, 94: 1–10, 1993.

J. Gray and G. J. Hancock. The propulsion of sea-urchin spermatozoa. *Journal of Experimental Biology*, 432:802–814, 1955.

J. S. Guasto, R. Rusconi, and R. Stocker. Fluid Mechanics of Planktonic Microorganisms. *Annual Reviews of Fluid Mechanics*, 44:373–400, 2012.

B. Hansen, P. K. Bjørnsen, and P. J. Hansen. The size ratio between planktonic predators and their prey. *Limnology and Oceanography*, 39(2):395–403, 1997a.

P. J. Hansen, P. K. Bjørnsen, and B. W. Hansen. Zooplankton grazing and growth: Scaling within the 2-2,000-μm body size range. *Limnology and Oceanography*, 42(4): 687–704, 1997b.

J. Happel and H. Brenner. *Low Reynolds number hydrodynamics*. Martinus Nijhoff Publishers, 1983.

G. R. Harbison. The parasites and predators of Thaliacea. In Q. Bone, editor, *The Biology of Pelagic Tunicates*. Oxford University Press, 1998.

K. Hausmann, N. Hülsmann, and R. Radek. *Protistology*. Schweizbart'sche Verlagsbuchhandlung Stuttgart, 2nd edition, 2003.

J. J. L. Higdon. The generation of feeding currents by flagellar motions. *Journal of Fluid Mechanics*, 94(2):306–330, 1979a.

J. J. L. Higdon. A hydrodynamic analysis of flagellar propulsion. *Journal of Fluid Mechanics*, 90(4):685–711, 1979b.

P. R. Hobson and J. Watson. The principles and practice of holographic recording of plankton. *Journal of Optics A: Pure and Applied Optics*, 4:S34–S49, 2002.

C. S. Holling. Some characteristics of simple types of predation and parasitism. *The Canadian Entomologist*, 91:385–398, 1959.

E. Holmqvist and T. Willen. Fish mortality caused by *Prymnesium parvum*. *Vatten*, 49:110–115, 1993.

A. I. Houston, J. M. McNamara, and J. M. C. Hutchinson. General results concerning the trade-off between gaining energy and avoiding predation. *Philosophical Transactions of the Royal Society B*, 341:375–397, 1993.

A. J. Hulbert. A Sceptics View: "kleiber's law" or the "3/4 rule" is neither a Law nor a Rule but Rather an Empirical Approximation. *Systems*, 2:186–202, 2014.

J. M. Jeschke, M. Kopp, and R. Tollrian. Consumer-food systems: why type i functional responses are exclusive to filter feeders. *Biological Reviews*, 79:337–349, 2004.

H. Jiang, T. R. Osborn, and C. Meneveau. The flow field around a freely swimming copepod in steady motion. part i: Theoretical analysis. *Journal of Plankton Research*, 24(3):167–189, 2002.

D. Joly, C. Bressac, and D. Lachaise. Disentangling giant sperm. *Nature*, 377:202, 1995.

R. I. Jones. Mixotrophy in planktonic protists as a spectrum of nutritional strategies. *Marine Microbial Food Webs*, 8:87–96, 1994.

C. B. Jørgensen. Quantitative aspects of flter feeding in invertebrates. *Biological Reviews*, 30:391–453, 1955.

W. Kauzmann. *Kinetic Theory of Gases*. W. A. Benjamin, 1966.

M. Kawachi and I. Inouye. Functional roles of the haptonema and the spine scales in the feeding process of *Chrysochromulina spinifera* (Fournier) Pienaar et Norris (Haptophyta = Prymnesiophyta). *Phycologia*, 34(3):193–200, 1995.

M. Kawachi, I. Inouye, O. Maeda, and M. Chihara. The haptonema as food-capturing device: observations on *Chrysochromulina hirta* (Prymnesiophyceae). *Phycologia*, 30(6):563–573, 1991.

J. B. Keller. Viscous flow through a grating or lattice of cylinders. *Journal of Fluid Mechanics*, 18(1):94–96, 1964.

S. R. Kerr. Theory of size distribution in ecological communities. *Journal of the Fisheries Research Board of Canada*, 31(12):1859–1862, 1974.

S. Kim and P. V. Arunachalam. The general solution for an ellipsoid in low-Reynolds-number flow. *Journal of Fluid Mechanics*, 178:635–547, 1987.

S. Kim and S. J. Karilla. *Microhydrodynamics*. Dover Publications, 2005.

T. Kiørboe. *A mechanistic approach to plankton ecology*. Princeton University Press, 2008.

T. Kiørboe. How zooplankton feed: mechanisms, traits and trade-offs. *Biological Reviews*, 86:311–339, 2011.

T. Kiørboe. Zooplankton body composition. *Limnology and Oceanography*, 58(5): 1843–1850, 2013.

T. Kiørboe. Fluid dynamic constraints on resource acquisition in small pelagic organisms. *The European Physical Journal Special Topics*, 225:669—-683, 2016.

T. Kiørboe and A. G. Hirst. Data from: Shifts in mass scaling of respiration, feeding, and growth rates across life-form transitions in marine pelagic organisms. american naturalist, 2013. URL `http://doi.pangaea.de/10.1594/PANGAEA.819856`.

T. Kiørboe and A. G. Hirst. Shifts in Mass Scaling of Respiration, Feeding, and Gowth rates across Life-Form Transitions in Marine Pelagic Organisms. *Limnology and Oceanography*, 158(4):E000, 2014.

T. Kiørboe and A. W. Visser. Predator and prey perception in copepods due to hydromechanical signals. *Marine Ecology Progress Series*, 179:81–95, 1999.

T. Kiørboe, A. Andersen, V. J. Langlois, H. H. Jakobsen, and T. Bohr. Mechanisms and feasibility of prey capture in ambush-feeding zooplankton. *Proceedings of the National Academy of Sciences*, 106(30):12394–12399, 2009.

T. Kiørboe, A. Andersen, V. J. Langlois, and H. H. Jakobsen. Unsteady motion: escape jumps in planktonic copepods, their kinematics and energetics. *Journal of the Royal Society Interface*, 7:1591–1602, 2010.

T. Kiørboe, H. Jiang, R. J. Gonçalves, L. T. Nielsen, and N. Wadhwa. How zooplankton feed: mechanisms, traits and trade-offs. *Proceedings of the National Academy of Sciences*, 111(32):11738—11743, 2014.

J. B. Kirkegaard and R. E. Goldstein. Filter-feeding, near-field flows, and the morphologies of colonial choanoflagellates. *Physical Review E*, 94:052401, 2016.

M. Kleiber. Body size and metabolism. *Hilgardia*, 6(11):315–353, 1932.

M. A. R. Koehl and J. R. Strickler. Copepod Feeding Currents: Food Capture at Low Reynolds Number. *Limnology and Oceanography*, 26:1062–1073, 1981.

M. A. R. Koehl and B. D. Wolcott. Can function at the organismal level explain ecological patterns? *Ecology*, 85(7):1808–1810, 2004.

S. Krause, X. Le Roux, P. A. Niklaus, P. M. Van Bodegom, J. T. Lennon, S. Bertilsson, H.-P. Grossart, L. Philippot, and P. L. E. Bodelier. Trait-based approaches for understanding microbial biodiversity and ecosystem functioning. *Frontiers in Microbiology*, 5(251):1–10, 2014.

H. Lamb. *Hydrodynamics*. Dover Publications, 6th edition, 1932.

V. J. Langlois, A. Andersen, T. Bohr, A. W. Visser, and T. Kiørboe. Significance of swimming and feeding currents for nutrient uptake in osmotrophic and interception-feeding flagellates. *Aquatic Microbial Ecology*, 54:35–44, 2009.

I. Langmuir. Report on Smokes and Filters. In G. Suits, editor, *The collected works by Irving Langmuir – Volume 10: atmospheric phenomena*. Pergamon Press, 1961.

E. Lauga. Life around the scallop theorem. *Soft Matter*, 7:3060–3065, 2011.

E. Lauga and T. R. Powers. The hydrodynamics of swimming microorganisms. *Reports on Progress in Physics*, 72:096601 (36 pp), 2009.

B. S. C. Leadbeater. The 'mystery' of the flagellar vane in choanoflagellates. *Beiheft zur Nova Hedwigia*, 130:213–224, 2006.

B. S. C. Leadbeater. *Choanoflagellates: Evolution, Biology and Ecology*. Cambridge University Press, 2015.

B. S. C. Leadbeater and R. Cheng. Costal strip production and lorica assembly in the large tectiform choanoflagellate *Diaphanoeca grandis* ellis. *Euopean Journal of Protistology*, 46:96–110, 2010.

J. T. Lehman. The filter-feeder as an optimal forager, and the predicted shapes of feeding curves. *Limnology and Oceanography*, 21(4):501–516, 1976.

V. G. Levich. *Physicochemical Hydrodynamics*. Prentice Hall, 1962.

J. Lighthill. On the Squirming Motion of Nearly Spherical Deformable Bodies through Liquids at Very Small Reynolds Numbers. *Communications on Pure and Applied Mathematics*, 5:109–118, 1952.

J. Lighthill. Flagellar Hydrodynamics: The John von Neumann Lecture. *SIAM Review*, 18(2):161–230, 1976.

E. Litchman and C. A. Klausmeier. Trait-Based Community Ecology of Phytoplankton. *Annual Review of Ecology, Evolution, and Systematics*, 39:615–639, 2008.

E. Litchman, M. D. Ohman, and T. Kiørboe. Trait-based approaches to zooplankton communities. *Journal of Plankton Research*, 35(3):178–185, 2013.

F. Lombard, E. Selander, and T. Kiørboe. Active prey rejection in the filter-feeding appendicularian Oikopleura dioica. *Limnology and Oceanography*, 56(4):1504–1512, 2011.

P. S. Lovely and F. W. Dahlqvist. Statistical measures of bacterial motility and chemotaxis. *Journal of Theoretical Biology*, 50:477–496, 1975.

L. P. Madin. Aspects of jet propulsion in salps. *Canadian Journal of Zoology*, 68: 765–777, 1990.

L. P. Madin, C. M. Cetta, and V. L. McAlister. Elemental and Biochemical Composition of Salps (Tunicata: Thaliacea). *Marine Biology*, 63:217–226, 1981.

J. L. Mah, K. K. Christensen-Daalsgard, and S. P. Leys. Choanoflagellate and choanocyte collar-flagellar systems and the assumption of homology. *Evolution and Development*, 16(1):25–37, 2014.

M. Majaneva, J.-M. Rintala, S. Hajdu, S. Hällfors, G. Hällfors, A.-T. Skjevik, S. Gromisz, J. Kownacka, S. Busch, and J. Blomster. The extensive bloom of alternate-stage *Prymnesium polylepis* (haptophyta) in the Baltic Sea during autumn–spring 2007–2008. *European Journal of Phycology*, 47(3):310–320, 2012.

A. M. Makarieva, V. G. Gorshkov, B.-L. Lib, S. L. Chown, P. B. Reich, and V. M. Gavrilov. Mean mass-specific metabolic rates are strikingly similar across life's major domains: Evidence for life's metabolic optimum. *Proceedings of the National Academy of Sciences*, 105(44):16994–16999, 2008.

J. H. Marden and L. R. Allen. Molecules, muscles, and machines: Universal performance characteristics of motors. *Proceedings of the National Academy of Sciences*, 99(7):4161–4166, 2002.

E. A. Martens, N. Wadhwa, N. S. Jacobsen, C. Lindemann, K. H. Andersen, and A. Visser. Size structures sensory hierarchy in ocean life. *Proceedings of the Royal Society B*, 282:20151346, 2016.

J. Mauchline. The Biology of Calanoid Copepods. In John H. S. Blaxter, B. Douglas, and P. A. Tyler, editors, *Advances in marine biology*, volume 33. Academic Press, 1998.

B. J. McGill, B. J. Enquist, E. Weiher, and M. Westoby. Rebuilding community ecology from functional traits. *Trends in Ecology and Evolution*, 21(4):178–185, 2006.

N. Meyer-Vernet and J.-P. Rospars. How fast do living organisms move: Maximum speeds from bacteria to elephants and whales. *American Journal of Physics*, 83(8): 719–722, 2015.

N. Meyer-Vernet and J.-P. Rospars. Maximum relative speeds of living organisms: Why do bacteria perform as fast as ostriches? *Physical Biology*, 13:066006, 2016.

J. D. Murray. *Mathematical Biology*. Springer Verlag, 2nd edition, 1993.

L. T. Nielsen, S. S. Asadzadeh, J. Dölger, J. H. Walther, T. Kiørboe, and A. Andersen. Hydrodynamics of microbial filter feeding. *Proceedings of the National Academy of Sciences*, 114(35):9373—-9378, 2017.

K. Nygaard and A. Tobiesen. Bacterivory in algae: A survival strategy during nutrient limitation. *Limnology and Oceanography*, 38(2):273–279, 1993.

C. W. Oseen. *Hydrodynamik*. Akademischer Verlag Leipzig, 1927.

O. S. Pak and E. Lauga. Theoretical models in low-Reynolds number locomotion. In C. Duprat and H. Stone, editors, *Fluid-Structure Interactions in Low-Reynolds-Number Flows*. Royal Society of Chemistry, 2012.

S. Pawar, G. Woodward, and A. I. Dell. *Advances in ecological research: trait-based ecology – from structure to function*. Elsevier, 1st edition, 2015.

G. J. Pazour, N. Agrin, J. Leszyk, and G. B. Witman. Proteomic analysis of a eukaryotic cilium. *The Journal of Cell Biology*, 170(1):103–113, 2005.

M. E. Pettitt, B. A. A. Orme, J. R. Blake, and B. S. C. Leadbeater. The hydrodynamics of filter feeding in choanoflagellates. *European Journal of Protistology*, 38:313–332, 2002.

J. Pich. Theory of aerosol filtration by fibrous and membrane filters. In C. N. Davies, editor, *Aerosol Science*. Academic Press New York, 1966.

W. F. Pickard. Absorption by a moving spherical organelle in a heterogeneous cytoplasm: Implications for the role of trafficking in a symplast. *Journal of Theoretical Biology*, 240:288–301, 2006.

E. M. Purcell. Life at Low Reynolds Number. *American Journal of Physics*, 45:3–11, 1977.

M. Raffel, C. E. Willert, S. T. Wereley, and J. Kompenhans. *Particle Image Velocimetry*. Springer Verlag, 2nd edition, 2007.

H. U. Riisgård and P. S. Larsen. Minireview: Ciliary filter feeding and bio-fluid mechanics–present understanding and unsolved problems. *Limnology and Oceanography*, 46(4):882–891, 2001.

H. U. Riisgård and P. S. Larsen. Particle capture mechanisms in suspension-feeding invertebrates. *Marine Ecology Progress Series*, 418:255–293, 2010.

B. Rodenborn, Chih-Hung Chen, H. L. Swinney, B. Liu, and H. P. Zhang. Propulsion of microorganisms by a helical flagellum. *Proceedings of the National Academy of Sciences*, 110(5):E338–E347, 2013.

M. Roper, M. J. Dayel, R. E. Pepper, and M. A. R. Koehl. Cooperatively Generated Stresslet Flows Supply Fresh Fluid to Multicellular Choanoflagellate Colonies. *Physical Review Letters*, 110:228104, 2013.

D. I. Rubenstein and M. A. R. Koehl. The Mechanisms of Filter Feeding: Some Theoretical Considerations. *The American Naturalist*, 111(981):981–994, 1977.

L. E. Schmidt and P. J. Hansen. Allelopathy in the prymnesiophyte *Chrysochromulina polylepis*: effect of cell concentration, growth phase and pH. *Marine Ecology Progress Series*, 216:67–81, 2001.

K. Schmidt-Nielsen. *Scaling: Why is animal size so important?* Cambridge University Press, 1984.

K. Schmidt-Nielsen. *Animal physiology: Adaptation and environment.* Cambridge University Press, 5th edition, 1997.

N. Azaña Schnedler-Meyer. *The lives and times of jellyfish: Modelling the population dynamics and ecological role of jellyfish in marine pelagic ecosystems.* PhD thesis, Technical University of Denmark, 2017.

T. W. Schoener. Mechanistic Approaches to Community Ecology: A New Reductionism? *American Zoologist*, 26:81–106, 1986.

R. W. Sheldon and T. R. Parsons. A Continuous Size Spectrum for Particulate Matter in the Sea. *Journal of the Fisheries Research Board of Canada*, 24(5):909–915, 1967.

R. W. Sheldon, A. Prakash, and W. H. Sutcliffe. The size distribution of particles in the ocean. *Limnology and Oceanography*, 17(3):327–340, 1972.

J. Sheng, E. Malkiel, and J. Katz. Digital holographic microscope for measuring three-dimensional particle distributions and motions. *Applied Optics*, 45(16):3893–3901, 2006.

J. Sheng, E. Malkiel, J. Katz, J. Adolf, R. Belas, and A. R. Place. Digital holographic microscopy reveals prey-induced changes in swimming behavior of predatory dinoflagellates. *Proceedings of the National Academy of Sciences*, 104(44):17512–17517, 2007.

J. Shimeta. Diffusional encounter of submicrometer suspension feeders. *Limnology and Oceanography*, 38(2):456–465, 1993.

J. Shimeta and P. A. Jumars. Physical mechanism and rates of particle capture by suspension feeders. *Oceanography and Marine Biology: An Annual Review*, 29:191–257, 1991.

N. R. Silvester. Some Hydrodynamic Aspects of Filter Feeding with Rectangular-Mesh Nets. *Journal of Theoreticak Biology*, 103:265–286, 1983.

M. A. Sleigh. Flagellar beat patterns and their possible evolution. *BioSystems*, 14: 423–431, 1981.

L. A. Spielman. Particle capture from low-speed laminar flows. *Annual Review of Fluid Mechanics*, 9:297–319, 1977.

G. J. Stephens, B. Johnson-Kerner, W. Bialek, and W. S. Ryu. Dimensionality and Dynamics in the Behavior of *C. elegans*. *PLOS Computational Biology*, 4(4):e1000028, 2008.

H. A. Stone and C. Duprat. Low-Reynolds-Number Flows. In *Fluid-Structure Interactions in Low-Reynolds-Number Flows*. Royal Society of Chemistry, 2012.

K. R. Sutherland and L. P. Madin. A comparison of filtration rates among pelagic tunicates using kinematic measurements. *Marine Biology*, 157:755–764, 2010a.

K. R. Sutherland and L. P. Madin. Comparative jet wake structure and swimming performance of salps. *The Journal of Experimental Biology*, 213:2967–2975, 2010b.

K. R. Sutherland, L. P. Madin, and R. Stocker. Filtration of submicrometer particles by pelagic tunicates. *Proceedings of the National Academy of Sciences*, 107(34): 15129–15134, 2010.

Y. Tadir, W. H. Wright, O. Vafa, T. Ord, R. H. Asch, and M. W. Berns. Micromanipulation of sperm by a laser generated optical trap. *Fertility and Sterility*, 52(5): 970–873, 1989.

K. Tamada and H. Fujikawa. The steady two-dimensional flow of viscous fluid at low Reynolds numbers passing through an infinite row of equal parallel circular cylinders. *The Quarterly Journal of Mechanics and Applied Mathematics*, 10:542–432, 1957.

G. I. Taylor. Analysis of the swimming of microscopic organisms. *Proceedings of the Royal Society A*, 209:447–461, 1951.

U. Tillmann. Phagotrophy by a plastidic haptophyte, *Prymnesium patelliferum*. *Aquatic Marine Ecology*, 14:155–160, 1998.

U. Tillmann. Kill and Eat your Predator: A Winning Strategy of the Planktonic Flagellate *Prymnesium parvum*. *Aquatic Microbial Ecology*, 32:73–84, 2003.

P. Tiselius and P. R. Jonsson. Effects of copepod foraging behavior on predation risk: An experimental study of the predatory copepod *Pareuchaeta norvegica* feeding on *Acartia clausi* and *A. tonsa* (Copepoda). *Limnology and Oceanography*, 42(1):164–170, 1997.

L. Turner, W. S. Ryu, and H. C. Berg. Real-Time Imaging of Fluorescent Flagellar Filaments. *Journal of Bacteriology*, 182(10):2793–2801, 2000.

A. W. Visser. Hydromechanical signals in the plankton. *Marine Ecology Progress Series*, 222:1–24, 2001.

A. W. Visser. Motility of zooplankton: fitness, foraging and predation. *Journal of Plankton Research*, 29(5):447–461, 2007.

A. W. Visser and T. Kiørboe. Plankton motility patterns and encounter rates. *Oecologia*, 148:538–546, 2006.

S. Vogel. *Comparative biomechanics: Life's Physical World*. Princeton University Press, 2nd edition, 2013.

N. Wadhwa. *Zooplankton Hydrodynamics – An investigation into the physics of aquatic interactions*. PhD thesis, Technical University of Denmark, 2015.

K. Y. Wan, K. C. Leptos, and R. E. Goldstein. Lag, lock, sync, slip: the many 'phases' of coupled flagella. *Journal of the Royal Society Interface*, 11:20131160, 2014.

E. Weiher, G. D. P. Clarke, and P. A. Keddy. Community assembly rules, morphological dispersion, and the coexistence of plant species. *Oikos*, 81(2):309–322, 1998.

G. B. West and J. H. Brown. The origin of allometric scaling laws in biology from genomes to ecosystems: towards a quantitative unifying theory of biological structure and organization. *The Journal of Experimental Biology*, 208:1575–1592, 2005.

D. R. Wilkie. The relation between force and velocity in human muscle. *Journal of Physiology*, 110:249–280, 1950.

C. Winter, T. Bouvier, M. G. Weinbauer, and T. F. Thingstad. Trade-offs between Competition and Defense Specialists among Unicellular Planktonic Organisms: the "Killing the Winner" Hypothesis Revisited. *Microbiology and Molecular Biology Reviews*, 74(1):42–57, 2010.

K. W. Wirtz. Intermittency in processing explains the diversity and shape of functional grazing responses. *Oecologia*, 169:879–894, 2012.

J. K. Wróbel, R. Cortez, D. Varela, and L. Fauci. Regularized image system for Stokes flow outside a solid sphere. *Journal of Computational Physics*, 317:165–184, 2016.

J. Yen, P. H. Lenz, and D. K. Hartline. Mechanoreception in marine copepods: electrophysiological studies on the first antennae. *Journal of Plankton Research*, 14: 495–512, 1992.

J. Yen, M. J. Weissburg, and M. H. Doall. The fluid physics of signal perception by mate-tracking copepods. *Philosophical Transactions of the Royal Society B*, 353: 787–804, 1998.